THESE DE DOCTORAT DE L'ETABLISSEMENT UNIVERSITE BOURGOGNE FRANCHE-COMTE PREPAREE AU LABORATOIRE INTERDISCIPLINAIRE CARNOT DE BOURGOGNE

Ecole doctorale n°553
Carnot-Pasteur

Doctorat de Physique

Par
Mme. María Daniela BARRIOS PÉREZ

Design and Computer Simulations of 2D MeX_2 (Me = transition metal) Nanopores for DNA and Protein Detection and Analysis

Thèse présentée et soutenue à Dijon, le 07/01/2020

Composition du Jury :

- M. MEUNIER, Vincent. Professeur à Rensselaer Polytechnic Institute. Président.
- M. MAURIN, Guillaume. Professeur à l'Institut Charles Gerhardt Montpellier. Rapporteur.
- Mme. RADENOVIC, Aleksandra. Professeure à l'École Polytechnique Fédérale de Lausanne. Rapporteur.
- M. POLITANO, Olivier. Maitre de conférences à l'Université de Bourgogne. Examinateur.
- M. SENET, Patrick. Professeur à l'Université de Bourgogne. Directeur de thèse.
- M. NICOLAÏ, Adrien. Maitre de conférences à l'Université de Bourgogne. Co-directeur de thèse.

Acknowledgements

I wish to express my deepest gratitude to my supervisors Prof. Patrick SENET and Dr. Adrien NICOLAÏ, and Prof. Patrice DELARUE from the Physique appliquée aux protéines (PhAP) group for their great advice, valuable time, guidance, encouragement and support during this PhD journey. I would also like to pay my special regards to the jury committee: Professors Vincent MEUNIER, Guillaume MAURIN, Aleksandra RADENOVIC and Dr. Olivier POLITANO, whose contributions in the revision of this thesis manuscript and presentation represented a milestone in the completion of this PhD. I am deeply grateful to our collaborators from Prof. Vincent MEUNIER's theoretical group at the Rensselaer Polytechnic Institute and Prof. Marija DRNDIĆ's experimental group at the University of Pennsylvania, to whom I had the opportunity to visit and exchange ideas on the progress of this work. Finally, I would like to thank the Ecole Doctoral Carnot-Pasteur and all the active members and colleagues from the Laboratoire Interdisciplinaire Carnot de Bourgogne for their technical assistance provided during this work.

This PhD project was supported by a grant from the Air Force Office of Scientific Research (AFOSR), as part of a joint program with the Directorate for Engineering of the National Science Foundation (NSF), Emerging Frontiers and Multidisciplinary Office Grant No. FA9550-17-1-0047, and the NSF Grant No. EFRI 2-DARE (EFRI-1542707). Part of the work was funded by the Conseil Regional de Bourgogne Franche-Comté (Grant Nos. PARI NANO2BIO and ANER NANOSEQ). The simulations were performed using HPC resources from DSI-CCuB (Université de Bourgogne).

Dedicado a mi familia. Quiero agradecer a mis padres Manuel y Esperanza, por su apoyo incondicional en la distancia y en todo momento. También quiero agradecer a mi esposo Rafael por su apoyo absoluto, total e ilimitado. Agradezco también a mis familiares (familias Barrios Reinoza, Pérez Ramírez y Arias García) y amigos, que a pesar de estar del otro lado del planeta y ahora en todas partes de éste, han estado presentes en cada etapa de este proceso.

Thank you.
Gracias.
Merci.

Résumé

Les membranes nanoporeuses solides [en anglais, SSN (Solid State Nanopore)] sont devenues des dispositifs polyvalents pour l'analyse des biomolécules. L'une des applications les plus prometteuses des SSN est le séquençage de l'ADN et des protéines avec un coût réduit et une vitesse d'exécution plus rapide que les méthodes actuelles de séquençage. Le séquençage par SSN est basé sur la mesure des variations de courant ionique observées quand une biomolécule, dans un milieu électrolytique, est forcée de traverser de manière séquentielle un nanopore sous l'action d'une différence de potentiel électrique appliquée. Lorsque la biomolécule passe au travers du nanopore, elle occupe de manière transitoire le volume du nanopore et bloque ainsi le passage des ions du milieu électrolytique. Le blocage du courant est dépendant de la nature et de l'encombrement stérique des groupements chimiques des monomères constituant la biomolécule. Donc la détection ultra-rapide des variations de courant ionique lors du passage de celle-ci au travers du nanopore, peut fournir des informations sur sa séquence. La résolution avec laquelle la séquence peut être déterminée dépend de la taille des nanopores et de l'épaisseur de la membrane. Les matériaux à deux dimensions tels que le graphène et les TMDC (Transition Metal DiChalcogenides) (MoS_2, WS_2,...) sont des candidats très prometteurs pour le développement des applications de séquençage par SSN. A partir de simulations de dynamique moléculaire (DM) tous atomes, nous avons étudié la faisabilité d'utiliser des SSN de type MoS_2 pour le séquençage des protéines. En premier lieu, nous avons étudié la conductance d'une membrane nanoporeuse de MoS_2 de 1 à 5 couches d'épaisseur possédant un seul nanopore de diamètre compris entre 1.0 et 5.0 nm et plongée dans un électrolyte de KCl. Nous avons démontré que le modèle de conductance macroscopique des membranes nanoporeuses cessait d'être valable pour les plus petits nanopores (diamètre < 5 nm). En analysant les simulations de DM des membranes de MoS_2, nous avons développé un modèle modifié qui permet d'interpréter les mesures de courant ionique quel que soit le diamètre du nanopore. En second lieu, nous avons simulé le passage de la lysine et du di-lysine, ainsi que d'une protéine modèle, au travers de nanopores de membranes de MoS_2, plongées dans un électrolyte de KCl, et soumises à une différence de potentiel électrique. A partir de nos résultats, nous avons proposé que l'utilisation d'acides aminés chargés positivement ou négativement fixés de manière covalente à une protéine pourrait s'avérer une technique efficace pour favoriser l'entrée des protéines à travers des nanopores dans des expériences de translocation. De plus, nous avons établi la relation entre la trajectoire de la protéine au travers du nanopore et les fluctuations de courant ionique simulées. En troisième lieu, nous avons examiné la conductance ionique de membranes de MoS_2 dont les pores ont un diamètre inférieur au nanomètre (sub-nm). Nous avons effectué des simulations de DM de ces systèmes en utilisant le potentiel réactif ReaxFF. Ce potentiel nous a permis de caractériser les variations de la structure atomique de ces très petits pores dans le vide et de simuler la conductance ionique de ce type de membranes. En utilisant le potentiel ReaxFF, des calculs préliminaires de la réactivité des nanopores de membranes de MoS_2 en présence de molécules d'éthanol, utilisées dans le protocole expérimental de la préparation des membranes de MoS_2, ont été réalisés.

Abstract

Solid-state nanopores (SSN) have emerged as versatile devices for biomolecule analysis. One of the most promising applications of SSN is DNA and protein sequencing, at a low cost and faster than the current standard methods. SSN sequencing is based on the measurement of ionic current variations when a biomolecule embedded in electrolyte is driven through a nanopore under an applied electric potential. As a biomolecule translocates through the nanopore, it occupies the pore volume and blocks the passage of ions. Hence, ultrafast monitoring of ionic flow during the passage of a biomolecule yields information about its structure and chemical properties. The size of the sensing region in SSN is determined by the size and thickness of the pore membrane. Therefore, two-dimensional (2D) transition metal dichalcogenides such as molybdenum disulfide (MoS_2) arise as great candidates for SSN applications as an alternative to graphene. In the present work, we investigated the feasibility of using MoS_2 nanopores for protein sequencing from all-atom molecular dynamics (MD) simulations. First, we studied the ionic conductance of MoS_2 nanoporous membranes by characterizing the KCl electrolyte conductivity through MoS_2 nanopores with diameters ranging from 1.0 to 5.0 nm and membranes from single to five-layers. Using MD simulations, we showed the failure of the usual macroscopic model of conductance for the nanoporous membranes with the smallest diameters and developed a modified model which proves usefulness to interpret experimental data. Second, we investigated the threading and translocation of individual lysine residues and a model protein with poly-lysine tags through MoS_2 nanopores under the application of an electric potential. A proof-of-principle technique based on the use of positively or negatively charged amino acids for protein translocation was proposed to promote the entrance of proteins through SSN in experiments. By analyzing the current-voltage curves simulated, we established the relationship between the translocation sequence events through the nanopores observed at the atomic scale in MD simulations, and the computed current fluctuations. Finally, experimental evidence of ionic conductance measurements in sub-nanometer (sub-nm) pores made of atomic defects has been recently reported. To give a better insight of the ionic transport through atomic scale pores, we performed MD simulations of sub-nm defect MoS_2 pores using the reactive potential ReaxFF. Here, we characterized the variations of the atomic structure of the pores in vacuum and then we investigated the ionic conductance performance of one of the MoS_2 defect pore membranes. ReaxFF potential was also useful to investigate the possible reactivity of MoS_2 defect pore membranes with ethanol molecules, in order to provide a better understanding of the experimental setup of DNA sequencing, in which ethanol plays an unknown role in the sample preparation of the SSN.

Contents

Chapter 1

Introduction

1.1 Nanopore based sensors for DNA sequencing: a brief review

DNA sequencing is an extremely rapidly evolving methodology to read off the sequence of bases in a genome. Given its role in human physiology and development, such sequence information leads to significant impact on diagnosis and treatment of diseases. Genome sequencing [1] has helped in the identification of genetic risk factors associated with complex diseases [2]. The growing need for cheaper and faster genome sequencing has prompted the development of new technologies that surpass conventional Sanger chain-termination methods [2–5]. Sanger sequencing method is a process based on the incorporation of chain-termination dideoxynucleotides by DNA polymerase in a single-stranded DNA (ssDNA) with unknown sequence. Although, Sanger procedure is time consuming due to the slow throughput with DNA fragment separation in gels [6], remains in wide use for validation of the so-called next-generation sequencing (NGS) technologies. NGS platforms usually involve *in vitro* amplification of DNA strands and sequencing by synthesis. Fluorescently tagged nucleotides are added by a polymerase chain reaction (PCR) for copying a specific DNA segment, enabling a signal for each base that can be instantly read off [4, 6–8].

Yet newer sequencing methods, based on nanotechnology approaches, now focus on single-molecule long-read-length without any amplification or labeling [6]. An interesting innovation that came out from Oxford Nanopore Technologies is a sequencing device based on biological nanopores [6, 9]. The principle of nanopore sensing is analogous to that of a Coulter counter. A nanoscale aperture (namely nanopore) is formed in an insulating membrane separating two chambers filled with conductive electrolyte. Charged molecules such as DNA for example, are driven through the pore under an applied electric potential (a process known as electrophoresis). The passage of the biomolecule modulates the ionic current through the nanopore as shown in Fig. 1.1 (b). The modulated current then recorded reveals useful information about the structure and dynamic motion of the molecule [2]. Measurements of the passage of molecules through a nanopore is called translocation.

The first experimental results of DNA sequencing through biological nanopore were reported in 1996 by Kasianowicz and co-workers, using a pore made of α-Hemolysin [10, 11]. The α-Hemolysin is a protein secreted by the *Staphylococcus aureus* bacteria, to create nanopores that spontaneously insert themselves into the lipid membrane of cells. It features a transmembrane channel that allows the ions of the electrolyte to pass through it [11]. The channel through this

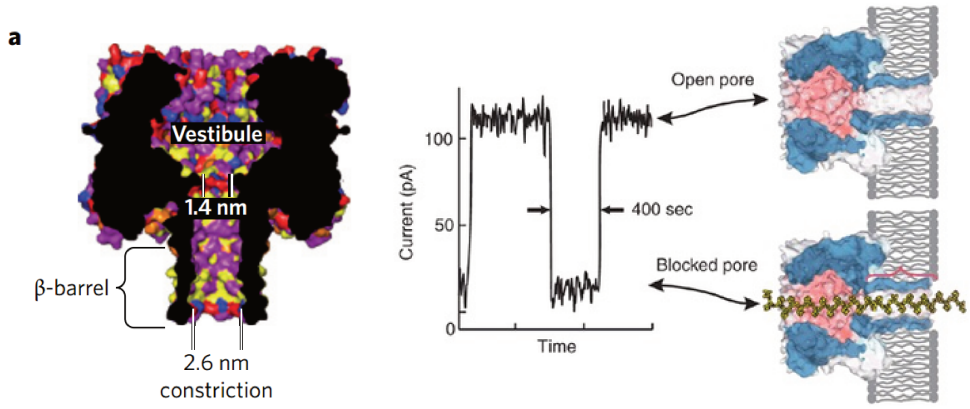

(a) (b)

Figure 1.1: (a) Structural cross-section of α-Hemolysin. Fig. extracted from Ref. [2]. (b) Schematic representation of DNA sequencing using ionic current blockade. A typical trace of the ionic current amplitude (left) through an α-Hemolysin pore clearly differentiates between an open pore (top right) and one blocked by a strand of DNA (bottom right) but cannot distinguish between the 12 nucleotides that simultaneously block the narrow transmembrane channel domain (red bracket). Fig. extracted from Ref. [15].

protein nanopore comprises a 3.6 nm diameter vestibule connected to a transmembrane β-barrel of ~ 2.6 nm wide and ~ 5 nm long. However, the channel is just 1.4 nm wide at the point where the vestibule meets the β-barrel [2] [Fig. 1.1 (a)]. Biological nanopores have been used for applications other than DNA sequencing such as DNA fingerprint, molecular and protein analysis [2, 12]. For example J. Nivala et al. [13] described controlled unfolding and translocation of model proteins (ubiquitin-like proteins Smt3) through α-Hemolysin nanopores. Also, very recently G. Di Muccio et al. [14] used equilibrium all-atom molecular dynamics (MD) simulations to study the current blockades in α-Hemolysin nanopore for homopeptide chains composed of standard amino acids [alanine (Ala), phenylalanine (Phe), tryptophan (Trp) and glutamine (Gln)]. Despite the remarkable sensitivity of biological nanopores, they also have some disadvantages such as fixed size and limited stability. In particular, their embedding lipid bilayer that supports the nanopore can become unstable due to changes in pH, salt concentration, temperature, mechanical stress, etc [11]. With the development of micro and nanofabrication, solid-state nanopores were proposed to study the molecule translocation process, as described in the following lines.

1.2 Solid-state nanopores for biological detection: the state of the art

Fabrication of nanopores from solid-state materials presents advantages over their biological counterpart due to their higher mechanical and chemical stability, robustness and durability, control of diameter and channel length, adjustable surface properties and integration into devices and arrays [2]. In addition, solid-state nanoporous membranes with nanometer-sized thicknesses (~ 5 nm) offer high bandwidth operation [nanoampere (nA) variations in measured currents which correspond to nanosiemens (nS) variations in conductance at low voltage (< 1 V)] [16]. Finally they also present strong stability for a wide range of salt concentrations and voltages compared to biological materials.

The first reports of DNA sensing using solid-state nanopores (SSN) emerged in early 2001, when Golovchenko and co-workers used a custom-built ion-beam sculpting tool with feedback control to make nanopores with well-defined sizes in thin silicon nitride (SiN_X) membranes [17]. SiN_X has traditionally been the nanopore membrane material of choice due to its high chemical resistance and low mechanical stress [18].

Since then large variety of synthetic nanopores fabricated in membrane materials have been tested experimentally [19]. For example, silicon-based nanomaterials such as silicon dioxide SiO_2 [20] or Si_3N_4 [21] have been used for the fabrication of nanopores, as well as aluminium oxide Al_2O_3 [22]. However, these nanopores are typically tens of nanometer thick, making it difficult to detect individual DNA base or residue-specific modulation in ionic currents. This occurs as multiple residue (DNA bases) pairs interact with the nanopore channel simultaneously. To give an example, during typical translocation experiments in 30 nm thick SiN_X membranes, DNA regions of approximately 30 nm long and containing ~ 100 base pairs (bps) are dwelling within a nanopore at any given time. Therefore single base resolution is not expected here [23]. Due to this limitation, several research groups started to became interested in membranes made of 2D nanomaterials, since they are characterized by thicknesses equal to a few atomic layers. The most well-known and studied 2D material is graphene.

1.2.1 DNA sequencing with solid-state nanopores: from graphene to other 2D materials

Over the past decade, stable nanomaterials have enabled the investigation of advanced thin-film nanopores such as graphene, in which single-residue discrimination should be possible. Graphene is a material with extraordinary electrical and mechanical properties, being made of one layer of carbon atoms arranged in a 2D hexagonal lattice with a ~ 3 Å thickness. In fact this distance is comparable to DNA base pair stacking distance of ~ 3.4 Å, making graphene nanopores a promising device for DNA sequencing [6, 24, 26–28]. In 2010, C. Dekker's group at Delft University of Technology studied the translocation of double-stranded DNA (λ-dsDNA) through nanopores fabricated in graphene monolayers [24] [Fig. 1.2 (a)].

Also in the same year, M. Drndić's group at University of Pennsylvania reported also DNA translocation through bare graphene and TiO_2-coated graphene nanopores for signal improvement [25] [Fig. 1.2 (b)]. Although graphene nanopores present great advantages for DNA sequencing, strong $\pi - \pi$ interactions between graphene and DNA leads to undesirable adsorption of DNA on its surface. This may hinder the DNA translocation through graphene nanopores [23]. Furthermore, low signal-to-noise ratio (SNR) of graphene nanopores (SNR ~ 3) [29] and low temporal resolution, have made them worse devices than their SiN_X counterparts. In fact, it is noise that limits temporal resolution in nanopore measurements. At low frequencies, noise is determined by the flicker noise through the pore (with a $1/f$ characteristic in the noise power spectrum). At moderate frequencies, noise is determined by white noise from the resistance of the pore itself and the feedback resistance of the amplifier. At high frequencies, noise is determined by amplifier input-referred voltage noise interacting with the total capacitance at the input of the amplifier [30]. An alternative solution is the use of other 2D materials as the membrane material, such as insulating hexagonal boron nitride (hBN), which is characterized by its one atom thickness [23, 31–36] or 2D transition metal dichalcogenides (TMDCs) [23, 37]. TMDCs are a class of 2D materials in the form of MeX_2 (Me =

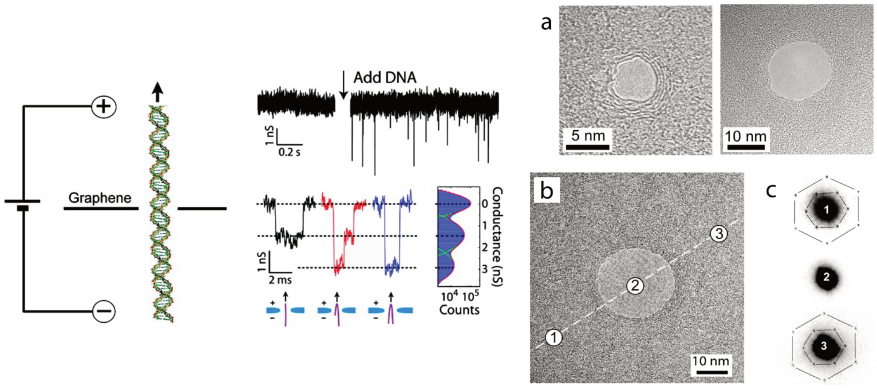

(a)

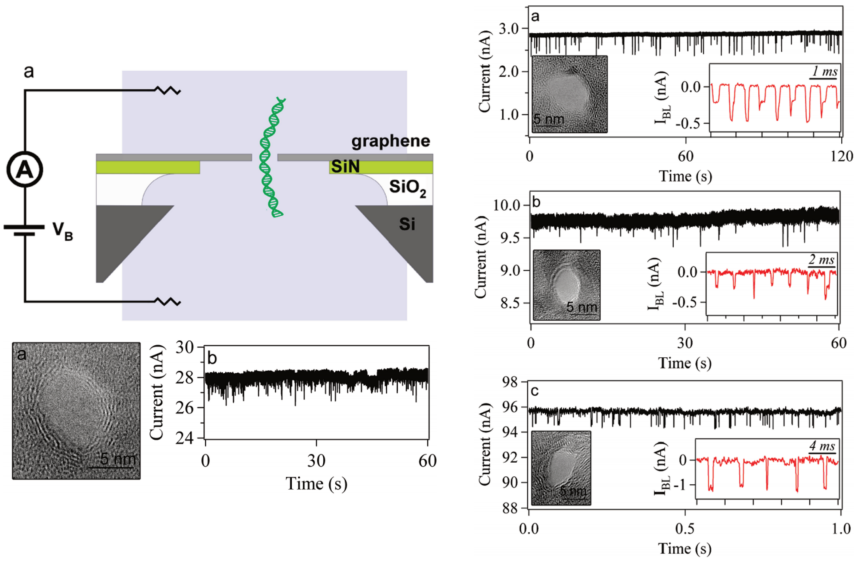

(b)

Figure 1.2: DNA translocation through graphene nanopores. (a) Schneider et al. (Ref. [24]) results of λ-dsDNA translocation across a 22 nm pore in graphene monolayer. Baseline conductance and blockade events are shown. Examples of translocation events of non-folded (black), partially folded (red), and fully folded (blue) DNA molecules recorded at 200 mV in the 22 nm pore (left panel). Transmission electron microscopy (TEM) images of some nanopores drilled into multi-layer graphene and a 22 nm diameter pore in monolayer graphene (right panel). (b) Graphene nanopore devices obtained at M. Drndić group (Ref. [25]). TEM image of an ~ 8 nm graphene nanopore and time trace of events for bare nanopore device (left panel). DNA translocations through graphene nanopores coated with 5 nm TiO_2 (right panel).

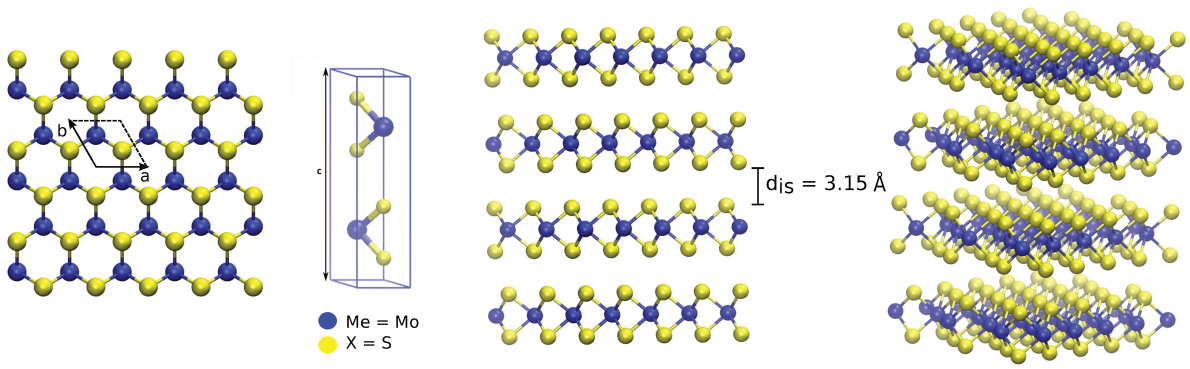

Figure 1.3: Atomic structure of TMDC MoS_2. The unit cell definition and interlayer distance d_{is} between each monolayer for four-layered MoS_2 is shown.

transition metal such as Mo, W, Ti, Nb, etc, and X = S, Se or Te) and are potentially advantageous for SSN applications due to their rich optoelectronic and mechanical properties [38, 39]. Structurally, one layer of Me atoms is sandwiched between two layers of X atoms and TMDC crystals are formed of monolayers bound to each other by van der Waals (vdW) attraction (Fig. 1.3). TMDCs materials, considered nowadays as materials beyond graphene such as molybdenum disulfide (MoS_2) or tungsten disulfide (WS_2) have also shown promising interests in biomolecule sensing applications [23, 37]. MoS_2 nanopores are of particular interest as they can be used for extended periods of time and their stability can be attributed to their relative thickness. Single-layer (SL) MoS_2 also has a direct bandgap of at least 1.8 eV, a feature that is essential for electronic base detection with field-effect transistors (FETs) [38–40]. Therefore, MoS_2 is a promising material for single-molecule detection, as it will be discussed below.

1.2.2 Transition metal dichalcogenides nanopores for DNA sequencing

Great scientific advances using MoS_2 nanopores for DNA sequencing and molecular analysis have been reported in the last few years. Fig. 1.4 (a) shows A. Radenovic's group results reported at École Polytechnique Fédérale de Lausanne in 2014 [23]. They showed that high SNR can be achieved [SNR > 10 (100 pA RMS noise and ~nA signal)] and strong interactions between DNA and MoS_2 membrane are reduced by Mo atoms in the pore region. They showed that as DNA translocates the MoS_2 nanopore, temporary blockades in ionic current on the time scale of approximately 100μs to 10 ms were produced [Fig. 1.4 (a)-right panel]. Moreover high sensitivity in MoS_2 nanopores for single nucleotide detection was reported by J. Feng et al. [40] in 2015, where a (RTILs)/KCl viscosity gradient was used to slow down the translocation process. The advantage of this viscosity gradient is that it can be used in standard ionic sensing experiments and it can be potentially combined with other schemes of nanopore sensing, such as transverse current signal detection [40]. In his experimental work, they showed that away from the pore, DNA motion is purely diffusive due to the negligible electro-osmotic effects. Furthermore, part of the DNA underwent conformational change and one end dived into the pore. The non-translocated part of the DNA polymer-monomers kept the coil conformation and experienced a strong Stokes dragging force from the ionic liquids. Consequently, DNA translocation was significantly slowed. The viscosity gradient system was used also to translocate short homopolymers [poly$(dA)_{30}$, poly$(dT)_{30}$, poly$(dG)_{30}$ and poly$(dC)_{30}$] through a 2.8-nm-diameter pore in SL-MoS_2. Control of DNA dynamics during translocation process via viscosity gradient method, is also used by A. D. Carral et al. [41] for ionic current blockade analysis using MoS_2 nanopores. In that work, they analyzed and classify various possible molecular configurations or events of single nucleotides translocation through 2D MoS_2 nanopores using a clustering algorithm.

Moreover, modeling and computational approaches are extremely useful tools for the interpretation of experimental results and to get a better understanding on the fundamental interactions of biomolecules traveling through nanopore devices at the atomic level [42–47]. For example, N. R. Aluru's group at University of Illinois at Urbana-Champaign [46] used MD simulations to computationally demonstrate the translocation and sequencing of dsDNA through $d = 2.3$ nm MoS_2 pores. They detected distinct ionic current blockade and conductance states for each nucleobase and in some cases, for two bases that coexisted at the same time in the pore (SNR being 15.02). In addition, they demonstrated via density functional theory (DFT) simulations that MoS_2 can be used as FET device for nucleobase detection. They computed the electronic structure changes induced due to the presence of DNA bases inside the nanopore, obtaining electronic charge density rearrangement. Moreover, they investigated the total density of states (DOS) of the

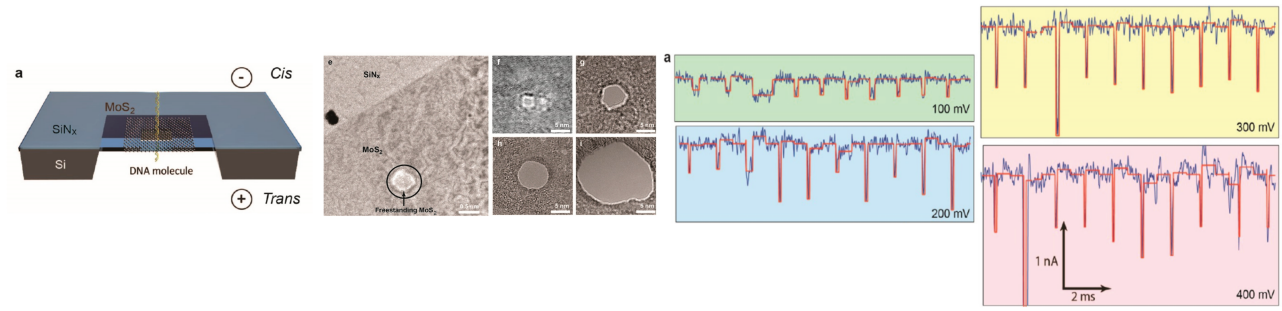

(a)

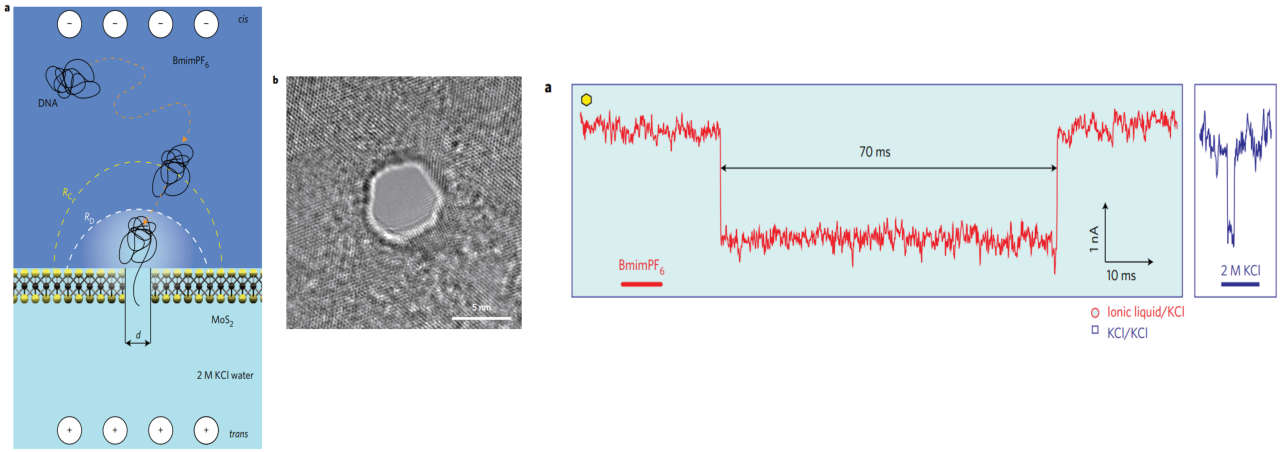

(b)

Figure 1.4: Experimental results from A. Radenovic's group. DNA translocation through MoS_2 nanopores. (a) Schematic illustration of MoS_2 nanopore membrane for DNA translocation. Concatenated events of pNEB plasmid DNA translocating through a 20 nm MoS2 nanopore in 2 M KCl. Raw signal is in blue and fits are shown in red. Fig. extracted from Ref. [23]. (b) Schematic of room temperature ionic liquids (RTILs)/KCl viscosity gradient system in MoS_2 nanopores. The cis chamber contains RTILs [1-butyl-3-methylimidazolium hexafluorophosphate ($BmimPF_6$)] and the trans chamber contains 2 M aqueous KCl solution. The two chambers are separated by a monolayer MoS_2 membrane with a nanopore. The scheme also shows the dynamics of DNA translocation through MoS_2 nanopore. Bright-field TEM image of a 5 nm nanopore fabricated in a monolayer MoS_2 membrane. 48.5 kbp λ-dsDNA translocation events recorded in the viscosity gradient system (red line), and in absence of the viscosity gradient, through a MoS_2 nanopore with a 20 nm diameter. Fig. extracted from Ref. [40].

system when DNA bases are placed inside the pore, observing a different response of DOS associated to each DNA base (being the highest DOS change associated to G base).

1.2.3 Transition metal dichalcogenides: towards protein sequencing

Driven by the success of DNA sequencing, nanopore platforms have been proposed to sequence proteins [13, 14]. Protein sequencing is of prominent significance, since the amino acid sequence determines how a protein folds and functions [48]. Mutations or modifications (such as insertions or deletions) of amino acids in a protein can seriously affect its biological functions and often lead to disease [49]. Conventional protein sequencing methods such as mass spectrometry and Edman degradation are subject to important limitations: they do not provide the complete sequence information when the protein size increases [48]. However, to date most of the nanopore based sequencing systems were tested using DNA single or double strands, due to the fact that DNA is comprised of a combination of only four bases among Adenine (A), Thymine (T), Cytosine

(C) and Guanine (G) nucleotides.

Moreover DNA strands are highly negatively charged molecules, where the total charge is proportional to the number of bases, which facilitates its translocation through nanopores. In contrast, proteins are synthesized from a combination of 20 different building-blocks (amino acids). Amino acids have side-chain of different lengths and proteins can exhibit neutral global charge independently of the number of residues, which hinder their sensitivity to the electric field. For this reason, it is more challenging to sequence proteins than DNA through SSN sensors. To the best of our knowledge, only a few experimental studies about protein translocation through silicon-nitride nanoporous membranes have been reported [50–52]. One of these studies was reported by E. Kennedy et al. [53], who demonstrated experimentally that sub-nanometer (sub-nm) diameter pores fabricated in 10 nm thick SiN_X membranes can be used to detect the primary structure of unfolded proteins, driven through a nanopore by an electric field.

Given the impact of 2D TMDC materials in DNA sequencing, two recent theoretical works about translocation of proteins through MoS_2 nanopores have been reported in 2018. Fist, H. Chen et al. [48] (Fig. 1.5) showed the feasibility of translocating uniformly (repetition of identical motifs) highly charged (up to ±24e) proteins through SL-MoS_2 nanoporous membranes in a bias electric field and water-flow, which generates a hydrostatic pressure gradient. The authors of this study showed that this latter method offers an alternative possibility, other than transmembrane bias, to drive peptides through MoS_2 nanopores, even though the fragility of such ultra-thin nanoporous membranes might be problematic [55]. Later on, B. Luan et al. [49] showed as proof-of-principle that mixing 2D materials (graphene/MoS_2 heterostructures) with different vdW interactions and consequently different chemical potentials might be the solution to transport and translocate neutral or weakly charged biomolecules through SSN. In that work, the authors did not present

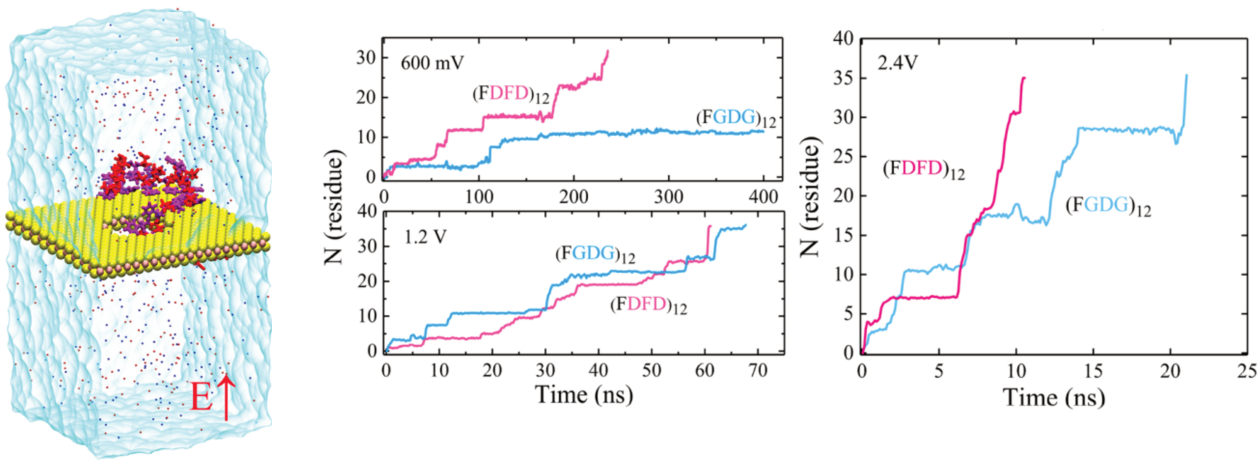

Figure 1.5: Step-wise voltage-driven transport of charged peptides formed by charged residues (e.g., aspartic acid (D), lysine (K), etc.) interspersed with neutral ones (e.g., phenylalanine (F), glycine (G), etc.). FG-nucleoporin (FG-Nup) repeating units, such as $(FKFK)_{12}$ (+24e), $(FDFD)_{12}$ (-21e), $(FKFG)_{12}$ (+12e), $(FGFG)_{12}$ (0e), and $(FDFG)_{12}$ (-12e), and so on, were studied. Mo and S atoms of the MoS_2 surface are drawn as pink and yellow balls, respectively. The snapshot corresponds to the $(FDFD)_{12}$ system, where phenylalanine is shown in magenta and aspartic acid is shown in red in the simulation box. Translocation traces of $(FDFD)_{12}$ and $(FGDG)_{12}$ peptides are represented by $N(residue)$, which is the number of translocated residues calculated by counting the number of residues that have crossed the nanopore. Image extracted from Ref. [48].

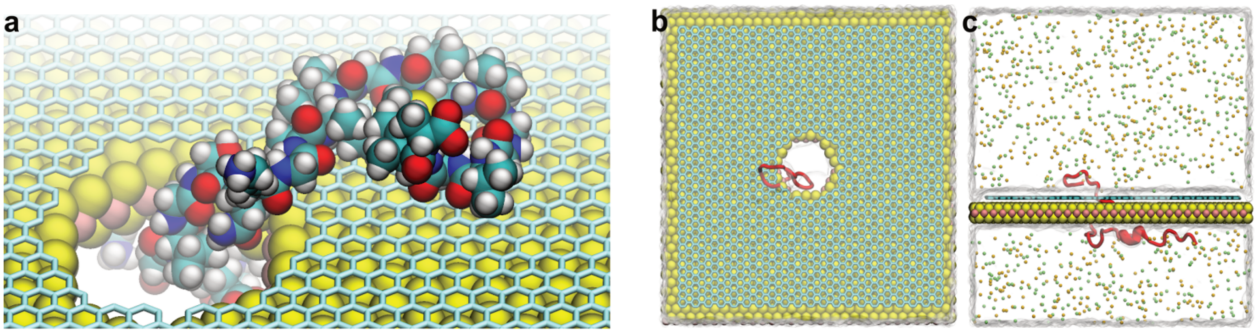

Figure 1.6: MD simulation of the translocation of an amyloid β peptide 1-42 (Aβ_{42}) that is the pathological hallmark of Alzheimer's disease, through a graphene-MoS_2 nanopore. (a) Perspective top view of the system. Atoms in the MoS_2 sheet are shown as vdW spheres (Mo: pink; S: yellow); the graphene sheet (cyan) is in the bond representation; the protein is in the vdW representation with each element colored differently (C: cyan; O: red; H: white; N: blue; and S: yellow). (b-c)Top and side views of the simulation system. The protein is in cartoon representation. Image extracted from Ref. [49].

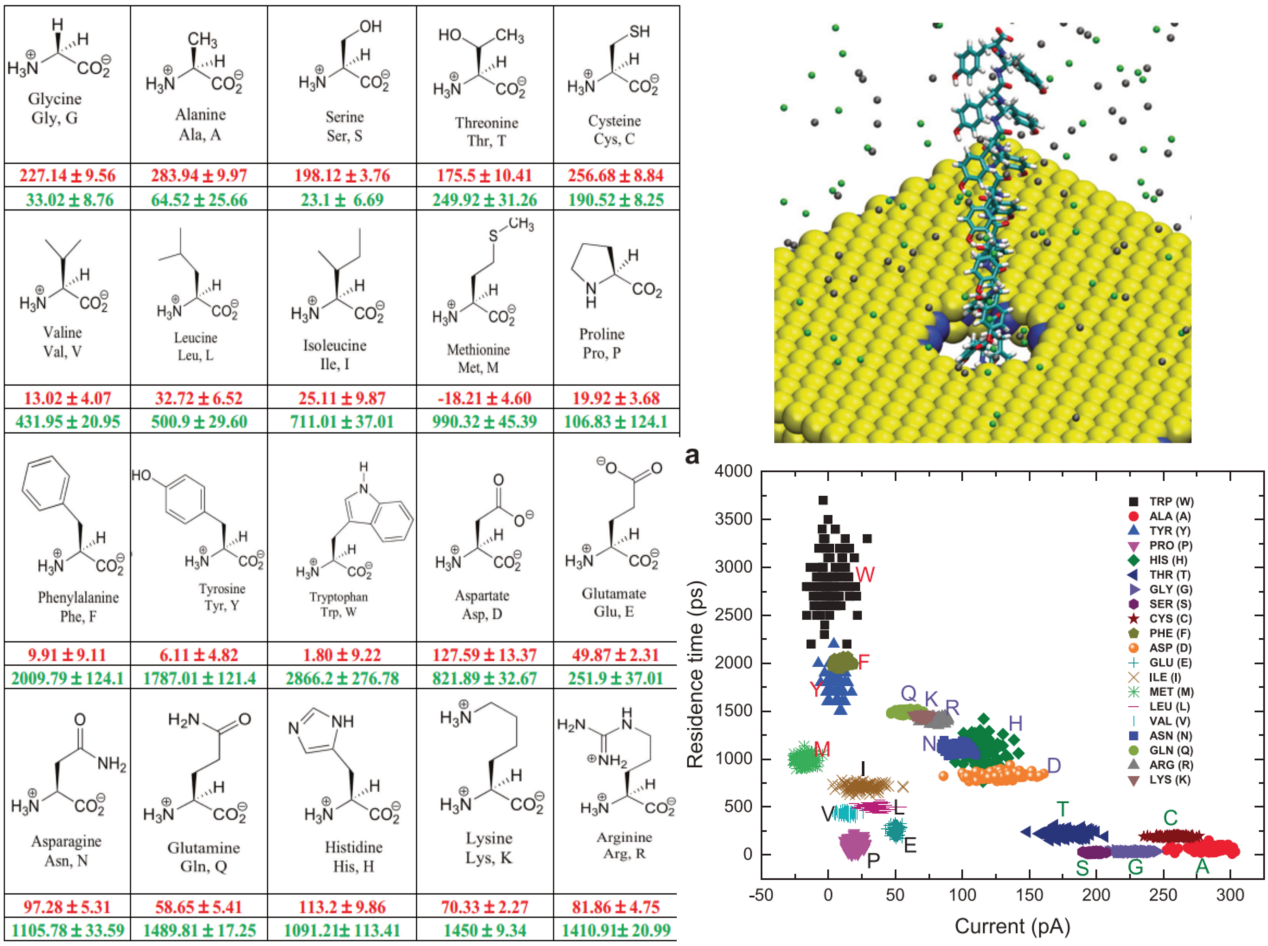

Figure 1.7: Left panel: ionic current (in red and in pA) and residence time (in green and in ps) associated with each amino acid. Each residence time and ionic current value is an average over 100 simulations. Top right panel: simulation set up for the polypeptide chain with 16 amino acids [here, TYR(Y)], MoS_2 nanopore and ions (water is not shown). Bottom right panel: ionic current and residence time data for 20 amino acids with their respective labels. Image extracted from Ref. [54]

ionic conductance signals recorded during the translocation of proteins and, therefore, no drops related to the passage of specific amino acids through the graphene/MoS_2 pores were presented. Moreover, given the significance of amino acids identification in health diagnosis and the potential of MoS_2 material, A. B. Farimani et al. [54] proposed SL-MoS_2 nanopores for amino acid detection using ionic current and residence time for machine learning-based predictive models. In that work, the authors used extensive MD simulations (with a total aggregate simulation time of 6 μs) to produce data of the translocation of 20 standard amino acids through a nanopore under constant bias of 200 mV (Fig. 1.7-left panel). The authors used polypeptide chains made of 16 replicas of each amino acid (Fig. 1.7-top right panel) and used an external force per residue to pull non-charged amino acids through the nanopore. In the training process, they used k-nearest neighbor, logistic regression and random forest machine learning models to predict the detection of amino acids and fed the models with labeled ionic current and residence time data (Fig. 1.7-bottom right panel). The prediction of amino acids identification with these models was reported to be up to 99.6% accurate. The authors also used the trained models to predict the type of amino acids detection in a practical amino acid chain (built of different amino acids) with ionic current and residence times unlabeled data, and obtained up to 62.20% accuracy of prediction.

It is important to remark that MD simulations constitute a powerful tool to understand molecular and atomic details during translocation processes in SSN, as demonstrated by H. Chen et al. [48], B. Luan et al. [49] and A. B. Farimani et al. [54]. However, there are still outstanding fundamental questions related to the design of SSN based sensors and translocation mechanisms that we addressed during the development of this thesis:

1. How do ionic conductance performances of nanoporous membranes depend on the geometry and size of the pore?
2. How does polypeptide, protein or DNA translocation process depend on the size of the pore?
3. How do polypeptides, proteins or DNA molecules interact with nanopores embedded in different single- and few- layered materials beyond graphene, such as MoS_2?
4. How does the chemical composition of a translocating biomolecule affect the guidance process?
5. Is it possible to detect the passage of a polypeptide or protein using ionic conductance signal?
6. How can the quality of the ionic conductance signal of a translocating biomolecule be improved by changing the geometry and size of the pore?

The purpose of the present thesis is to answer those questions and understand how biomolecule dynamics and translocation can be controlled from a precise interaction with the nanopore. To do that we performed all-atom MD simulations to study the feasibility of using MoS_2 nanopores for protein sequencing, and to describe at the atomic level the translocation of ions and biological peptides. We organized the manuscript as follows:

i In Chapter 2, we present and describe the methodology and computational tools used to perform the corresponding MD simulations for the different systems and situations studied here.

ii In Chapter 3, we investigate conductance performances of different MoS_2 nanoporous membranes by studying the ionic conductance of a KCl electrolyte through open pore systems without the presence of biomolecule. From this study, we were able to discuss the capability of the different nanopores to conduct ions and confront the usual macroscopic model of conductance. We provide a correction of the macroscopic conductance model that can be used to interpret experimental data. The study of conductance performances and transport properties of nanoporous membranes is extremely important for the design of biomolecule sensors based on nanopores. Furthermore, it allows to provide benchmark signals for subsequent translocation simulations and experiments.

iii In Chapter 4, we analyze MD simulations in order to provide a detailed picture of MoS_2 nanopores performance as biomolecule sensing devices using translocation technology. Particularly we investigate the feasibility of threading and translocating first individual lysine residues and second, a model protein with poly-lysine tags through MoS_2 nanopores under the application of an electric potential. The idea behind this specific strategy is to prove that it is possible to promote the entrance of a proteins inside a nanopore by using positively or negatively charged amino acid residues (tags) to functionalize the N- or C- terminal part of such protein. Then, this method can be used to establish the relationship between the translocation sequence events through the nanopores and the detected ionic conductance. We insist on the fact that before the start of this PhD thesis, there were no reported works about simulations of protein translocation through SSN.

iv In Chapter 5, we characterize the atomic structure of sub-nm pores made of atomic defects in MoS_2 membranes in vacuum and we discuss also the ionic conductance performance of one of these pore membranes. Furthermore, we discuss the possibility of simulating the reactivity of MoS_2 defect pore membranes with ethanol molecules, by using the reactive potential ReaxFF. In addition, these simulations might provide a better understanding of the experimental setup for conductance measurements and DNA sequencing, in which ethanol plays an unknown role in the sample preparation of the SSN.

v In Chapter 6, we discuss the general conclusions and perspectives of this work.

Chapter 2

Computational Methods

In the present chapter, we express the motivations of using classical MD to carry out *in silico* nanopore experiments and we describe briefly theory and fundamentals of MD simulations.

2.1 Simulating reality

Over the past 60 years, the speed at which computers perform elementary calculations has increased by a factor 10^{15}, and the size of computer memories and the capacity of data storage devices have undergone similarly spectacular increases [56]. Thanks to the computational resources available today, numerical simulations at the atomic scale provide a way to understand the properties of assemblies of molecules in terms of their structure and the microscopic interactions between them. Numerical simulations are constantly used to complement experiments or, more precisely, to guide experiments. Thus, two increasing fields of applications of computer simulations are computational materials science and computational molecular design [56]. Indeed, computer simulations allow us to predict the properties of potentially useful substances, *e.g.* pharmaceutical compounds or materials with unique physical properties. In addition, simulations are useful to predict the properties of materials under conditions that are difficult to achieve in controlled experiments [56].

The main advantage of computer simulations at the atomic scale is that hidden microscopic details behind experimental measurements can be revealed [57]. A wide variety of modeling techniques at the atomic scale based on quantum mechanics or semi-classical methods have been developed over the years. Those relevant to describe the dynamics of large heterogeneous systems at the molecular level, are the classical MD techniques. Classical MD refers to numerically solving the equations of motion for a group of atoms. However, although the laws of classical mechanics were first postulated to study the motion of planets, stars and other large-scale objects, they turn out to be a surprisingly good approximation at the molecular level at room temperature. MD has been remarkably successful in its ability to predict macroscopic thermodynamics and dynamical observables for a wide variety of systems using the rules of classical statistical mechanics [58]. In MD, atomic motions are simulated by solving Newton's equations of motion simultaneously for all the atoms in the system. MD simulations can be used to obtain both equilibrium and transport properties of a system.

The increasing ability to fabricate SSN devices, has opened the possibilities towards fluid filtration, biomolecule sequencing, and energy generation [59] applications. In the context of the

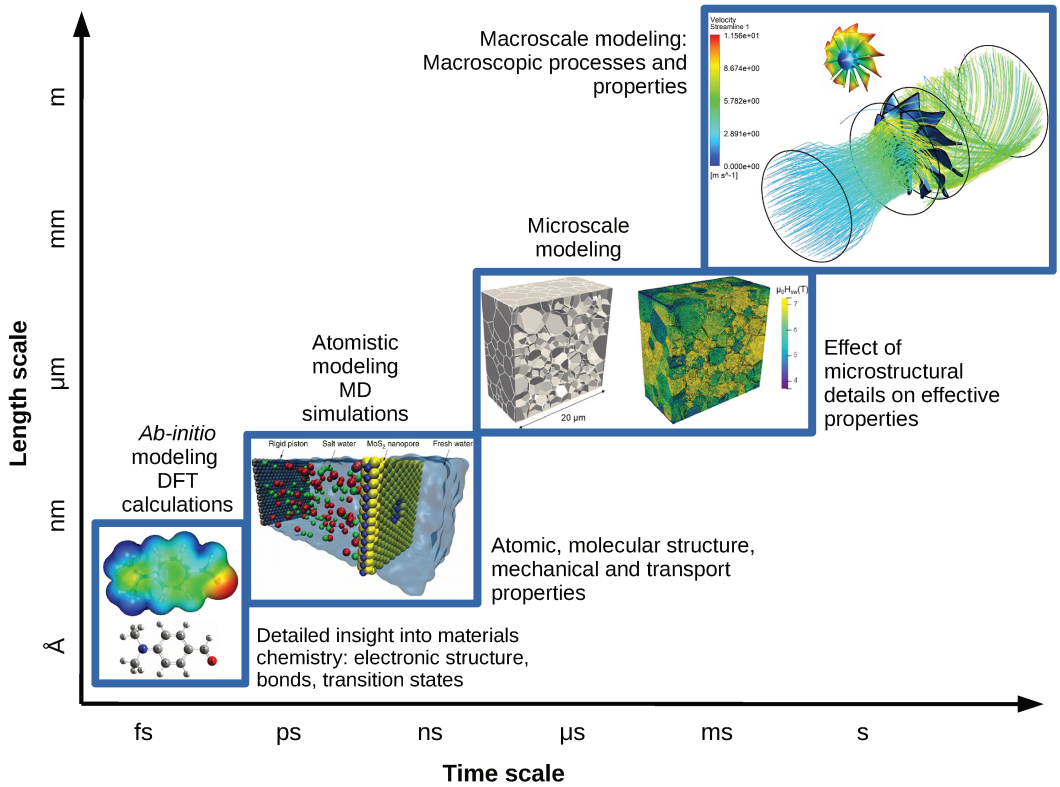

Figure 2.1: Length scale as a function of the time scale of different systems and the corresponding computer simulations techniques used for studying them. *Ab-initio* and density functional theory (DFT) calculations are performed to study the molecular structure of 4-(Dimethylamino) Benzaldehyde (image extracted from M. Rocha et al. Spectrochimica Acta Part A: Molecular and Biomolecular Spectroscopy 136 (2015) 635-643). MD simulations are performed to study the water desalination with a SL-MoS_2 nanopore (image extracted from M. Heiranian et al. Nature Communications volume 6, Article number: 8616 (2015)). For larger length and time scale, magnetic microstructure in large-grained $Nd_2Fe_{14}B$ permanent magnets is studied from simulations using finite element method (image extracted from L. Exl et al. J. Phys.: Mater. 2 (2019) 014001). For the macroscale case, a simulation of the airflow inside a turbofan using ANSYS Fluent software is shown as a simulation example (image extracted from https://www.mr-cfd.com/portfolio-item/simulation-of-airflow-inside-a-turbofan/).

present work, we performed MD simulations and numerical analyses in order to discover new insights that can provide realistic solutions based on computational modeling, for subsequent testing by our experimental collaborators [60–62]. In the present thesis, we simulate systems of hundreds of thousands of atoms comprised by a nanoporous membrane and a biological molecule in a fluid environment, in order to mimic solid-state nanopores biomolecule translocation experiments. By confronting the simulations carried out in the present thesis with experimental data, our aims are: 1) to improve the current understanding of the physics of ionic currents in nanoporous materials and of biomolecule translocation, and 2) to guide future experiments.

2.2 Modeling of the all-atom structures

Performing all-atom MD simulations of SSN made of MoS_2 materials for biomolecule detection, close to experimental conditions constitutes the main objective of the present work. To achieve this, different tasks must be executed: (i) the hybrid system composed by: nanoporous membrane + solvent + biological molecule, for which the parametrization of the interactions between each component must be built, and (ii) the simulation of the translocation of the biomolecule under applied voltage must be performed. This process requires the use of different methods and open source software packages, such as *VMD - Visual Molecular Dynamics* [63], *Moltemplate* [64], *GROMACS - (GROningen MAchine for Chemical Simulation v 5.1)* [65], *AmberTools package - Assisted Model Building and Energy Refinement* [66], *LAMMPS - Large-scale Atomic/Molecular Massively Parallel Simulator* software package [open source `http://lammps.sandia.gov`], as shown in Fig. 2.2. Here we investigated two systems: the open pore system and the translocation system, as indicated in Fig. 2.2 and detailed below:

1. **Open pore system**:

   The open pore system is composed of the nanopore + solvent (KCl aqueous solution). The MoS_2 nanopores considered in the present work, as presented in Figs. 2.5 (a) and (b) are: (a) SL-MoS_2 circular pores for diameters d = 1.0, 1.5, 2.0, 2.5, 3.0, 4.0 and 5.0 nm, and (b) SL-MoS_2 sub-nanometer sized pores created from atom defects. Bilayer (2L), trilayer (3L), four-layer (4L) and five-layer (5L) MoS_2 nanopores are studied as well, as shown in Fig. 2.6. The study of the open pore systems allows us to characterize the ionic transport through these nanopores and to estimate their performances in terms of their ionic conductance.

2. **Translocation system**:

   The system is comprised of the nanopore + biological peptide + solvent. The idea here is to perform the translocation of different biological peptide sequences through MoS_2 nanopores

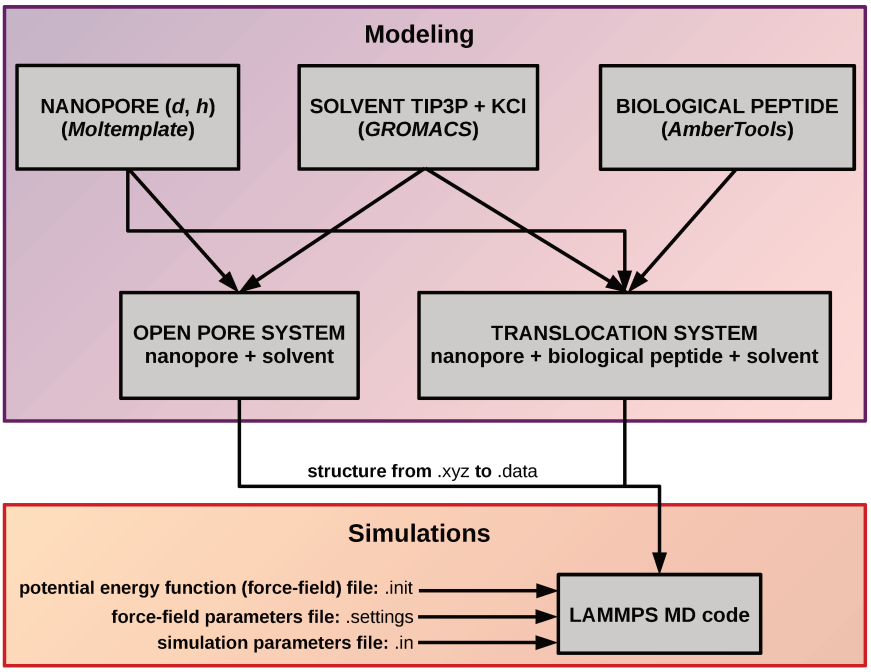

Figure 2.2: Modeling and MD simulations of the systems studied in this work.

using MD simulations. Nanopores considered in the translocation systems are made of SL-MoS_2 with d = 1.5 nm and d = 2.0 nm, and bilayer-MoS_2 with d = 2.0 nm. In general, once the MoS_2 nanopores conductance is characterized, then a suitable pore geometry can be chosen for the biomolecule translocation simulations. Translocation simulations can be useful for the interpretation of experimental conductance signals and for the design of new experiments.

As performed in real life experiments, a proper set up is necessary before any measurement process. In MD simulations, one follows the same kind of protocol. Building up the molecular system is the first step. Here, each subsystem is built using a different suitable software. Furthermore, all the systems were visualized using the molecular graphics program *VMD* [63].

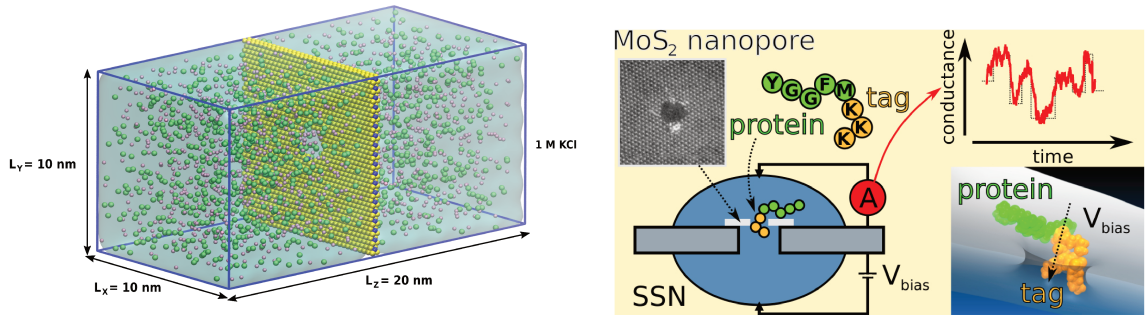

(a) (b)

Figure 2.3: (a) Representation of the simulation box, containing a MoS_2 nanopore immersed in 1 M KCl solution. Mo and S atoms are represented with blue and yellow spheres K^+ and Cl^- ions are represented with purple and green spheres, respectively. (b) Schematic representation of the translocation system, composed of a MoS_2 nanopore immersed in 1 M KCl solution and a biological peptide sequence. An applied bias drives the biological peptide through the nanopore as the ionic conductance signal is recorded.

2.2.1 MoS_2 nanoporous membranes

Nanoporous membrane structures were built using the *Moltemplate* package. MoS_2 membranes are characterized by a 2D layer of dimensions $L_x \times L_y$ nm^2. Each *Moltemplate* input file used to generate the membrane structure, contains the system unit cell, atom types, molecule index, xyz coordinates, masses, partial charges of each atom and finally of the simulation box lengths.

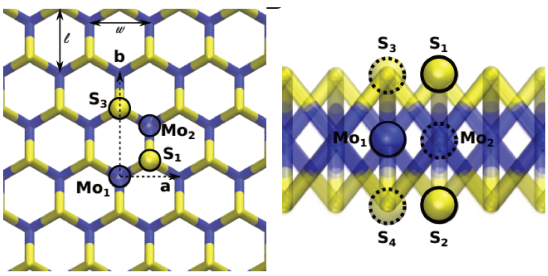

Figure 2.4: Definition of the MoS_2 monolayer unit cell in the top view (x,y-plane) and side view (x,z-plane), where the Mo atoms are represented in blue and the S atoms in yellow.

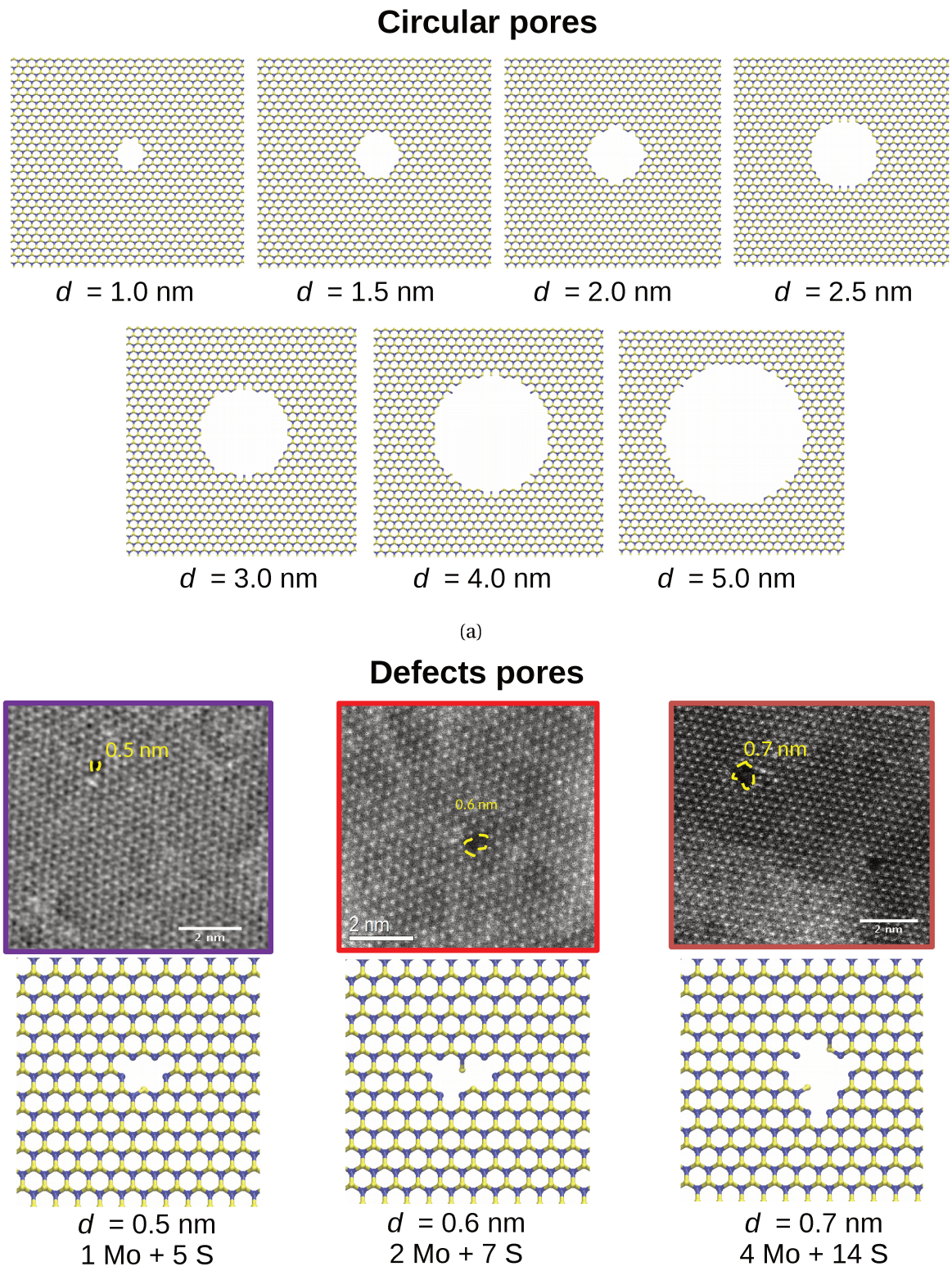

Figure 2.5: (a) Circular and (b) atomic defects MoS_2 pores built from the SL-MoS_2 membrane defined in Fig. 2.4. The number and nature of atoms removed are indicated. The TEM images are from experimental samples of MoS_2 sub-nm pores obtained by our collaborators at University of Pennsylvania (Prof. Drndić's group.

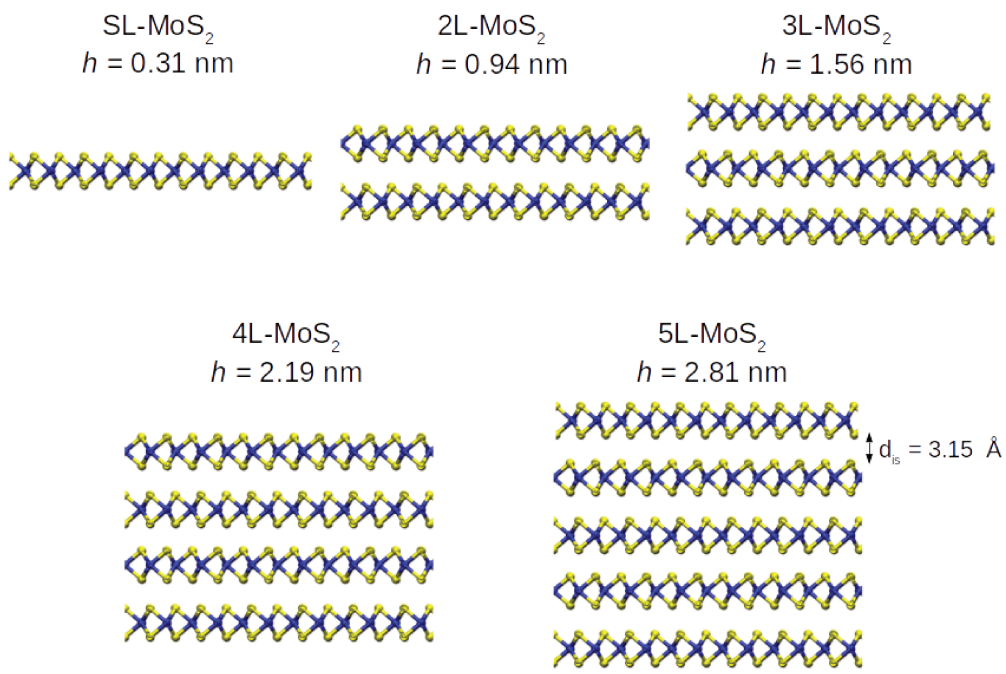

Figure 2.6: ML-MoS_2 systems studied in this work. CPK and dynamic bonds representations in *VMD* are used, where the Mo atoms are colored in blue and the S atoms in yellow.

2D MoS_2 membrane was built from a honeycomb lattice type, where the Mo atoms are surrounded by 6 first neighbors which are S atoms (3 on the top and 3 on the bottom in the z-direction). In 2D TMDC monolayer structures, S atoms do not belong to the same plane as Mo atoms, thus the vertical distance between S atoms corresponds to $d_{S-S} = 3.11$ Å. MoS_2 unit cell is defined by 6 atoms, *i.e.* 2 Mo and 4 S atoms, as shown in fig. 2.4, where the lattice vectors are $\vec{a} = (3.13, 0, 0)$ and $\vec{b} = (0, 5.42, 0)$.

MoS_2 membranes of $\sim 10 \times 10 \times 20$ nm^3 with circular nanopores [Fig. 2.5 (a)] and $\sim 7.5 \times 7.5 \times 15$ nm^3 with defect pores [Fig. 2.5 (b)] were built. The circular nanopores were created by removing the atoms with coordinates that satisfy the condition $x^2 + y^2 \leq r^2$, where r is the radius of the nanopore, or in the case of atomic defect pores, selected atoms were removed from the structure using TEM images as templates [see Fig. 2.5 (b)]. For a nanoporous membrane of $\sim 10 \times 10 \times 20$ nm^3 and $d = 2.0$ nm, the system is comprised of 1180 Mo atoms and 2260 S atoms. Furthermore, we do not consider the membrane to be rigid as done in recent works about protein translocation through MoS_2 nanopores and graphene/MoS_2 heterostructures, since it has been demonstrated that the dynamics of the nanoporous membrane plays a role in the biomolecule diffusion on the surface and in the threading of the biomolecule through the pore [62].

Multi-layer (ML) MoS_2 nanopores were built also using *VMD* software, as indicated in Fig. 2.6. For this, SL-MoS_2 membranes were generated as previously described, and then displayed in *VMD* as many times as the desired number of layers. Single-layer membranes are placed by hand at an interlayer spacing of $d_{is} = 3.15$ Å [62]. Circular nanopores of diameter 2.0 nm were drilled on the multi-layer systems as previously described for single-layer situations.

2.2.2 Biological peptides (K, KK, YGGFM, YGGFM + K-tail)

Biological peptides studied in this work are:

- 1 capped lysine residue (ACE-LYS-NME) ≡ K.
- 2 capped lysine residues (ACE-LYS-LYS-NME) ≡ KK.
- Met-Enkephalin (TYR-GLY-GLY-PHE-MET) + (LYS)-tail ≡ YGGFM + K-tail.

Capping between acetyl group (ACE) and N-methyl group (NME) is used to reproduce the peptide bonds between amino acids in proteins. The Met-Enkephalin structure is extracted from the Protein Data Bank (PDB) (PDB code: 1PLW). The structures were created using *AmberTools*, by providing the sequence of the peptide. The *Moltemplate* topology files for the associated force field (AMBER99sb-ILDN), atomic coordinates, bonds, angles and masses must be generated by *AmberTools*. Originally, the biological peptide is placed above the MoS_2 nanoporous membrane at a vertical distance of 20 Å. By doing that, we avoid biased threading when the peptide is originally placed into the pore [62].

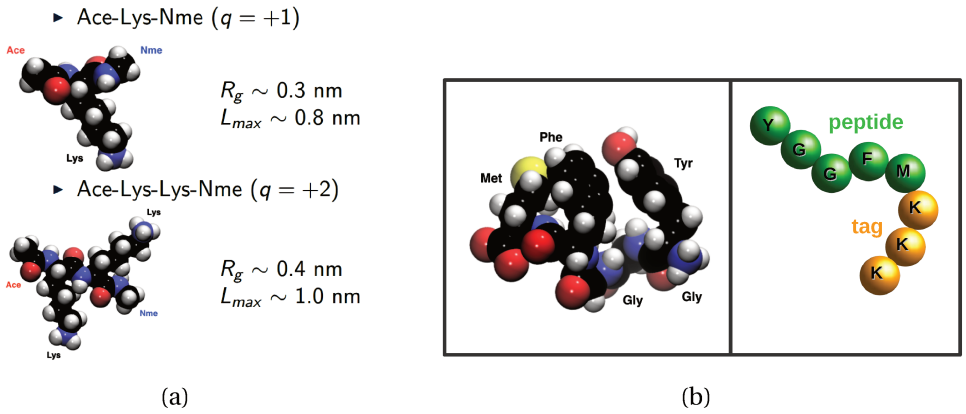

(a) (b)

Figure 2.7: vdW representation using *VMD* of: (a) caped 1-lysine and 2-lysine residues, and (b) the five-residue protein Met-Enkephalin. Carbon, hydrogen, nitrogen, oxygen and sulfur atoms are represented in black, white, blue, red and yellow spheres, respectively. Green and orange spheres on the right panel represent the Met-Enkephalin protein and the lysine tag.

2.2.3 Solvation of the system

Solvating the system means adding explicit solvent molecules to the simulation box considering steric effects. The solvent made of a KCl aqueous solution is comprised of water molecules, using the TIP3P model [67,68], K^+ and Cl^- ions. The number of water molecules and ions depends on the concentration in the simulation box. For a 1M KCl solution for example, the system is comprised of 62323 water molecules, 1233 K^+ ions and 1233 Cl^- ions in a $\sim 10 \times 10 \times 20$ nm^3 simulation box. The solvation was prepared using the *GROMACS* software package, to obtain the atomic Cartesian coordinates `.xyz` file [60]. For the translocation of 1-lysine residue, which is positively charged ($q = +1e$), the ionic solution is comprised of 59927 water molecules, 1177 K^+ ions and 1178 Cl^- ions due to the neutrality of the entire system.

2.3 Molecular dynamics

Classical MD has evolved towards the solution of a wide variety of problems. In classical MD simulations, electrons are not treated explicitly and the potential energy of the system is defined within the so-called Born-Oppenheimer approximation [69]. Forces between atoms are calculated using an empirically derived force field, being a collection of mathematical functions and parameters that describe the interaction between different types of atoms [70, 71]. The Newton equations of motion are solved from these forces and the atom trajectories are computed at each time step.

In MD simulations we proceed in a very similar way to real life experiments in terms of reliability and reproducibility of the data. Hence, to study a material we take a sample of it and then we connect it to a simulated measuring instrument. Then we measure the desired property during a certain time or a certain number of times, and the larger the amount of measurements, the more accurate the average of measurements is. Observable quantities are measured in MD simulations, by first expressing observables as a function of the positions and momenta of the particles in the system. At the microscopic level, MD trajectories are dependent on the initial positions and velocities of the atoms. In a MD simulation, we monitor an ensemble property as a function of time, as for example the energy, to define the equilibration time (convergence to the average) [69]. After the equilibration period, statistical properties can be calculated from the time series of atomic positions and momenta as for example the equilibrium temperature, internal energy, multipolar momenta, transport properties, and others.

2.3.1 MD algorithm

In MD formulation, the system is comprised of N interacting particles which are treated as point masses, so together with Newton's equations, motion of the ensemble of the N particles is computed. As mentioned previously, the physics of the model is contained in a potential energy function $V(\vec{r}_i)$, $i = 1, \ldots, N$ (force field) for the system from which the force equations for each atom is derived:

$$\vec{F}_i = -\frac{\partial V(\vec{r}_i)}{\partial \vec{r}_i}. \tag{2.1}$$

The second-order Newton differential equations:

$$\vec{F}_i = \frac{d\vec{p}_i}{dt} = \frac{d}{dt}(m_i \vec{v}_i) = m_i \frac{d\vec{v}_i}{dt} = m_i \frac{d^2\vec{r}_i}{dt^2} = m_i \vec{a}_i, \tag{2.2}$$

are solved for initial momenta $\vec{p}_i(t_0)$ and position $\vec{r}_i(t_0)$, where $t_0 = 0$ is the initial time of the MD simulation and $\vec{a}_i(t)$, the acceleration. The best way to introduce how does MD simulations work is to consider the simplest pseudo-algorithm, as shown in Fig. 2.8 [69].

As shown in Fig. 2.8, a MD simulation starts from an initial configuration of particles in a given volume, referred as the simulation box. Positions of the particles are chosen such that no overlapping occurs between the particles. For example, in the case of Lennard-Jones (LJ) interactions, all particle-particle distances are at least equal to σ, which is the finite distance at which the inter-particle potential is zero. Particles can be placed randomly in the simulation box or they can be placed on lattice sites. Next, velocities of the particles are assigned, either randomly or

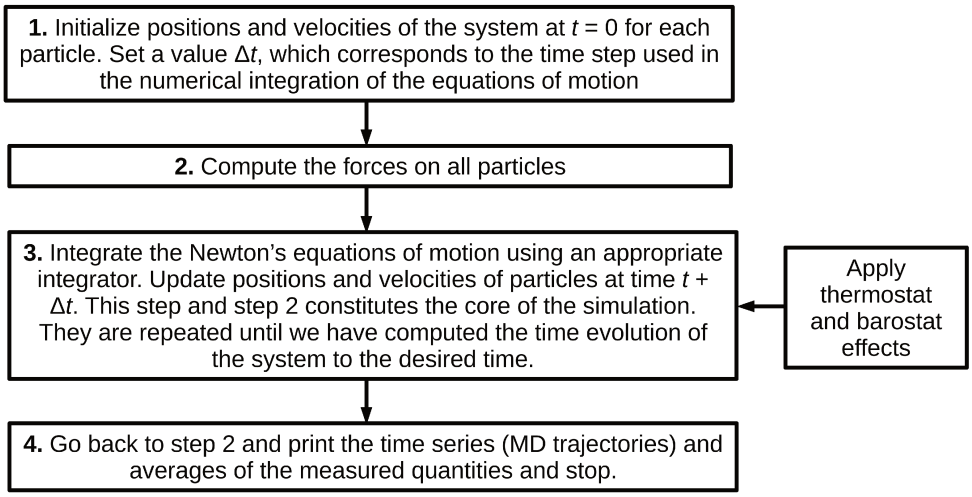

Figure 2.8: Simple scheme of the steps during a MD simulation.

can be taken from a Maxwell-Boltzmann velocity distribution. Velocities are scaled such that the mean kinetic energy matches the desired temperature using the equipartition theorem. In a MD simulation, we solve Newton's equations of motion starting from an initial configuration of the system until its properties no longer change in time (the system loses the memory of its initial conditions). This is known as the equilibration of the system, which is a crucial step we perform before monitoring and recording the properties of the system from MD trajectory (or the so-called production part of the MD simulation) [69].

2.3.1.1 Force calculation

After initializing the positions and velocities of the system at $t = 0$, the calculation of the force acting on each particle is performed. For a two-body potential, it requires the calculation of the distance between each pair of particles i and j. The most time-consuming part of all the simulation process, is the calculation of the force on each particle i [72]. For a two-body potential as the LJ model, the time needed for the evaluation of the forces scales as N^2, since we must evaluate $N \times (N-1)/2$ pair distances [69]. To reduce the number of force pairs evaluated, the interaction potential between pairs of particles is typically truncated at a radial cut-off distance where the force has decayed sufficiently so that truncation does not significantly influence the properties of interest. A neighbor list of particles that are within the cutoff is then created for each particle. The pair forces only need to be computed for the particles in the neighbor list, which is a small subset of N for each particle [72, 73]. Furthermore, the neighbor list can be rebuilt less frequently than every MD step [72].

2.3.1.2 Integration of equations of motion

The following step in MD simulations is the integration of Newton's equations, now that all forces between particles have been computed. To perform this task, MD uses numerical methods, where Verlet integrator [74, 75] is one of the simplest and best algorithms. One of the main reasons this integration method is used is because it generates stable solutions with great accuracy, since it efficiently reduces local errors that can accumulate during the evolution of the system [70]. Verlet algorithm presents also several other advantages: time reversibility, easy implementation of

constraints on the rigidity and position of the particles, which is an important practice in MD [70]. Verlet algorithm is derived by adding the Taylor expansions of a particle coordinate $\vec{r}(t+\Delta t)$ and $\vec{r}(t-\Delta t)$ about time t, where Δt is the time step in the MD scheme:

$$\vec{r}_i(t+\Delta t) = 2\vec{r}_i(t) - \vec{r}_i(t-\Delta t) + \frac{1}{m_i}\vec{F}_i(t)(\Delta t)^2 + \mathcal{O}(\Delta t^4), \tag{2.3}$$

where $\frac{1}{m_i}\vec{F}_i(t) = \vec{a}_i(t)$. Typically, time step for MD simulations is in the order of 1 fs. The time step in a MD simulation should be chosen so that the simulations is long enough to be relevant to the time scales of the natural processes being studied. Here, the new position $\vec{r}_i(t+\Delta t)$ is computed from the two previous positions, and is accurate to order Δt^4. Verlet algorithm does not use the particle velocity to compute the new position, but the velocity can be derived from the trajectory, and is accurate to order Δt^2:

$$\vec{v}_i(t) = \frac{\vec{r}_i(t+\Delta t) - \vec{r}_i(t-\Delta t)}{2\Delta t} + \mathcal{O}(\Delta t^2). \tag{2.4}$$

This means that quantities depending on the velocities as the total kinetic energies are not very accurately determined. Since the position of the particles at time step $t+\Delta t$ depends on positions at times t and $t-\Delta t$, the initialization is solved then by approximating $\vec{r}_i(\Delta t)$ for $\vec{r}_i(0)$ and $\vec{v}_i(0)$:

$$\vec{r}_i(\Delta t) \approx \vec{r}_i(0) + \vec{v}_i(0)\Delta t + \frac{\vec{a}_i(0)}{2}\Delta t^2. \tag{2.5}$$

From $\vec{r}_i(\Delta t)$, one can calculate the forces, hence $\vec{a}_i(\Delta t)$, and then apply iteratively Eq. 2.3. An integration scheme where positions and velocities are simultaneously updated is the velocity Verlet algorithm:

$$\vec{r}_i(t+\Delta t) = \vec{r}_i(t) + \vec{v}_i(t)\Delta t + \frac{\vec{a}_i(t)}{2}(\Delta t)^2 + \mathcal{O}(\Delta t^4), \tag{2.6}$$

$$\vec{v}_i(t+\Delta t) = \vec{v}_i(t) + \frac{\vec{a}_i(t+\Delta t) + \vec{a}_i(t)}{2}\Delta t + \mathcal{O}(\Delta t^2). \tag{2.7}$$

Being mathematically equivalent to the Verlet scheme, the derivation approach in Velocity Verlet algorithm explicitly incorporates velocity, solving the first time step problem in the basic Verlet algorithm form. The standard implementation of this algorithm follows these steps:

1. Start from the initial configuration of the system.

2. Calculate new position as:

$$\vec{r}_i(t+\Delta t) = \vec{r}_i(t) + \vec{v}_i(t)\Delta t + \frac{1}{2}\vec{a}_i(t)\Delta t^2. \tag{2.8}$$

3. Calculate the intermediate velocity:

$$\vec{v}_i\left(t+\frac{1}{2}\Delta t\right) = \vec{v}_i(t) + \frac{1}{2}\vec{a}_i(t)\Delta t. \tag{2.9}$$

4. Compute new acceleration $\vec{a}_i(t+\Delta t)$ (knowing $\vec{r}_i(t+\Delta t)$).

5. Calculate new velocity:

$$\vec{v}_i(t+\Delta t) = \vec{v}_i\left(t+\frac{1}{2}\Delta t\right) + \frac{1}{2}\vec{a}_i(t+\Delta t)\Delta t. \tag{2.10}$$

2.3.1.3 Periodic boundary conditions

An important feature in MD simulations is the use of periodic boundary conditions (PBC). When PBC are applied, an image of the simulation box is repeated infinitely in *x,y,z* directions around a central box, forming an infinite lattice. In each replicated box, the periodic images of the particles or molecules will move exactly the same way as in the initial simulation box. When a molecule leaves the central box, one of its images will enter through the opposite face. Due to its simple geometry, cubic and rectangular boxes are the most common choices [70].

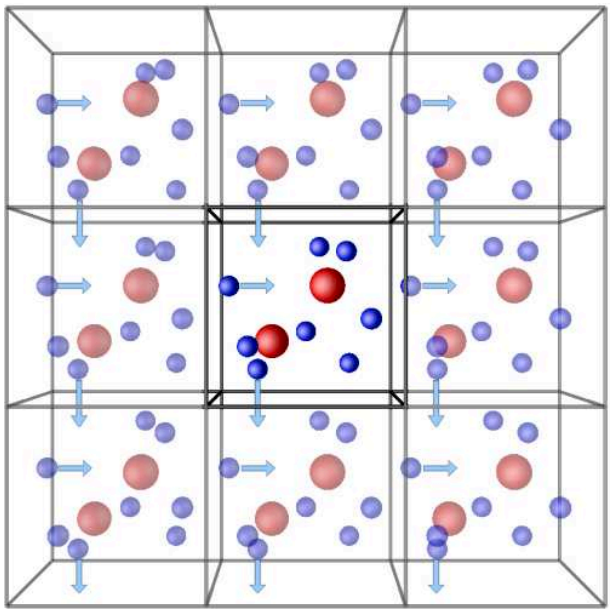

Figure 2.9: Schematic representation of the idea of periodic boundary conditions. Image extracted from http://isaacs.sourceforge.net/over.html.

2.3.1.4 Thermostat and barostat

Assuming a classical description of the particle motion, as in classical MD, the temperature of a particle system is related to the average of the velocity of the particles:

$$\left\langle \frac{1}{2}mv^2 \right\rangle = \frac{1}{2}k_B T N_f. \tag{2.11}$$

The initial velocities can be given from a Maxwell-Boltzmann distribution at the desired temperature. In practice, total kinetic energy is calculated and divided by the total degrees of freedom $N_f = 3N$, so the instantaneous temperature of the system equals:

$$T = \sum_{i=1}^{N} \frac{m_i v_i^2}{k_B N_f}, \tag{2.12}$$

being $k_B = 1.38 \times 10^{-23}$ JK^{-1} the Boltzmann constant. In order to control the temperature and the pressure in MD simulations, barostating and thermostating methods are used. Nosé-Hoover (NH) thermostat provides a way to control the temperature and pressure in MD simulations [76, 76–78]. The main idea in this method is to introduce a fictitious dynamical variable ζ, whose physical meaning is that of a friction, which slows down or accelerates particles until the temperature is equal to the desired one. The equations of motion in the NH formulation are:

$$m_i \frac{d^2\vec{r}_i}{dt^2} = \vec{F}_i + \zeta m_i \vec{v}_i, \tag{2.13}$$

$$\frac{d\vec{\zeta}}{dt} = \frac{1}{Q}\left[\sum_{i=1}^{N} m_i \frac{\vec{v}_i^2}{2} - \frac{3}{2} N k_B T\right], \tag{2.14}$$

where Q determines the relaxation of the dynamics of the friction, and T denotes the target temperature. Since the friction coefficient can be either positive or negative in time, it cannot be considered as a real friction coefficient. If ζ is positive, energy is taken from the system, whereas if ζ is negative, energy is given to the system. The equations of NH formulation follow from an extended Hamiltonian in which the system and the bath degrees of freedom are coupled. On the other hand, since pressure includes a kinetic component due to particle velocities, both barostating and thermostating require the calculation of the temperature. NH barostat is based on Andersen barostat [77], and involves coupling the system to the volume of the simulation box. This coupling mimics a system simulated in a container that can be compressed by a piston due to the action of an external constant pressure. NH thermostat and barostat are implemented in *LAMMPS* (see `https://lammps.sandia.gov/doc/Howto_thermostat.html` and `https://lammps.sandia.gov/doc/Howto_barostat.html`). Once the target average temperature and/or pressure is reached, the system is equilibrated.

2.3.2 Interatomic potentials

In MD simulations, forces acting on every atom are obtained from the appropriate mathematical functions that represent the potential energy evaluated from the molecular structure. These mathematical functions are the so called force fields, where the associated parameters are determined as much as possible from experimental data measured by using electron and/or X-ray diffraction and NMR or Raman spectroscopy, and/or supported by data obtained from *ab-initio* or semi-empirical quantum mechanics calculations. It is worth emphasizing that not all force fields allow to represent all molecule types [75]. The force acting on a certain atom depends on its neighbors or binding partners, and in its chemical environment, therefore the force fields usually have several atom types describing the different systems [70].

Force-fields represent two groups of atomic interactions: (i) bonded interactions (V_{bonded}), which act between atoms that are linked together by covalent bonds and characterize stretching of bonds, bending of valence angles and the rotation of dihedrals, and (ii) non-bonded interactions ($V_{non-bonded}$), which act between atoms that are governed by electrostatic and vdW interactions [75]. In this study, the total system is comprised of three subsystems: pore + solvent + biological peptide, then one is dealing with an hybrid system, whose interatomic forces are of different nature. For this, different force fields were used to model each of them. In addition, non-bonded interactions between subsystems(pore + solvent and/or pore + biological peptide) are included. The total potential energy of the system is described as:

$$\begin{aligned} V_{total} &= V_{bonded} + V_{non-bonded}, \\ V_{bonded} &= V_{pore} + V_{peptide} + V_{water}, \\ V_{non-bonded} &= V_{LJ} + V_{Coulomb}. \end{aligned} \tag{2.15}$$

There have been huge numbers of available potential models for the atomic interactions within different materials, which have been developed since the 1970s, when a deeper analysis and knowledge about molecular mechanics increased. In covalent materials, the atoms are held together by covalent chemical bonds and are represented by models such as the valence force field model (VFF) [79], Stillinger-Weber potential (SW) [80, 81], Tersoff potential [82], Brenner potential [83] and *ab-initio* approaches [84]. Also, some commonly used force fields for biological systems are CHARMM, GROMOS, AMBER, UFF, OPLS, among others [70, 75]. However, all these force fields are well suited for non-reactive interactions, but they result to be inadequate for modeling changes in atom connectivity, in chemical reactions as bonds break and form. This has motivated the inclusion of connection-dependent terms in the force field description, yielding a reactive force field, Reax force field (ReaxFF) [85]. Based on the nature of each subsystem in this work, we present all the potentials used here.

Empirical potential models are widely used to study solid-state materials. Among the potentials that characterize Mo and S interactions for MoS_2, a VFF was first used to study the dynamical properties of MoS_2 lattices and nanotubes, where the interactions were assumed to be associated with the stretching and bending Mo-S bonds and two-body potentials for the interlayer interactions. More recently, Jiang et al. [84] developed a SW potential for SL-MoS_2 starting from the VFF model by fitting parameters to the experimental phonon spectrum [86]. In the last two years, Ostadhossein et al. developed a ReaxFF parameter set for Mo and S to study energy and reaction mechanisms in SL and ML-MoS_2, to model vacancy formation energies in MoS_2 and the possibility to use these defects to functionalize MoS_2 surface [87]. In this work, SL and ML-MoS_2 circular nanopores were modeled using SW potential while, the sub-nm pores, created from atomic defects, were simulated in vacuum under the ReaxFF context. Next, we describe the SW potential and ReaxFF formulations for a better understanding of these force fields formulations.

2.3.2.1 Stillinger-Weber potential for V_{pore} (circular pores)

Stillinger-Weber (SW) potential was originally proposed by Stillinger and Weber to describe the interaction in solid and liquid forms of silicon [80]. In the SW potential formulation, the energy increments for the bond stretching and angle bending are described by the following two-body and three-body terms [84]:

$$V_2(r_{ij}) = A\left(\frac{B}{r_{ij}^4} - 1\right) exp\left[\frac{\rho}{r_{ij} - r_{max}}\right], \tag{2.16}$$

$$V_3(\theta_{ijk}) = K\, exp\left[\frac{\rho_1}{r_{ij} - r_{max_{ij}}} + \frac{\rho_2}{r_{ik} - r_{max_{ik}}}\right]\left(\cos(\theta_{ijk}) - \cos(\theta_0)\right)^2, \tag{2.17}$$

where V_2 corresponds to the bond stretching and V_3 associates with the angle bending. The cut-offs r_{max}, $r_{max_{ij}}$ and $r_{max_{ik}}$ are geometrically determined by the material's structure. As shown by Jiang et al, the geometrical parameters ρ, ρ_1 and ρ_2 are determined analytically considering that the structure is in the equilibrated configuration:

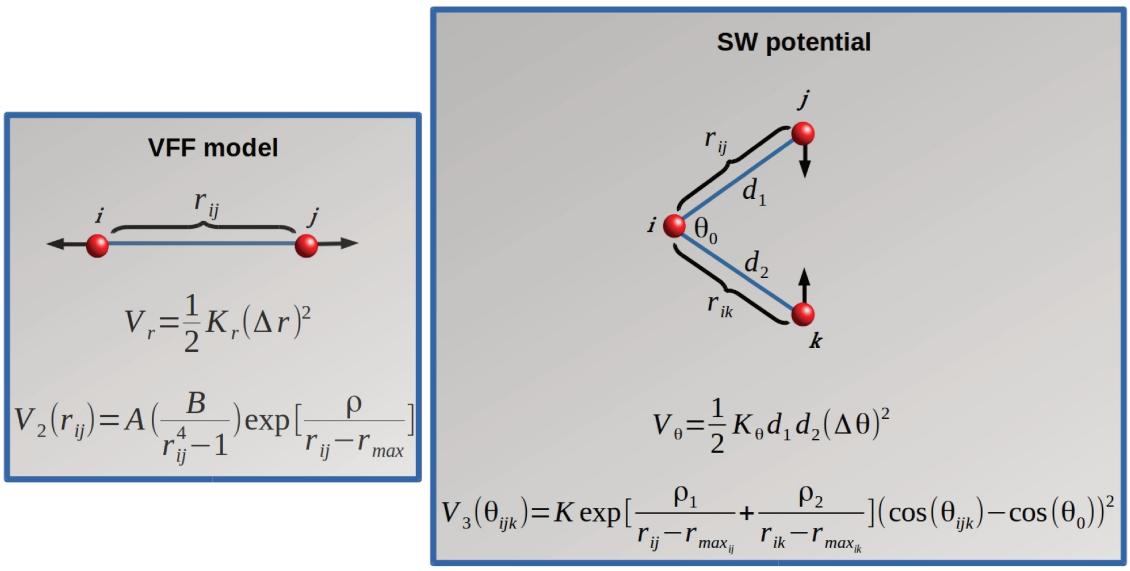

Figure 2.10: Comparison between bond-stretching V_r and angle-bending V_θ interactions from VFF model, and two-body $V_2(r_{ij})$ and three-body $V_3(\theta_{ijk})$ interaction from SW potential, in a covalent material. Atoms movement directions are indicated with black arrows. The scheme is taken from Ref. [84].

$$\frac{\partial V_2}{\partial r}\Big|_{r=d} = 0, \quad \frac{\partial V_3}{\partial \theta}\Big|_{\theta=\theta_0} = 0. \tag{2.18}$$

The equilibrium bond length d and θ_0 (Eq. 2.18) are determined experimentally or by theoretical methods, from the material structure. Geometrical parameter B on the other hand, is related to the nonlinear mechanical behavior of the stress-strain relation during the tension applied on a SL-MoS_2 system [84]. The constants A and K (Eqs. 2.16 and 2.17), which are energy parameters, are determined analytically from the VFF model [84]. In the parametrization performed by Jiang et al. of the SW potential, the geometrical parameters are determined analytically based on the equilibrium state of each individual potential energy term, while the energy parameters A and K are taken from the valence force field model (see Ref. [84] for more details).

It turns out that SW potential derived by Jiang et al. presents great stability during MD simulations of MoS_2 due to the accuracy inherited directly from the VFF model. SW potential can be easily implemented in many open source MD simulations packages such as *LAMMPS* (https://lammps.sandia.gov/doc/pair_sw.html). SW potential parameters for SL-MoS_2 obtained for *LAMMPS* are available in Ref. [84].

2.3.2.2 Reax force field (ReaxFF) for V_{pore} (defect pores)

ReaxFF was developed to bridge the gap between quantum chemical (QC) and empirical force field (EFF) based computational chemical methods. QC methods are, in general, applicable to all chemical systems, regardless of connectivity, their computational expense makes them inapplicable for large (several thousands atoms) systems. Their computational expense also makes QC methods primarily applicable for single point or local energy minimization: high-temperature MD simulations are generally too-time consuming [88]. To overcome this issue, quantum mechanics (QM) structure and energy data are used to train empirical force fields that require

significantly fewer computational resources, thereby enabling simulations to better describe dynamic processes. Such empirical methods, trade accuracy for lower computational expense, making it possible to reach simulation scales that are orders of magnitude beyond what is tractable for QM [85].

Atomistic force field methods use empirically determined interatomic potentials to calculate system energy as a function of atomic positions. Classical approximations are well suited for non-reactive interactions, such as angle-strain represented by harmonic potentials, dispersion represented by vdW potentials and Coulombic interactions represented by various polarization schemes. However, such descriptions are inadequate for modeling changes in atom connectivity (i.e., for modeling chemical reactions as bonds break and form). This motivates the inclusion of connection-dependent terms in the force field description, yielding a reactive force field. In ReaxFF, the interatomic potential describes reactive events through a bond order formalism, where bond order is empirically calculated from interatomic distances [85]. The bond order is the overlap population of the electrons between atoms, or in other words, this is a measure of the strength of the covalent bond between atoms [89]. Electronic interactions driving chemical bonding are treated implicitly, allowing the method to simulate chemical reactions without explicit QM consideration. The classical treatment of reactive chemistry made available by the ReaxFF methodology has opened the door for numerous studies of phenomena occurring on scales that were previously inaccessible to computational methods.

One of the main advantages of ReaxFF is that it enables simulations involving reactive events at the interface between solid, liquid, and gas phases, which is made possible because the ReaxFF description of each element is transferable across phases [85]. For example, an oxygen atom is treated with the same mathematical formalism whether it is in the gas phase as O_2, in liquid phase in a H_2O molecule, or in a solid oxide. ReaxFF allows furthermore to simulate complex processes involving multiple phases in contact with one another, by considering phenomena dependent on reactivity of the involved species, their diffusivity and solubility [85]. ReaxFF functional form has evolved from its original 2001 ReaxFF hydrocarbon description [90], and it has been stable although optional terms are added to the potential for specific cases. Chenoweth et al. [91] describe the ReaxFF current functional form in the hydrocarbon combustion work, referred to as 2008-C/H/O, which has demonstrated significant transferability across the periodic table.

To ensure ReaxFF transferability, the following general guidelines have been adopted in its development [88]:

- No discontinuities in energy or forces (even during reactions).
- Each element is described by just one force field atom type.
- Atoms hybridization from its chemical environment.
- No pre-definition of reactive sites required, this is, drive reactions using restraints is possible and at the right temperature and chemical environment, reactions can occur automatically.

Technically, ReaxFF provides accurate description of bond breaking and bond formation, where the connectivity determined by bond orders obtained from the interatomic distances is updated every MD step. This allows the bonds to break and form during the simulation. The non-bonded interactions, such as vdW and Coulomb, are calculated between every pair of atoms. In this process, any excessive close-range non-bonded interactions are avoided by inclusion of a shielding term

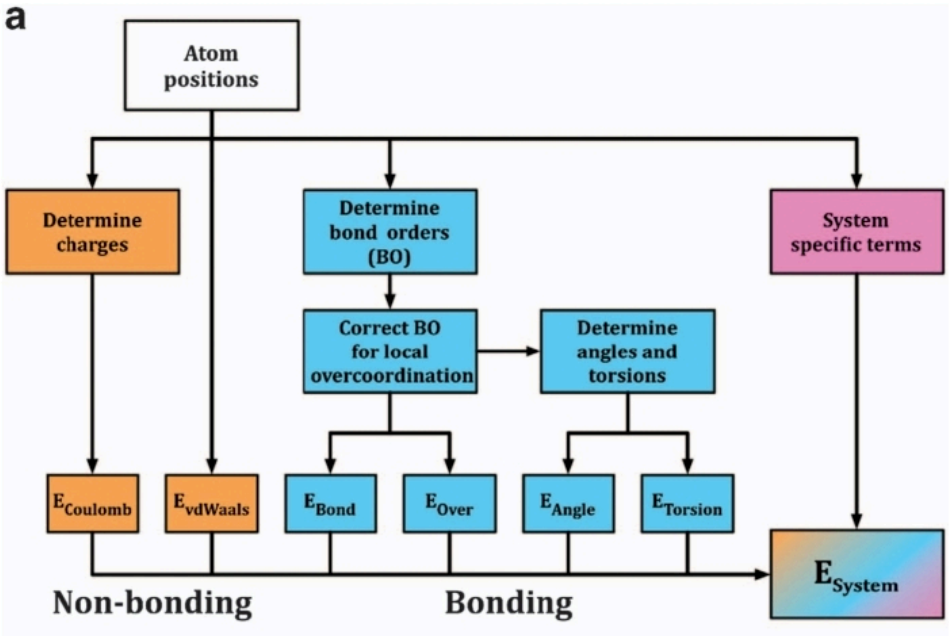

Figure 2.11: Schematic representation of the overview of ReaxFF total energy components. Figure extracted from Ref. [85].

[91]. Moreover, a polarizable charge description and bond order-dependent three and four-body terms are also included in the force field description [92]. Bond orders are incorporated in all valence terms (i.e. energy contributions depend on connectivity, like valence and torsion angle energy) ensuring that energies and forces associated with these terms go to zero upon dissociation. Excessive short-range repulsive/attractive non-bonded interactions are circumvented by inclusion of a shielding term in the vdW and Coulomb interaction. The following expression to derive the forces on each atom is [85]:

$$E_{system} = E_{bond_{ij}} + E_{val_{ijk}} + E_{tor_{ijkl}} + E_{over_i} + E_{under_i} + E_{lp_i} + E_{vdw_{ij}} + E_{coul_{ij}} + E_{HB_{iHj}} + E_{specific}. \tag{2.19}$$

In Eq. 2.19 the total energy is divided into bond-order contributions, where $E_{bond_{ij}}$ is a function of interatomic distance and describes the energy associated with forming bonds between atoms i and j. $E_{val_{ijk}}$ and $E_{tor_{ijkl}}$ are the energies associated with three-body valence angle strain and four-body torsional angle strain. E_{over_i} and E_{under_i} are interactions directly involving all bonded neighbors of atom i. This terms involve an energy penalty that prevents the over and under coordination of atoms based on atomic valence rules. Lone-pair E_{lp_i} contribution is a single-body potential computed over the atom i resulting from the energy and forces due to unpaired electrons of this atom. $E_{HB_{iHj}}$ computes the interaction between atoms i and j that interact through a hydrogen bond. $E_{specific}$ represents system specific terms that are not generally included, unless required to capture properties particular to the system of interest [85]. Finally, non-bonded terms include vdW and Coulomb interactions computed between atom pairs i and j [85].

A schematic representation of ReaxFF potential is shown in Fig. 2.11, showing that the potential is divided into bond-order-dependent and -independent contributions. Bond order calculation from the interatomic distances uses the empirical formula:

$$
\begin{aligned}
BO_{ij} = \quad & BO_{ij}{}^{\sigma} + BO_{ij}{}^{\pi} + BO_{ij}{}^{\pi\pi} \\
= \quad & \exp\left[p_{bo1}\left(\frac{r_{ij}}{r_0{}^{\sigma}}\right)^{p_{bo2}}\right] + \exp\left[p_{bo3}\left(\frac{r_{ij}}{r_0{}^{\pi}}\right)^{p_{bo4}}\right] + \exp\left[p_{bo5}\left(\frac{r_{ij}}{r_0{}^{\pi\pi}}\right)^{p_{bo6}}\right], \qquad (2.20)
\end{aligned}
$$

where BO is the bond order between atoms i and j, r_{ij} is the interatomic distance, r_0 terms are equilibrium bond lengths, and p_{bo} terms are empirical parameters [85, 90, 93, 94]. Eq. 2.20 is continuous, so no discontinuities through transitions between σ, π and $\pi\pi$ bonds are present. This bond-order formula accommodates long-distance covalent interactions characteristic in transition state structures, allowing the force field to accurately predict reaction barriers [85]. The three exponential terms contained in Eq. 2.20 describe: (1) the σ bond (p_{bo1} and p_{bo2}), (2) the first π bond (p_{bo3} and p_{bo4}) and (3) the second π bond (p_{bo5} and p_{bo6}) [90].

The covalent range of the bond order terms is typically taken to be 5 Å, which is sufficient for most elements to describe even the weakest of covalent interactions, but can be extended beyond this range. This may occasionally be required for elements with very large covalent radii. The long-distance covalent bond feature requires an extra step of bond-order correction, to avoid the inclusion of non-bonded neighbors. Terms in the potential that are dependent on bond order, such as bond energy and angle strains, are calculated directly from the corrected bond order [85].

In contrast with classical force fields such as SW potential, which rely on static bonds and fixed partial charges associated with atoms, an important feature of ReaxFF framework is the charge equilibration procedure (QEq). A QEq scheme is applied at each iteration to calculate partial atomic charges, which are then used to compute Coulombic interactions. QEq developed by Rappé and Goddard [95], corresponds to the problem of assigning partial charges to atoms by minimizing the electrostatic energy of the system, including the energy required to create the charge of an atom under constraints of charge neutrality. It is important to solve the QEq problem with high accuracy, since otherwise the energy of the system may show unacceptable drifts during constant energy NVE simulations [96]. QEq method is mathematically formulated as the solution of a large sparse linear system of equations [95], for instance QEq needs to be performed accurately at each time step due to the great impact on the forces and the total energy of the system. From a technical aspect, smaller time step lengths (compared to 1 fs for SW potential) need to be used for ReaxFF implementation, tenth of femtosecond for instance [96]. Additionally, the QEq approach allows the atomic partial charges to respond to changes in the environment, including under non-equilibrium dynamics. This method is used to calculate the Coulombic interactions. The QEq method is calculated independently from $BO(r_{ij}, r_0)$ calculations, which means that there is no information transfer between this two processes.

Non-bonded and bonded terms in ReaxFF are computed independently. vdW and Coulomb forces are included for all atom pairs, where to account for the vdW interactions, a distance-corrected Morse-potential is used as shown by Mueller et al. in their work on the "Development and Validation of ReaxFF Reactive Force Field for Hydrocarbon Chemistry Catalyzed by Nickel" [93] and as formulated by van Duin et al. [90] in the original functional form of ReaxFF potential. ReaxFF has been used to simulate processes such as heterogeneous catalysis and atomic layer deposition, where ReaxFF strength is shown by modeling reactive chemistry at heterogeneous interfaces [85].

We have used ReaxFF potential to perform MD simulations of sub-nm pores (Fig. 2.5). ReaxFF can be implemented in *LAMMPS* simulations package (https://lammps.sandia.gov/doc/pair_reaxc.html) and the parameters associated to Mo/S/C/H/O interactions used in this work are available in Yilmaz et al. [87] work. We acknowledge to Prof. A. van Duin for providing us the parameters file and for helpful discussions.

2.3.2.3 AMBER99sb-ILDN for $V_{peptide}$

One well know functional form to model the potential energy of a biomolecule is:

$$V = \sum_{bonds} k_i(l_i - l_{i_0})^2 + \sum_{angles} k_i(\theta_i - \theta_{i_0})^2 + \sum_{torsions} \frac{1}{2} V_n[1 + cos(n\omega - \gamma)]^2. \tag{2.21}$$

The first term in Eq. 2.21 models the interaction between pairs of bonded atoms, it corresponds to a harmonic potential that describes the change of energy as the bond length l_i deviates from the equilibrium value l_{i_0}. The second term represents the energy change associated with a variation of the valence angles between the bonds and again is described with a harmonic potential. The third term is a torsional potential and involves three bonds [97].

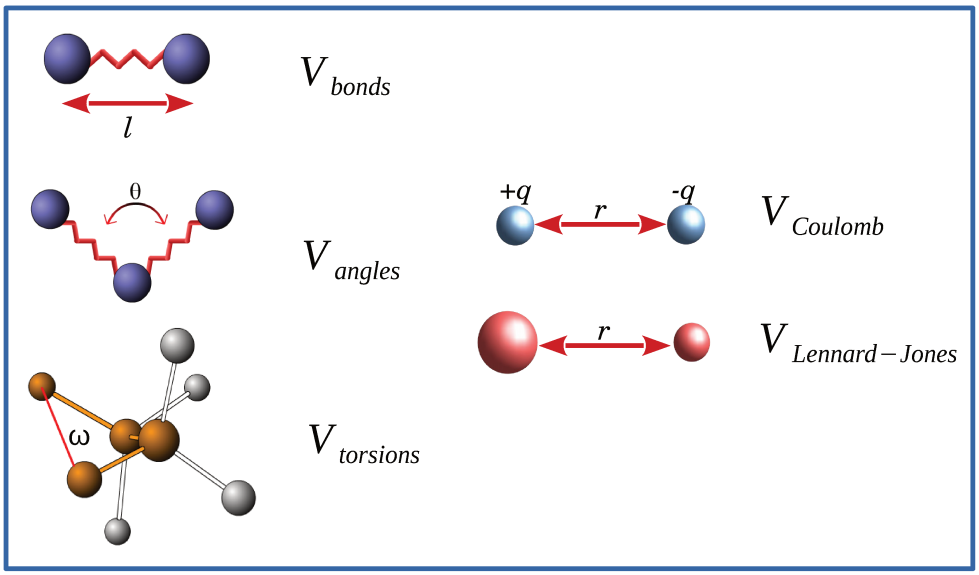

Figure 2.12: Schematic representation of the key contributions to a molecular force field bond stretching, angle bending, torsional term and non-bonded interactions.

One of the force fields that performs well for biological and organic molecules, is the AMBER force field, whose functional form is given by Eq. 2.21 [75, 98, 99]. AMBER99 is the third generation of AMBER parametrization, with the parameters for both amino acids and nucleic acids. Biological peptides where modeled here with the AMBER99sb-ildn force field, which exhibits considerably good agreement with the NMR experimental data [100]. Furthermore, it is a well known and widely used by the **PHysics applied** to **Proteins** (PHaP) group members in simulations of protein conformational dynamics.

2.3.2.4 TIP3P for water

A wide range of water models have been developed and tested for different problems. These rigid non-polarizable models are the simplest and the most computationally efficient, with between three and five interaction sites and a rigid geometry, water is represented as a set of point charges at fixed positions relative to the oxygen nucleus. In these models, covalent bonds are implicitly treated by holonomic constraints [101]. Most commonly used models of this category are: TIP3P and SPCE 3-point, TIP4PEw 4-point and TIP5P 5-point ([102]). In the specific case of TIP3P model [67] the partial positive charges on the hydrogen atoms are exactly balanced by an appropriate negative charge located on the oxygen atom. In this 3 point charge models, the vdW interaction between two water molecules is computed using a LJ function with just a single interaction point per molecule centered on the oxygen atom, and no vdW interactions involving the hydrogen atoms are calculated [97]. In TIP3P water model bonds and angles are constrained during the MD simulations. A useful tool to impose the general holonomic constraints during simulations is the SHAKE algorithm developed by Ryckaert et al. [103–105], which is based on the Verlet algorithm. SHAKE algorithm includes the physical forces of intermolecular, intramolecular interaction, and the forces associated with the constraints, where equations of motion can be derived from the constrained system as:

$$m_i \frac{d^2 \vec{r}_i}{d t^2} = \vec{F}_i + \sum \vec{G}_i, \tag{2.22}$$

where the last term is a sum over the constraints forces [70]. We chose specifically TIP3P model because it is recommended using AMBER99sb-ILDN. Furthermore, Table 2.1 shows the parameters for TIP3P water model used in *LAMMPS* in the present work.

m_{O} [u]	15.9994
m_{H} [u]	1.00800
$k_{bond_{\mathrm{OH}}}$	450
$r_{0_{\mathrm{OH}}}$	0.9572
$k_{angle_{\mathrm{HOH}}}$	55
$\theta_{angle_{\mathrm{HOH}}}$	104.52
m_{K} [u]	39.0983
m_{Cl} [u]	35.4530

Table 2.1: Mass m_i of O, H, K and Cl atomic species. Water equilibrium parameters k_{bond}, $r_{0_{bond}}$, k_{angle} and θ_{angle} for TIP3P model used in *LAMMPS*, extracted from Ref. [106].

2.3.2.5 $V_{LJ} + V_{Coulomb}$

The non-bonded interactions between atoms in MD simulation are governed by the LJ and Coulomb potentials, which are given by:

$$V_{LJ} + V_{Coulomb} = \sum_{j=1}^{N} \sum_{i=j+1}^{N} \left\{ 4\epsilon_{ij} \left[\left(\frac{\sigma_{ij}}{r_{ij}} \right)^{12} - \left(\frac{\sigma_{ij}}{r_{ij}} \right)^{6} \right] + \frac{q_i q_j}{4\pi\epsilon_0 r_{ij}} \right\}. \tag{2.23}$$

For a given pair of atoms (i, j), the potential depends on the distance between them, r_{ij}, as well as their charges q_i and q_j (in the Coulombic case), or the parameters ϵ_{ij} and σ_{ij} (in the LJ case). In

order to obtain the forces on atoms, one can compute these potential functions for all pairs of atoms with the introduction of a cut-off distance. Only interactions among atoms within a given cut-off are considered. There are, however, numerous situations in which long-range interactions between atoms cannot be neglected, and instead have to be approximated numerically. In these cases, it is necessary to approximate the long-range interactions without explicitly computing pair-wise potentials. For this task, "Particle-Particle Particle Mesh" (PPPM) method is a convenient choice. PPPM approximates long-range interactions in a periodic system by obtaining the potential of the entire system of atoms as a function of space, discretized on a grid. (see refs. [107] and [108] for more details).

To properly model alkali and halide monovalent ions in explicitly solvated simulations, Joung et al. [68] developed the associated parameters for the pair-wise interactions between the different ionic species and non-polarizable water models, such as TIP3P, using Coulombic and LJ potentials with fixed charges. TIP3P water model parameters with long-range Coulombic solver PPPM were extracted from reference [106]. The optimized LJ parameters σ_{ij} and ϵ_{ij} are used in Lorentz-Berthelot (LB) combining rules (Eqs. 2.24 and 2.25) and are available in the mentioned work [68]. PPPM method solver for r^{-6} dispersion interaction is implemented in *LAMMPS* MD package. In this work, pore/solvent and pore/peptide interactions are modeled by a Coulomb potential and a LJ potential, which is based on the LB mixing rules:

$$\epsilon_{ij} = \sqrt{\epsilon_{ii}\epsilon_{jj}}, \tag{2.24}$$

$$\sigma_{ij} = \frac{\sigma_{ii} + \sigma_{jj}}{2}. \tag{2.25}$$

The parameters for the MoS_2 nanoporous membranes were extracted from Ref. [84], and the LJ parameters were taken from [109], while the parameters for the TIP3P water model and the K^+ and Cl^- associated Coulomb and LJ parameters were extracted from [68,106]. It is noteworthy to mention that ϵ_{ij} and σ_{ij} values for pore/solvent and pore/peptide interactions (Tables 2.3 and 2.4) were computed by hand (it is mandatory for hybrid systems in *LAMMPS*), from the corresponding values indicated in Table 2.2.

	ϵ [kcal/mol]	σ [Å]	q_i [e$^-$]
Mo Mo	0.0135	4.200	q_{Mo} = +0.76
S S	0.4612	3.130	q_S = -0.38
K^+ K^+	0.1937	3.039	q_K = +1
Cl^- Cl^-	0.0356	4.480	q_{Cl} = -1
O O	0.1020	3.188	q_O = -0.8300
H H	0.0	0.000	q_H = 0.4150

Table 2.2: LJ parameters and charge q_i used in this work for MoS_2, TIP3P water model, and K^+ and Cl^- ions.

pair $i-j$	ϵ_{ij} [kcal/mol]	σ [Å]
1-3	0.037108	3.694
1-4	0.0	2.100
1-5	0.051134	3.620
1-6	0.021920	4.340
2-3	0.216893	3.159
2-4	0.0	1.565
2-5	0.298875	3.085
2-6	0.128119	3.805

Table 2.3: LJ parameters ϵ_{ij} and σ_{ij} for pore/solvent interactions computed from Eqs. 2.24 and 2.25. Atom type 1 is Mo, type 2 is S, type 3 is O (water), type 4 is H (water), type 5 is K^+ and type 6 is Cl^-.

pair $i-j$	ϵ_{ij} [kcal/mol]	σ [Å]
1-3	0.014559	3.424766
1-4	0.038431	3.799835
1-5	0.034074	3.799835
1-6	0.053245	3.579961
1-7	0.047906	3.724910
1-8	0.014559	2.634539
1-9	0.014559	3.335677
1-10	0.014559	3.079987
1-11	0.037108	3.694000
1-12	0.0	2.100000
1-13	0.051134	3.619500
1-14	0.021911	4.340000
2-3	0.085093	2.889766
2-4	0.224623	3.264835
2-5	0.199156	3.264835
2-6	0.311211	3.044961
2-7	0.280007	3.189991
2-8	0.085093	2.099539
2-9	0.085093	2.800677
2-10	0.085093	2.544989
2-11	0.216893	3.159000
2-12	0.0	1.565000
2-13	0.298876	3.084500
2-14	0.128119	3.805000

Table 2.4: LJ parameters ϵ_{ij} and σ_{ij} for pore/solvent, pore/peptide and solvent/peptide interactions. Atom type 1 is Mo, type 2 is S, type 3 to 10 are peptide atom types, type 11 is O (water), type 12 is H (water), type 13 is K^+ and type 14 is Cl^-.

2.3.3 MD simulations procedure

MD simulations of the open pore and translocation systems were performed using *LAMMPS* software package [10Aug15 version (http://lammps.sandia.gov)]. *LAMMPS* is a classical MD code, which includes an important number of potentials for solid-state materials and soft matter, and coarse-grained or mesoscopic systems. It can be used as a parallel particle simulator at the atomic, meso or continuum scale. Also, it runs on single processors or in parallel using message-passing (MPI) or threads techniques.

In parallel MD, forces on each atom can be computed simultaneously, and positions and velocities can be as well updated simultaneously. This represents an advantage for large systems. For more information about the code, please visit http://lammps.sandia.gov. After the modeling procedure, a structure file in `.xyz` format is obtained. To generate the *LAMMPS* input files, *Moltemplate* is used. *Moltemplate* requires a topology file `.lt`, in order to generate the following set of files, which have been already foreshadowed in Fig. 2.2:

- `system.data`: this file contains information about the atom types of the system, simulation box parameters, atomic coordinates, masses, charges, connectivity between the atoms and velocities.

- `system.in.init`: this file contains the global parameters of the potential energy function such as the pair styles associated to the atom types. This file is dependent on the force field to be used. An example of a `system.in.init` file for a pore + solvent system ready to be used by *LAMMPS* is shown:

```
units real
atom_style full
pair_style hybrid sw lj/charmm/coul/long 9.0 10.0 10.0
bond_style harmonic
angle_style harmonic
kspace_style pppm 0.0001
pair_modify mix arithmetic
```

- `system.in.settings`: this file contains the local settings associated to the force field indicated in the `.init` file. Here the coefficients associated to the potential energy functions are included for bonds, angles, dihedrals and pair styles. After the addition of all pair coefficients into the `system.in.settings`, for a pore + solvent system for example, the file is ready to be used by *LAMMPS*:

```
pair_coeff * * sw MoS2_real.sw Mo S NULL NULL NULL NULL
pair_coeff 3 3 lj/charmm/coul/long 0.102 3.188
pair_coeff 4 4 lj/charmm/coul/long 0.000 0.400
pair_coeff 5 5 lj/charmm/coul/long 0.193683 3.039
pair_coeff 6 6 lj/charmm/coul/long 0.035591 4.480
pair_coeff 1 3 lj/charmm/coul/long 0.037108 3.694
pair_coeff 1 4 lj/charmm/coul/long 0.00 2.300
pair_coeff 1 5 lj/charmm/coul/long 0.051134 3.620
pair_coeff 1 6 lj/charmm/coul/long 0.021920 4.340
pair_coeff 2 3 lj/charmm/coul/long 0.216893 3.159
pair_coeff 2 4 lj/charmm/coul/long 0.00 1.765
pair_coeff 2 5 lj/charmm/coul/long 0.298876 3.085
```

```
pair_coeff 2 6 lj/charmm/coul/long 0.128119 3.805
bond_coeff 1 harmonic 450.0 0.9572
angle_coeff 1 harmonic 55.00 104.52
group nanopore type 1 2
group tip3p type 3 4
group ions type 5 6
fix fShakeTIP3P tip3p shake 0.0001 10 100 b 1 a 1
```

After generating the proper required files, *LAMMPS* is ready to go. Usually, 3 steps are needed to perform proper MD simulations:

2.3.3.1 Energy minimization

First, one performs a minimization of the system, also called geometry optimization. This step is performed in order to "roughly" minimize the global energy/forces of the system that was just built, in order to avoid steric clashes or bad contacts between atoms and molecules that could come from the modeling part. Energy minimization is performed by iteratively adjusting atom coordinates. Iterations stop when one of the stopping criteria is satisfied. At that point, the configuration will be in local potential energy minimum. Furthermore, in the minimization, highly overlapped atoms (large energies and forces), are pushed off each other. In this case, the minimization runs were made using the conjugate gradient (CG) algorithm, that is a simple way to describe it, an iterative process in which an approximation to the function in a neighborhood of the current point in space is minimized. In all cases, the objective function being minimized is the total potential energy of the system as a function of the N atom coordinates [110, 111]. As implemented in *LAMMPS*, the procedure stops after the energy/force tolerance is met: 1.0×10^{-4} for the energy (kcal/mol) or 1.0×10^{-6} for the force (units real [kcal/mol/Å]).

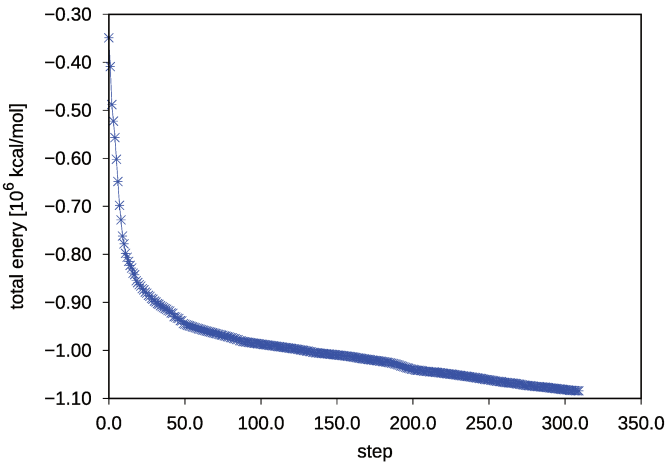

Figure 2.13: Total energy in kcal/mol of the nanopore+solvent system as a function of the minimization steps.

2.3.3.2 Equilibration of the system

The equilibration of the system is performed in the isothermal-isobaric *NPT* ensemble. This step is necessary to relax the simulation box volume and equilibrate the system at the desired temperature T and pressure P. In equilibration simulations, the volume of the simulation box is allowed to change. The equilibration runs were performed during 100 ps at $T = 300$ K and $P = 1$ bar, which are kept constant using a NH thermostat and barostat.

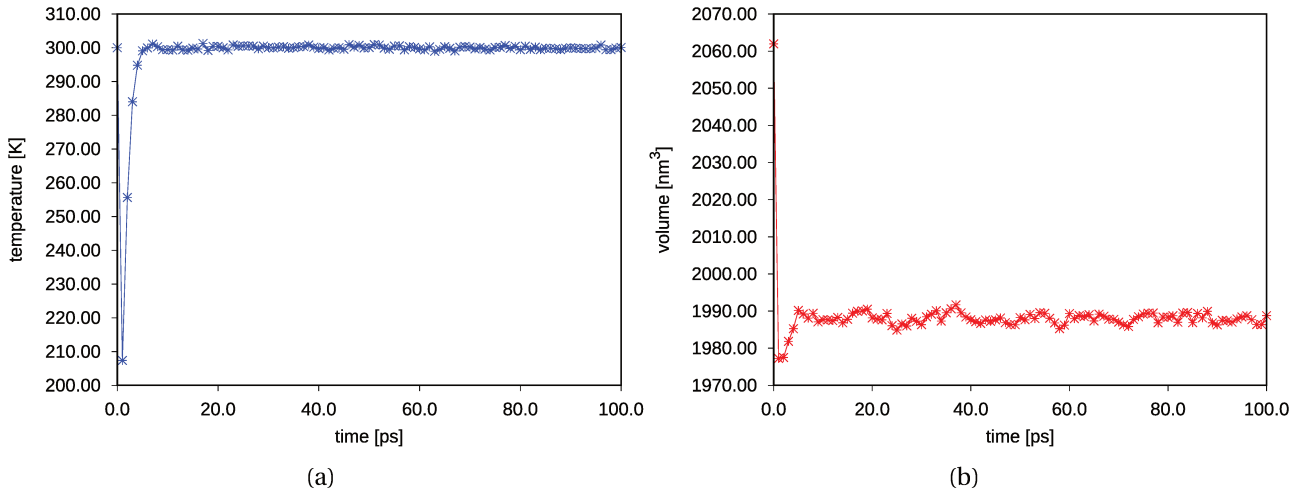

Figure 2.14: (a) Evolution as a function of time of the temperature T in K of the system during equilibration. (b) Evolution of the volume V in nm^3 of the simulation box during equilibration.

When the minimization and equilibration of the systems have reached convergence after 300 steps (Fig. 2.13) and after 100 ps (Fig. 2.14), one can start the so-called production run.

2.3.3.3 Production run

Finally, after the equilibration run, a production run was performed in the canonical ensemble NVT at $T = 300$ K for the different systems.

- **Equilibrium MD simulations:** First, equilibrium MD simulations were carried out in absence of electric field during 10 ns using the velocity Verlet algorithm with a time step of 1 fs, and coordinates saved every 1 ps.

- **Non-equilibrium MD (NEMD) simulations:**

  Non-equilibrium MD (NEMD) were performed at $V = 0, 0.25, 0.5, 0.75$ and 1.0 V, in order to simulate the ionic conduction through each MoS_2 nanopores, with 10 ns of simulation duration. The corresponding applied voltage is:

$$V = -L_z E_z, \tag{2.26}$$

  where L_z is the length of the simulation box in the z-direction [60, 61].

The value of 1.0 V, corresponding to an electric field of $E_z = 5 \times 10^{-3}$ V/m was used in the translocation systems, to accelerate MD simulations in order to observe translocation events [62].

The `production.in` file example for a non-equilibrium MD simulation of a pore + solvent system at $V = 1$ V is the following:

```
# --------- Init Section ---------
include ‘‘nanopore+solvent.in.init’’
# --------- Atom Definition Section ---------
read_data ‘‘nanopore+solvent_eq.data’’
# --------- Settings Section ---------
include ‘‘nanopore+solvent.in.settings’’
# --------- Run Section ---------
timestep 1.0
velocity all create 300.0 12345
thermo 1000
# - save trajectory -
dump dmd all custom 1000 traj_md.lammpstrj id mol type x y z ix iy iz
# - run at constant volume -
fix fxef all efield 0.0 0.0 0.005
fix fxmd all nvt temp 300.0 300.0 100.0 tchain 1
restart 1000000 restart_md
run 10000000
write_data nanopore+solvent_md.data
undump dpmd
unfix fxef
unfix fxmd
```

Using 108 processors, the order of magnitude of CPU time for a MD run corresponding to a 10 ns trajectory of a system containing 192 975 atoms is 1000 h. Thus, for a total length of open pore trajectories of 10 ns (59 MD runs) CPU time is 59 000 hours. The simulations performed in the present work for the open pore and translocation systems, are listed in the following tables:

System	h [nm]	d [nm]	V [V]	N_{atom}	Box size [nm^3]
SL-MoS_2	0.31	1 Mo + 5 S	0	2010	$7.5 \times 7.5 \times 15$
		2 Mo + 7 S		2007	
		4 Mo + 14 S		1998	
		1.0	0, 0.25, 0.5, 0.75, 1.0	192927	$10 \times 10 \times 20$
		1.5		192951	
		2.0	0, 0.25, 0.5, 0.75, 1.0, 1.5, 2.0, 2.5, 3.0	192975	
		2.5		193005	
		3.0	0, 0.25, 0.5, 0.75, 1.0	193050	
		4.0		193233	
		5.0		193416	
2L-MoS_2	0.94	2.0	0, 0.25, 0.5, 0.75, 1.0	190407	
3L-MoS_2	1.56			187763	
4L-MoS_2	2.19			185151	
5L-MoS_2	2.81			182703	

Table 2.5: Summary of the MD simulations performed in this work corresponding to the open pore systems. Diameters d and thicknesses h for each system are indicated. Each voltage corresponds to a MD run. Simulations of pores made of atomic defects with diameter <1-sub nm are performed in vacuum with a total of 3 MD runs of 2 ps each. Simulations of circular pores embedded in 1 M KCl solution are performed with a simulation time of 10 ns per MD run. A total of 62 open pore MD runs were performed. The nomenclature for the sub-nm defect pores systems is given by the nature of the atoms removed.

System [nm]	d	peptide	run 1 [ns]	run 2 [ns]	run 3 [ns]	total run [ns]
SL-MoS_2	2.0	K	100	100	-	200
		KK	50	57	23	130
		YGGFM	100	100	-	200
		YGGFM-1K	100	150	-	250
		YGGFM-2K	200	250	-	450
		YGGFM-3K	100	300	-	400
		YGGFM-4K	200	50	-	250
		YGGFM-5	250	150	-	400
	1.5	KK	100	100	-	200
bilayer-MoS_2	2	KK	100	100	-	200

Table 2.6: Summary of MD simulations performed on translocation of different biological peptides through MoS_2 nanoporous membranes with diameter d and different number of layers of 2D materials. The solvent is 1 M KCl solution and the applied voltage is 1.0 V for all the simulations. MD run 1, run 2 and run 3 have different initial conditions. Total run corresponds to the total simulation time per system. The simulation box size is $10 \times 10 \times 20$ nm^3 for all the systems. A total of 21 MD runs were performed.

Chapter 3

Characterization of the ionic conductance through MoS_2 nanopores

Experimental detection and characterization of molecules using SSN, has mostly relied on measuring changes in ionic current flowing across the nanoporous membranes as charged molecules in solution translocate through the pore, when an external voltage is applied across the membrane. Charged molecules that pass through the nanopore displace ions from the pore volume, therefore ultrafast monitoring of ion flow during their passage yields information about the particle structure and chemical properties [60, 112]. The magnitude and duration of the change of ionic current provide information on the diameter and length of the molecule, respectively [6]. More precisely, SSN can be used to detect the presence of a molecule, via changes in the ionic conductance ΔG. ΔG represents a drop in ionic conductance, such as $\Delta G = G_0 - G_m$, where G_0 is the open pore conductance and G_m is the conductance when the nanopore is obstructed by a translocating molecule, also called translocation conductance. Therefore, increasing ΔG and decreasing the signal noise yield a higher signal-to-noise ratio (SNR). Thus, assuming constant noise, increasing ΔG improves the performance of nanopore devices. Hence, the magnitude and statistical properties of ΔG provide good metrics for the nanopore sensing capability [43].

Overall, the sensing capacity of a nanopore is determined by the pore size and thickness of the membrane. For sequencing, each nucleotide should block the ionic current in a unique way that is dependent on its molecular size and shape [6]. Understanding the transport properties such as the conductance of ions in such nanopores is fundamental for the interpretation of translocation experiments for biomolecule detection and for the design of more efficient nanopore based sensors. Given the compromise between the nanopore geometry (membrane thickness and pore diameter) and their transport properties [6, 59, 60, 113, 114], the diameter of the pore is chosen according to the size of the molecule to probe. If a molecule that translocates through a SSN is characterized by the same size as the pore dimension, for instance a double strand DNA molecule translocating in a SSN of diameter $d \sim 2.2$ nm, the theoretical conductance drop is maximum and equal to the open pore conductance, $\Delta G = G_0$ ($G_m = 0$). In order to fabricate DNA or proteins sequencing devices with a high-resolution recognition and detection of DNA bases or protein residues, the diameter of the nanopore must be of the same order of magnitude as that of the molecule to be detected [60].

Although previous experimental [115–117] and theoretical [114, 118–121] works explored the ionic and molecular transport in nm and sub-nm graphene pores, ionic transport through MoS_2 nm and sub-nm pores made of atomic defects has not been yet explored in detail [59]. More

studies on transport properties through these systems are needed to explore applications of this material at the atomic scale. Water desalination and molecular analysis for example, are within the most promising applications, where atomic scale pores provide unique benefits. This is because water transport scales inversely with the membrane thickness allowing for high water fluxes, and membranes with sub-nm pores are highly selective [6, 59, 113]. Furthermore experimental drilling of sub-nm pores has been possible with high reproducibility [59, 122]. For example, ionic irradiation is used to reveal the presence of defects with Å and nm sizes in MoS_2 and WS_2, as recently reported by Thiruraman et al [123].

In the present work, one of the main objectives is to characterize the ionic conductance of MoS_2 nanoporous membranes with different diameters and thicknesses, in order to provide information about the optimal geometry of MoS_2 nanoporous membranes for further experimental verification of single protein translocation based on their ionic transport properties. In the present chapter, we discuss the characterization of the ionic conductance of a KCl aqueous solution through MoS_2 open pore systems without the presence of any biomolecule, in order to study the level of ionic conductance performance of such nanopores.

The study of the open pore systems was performed in different stages: first sub-5 nm SL-MoS_2 nanopores were characterized by studying the interfacial interactions of the solvent with the pore. Particularly, we computed the distribution of water molecules in the vicinity of the nanoporous membrane in order to obtain the *effective* geometrical parameters h^* (effective membrane thickness) and d^* (effective pore diameter). We also studied the effect of the atoms at the edges of the porous region on the concentration of ions in the nanopore volume. The next step corresponds to the pore conductance calculations by determining the ionic current of 1 M KCl solution and the MoS_2 open pore conductance G_0 using NEMD simulations, which is quantified by following the experimental procedure, this is, by computing the ion current-voltage ($I-V$) curves at low voltages (V = 0, 0.25, 0.5, 0.75 and 1.0 V). Then, MD data of open pore conductance values were compared to a conventional analytical model of conductance (macroscopic model of ionic conductance), as explained in more detail in the following sections. With this comparison, we observed that this model fails to predict the conductance values for pores below certain regime of sizes. As it will be discussed in the following sections, inspired in a work on the ionic transport through graphene nanopores [114], we were able to derive an empirical correction to the macroscopic model of conductance, to improve the theoretical predictability of the open pore conductance in SL-MoS_2 nanopores. Furthermore, open pore conductance MD data for multi-layer (ML) (bilayer 2L-, trilayer 3L-, fourlayer 4L- and fivelayer 5L-) was determined as well in order to extend the improved model of conductance for ML-MoS_2 nanoporous systems. Conductance performances of MoS_2 nanopores were studied in order to establish a reference that allows to estimate the ideal conductance drops ΔG in further analysis of the simulations of biological molecules translocation.

3.1 Interfacial interactions of solvent with MoS_2 nanoporous membranes

The interactions at the interface between MoS_2 nanopores and the ionic solution made of water molecules and K^+ and Cl^- ions are strongly influenced by the nature of the 2D materials. Few-layer materials provide a variety of extended atomically flat surfaces with different long-range (vdW) and hydrophobic interactions [124, 125]. These interactions modify the bulk solvent properties at the interface due to the presence of the membrane. For nanoelectronics applications, it is extremely important to understand wetting properties of exposed surface. For example, MoS_2 transistors characteristics highly depend on these properties, since hydrophilicity (i.e., wettability) and hydrophobicity are reported to be related with the fabrication process and the surface chemical composition (possible contaminants due to unreacted species like Mo or S atoms or S deficient or Mo rich regions) [126]. MoS_2 wetting behavior on SiO_2/Si substrates grown by CVD was studied where chalcogen (S) substitution with oxygen (O) resulted in hydrophobic to hydrophilic wettability transition [127]. MoS_2 hydrophobic nature [23, 128] on the other hand may require further treatments for biomolecule translocation and ionic transport experiments [59]. Likewise, the interfacial water structure should influence the interactions of 2D materials with other materials, solvents, ions and small molecules [124]. We quantified such interactions by determining the effective membrane thickness h^* and effective diameter d^* as shown below.

3.1.1 Distribution of water molecules near the pore

Interfacial interactions of water with the MoS_2 membranes were studied by computing the distribution of water molecules in the normal direction to the membrane (z direction) and the radial distribution of water molecules inside the pore in the ρ direction. The radial and normal distributions reported below were averaged over 10 ns MD runs with voltages from 0 to 1.0 V, for a total of 40 ns MD data (4 runs), see Table 2.5.

First, the normal distribution $P(z)$ was computed by counting the number of water molecules in slices of dimension $L_x \times L_y \times \Delta z$, with $\Delta z = 1.0$ Å. Starting from the membrane, the slice was displaced by 0.1 Å in the normal direction up to reaching the top of the simulation box. Fig. 3.1 (a) shows $P(z)$ for MoS_2 nanoporous membranes made of multiple layers (from 1 to 5). On the other hand, the in-plane radial distribution of water was computed inside cylinders defined by the pore diameter, over concentric cylinders with the its axis. Each ring is characterized with a height corresponding to the $z-$position of the center of the nanopore ± 1.0 Å (total height of 2.0 Å) and with a 1.0 Å width from the inner to the outer boundaries. Starting from the center of the pore, the inner boundary of each cylinder was displaced by 0.25 Å in the radial direction, up to reaching the nanopore edge.

From $P(z)$ plots we observed that profiles of water are similar in shape (not dependent on thickness), with a maximum in the vicinity of the nanoporous membrane due to an accumulation of the water molecules as a consequence of the hydrophobicity of MoS_2. Such behavior was reported experimentally by Uhlig et al. [124], where the formation of water layers near 2D materials such as graphene and few-layer MoS_2 and WSe_2 was observed, which is a general property of hydrophobic surfaces in contact with water. Nevertheless, their findings show that interfacial water structure near 2D materials, cannot be entirely explained in terms of the interactions between the

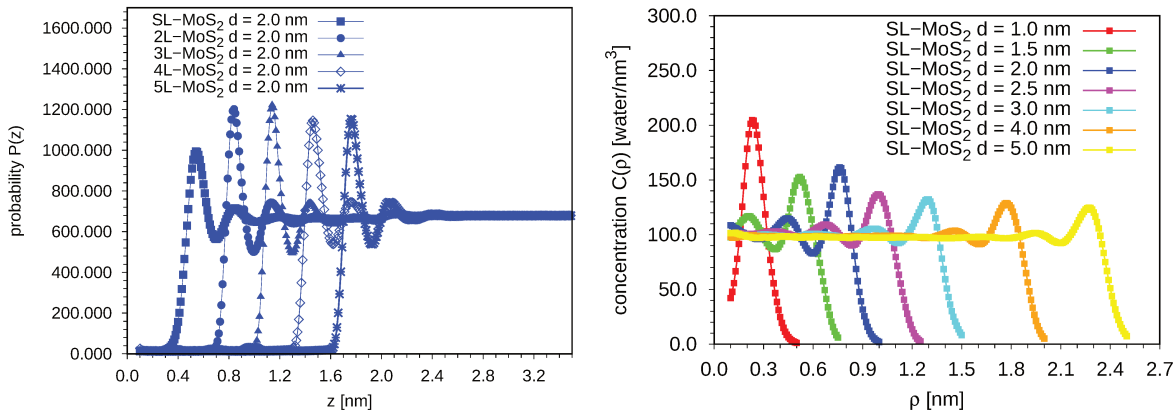

(a) (b)

Figure 3.1: (a) Probability distribution functions $P(z)$ of water molecules in the normal directions (z-direction) of the nanoporous membranes for SL- (blue squares), 2L- (blue circles), 3L- (blue triangles), 4L- (blue empty rhombus) and 5L- (blue star) MoS_2 nanopores of diameter $d = 2.0$ nm. (b) In plane radial distribution $C(\rho)$ of water molecules inside the nanopore. Data are shown for the SL-MoS_2 nanopores of diameter $d = 1.0$ (red), $d = 1.5$ (green), $d = 2.0$ (blue), $d = 2.5$ (magenta), $d = 3.0$ (cyan), $d = 4.0$ (orange), and $d = 5.0$ nm (yellow).

2D materials surface and water. Their results show that molecules coming from the air (N_2 and O_2) are absorbed and dissolved into the liquid water, forming hydrophobic layers that tend to displace the water molecules from the 2D materials surface. Experimentally, the existence of hydrophobic layers on the vicinity of 2D materials surfaces should influence the interactions of those materials with molecules, salts or proteins present in water.

For SL-MoS_2 nanopores of different diameters, as shown in Fig. 3.1 (b), the shape of the concentration profiles remain identical. The property which is modified by the increase or decrease of the diameter d of the nanopore is the length of the plateau $C(\rho)$, leading to larger effective diameters d^* for larger diameters d.

3.1.1.1 Extracting the geometrical parameters of the membrane

As shown in Fig. 3.2 (a), the probability distribution $P(z)$ allowed us to extract the effective thickness h^* of the nanoporous membrane, which represents the minimum thickness from which the water structure is significantly modified. Our definition of h^* is the following: starting from the surface of the membrane, where $P(z) \sim 0$, the first value of z giving the bulk value of P [as indicated with the red dashed line in Fig. 3.2 (a)] is considered as $h^*/2$. According to our simulations, the effective thickness is found to be ~ 0.96 nm for SL-MoS_2, compared to 0.31 nm for S-S distance. Furthermore, pores of different diameters do not influence the structural properties of water in the normal direction of the membrane, since the surface of the pore ($S_{pore} = \pi r^{*2}$) represents a relatively small fraction of the total surface of the nanoporous membrane ($0.02 < S_{pore}/S_{membrane} < 0.69$ for SL-MoS_2 nanopores with $1.0 < d < 5.0$ nm). As shown in table 3.1, the values of the effective thicknesses corresponds to a factor of ~3 between h and h^* for SL-MoS_2, while for 2L-, 3L-, 4L- and 5L- the associated factors correspond to ~1.5, 1.4, 1.3 and 1.2, respectively. In fact, it underlines that hydrophobic features of ultra-thin 2D materials are enhanced at the atomic and molecular level and depends highly on the dimensions of the system and its geometry.

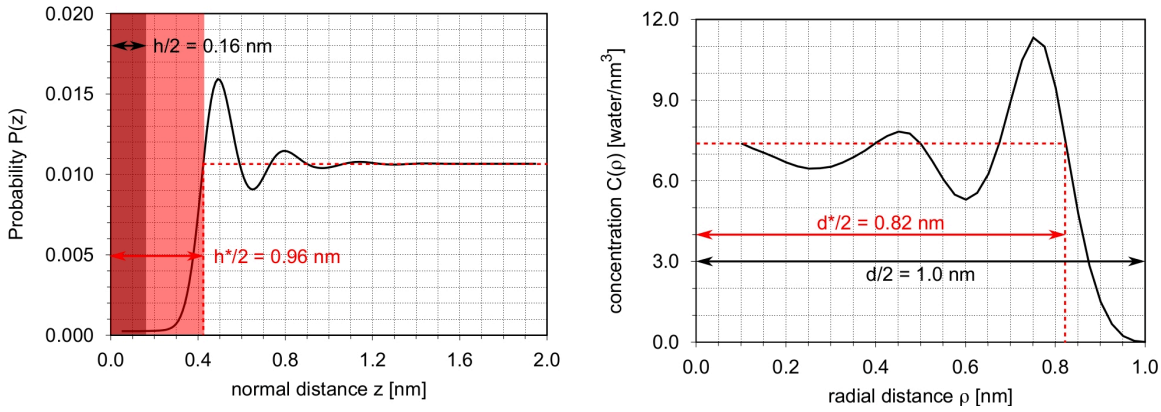

(a) (b)

Figure 3.2: (a) Probability distribution function $P(z)$ of water molecules in the normal direction (z-direction) of the SL-MoS_2 nanoporous membrane. Red dashed line represent the value of the effective thickness h^* extracted from the distribution profile. (b) Radial distribution $C(\rho)$ of water molecules inside the SL-MoS_2 nanopore of diameter $d = 2.0$ nm. Red dashed line represent the value of the effective diameter d^* extracted from the concentration profile.

SSN	h [nm]	h^* [nm]	d [nm]	d^* [nm]
			1.0	0.70
			1.5	1.20
SL-MoS_2	0.31	0.96	2.0	1.64
			2.5	2.14
			3.0	2.72
			4.0	3.68
			5.0	4.68
2L-MoS_2	0.94	1.44	2.0	1.64
3L-MoS_2	1.56	2.16	2.0	1.64
4L-MoS_2	2.19	2.80	2.0	1.64
5L-MoS_2	2.81	3.42	2.0	1.64

Table 3.1: SSN studied in the present work using NEMD simulations. Diameters d and d^* as well as thicknesses h and h^* obtained from the distribution of water molecules in the pore.

The same type of analysis was performed from $C(\rho)$ in order to extract the effective diameter d^* of the nanopores from the water in-plane radial distribution inside the pore. Fig. 3.2 (b) shows the results extracted from MD simulations for the SL-MoS_2 nanopore with $d = 2.0$ nm. In this work, d^* is defined as: starting from the center of the pore with corresponds to the value $C(\rho = 0)$, the last value of ρ for which the radial distribution completely decreases approaching the edges is considered as $r^* = d^*/2$, leading to an effective diameter of $d^* = 1.64$ nm, as indicated with the red dashed line. Overall, evolution of d^* as a function of d is observed in Fig. 3.3 and can be represented by the equation:

$$d^* = d - 0.3nm. \tag{3.1}$$

Values of the effective thickness h^* and effective diameter d^* of each system are shown in the table 3.1. The estimation of the effective geometrical parameters h^* and d^* will be useful for the study of the radial ionic concentration inside the MoS_2 nanopores, and for the conductance G_0 dependency on the geometry of the nanoporous membranes analyses, which will be presented in

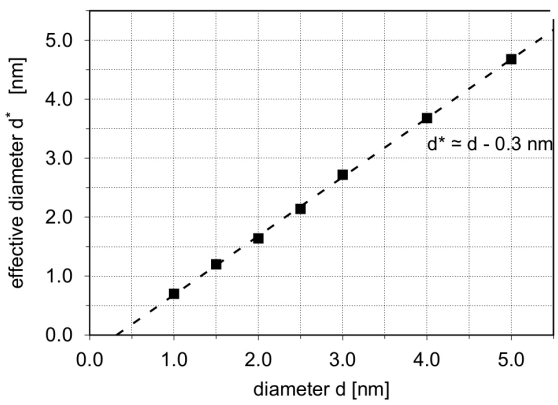

Figure 3.3: Evolution of the effective diameter d^* as a function of pore diameter d. The dashed line represents the equation $d^* = d - 0.3$ nm.

the following sections.

3.1.2 Concentration of ions in the pore

The presence of dangling atoms on the edges of the nanopores may affect the concentration of ions in their volume, which is an important factor to take into account when guiding the design of nanopore sensing experiments. The main advantage of the present analysis is to quantify these effects from MD simulations and present the behavior of ions in the vicinity of the nanopore walls. For this, we investigated the ion distribution inside nanopore and particularly near the nanopore edges, by computing the ion concentration (number of ions/nm^3) as a function of the radial distance ρ from the center of the pore at $\rho = 0$ from MD trajectories. For that purpose, we averaged the ion concentration over concentric cylinders with the pore axis. Each ring has a height corresponding to the effective height of the nanopore h^* and a width of 1.0 Å from the inner to the outer boundaries. Starting from the center of the pore, the inner boundary of each cylinder was displaced by 0.25 Å in the radial direction, up to reaching the nanopore edge as shown in Fig. 3.4. The radial ionic concentrations reported in Fig. 3.4 are average values over positively and negatively charged ions, for the 10 ns MD runs with voltages $0 \leq V \leq 1.0$ V, for a total duration of 40 ns (4 runs).

As shown in Fig. 3.4, the radial concentration of ions inside SL-MoS_2 nanopores is characterized by a plateau starting at $\rho = 0$ (center of the pore) up to ρ_{max}, indicated with the colored dashed line, followed by a linear decrease from ρ_{max} to r^*, the effective radius of the nanopore. Here the length of the plateau is larger as the diameter increases. In addition, the concentration of ions at the center of the pore decreases with the diameter from 1.5 nm to 5.0 nm. For larger diameters, KCl ions tend to occupy the entire space of the pore whereas for smaller diameter they are confined at the center of the pore due to the repulsion forces involved by the edges of the pore. On the other hand, for MoS_2 nanopores made of multiple layers, the ionic concentration profiles are similar to those of the single-layer. The concentration at the center of the pore is larger than in single-layer nanopores ($C(\rho)_0 \sim 2.0$ ions/nm^3) due to the fact that the effective volume of the cylinders is larger [60].

The main question that arises here is: what is the impact of such ionic concentration profiles on conductance drop measured during experiments. In order to answer this question, we considered a SL-MoS_2 nanopore of diameter $d = 3.0$ nm. From the concentration profile shown in Fig. 3.4,

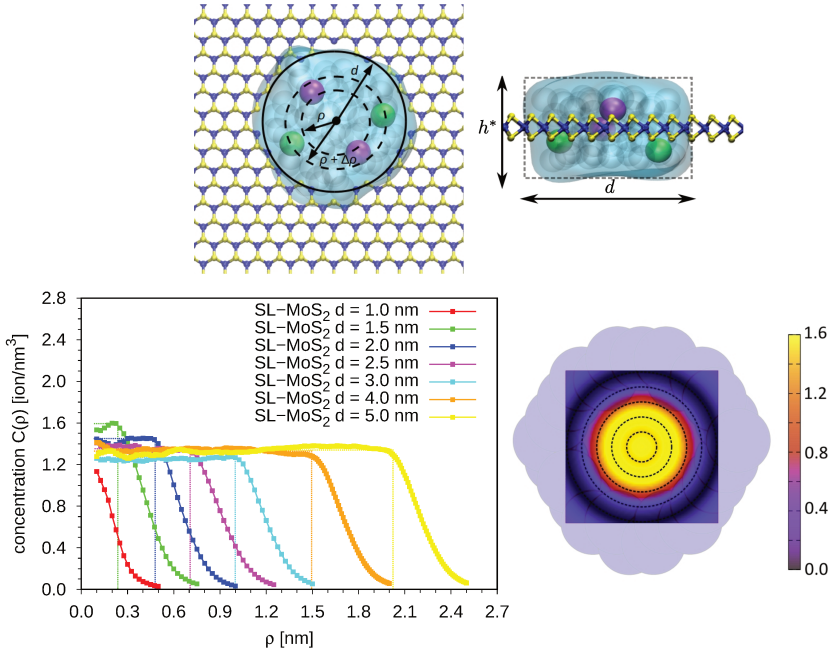

Figure 3.4: Snapshot of MD simulations representing water molecules and KCl ions inside a SL-MoS_2 nanopore of diameter $d = 2.0$ nm. Water molecules are represented with blue transparent spheres and a blue surface. K^+ and Cl^- ions are represented by magenta and green spheres, respectively. Radial concentration of KCl ions inside a SL-MoS_2 nanopore of diameters $d = 1.0$ (red), $d = 1.5$ (green), $d = 2.0$ (blue), $d = 2.5$ (magenta), $d = 3.0$ (cyan), $d = 4.0$ (orange), and $d = 5.0$ nm (yellow). Color map of ionic concentration (color box in ion/nm^3) in a SL-MoS_2 nanopore of diameter $d = 2.0$ nm.

we estimated the length of the plateau $C(\rho)_0$ to be around 2.0 nm. This means that if a molecule such as a rigid double-strand B-DNA molecule ($d_{DNA} = 2.0$ nm) translocates into the nanopore, the ionic concentration between the molecule and the edges of the pore would be ~ 0. Therefore, the conductance drop ΔG would be similar to G_0, the open pore conductance [60].

3.2 $I-V$ curves from non-equilibrium MD simulations

One of the most important measurements to characterize nanopores in sensing experiments is their ionic conductance response to applied voltages. The average current is measured as a function of ramped voltage. The linearity between current and voltage in both, negative and positive bias is usually tested, and finally the open pore conductance is obtained as the slope of $I-V$ curve [129]. In the present work, NEMD simulations were performed with transmembrane voltages in order to monitor first, the time-dependent ionic current $I(t)$ in the nanopore for each applied voltage and second, to extract $I-V$ curves corresponding to each of the MoS_2 nanopores.

3.2.1 Ionic current as a function of time

Ionic current in nanopore experiments is measured when an applied electric field induces longitudinal displacements of the ions of an electrolytic solution through the pore. The corresponding response depends on the applied voltage V. In order to study the $I-V$ characteristics of MoS_2 nanopores of different sizes, we performed NEMD simulations for voltages from $V = 0, 0.25, 0.50, 0.75, 1.0, 1.5, 2.0, 2.5$ and 3.0 V. Then we computed the total net ionic current of the KCl solution $I(t)$ as:

$$I(t) = \frac{1}{\Delta t L_z} \sum_{i=1}^{N} q_i \left[z_i(t+\Delta t) - z_i(t) \right], \tag{3.2}$$

where Δt is the time between MD frames chosen to be 10 ps here, L_z is the dimension of the simulation box in the z-direction, which is the direction of the applied electric field, N is the total number of ions, q_i is the charge of the ion i and $z_i(t)$ is the z-coordinate of the ion i at time t. The values of ionic current are computed as the simple moving average (SMA) of the $I(t)$ fluctuations during the 10 ns MD runs, as shown in Fig. 3.5. Also, the standard error was computed using the following equation:

$$SE = \frac{\sigma}{\sqrt{N_f}}, \tag{3.3}$$

where N_f is the number of frames used for calculating the average current and σ is the standard deviation. Once the ionic current is obtained for each voltage, the ionic conductance can be determined by interpreting the $I-V$ characteristics of the nanopores for low voltages from 0 to 1.0 V, as discussed in the following sections.

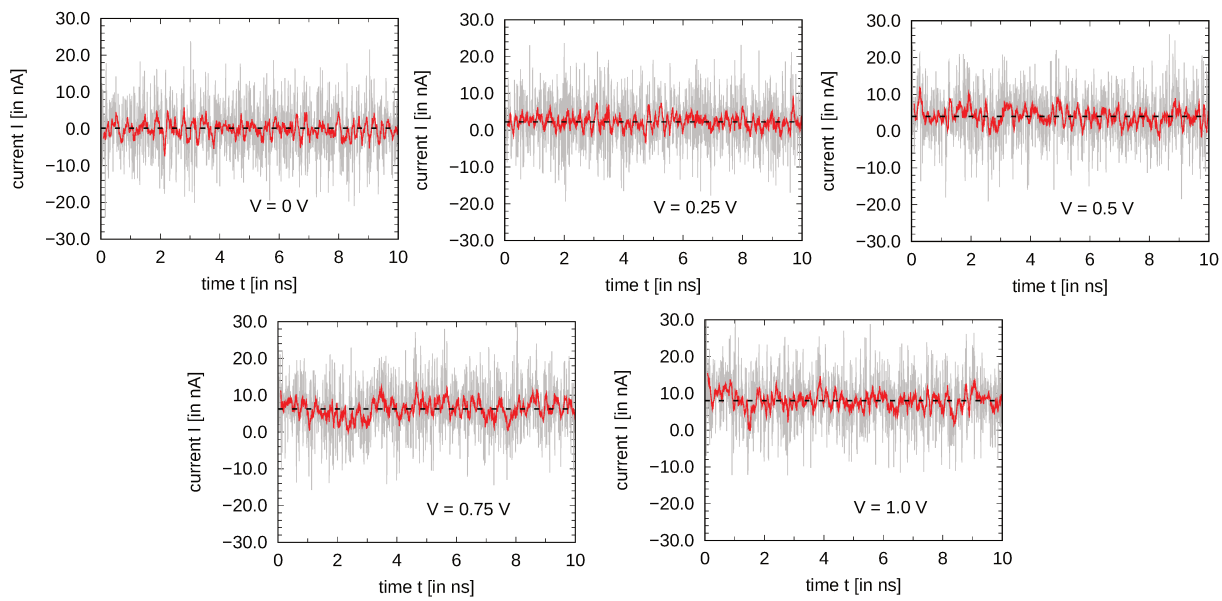

Figure 3.5: Variation of the ionic current $I(t)$ depicted by the gray line with the respective SMA represented by the red line, for the system SL-MoS_2 with $d = 2.0$ nm, for voltages from $V = 0$ to 1.0 V. Window size for SMA is 100 ps.

3.2.2 Ionic conductance of MoS_2 nanopores from $I-V$ curves

Experimentally, the value of the nanopore ionic conductance G_0, can be measured from the corresponding $I-V$ curve by recording the ionic current at a specific voltage [130]. Under good conditions, linear $I-V$ characteristics can be measured up to a high voltage (1.0 V) [11]. Nevertheless, due to asymmetric charge distributions and pore geometries for example, $I-V$ dependence is not always linear, resulting in ionic current rectification (ICR). ICR is a nonlinear $I-V$ behavior observed in biological systems such as transmembrane proteins and voltage-gated ion channels [131, 132], which are responsible for the propagation of electrical signals in excitable cells [133]. This behavior was first described by Wei et al. [134] in nanopipettes systems [135], and since then has been observed in various materials and geometries, such as conical silica nanopores [136], ion-track-etched conical polymer membranes [137, 138], nanochannels [139, 140], and micropores [141]. ICR affects the ionic resistance of the solution within the pore, and produces a dependence on the direction of the current flow. Moreover, when an asymmetric electrostatic potential inside the pore is produced, and when polarity of the applied bias is inverted, different electrostatic profiles arise and consequently current rectification occurs [136], as shown in Fig. 3.6. In other words, ICR occurs when charged surfaces support a Debye layer, so the electrolyte may not remain as a uniform conducting medium. Then, the pore size is no longer large compared to the Debye length ($\sim 1-10$ nm) [142–144]. Influence of pH and ion concentration gradient on ionic transport properties inside nanochannels was also reported [145], and asymmetric ionic currents and diffusive ion flow through charged conical nanopores, was reported as well [137, 146].

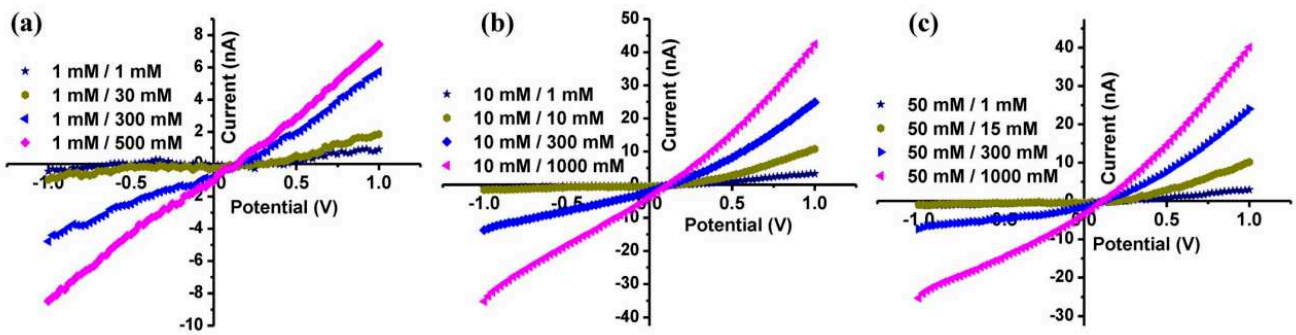

Figure 3.6: ICR for KCl solutions with concentration gradient observed in nanopipettes systems. Typical $I-V$ curves of ICR for different concentration gradients (different KCl concentrations inside and outside the pipettes), are reported by Deng et al. [135].

An important clarification to mention is that $I-V$ curves computed from the MD simulations, correspond only to positive voltages since MoS_2 nanoporous membranes are symmetric and extremely thin along the normal direction of the membrane in z, and in consequence ICR is negligible. From the simulations performed for $V = 0$ to 3.0 V we observed two types of regimes in the $I-V$ curves, a linear regime from 0 to 1.0 V, corresponding to an ohmic behavior of the nanopore, and a sublinear regime from 1.0 to 3.0 V, as shown in Fig. 3.7, for a SL-MoS_2 nanopore with $d = 2.0$ nm.

The sublinear or non-ohmic regime, is a consequence of a saturation of I at high voltages. This saturation is reached when the ion permeation is limited by the process in which it cannot be accelerated by V. Although the physical meaning of the sublinear behavior of $I-V$ curves at high voltages still remains unclear, several interpretations are still being debated in the literature. One discussed interpretation is the diffusion-limited permeation of ions through small confined spaces

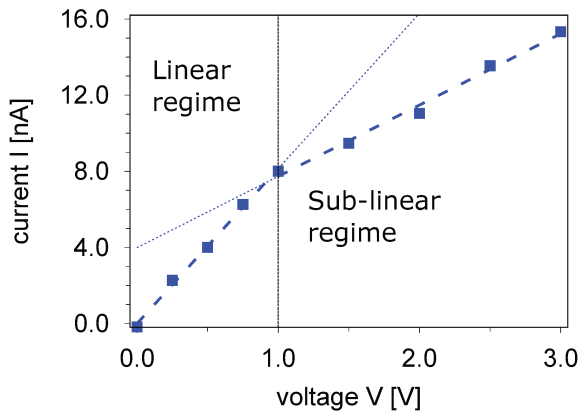

Figure 3.7: Current-voltage $I-V$ characteristics for the system SL-MoS_2 with $d = 2.0$ nm in the present work, from 0 to 3.0 V. Ohmic and non-ohmic behaviors are well discernible in the $I-V$ curve.

such as ionic channels. Nevertheless, in contrast to the conventional permeation theory [147–149], sublinearity of the curve does not necessarily mean that the permeation is diffusion-limited. Factors such as ions hydration and their configurational restraint due to the coordination with water molecules while crossing the channel, induce a free-energy barrier that leads to a saturation of the current I at high voltages [150]. In the present work, we are interested in the interpretations of the linear regime and the behavior of the systems for low voltages, since experimentally, the applied voltages are usually of a magnitude of several hundreds of mV at maximum [6, 23–25, 32, 36, 59, 151]. Furthermore, according to linear response theory [69], the response of a system to small driving forces is quantitatively related to the magnitude of equilibrium fluctuations. In fact, it has been reported from MD simulation that the permeability of single-file water channels can be determined by monitoring equilibrium water translocation rates [152, 153]. More specifically, equilibrium water transport [121] and ionic selectivity in graphene and other atomically thin pores [114, 118] was reported, providing useful models that can be used to describe the ionic transport properties from equilibrium systems.

As observed in Fig. 3.8, linear $I-V$ curves for low voltages allowed us to extract the open pore conductance G_0 using Ohm's law, as the slope of the $I-V$ characteristics.

$$G_0 = \frac{I_0}{V}. \tag{3.4}$$

Open pore conductances corresponding to each MoS_2 nanopore studied are indicated in Table 3.2, observing that G_0 decreases as the pore diameter decreases, where $d = 1.0$ nm is a critical diameter for MoS_2 nanopores since G_0 is around 0.7 nS, whereas $G_0 = 4.3$ nS for $d = 1.5$ nm. The dependency of G_0 with the nanopore size will be discussed in the following sections, where we analyzed via equilibrium MD simulations (EMD) the transport and permeation mechanisms of K^+ and Cl^- ions of the electrolyte solution through the sub-5 nm pores. Also, since transport properties of ions in nanoporous systems is highly dependent on the nanopore geometry (pore diameter and membrane thickness), we performed additional MD simulations for ML-MoS_2 nanopore systems with a constant diameter ($d = 2.0$ nm). Following the exact same procedure as for single-layer membranes with different diameters, we computed the $I-V$ curves and extracted G_0 for the multi-layer systems, as indicated in Fig. 3.8 (b), observing this time that open pore conductance decreases as the number of MoS_2 layers increases.

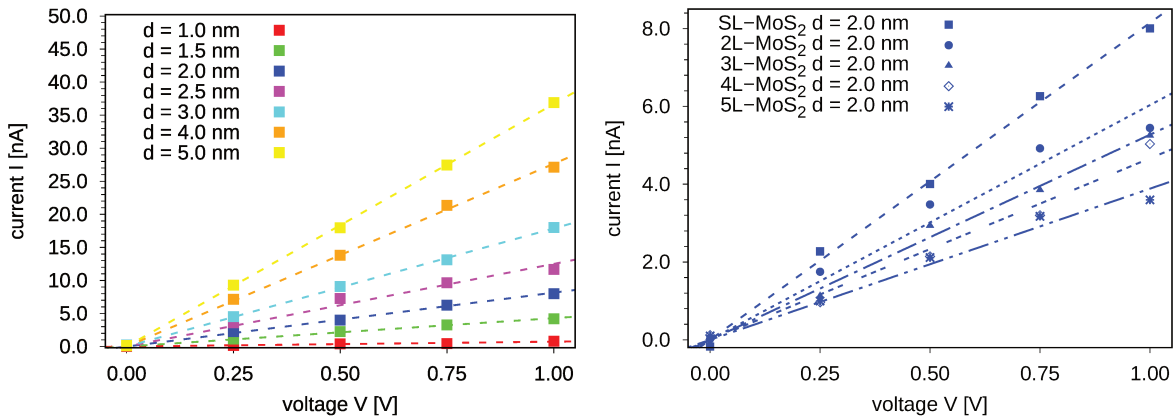

(a) (b)

Figure 3.8: Current-voltage $I-V$ characteristics of nanopores studied in the present work. Data from 0 to 1.0 V are shown for: (a) SL-MoS_2 nanopores of diameter d = 1.0 (red), d = 1.5 (green), d = 2.0 (blue), d = 2.5 (magenta), d = 3.0 (cyan), d = 4.0 (orange), and d = 5.0 nm (yellow). Dashed lines represent the linear behavior fitted onto the MD data. Open pore conductances G_0 were obtained as the slope of the linear fits. Determined G_0 values corresponding to each nanopore diameter is indicated as well. (b) $I-V$ curves for SL- (blue squares), 2L- (blue circles), 3L- (blue triangles), 4L- (blue empty rhombus) and 5L- (blue stars) MoS_2 nanopores of diameter d = 2.0 nm.

SSN	h [nm]	d [nm]	G_0 [$\pm 10^{-1}$ nS]
		1.0	0.73
		1.5	4.29
SL-MoS_2	0.31	2.0	8.15
		2.5	12.50
		3.0	17.87
		4.0	27.65
		5.0	36.70
2L-MoS_2	0.94	2.0	6.03
3L-MoS_2	1.56	2.0	5.27
4L-MoS_2	2.19	2.0	4.67
5L-MoS_2	2.81	2.0	3.89

Table 3.2: Conductances G_0 for the corresponding SSN studied in this work

By comparing these values, there is a difference of 2.1 nS between SL- and 2L-MoS_2, which represents a variation of ~35% by increasing the thickness by a factor 3. However, there is no significant difference between 2L- and 3L-MoS_2 (0.76 nS which represents a decrease of ~13%). It means that 3L-MoS_2 could be an efficient alternative to 2L-MoS_2 in terms of open pore conductances G_0 and fabrication process since, at the nanoscale, manipulating thicker objects might be easier. On the other hand, variations of 0.6 and 0.8 nS were observed by comparing 3L- and 4L-, and 4L- and 5L-MoS_2 nanopores, respectively. In fact, a decrease of ~50% in conductance performance is observed when the thickness is increased from SL- to 5L-, by a factor of 9. While there has been growing interest on SL-MoS_2 nanopores for biomolecule translocation due to the close proximity between their thickness, DNA inter-base distance and peptide bond length, ML-MoS_2 configurations might be interesting to explore due to the strong relation between the

translocation signal, the biomolecule size and the geometry of the nanopore. In this regard, the spatial resolution in translocation events may be compromised by increasing the thickness of the nanoporous membrane [23]. Furthermore, the conductance performance G_0 dependency with the nanopore thickness is still a matter of study and more analyses are needed to asses the ionic transport through ML-MoS_2 nanopores.

3.3 Macroscopic model of ionic conductance and comparison with MD and experimental data

Understanding atomic and sub-nm sized pores in bare and functionalized 2D membranes used for molecular and ionic selectivity are still a matter of study [118, 154–158]. In most conductance measurements, a membrane containing channels is immersed in an electrolyte solution and the electrodes are placed on the solution chambers on both sides of the membrane. If the permeability of the channel is high enough, in some cases the ion flux may be ultimately limited by the rate at which ions arrive from the bulk to the mouth of the channel [148, 149]. Thus, for a correct interpretation of channel conductance measurements in such a system, it is necessary to take into account that the channel itself is only one part of this system [159]. Classically, the total resistance of such a system results from the sum of three contributions: first the resistance within the channel or pore itself and second contributions from the ion flux paths converging to the pore region [113, 159] known as access resistance [160], as shown in Fig. 3.9.

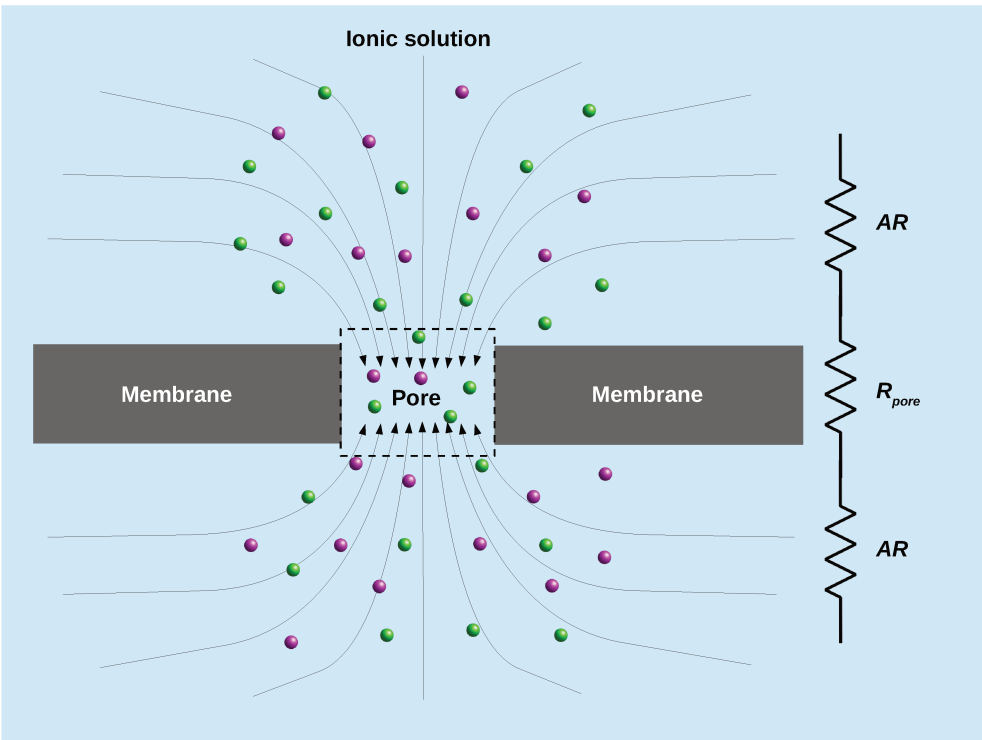

Figure 3.9: Schematic representation of the ionic flow through a nanoporous membrane, which is described classically using a series of three resistances that depend on the geometry of the system.

In order to describe the total resistance of the channel or pore in a membrane, one needs to consider the system in the high-salt limit where the effect of surface charges of the membrane can

be neglected. Then, on the geometry-based models of conductance framework, we first consider the simple expression for a cylindrical pore [113]:

$$R_{pore} = \frac{4h}{\sigma_{bulk}\pi d^2}. \tag{3.5}$$

Here σ_{bulk} is the bulk ionic conductivity, which is the reciprocal of the bulk ionic resistivity $\rho_{bulk} = 1/\sigma_{bulk}$ (not to be confused with radial distance ρ from the water concentration $C(\rho)$ inside the pore), d is the diameter of the circular pore, and h is the thickness of the membrane. Furthermore, the only role of the membrane here is the obstruction of space available for the ionic flux, not other physical effects are considered [113]. In fact, Eq. 3.5 indicates that $R_{pore} \to 0$ as $h \to 0$, which holds only if $h \gg d$. As $h \to 0$, the total resistance is dominated by the access resistance [142]. The concept of access resistance stems from the consideration of the electrical resistance of a medium between two spherical electrodes submerged on it, which does not depend on the distance between the electrodes, but only on their sizes. This happens because the resistance is dominated by the narrow region where the ionic flux approaches the electrode. In other words, the field lines were assumed to converge radially to the pore center [142]. More specifically, the resistance between two spherical electrodes in an infinite medium equals $4/\sigma\pi d$, where d is the diameter of the electrode. Based on this, Hille [161, 162], under the idea that access resistance of a channel should also depend on its dimensions, estimated the access resistance by considering a semi-spherical cupola above the pore entrance as an effective electrode, leading to the expression $AR = 1/\sigma\pi d$. Later on, Hall [160] argued that a semi-spherical cupola is not a reasonable representation of the electrode, instead he considered a planar disc at the pore entrance, and expressed the access resistance as:

$$AR = \frac{1}{\sigma_{bulk}2d}. \tag{3.6}$$

Therefore, one can write the total resistance of an ionic channel or a pore as:

$$R = R_{pore} + 2AR = \frac{4h}{\sigma_{bulk}\pi d^2} + \frac{1}{\sigma_{bulk}d} = \frac{1}{\sigma_{bulk}}\left(\frac{4h}{\pi d^2} + \frac{1}{d}\right). \tag{3.7}$$

Eq. 3.7, which can be presented in terms of the conductance G_0 of the pore, corresponds to an analytical continuum macroscopic model that is given by the following equation:

$$G_0 = \frac{1}{R} = \sigma_{bulk}\left(\frac{4h^* + \pi d^*}{\pi d^{2*}}\right)^{-1}, \tag{3.8}$$

where d^* and h^* correspond to the effective dimensions of the ionic conducting cylindrical channel of the nanoporous membrane. In experiments, the model given by Eq. 3.8 is used to extract indirect measurements of d^* and h^* from the conductance G_0 of nanoporous membranes, and to predict G_0 values from the knowledge of their dimensions. For example, Fig. 3.10 show different reported works where the values of nanopore diameter and membrane thickness were obtained from a fit to a model of nanopore conductance.

In order to confront the classical model of conductance from Eq. 3.8 with G_0 obtained from MD data, we represented the conductance values as a function of the effective diameter d^* for SL-MoS_2, and as a function of the effective thickness h^* for ML-MoS_2 nanopores, as shown in

Reference	Membrane material	t (nm)	d (nm)	DNA	Electrolyte solution	σ (S m^{-1})	V (V)	ΔI (nA)	ΔG (nS)	ΔG (nS) scaled to 1 M KCl @ 23°C (σ = 10.8 S m^{-1})	ΔG / ($\sigma \times d_{DNA}$) (dimensionless)
Carlsen *et al.*[29]	SiN_x	1.5*	3.4	ds 3 kbp	0.9 M NaCl	7.6†	0.4	3.5	8.7	12.4	0.52
Larkin *et al.*[23]	HfO_2	2*	1.7*	ss 89 b	1 M KCl	9.6 (25°C)	0.4	1.9	4.7	5.3	0.44
Garaj *et al.*[20]	Graphene	0.6*	2.8	ds 10 kbp	3 M KCl	27.5	0.16	4.1	25.6	10.1	0.42
Wanunu *et al.*[14]	SiN_x	2.6*	4	ds 3 kbp	1 M KCl	13.7 (21°C)	0.3	3.8	12.7	10.0	0.42
This work	*a*-Si	1.5	2.7*	ds 15 kbp	1.1 M KCl	12.0	0.5	5.4	10.8	9.7	0.41
Yanagi *et al.*[30]	SiN_x	3.7*	2.3*	ss 5.3 kb	1 M KCl	10.5 (22.5°C)	0.3	1.4	4.7	4.8	0.40
Venta *el al.*[15]	SiN_x	1.7*	1.4	ss 30 b	1 M KCl	10.8†	1	4.2–5.1	4.2–5.1	4.2–5.1	0.35–0.43
Merchant *et al.*[17]	Graphene / TiO_2	6 –10	5 × 7	ds 400 bp	1 M KCl	10.8†	0.15	1.1	7.3	7.3	0.31
Liu *et al.*[21]	BN	1.1	5 × 6	ds 10 kbp	3 M KCl	28.7†	0.16	1.6	10.0	3.8	0.16
Zhou *et al.*[22]	BN	–	4	ds 48 kbp	1 M KCl	10.8†	0.15	0.4	2.8	2.8	0.12
Garaj *et al.*[19]	Graphene	0.6*	4.6*	ds 10 kbp	3 M KCl	28.9† (24°C)	0.16	1.2	7.8	2.9	0.12
Liu *et al.*[25]	MoS_2	1.6*	20	ds 48 kbp	2 M KCl	20.0 (20°C)	0.2	1.0	5.0	2.7	0.11
Schneider *et al.*[18]	Graphene	0.3	22	ds 48 kbp	1 M KCl	10.8†	0.2	0.3	1.5	1.5	0.06

Figure 3.10: Change in ionic conductance caused by translocating DNA through nanopores fabricated in solid-state membranes. The data extracted from literature, shows different materials with different nanopore dimensions (thickness t and diameter d), in different experimental conditions (electrolyte conductivity σ, applied voltage V, change in nanopore ionic current ΔI and change in nanopore ionic conductance ΔG. (*) Indicates that values of d or t quoted in the reference were obtained indirectly from a fit to a model of nanopore conductance. Figure extracted from Ref. [43].

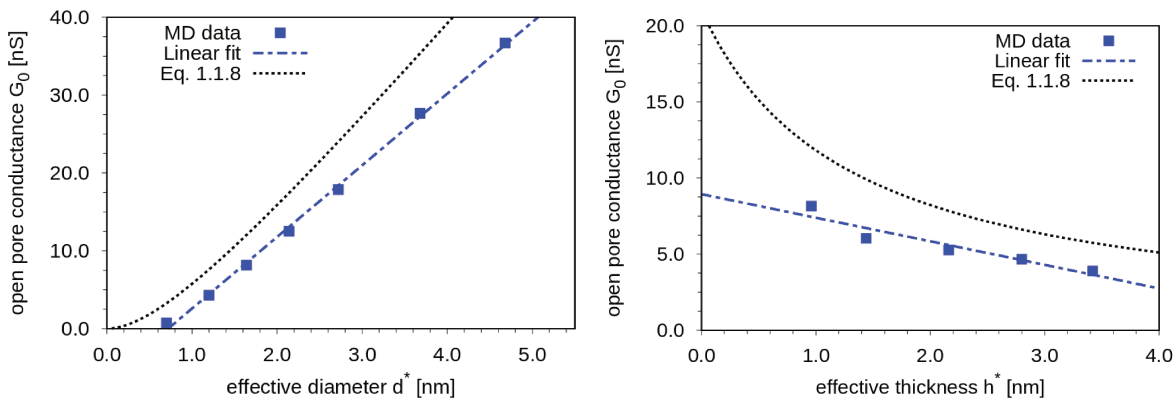

(a) (b)

Figure 3.11: (a) Open pore conductances G_0 as a function of the effective diameter d^* for SL-MoS_2 nanopores. (b) Open pore conductances G_0 as a function of the effective thickness h^* for MoS_2 nanopores of effective diameter $d^* = 1.64$ nm. MD data are represented by blue squares. Black dashed lines represent the conductance G_0 predicted from Eq. 3.8. Blue dashed lines represent a linear fitting of the MD data.

Fig. 3.11 (a) and (b), respectively.

Values of the open pore conductance G_0 obtained from NEMD simulations were compared to the analytical model of conductance given by Eq. 3.8 (Fig. 3.11), using bulk ionic conductivity σ_{bulk} of 1M KCl computed by performing NEMD simulations of the ionic solution only (without nanopore in a simulation box of volume $10 \times 10 \times 20$ nm^3). The obtained bulk ionic conductivity $\sigma = 12.8$ S m^{-1}, is in very good agreement with values reported in the literature, *i.e.* $\sigma \sim 10 - 12$ S m^{-1} [43] (Fig. 3.10). The conductance value G_0 extracted for 1M KCl from the corresponding $I - V$

curve from MD data is 67 nS, then the electrolyte ionic conductivity σ_{bulk} was obtained as:

$$\sigma_{bulk} = G_0 \frac{L_z}{L_x L_y}. \tag{3.9}$$

The comparison of open pore conductance of the different MoS_2 nanopores extracted from MD simulations and the macroscopic model of conductance of Eq. 3.8, shows that conductance values are overestimated by the classical model, either for SL-MoS_2 nanopores [Fig. 3.11 (a)] and for ML-MoS_2 systems [Fig. 3.11 (b)]. As shown in Fig. 3.11, a linear model of conductance would be a better fit for MD data of G_0, leading to:

$$G_0(d^*) = \alpha d^* + \beta, \tag{3.10}$$

$$G_0(h^*) = \gamma h^* + \delta. \tag{3.11}$$

The values of the linear fit parameters are: $\alpha = 9.20$ nS m^{-1}, $\beta = -6.61$ nS, $\gamma = -1.55$ nS m^{-1} and $\delta = 8.94$ nS. In this simple linear relation, no current can be detected below a critical diameter $d^*{}_{min} = -\beta/\alpha$, i.e., when $G_0(d^*{}_{min}) = 0$, which goes in agreement with recent experimental measurements of ionic transport through sub-nm sized pores made of atomic vacancies. In this experimental work, Thiruraman et al. [59] show that pores with diameters < 0.6 nm display negligible conductance, as shown in Fig. 3.12.

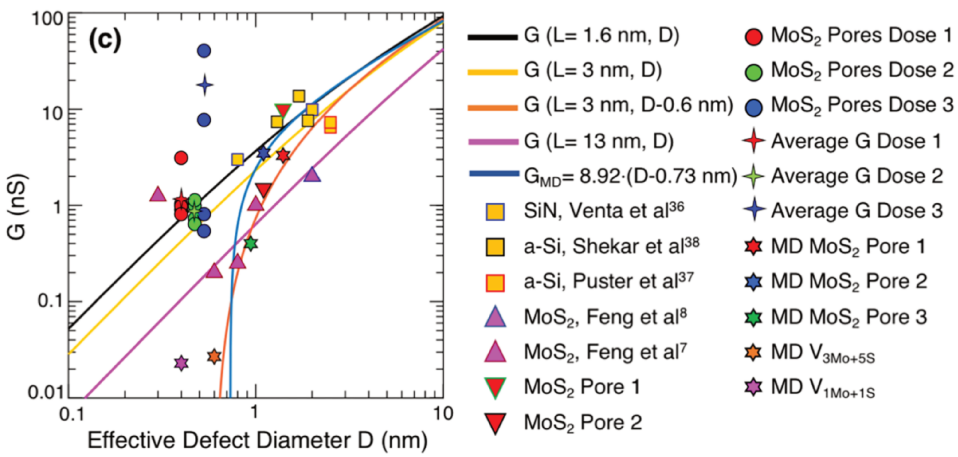

Figure 3.12: Ionic conductance G as a function of pore diameter D, obtained experimentally for MoS_2 nanoporous membranes and from reported works on SiN, a-Si and MoS_2 nanopores. Black, yellow, orange and pink lines represent the continuum model from Eq. 3.8. Blue line represents the linear model from Eq. 3.10 obtained from MD simulations results. Figure extracted from Ref. [59].

In nanopore conductance analysis, many authors argue about the accuracy of the theoretical macroscopic model used to describe ionic conductance from Eq. 3.8, due to the lack of accuracy of the values predicted by the model for nanopores with diameters $\lesssim 20$ nm [114], as evidenced in Fig. 3.2. The source of discrepancy was explained by Suk and Aluru [114] in terms of the dependency of Eq. 3.8 on bulk ionic conductivity σ_{bulk}. In their computational work about ionic transport in sub-5 nm graphene nanopores, the conductance of pores with diameters smaller than 1.80 nm, is found to be lower compared to the predicted one (Eq. 3.8). Their findings evidence that

σ_{bulk} in Eq. 3.8 is not relevant. Instead, bulk conductivity σ_{bulk} should be replaced in this model by an ionic conductivity which depends on the diameter of the pore $\sigma_{pore}(d^*)$. In fact, it also depends on the thickness h^* for multiple layers SSN and on the interactions between the ionic solution and the 2D materials. In the following section, we discuss in more details this statement by presenting an improved model of ionic conductance for SL-MoS_2 nanopores. By replacing σ_{bulk} with $\sigma_{pore}(d^*)$ in Eq. 3.8, the validity of the model is restored for the present nanopores, since the diameter dependency of the electrolyte conductivity is now taken into account. On the contrary, we have not performed yet this analysis for ML-MoS_2 nanoporous systems, in order to find the proper expression to evaluate G_0 as a function of the membrane thickness h^* for an extended improved model.

3.4 Improved model of ionic conductance through SL-MoS_2 nanopores

In the former section, we showed that open pore conductance G_0 values predicted from Eq. 3.8 using σ_{bulk}, were overestimated compared to MD data for SL-MoS_2 nanopores with diameters ranging from 1.0 to 5.0 nm. Such a discrepancy requires to reexamine the modeling of G_0 at the atomic scale.

3.4.1 Ionic conductivity

First, the conductivity exhibited by a bulk ionic solution is expressed as the product of the concentration c^i of the ionic species, their charge $q^i = ez^i$ and their electrical mobility μ^i

$$\sigma_{bulk} = e\sum \left|z^i\right| c^i_{bulk}\mu^i_{bulk}, \tag{3.12}$$

where e is the elementary (positive) charge, z is the charge number, and the index i represents the ionic species. Specifically, for a neutral ionic solution, such as 1M KCl, where the number of K^+ and Cl^- is the same, Eq. 3.12 can be rewritten as:

$$\begin{aligned}\sigma_{bulk} = &\left(e\left|z^{K^+}\right| c^{K^+}_{bulk}\mu^{K^+}_{bulk}\right) + \left(e\left|z^{Cl^-}\right| c^{Cl^-}_{bulk}\mu^{Cl^-}_{bulk}\right)\\ = &\ e\left[\left(c^{K^+}_{bulk}\mu^{K^+}_{bulk}\right) + \left(c^{Cl^-}_{bulk}\mu^{Cl^-}_{bulk}\right)\right]\\ = &\ 2ec_{bulk}\left\langle\mu_{bulk}\right\rangle,\end{aligned} \tag{3.13}$$

where c_{bulk} is the concentration of K^+ or Cl^- species, and the mean bulk mobility $\langle\mu_{bulk}\rangle$ equals:

$$\left\langle\mu_{bulk}\right\rangle = \left(\frac{\mu^{K^+}_{bulk} + \mu^{Cl^-}_{bulk}}{2}\right). \tag{3.14}$$

One important remark is that, at the nanoscale, ions are confined in spaces whose dimensions are of similar sizes to that of the ionic radii. It follows that their concentration, mobilities, and hydration are different than their bulk counterparts, as already shown for graphene nanopores [114, 119]. Consequently, the conductivity of the electrolyte in nanopores is expected to deviate from its bulk value and the conductance of open nanopores predicted by Eq. 3.8 is inaccurate for the smallest pores, as shown previously.

In this work, thanks to all-atom EMD simulations at 300 K for SL-MoS_2 membranes with diameters ranging from 1 to 5 nm, we derived an analytical model of the electrolyte conductivity at room temperature in SL-MoS_2 nanopores as a function of the pore diameter, which is referred as $\sigma_{pore}(d^*)$. Thus, Eq. 3.8 depends on $\sigma_{pore}(d^*)$ as:

$$G_0 = \sigma_{pore}(d^*)\left(\frac{4h^* + \pi d^*}{\pi d^{2*}}\right)^{-1}. \tag{3.15}$$

The goal is to define analytically the expression of $\sigma_{pore}(d^*)$, which in analogy with Eq. 3.12, can be computed for all the SL-MoS_2 nanopores as:

$$\begin{aligned}\sigma_{pore} = &\quad \left(e\left|z^{K^+}\right| c^{K^+}_{pore}\mu^{K^+}_{pore}\right) + \left(e\left|z^{Cl^-}\right| c^{Cl^-}_{pore}\mu^{Cl^-}_{pore}\right) \\ = &\quad e\left[\left(c^{K^+}_{pore}\mu^{K^+}_{pore}\right) + \left(c^{Cl^-}_{pore}\mu^{Cl^-}_{pore}\right)\right],\end{aligned} \tag{3.16}$$

where c_{pore} and μ_{pore} are unknown. In order to quantify how σ_{pore} changes from σ_{bulk}, we first computed from MD simulations the corresponding ionic concentrations and mobilities, in bulk (system without the membrane, i.e. simulation box containing only water molecules and ions for 1 M KCl) and inside SL-MoS_2 nanopores, as explained below.

3.4.2 Concentrations and mobilities inside the pore

Concentration c^i of an ionic specie i is computed by considering that the concentration of ions is the number of charge carriers per unit volume, so first the bulk ionic concentration is defined as:

$$c_{bulk} = \frac{N^i{}_{bulk}}{V_{simbox}}, \tag{3.17}$$

where $N^i{}_{bulk}$ is either number of K^+ or Cl^- ions and $V_{simbox} = L_x \times L_y \times L_z$ is the volume of the simulation box. Here the neutral KCl solution contains 1233 K^+ and 1233 Cl^- ions, then $c_{bulk} = 6.20 \times 10^{28}$ ions.m^{-3} = 1 M. Moreover, the number of ions N^i inside the pore as a function of simulation time t is extracted from MD simulations as shown in Fig. 3.13. An ion is considered being inside the pore if its radial distance from the center of the pore $\rho \leq d^*/2$ and its normal distance from the membrane $|z| \leq h^*/2$. From the average number of ions $\langle N^i \rangle$ computed over the 10 ns MD simulation, the concentration is computed as:

$$c^i{}_{pore} = \frac{\langle N^i \rangle}{V^*}, \tag{3.18}$$

where $V^* = \pi d^{*2} h^*/4$ is the effective volume of the pore. Values of the concentrations in bulk and for each nanoporous membrane studied here are given in table 3.3. Error bars Δc^i are estimated by computing the absolute difference between the concentration computed on the two halves of the MD trajectory, *i.e.*:

$$\Delta c^i = \left|c^i(0-5ns) - c^i(5-10ns)\right|. \tag{3.19}$$

On the other hand, mobility μ^i of an ionic specie i is computed from the Einstein-Townsend equation:

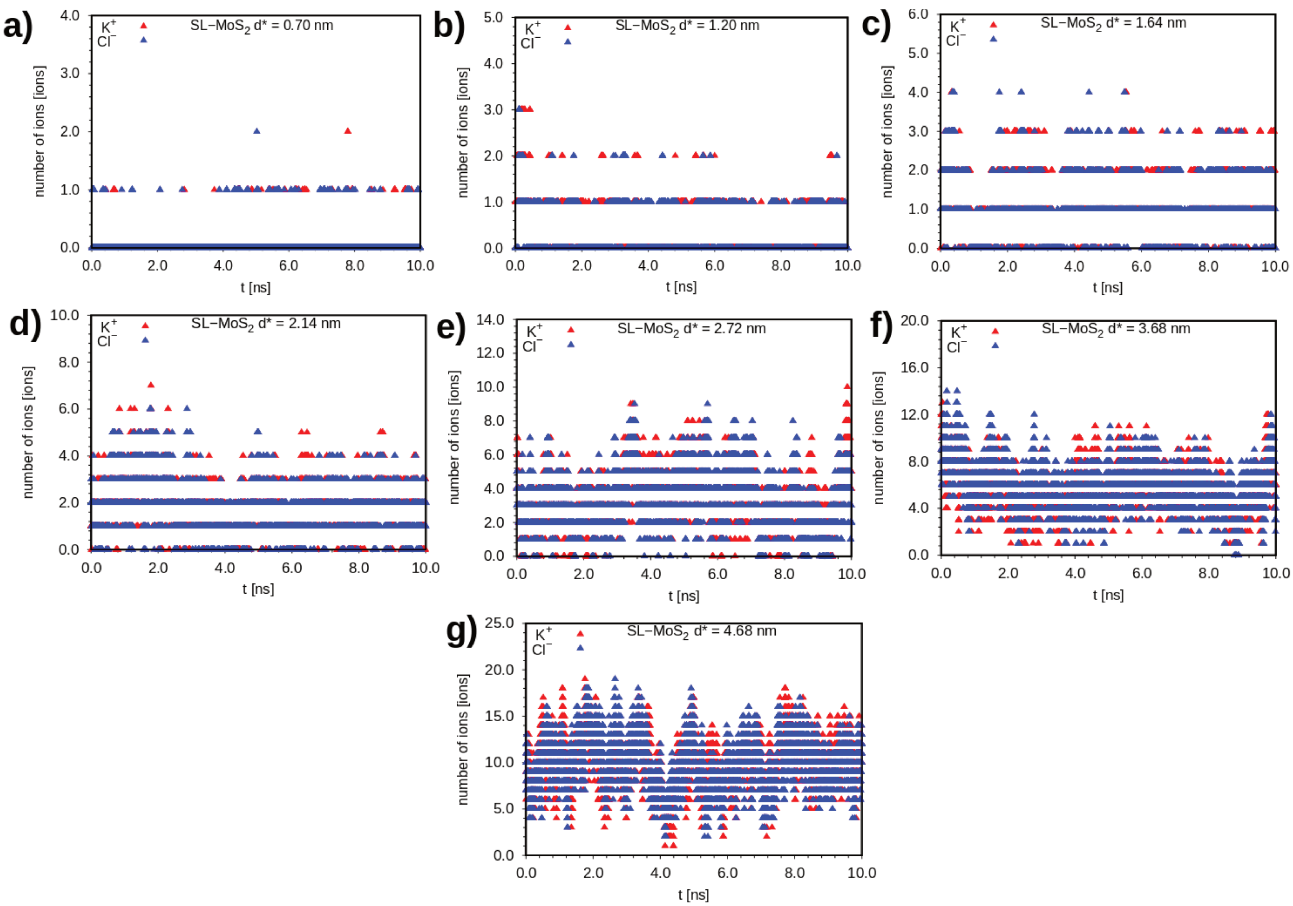

Figure 3.13: Number of ions inside the pore as a function of time extracted from MD simulations. Panels from a) to g) correspond to SL-MoS_2 nanoporous membranes with effective diameters d^* of 0.70, 1.20, 1.64, 2.14, 2.72, 3.68 and 4.68 nm, respectively. The color code is the following: K^+ ions in red and Cl^- ions in blue.

$$\mu^i = \frac{qD^i}{k_B T}, \tag{3.20}$$

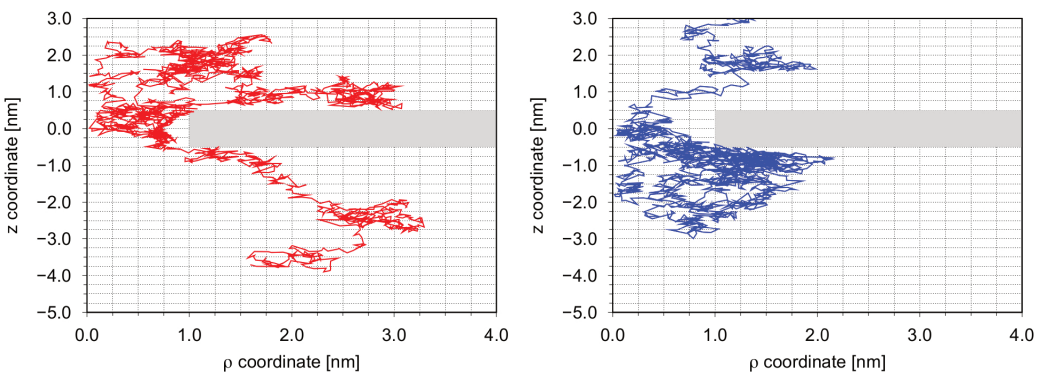

Figure 3.14: 2-D spatial trajectories of K^+ (left panel) and Cl^- crossing the nanopore (d = 2.0 nm) obtained from MD simulations. Cylindrical coordinates are used here to illustrate the trajectories.

where D^i represents the diffusion coefficient of an ionic specie i, k_B is the Boltzmann constant and T the temperature. The diffusion coefficient D^i is determined by computing the mean square

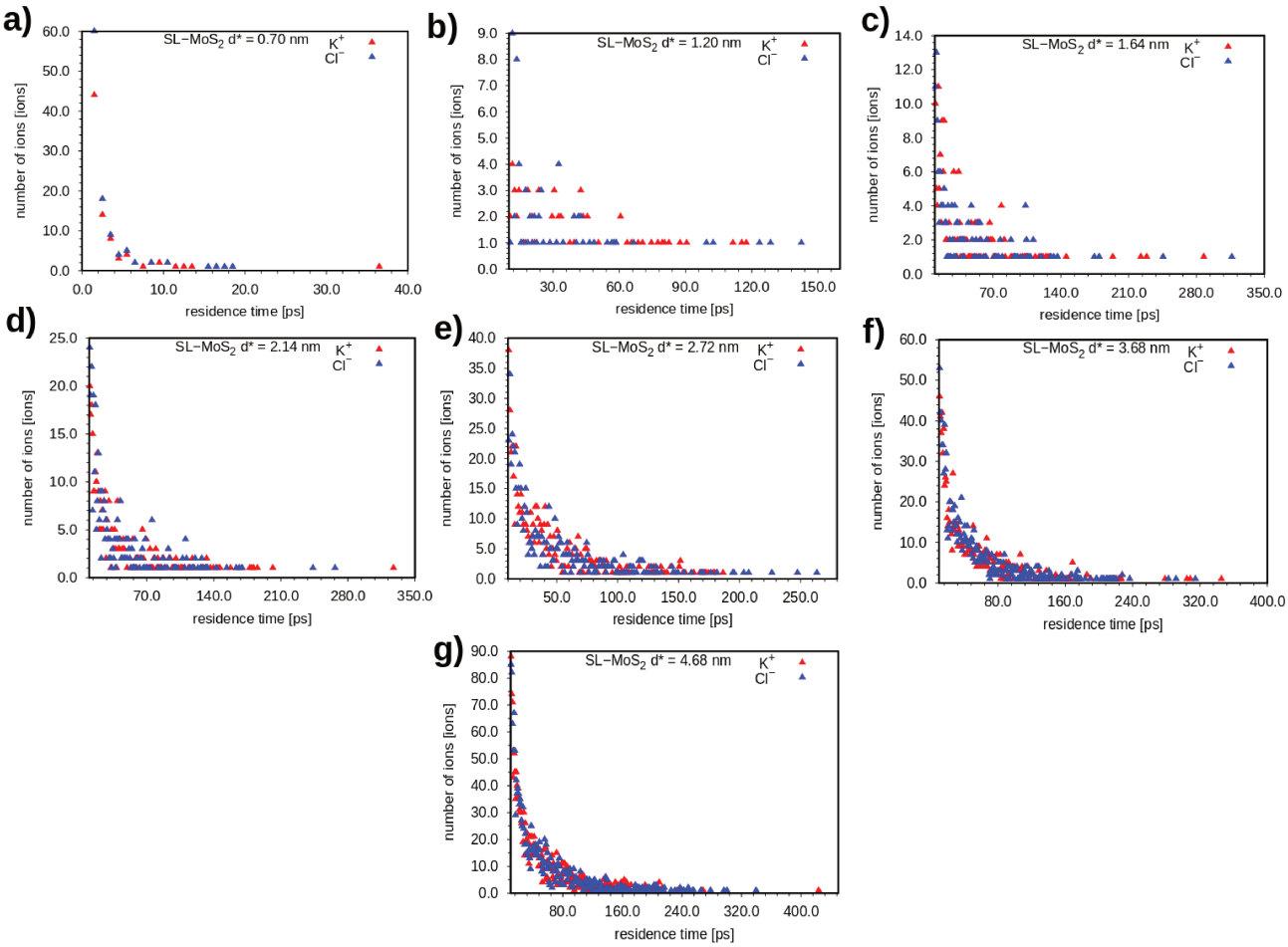

Figure 3.15: Residence time (in ps) of ions inside the SL-MoS_2 nanopores extracted from MD simulations. Panels from a) to g) correspond to SL-MoS_2 nanoporous membranes with effective diameters d^* of 0.70, 1.20, 1.64, 2.14, 2.72, 3.68 and 4.68 nm, respectively. The color code is the following: K^+ ions in red and Cl^- ions in blue.

displacement $msd(t) = \left\langle \left| r_i(t'+t) - r_i(t') \right| \right\rangle_{t'}$, average over initial conditions t', of the ionic specie i. We extracted K^+ and Cl^- ions diffusion coefficients from their corresponding computed msd in bulk and inside SL-MoS_2 nanopores, by performing a linear fitting according to $msd = 6D\tau$ (Fig. 3.16), for normal diffusion of Brownian motion. Fig. 3.14 shows such behavior on the ions movement, when crossing a SL-MoS_2 nanopore with $d = 2.0$ nm, for example. Bulk D^{K^+} and D^{Cl^-} were computed from msd calculations performed over 100 ps of the corresponding 10 ns equilibrated trajectory of 1 M KCl solution. It leads to respectively $D^{K^+}_{bulk} = 2.39 \times 10^{-9}$ m^2/s and $D^{Cl^-}_{bulk} = 2.26 \times 10^{-9}$ m^2/s. The corresponding bulk ionic mobilities are indicated in table 3.3. K^+ and Cl^- diffusion coefficients inside the nanopores were extracted from the linear fitting performed on the first 20% of the data. More specifically, D^i calculations in the pores were performed while the K^+ and Cl^- ions were only diffusing inside the pore. According to the residence time of ions inside the pore, which is in the order of magnitude of hundreds of picoseconds as shown in Fig. 3.15, the maximum time window used for the calculations is 50 ps, as shown in Fig. 3.16. For SL-MoS_2 nanoporous membrane with $d^* = 0.70$ nm, the maximum time window used is 10 ps and the linear fitting was performed on the first 50% of the data due to the fact that the residence time drops drastically for the smallest pore. Error bars ΔD^i were estimated by computing the absolute difference between the diffusion coefficients extracted from msd curves computed over a 50 ps maximum time window and 25 ps maximum time window, *i.e.*:

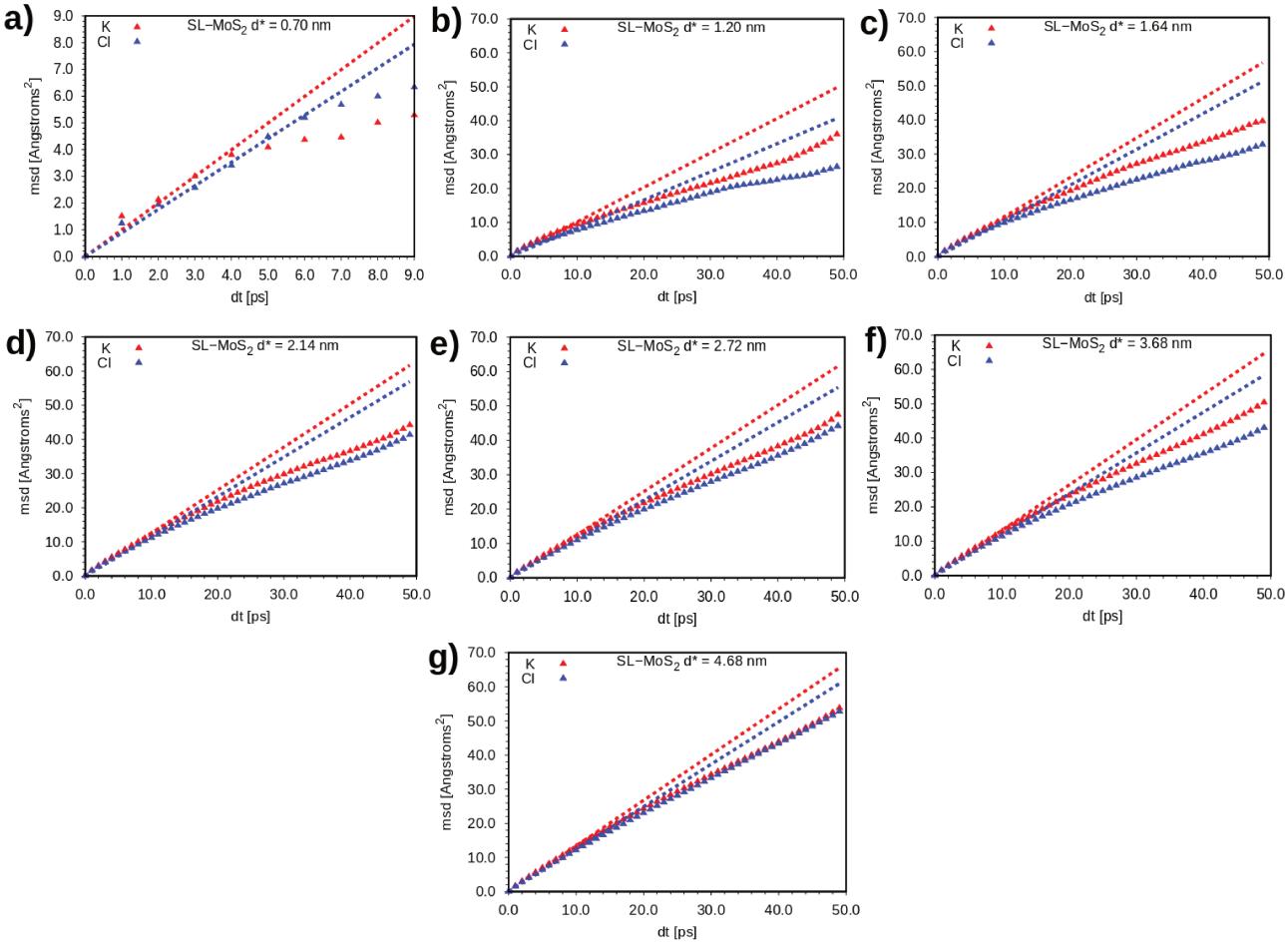

Figure 3.16: Mean square displacements (in Å^2) as a function of time window dt (in ps) computed from MD simulations. Panels from a) to g) correspond to SL-MoS_2 nanoporous membranes with effective diameters d^* of 0.70, 1.20, 1.64, 2.14, 2.72, 3.68 and 4.68 nm, respectively. Dashed lines represent the linear model obtained from least-square fitting. The color code is the following: K^+ ions in red and Cl^- ions in blue.

$$\Delta\mu^i = \frac{q\Delta D^i}{k_B T} = q\frac{|D^i(50ps) - D^i(25ps)|}{k_B T}. \tag{3.21}$$

The values obtained for the electrical mobilities corresponding to the different SL-MoS_2 nanopores are indicated in table 3.3. Once we extracted K^+ and Cl^- concentrations and electrical mobilities from MD simulations for each system, we computed the bulk electrolyte conductivity $\sigma_{bulk} = 17.866$ Sm^{-1} (Eq. 3.13), and pore conductivity (Eq. 3.16) for SL-MoS_2 nanopores. Fig. 3.17 shows the ratio of σ_{pore} over σ_{bulk} as a function of the effective diameter. We observed that the ionic conductivity inside the pore deviates significantly from its counterpart in bulk, as well as the concentrations and mobilities (table 3.3). The $\sigma_{pore}/\sigma_{bulk}$ ratio shows also that for diameters around 2.0 nm, the pore conductivity is about half the bulk value, which means that the macroscopic model (Eq. 3.8) indeed overestimates the membrane conductance by a factor of 2. For diameters approaching 1.0 nm, the pore conductivity is only a third of the bulk value.

d^* (nm)	c^i ($\times 10^{28}$ions.m^{-3})		μ^i ($\times 10^{-8}$ m^2.V^{-1}.s^{-1})	
0.70	0.70 (±0.20)	0.83 (±0.19)	5.91 (±1.12)	5.73 (±0.70)
1.20	2.90 (±0.60)	2.60 (±0.44)	6.75 (±0.36)	6.35 (±0.17)
1.64	4.56 (±0.41)	4.36 (±0.10)	7.47 (±0.89)	6.74 (±0.87)
2.14	5.09 (±0.44)	4.89 (±0.38)	8.12 (±0.84)	7.49 (±0.56)
2.72	5.64 (±0.06)	5.63 (±0.04)	8.10 (±0.52)	7.29 (±0.56)
3.68	5.31 (±0.03)	5.61 (±0.14)	8.51 (±0.50)	7.68 (±0.74)
4.68	5.85 (±0.04)	5.85 (±0.17)	8.63 (±0.60)	8.02 (±0.49)
∞	6.20	6.20	9.24 (±0.11)	8.72 (±0.04)

Table 3.3: Concentrations c^i and mobilities μ^i of K^+ and Cl^- ions extracted from equilibrium MD simulations of sub 5-nm pores. Values in parenthesis represent the error bar.

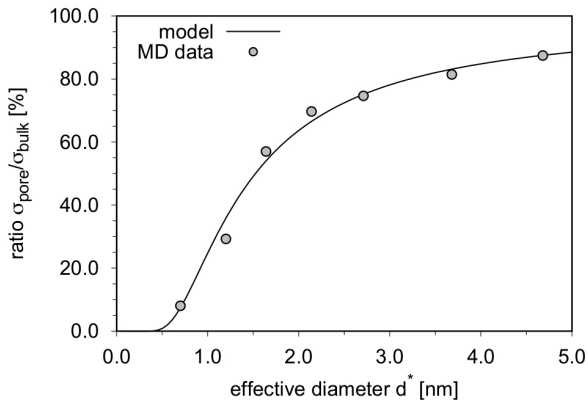

Figure 3.17: Ratio between KCl bulk and pore conductivity as a function of effective diameters d^* extracted from equilibrium MD simulations. The solid black line represents the ratio of σ_{pore} over σ_{bulk} (in %) as a function of d^* (in nm), obtained from .

3.4.3 Partition coefficients of ions concentrations and mobilities

To gain further insight about the origin of the deviations of the conductivity at the nanoscale, and in agreement with Suk and Aluru's work about ionic transport in sub-5 nm graphene nanopores [114], we reformulated the problem in terms of concentration and mobility partition coefficients:

$$\Phi^i \equiv \frac{c^i{}_{pore}}{c_{bulk}}, \tag{3.22}$$

$$\Gamma^i \equiv \frac{\mu^i{}_{pore}}{\langle \mu_{bulk} \rangle}. \tag{3.23}$$

Furthermore, since our goal here is to define an analytical model that describes the ionic conductivity σ_{pore} as a function of the effective diameter d^* for the sub-5 nm SL-MoS_2 nanopores, we rewrote the ratio $\sigma_{pore}/\sigma_{bulk}$ using Eqs. 3.12 and 3.16, in terms of the partition coefficients Φ^i and Γ^i:

$$\begin{aligned}\frac{\sigma_{pore}}{\sigma_{bulk}} &= \frac{e\left[\left(c^{K^+}_{pore}\mu^{K^+}_{pore}\right)+\left(c^{Cl^-}_{pore}\mu^{Cl^-}_{pore}\right)\right]}{2ec_{bulk}\left\langle\mu_{bulk}\right\rangle} \\ &= \frac{1}{2}\left(\frac{c^{K^+}_{pore}\mu^{K^+}_{pore}}{c_{bulk}\left\langle\mu_{bulk}\right\rangle}+\frac{c^{Cl^-}_{pore}\mu^{Cl^-}_{pore}}{c_{bulk}\left\langle\mu_{bulk}\right\rangle}\right) \\ &= \frac{1}{2}\left(\Phi^{K^+}\Gamma^{K^+}+\Phi^{Cl^-}\Gamma^{Cl^-}\right) \\ &= \frac{1}{2}\sum\Phi^i\Gamma^i. \end{aligned} \tag{3.24}$$

Similarly to σ_{pore}, the partition coefficients are also diameter dependent. The formulation of $\Phi^i(d^*)$ and $\Gamma^i(d^*)$ is explained below. First, the coefficient Φ^i can be rewritten as:

$$\Phi^i = \frac{P^i{}_{pore}}{P^i{}_{bulk}}, \tag{3.25}$$

where $P^i{}_{pore}$ and $P^i{}_{bulk}$ correspond to the probabilities to find an ion of species i in the pore and in an equivalent volume in the bulk electrolyte, respectively. Therefore, Φ^i is related to the difference between the free-energy of an ion of species i in the pore and in the bulk electrolyte, named ΔG^i, by the Boltzmann law:

$$\Phi^i = exp\left(-\frac{\Delta G^i}{RT}\right), \tag{3.26}$$

where R is the perfect gas constant and T the temperature. The free-energy difference is expected to be positive due to the loss of entropy and to the dehydration phenomenon that ions experience when they cross the nanopore from the bulk region, these two causes being dependent on the pore size as well [114, 118, 163]. From the ion concentrations computed from MD data, we found that ΔG^i is well represented by the following relation:

$$\Delta G^i = \varphi^i\left(\frac{RT}{A^*}\right), \tag{3.27}$$

here $A^* = \dfrac{\pi d^{*2}}{4}$ is the nanopore effective surface area and φ^i is a positive fitted parameter, obtained from least-squares fitting of Eq. 3.27 to the MD data: $\varphi^{K^+} = 0.832$ nm^2 and $\varphi^{Cl^-} = 0.793$ nm^2. As shown in Fig. 3.18 (a), Eq. 3.27 is in very good agreement with MD data for sub-5 nm SL-MoS_2 nanopores, and as shown in the inset figure, for the sub-3 nm nanopores.

The variation of the free-energy difference ΔG^i as a function of $1/d^{*2}$ observed in MD data from the present work, is significantly different from the one found by Suk and Aluru [114] in graphene nanopores, where ΔG^i was fitted by the $1/d^*$ law. This could be a consequence of the influence of the three-atom thick SL-MoS_2, in contrast to the one-atom thick graphene membrane. A relation between the material and the cost of energy ΔG^i for ionic species should be expected then.

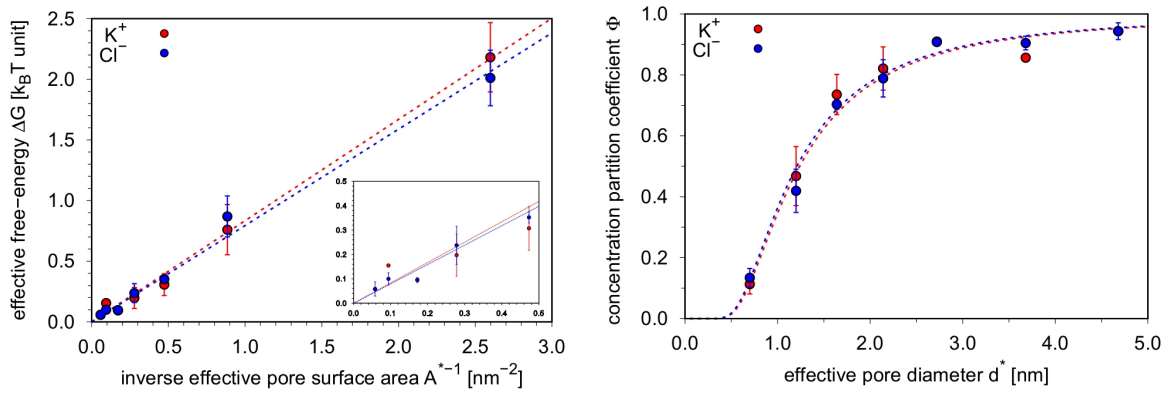

(a) (b)

Figure 3.18: (a) Effective free-energy ΔG as a function of the inverse of the effective pore surface area A^{*-1}. Dashed lines represent a linear fitting of the MD data (blue and red circles, for K^+ and Cl^- ions, respectively). (b) Concentration partition coefficient as a function of effective diameter d^*. Dashed lines represent the model given by Eq. 3.28.

Eqs. 3.26 and 3.27 lead to the following expression for $\Phi^i(d^*)$:

$$\Phi^i(d^*) = exp\left(\frac{-4\varphi^i}{\pi d^{*2}}\right). \tag{3.28}$$

Fig. 3.26 (b) shows that Eq. 3.28 is in very good agreement with MD data and that there is no large difference observed between K^+ and Cl^- species for the concentration partition coefficient.

Next, we studied the mobility partition coefficient Γ^i inside SL-MoS$_2$ nanopores as a function of d^*. Empirically, by plotting the inverse mobility as a function of the inverse effective diameter, as shown in Fig. 3.19 (a), we find that $(1/\mu^i{}_{pore} - 1/\mu^i{}_{bulk})$ scales as $1/d^*$, leading to:

$$\left(\mu^i{}_{pore}\right)^{-1} = \gamma^i\left(d^*\right)^{-1} + \left(\mu^i{}_{bulk}\right)^{-1}. \tag{3.29}$$

Eq. 3.29 can be rewritten as:

$$\mu^i{}_{pore} = \left(\frac{\gamma^i}{d^*} + \frac{1}{\mu^i{}_{bulk}}\right)^{-1}. \tag{3.30}$$

This behavior was also observed by Suk and Aluru [114] for K^+ and Cl^- mobilities in graphene nanopores. Then, by performing a linear fitting of Eq. 3.29 to MD data, as shown in Fig. 3.19 (a), we obtained the parameters γ^i for each specie i: $\gamma^{K^+} = 4.27 \times 10^{-3}$ V.s.m^{-1} and $\gamma^{Cl^+} = 4.61 \times 10^{-3}$ V.s.m^{-1}, which are subsequently inserted in Eq. 3.31.

As observed in Fig. 3.19 (a), there is a significant difference between K^+ and Cl^- mobilities, since diffusion coefficient of K^+ species is larger than that of Cl^-. This can be explained from Stoke's law. where $D^{K^+}/D^{Cl^-} = R^{K^+}/R^{Cl^-} \approx 1.1$, where R^{K^+} and R^{Cl^-} are the ionic radii [164]. Moreover, Fig. 3.19 (b) shows the mobility partition coefficient Γ^i as a function of the effective diameter, computed from Eq. 3.23. The corresponding analytical model of $\Gamma^i(d^*)$ is obtained by inserting Eq. 3.30 in Eq. 3.23 as detailed below:

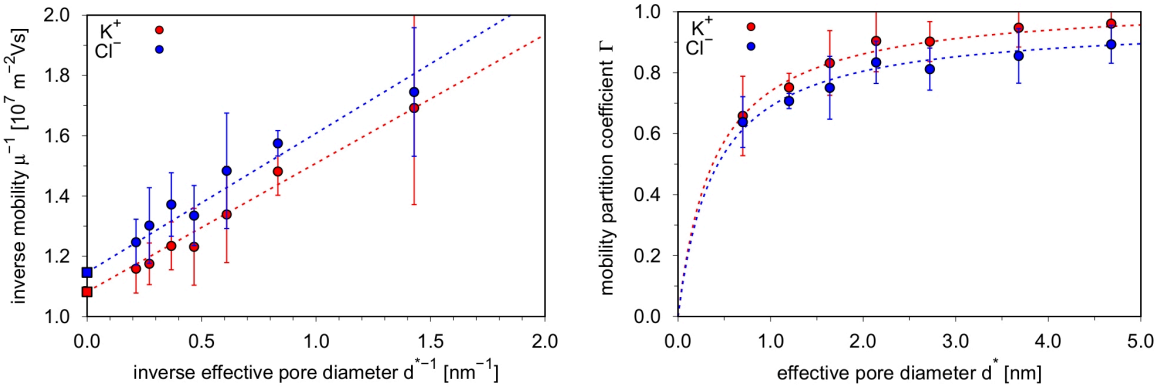

(a) (b)

Figure 3.19: (a) Inverse mobility μ^{-1} as a function of inverse effective diameter d^{*-1}. Dashed lines represent the linear fitting of Eq. 3.29 to MD data (blue and red circles, for K^+ and Cl^- ions, respectively). (b) Mobility partition coefficient as a function of effective diameter d^*. Dashed lines represent the model given by Eq. 3.31.

$$\begin{aligned}
\Gamma^i = \quad & \frac{\mu_{pore}{}^i}{\langle \mu_{bulk} \rangle} = \frac{1}{\langle \mu_{pore} \rangle} \left(\frac{\gamma^i}{d^*} + \frac{1}{\mu^i{}_{bulk}} \right)^{-1} \\
= \quad & \frac{d^* \mu^i_{bulk}}{\langle \mu_{bulk} \rangle \left(\gamma^i \mu^i_{bulk} + d^* \right)} \\
= \quad & \frac{d^*}{\frac{\langle \mu_{bulk} \rangle}{\mu^i_{bulk}} \left(\gamma^i \mu^i_{bulk} + d^* \right)} \\
= \quad & \frac{d^*}{\delta^i + \epsilon^i d^*},
\end{aligned} \tag{3.31}$$

where $\delta^i = \gamma^i \langle \mu_{bulk} \rangle$ and $\epsilon^i = \frac{\langle \mu_{bulk} \rangle}{\mu^i_{bulk}}$, with $\delta^{K^+} = 0.38$ nm and $\delta^{Cl^-} = 0.41$ nm, $\epsilon^{K^+} = 1.03$ and $\epsilon^{Cl^-} = 0.97$. Fig. 3.19 (b) also shows quantitatively that there is a very good agreement between MD data and the analytical expression given by Eq. 3.31. When the pore diameter is around 1.0 nm, mobility is reduced from the bulk value by about 40%. For the same diameter, the concentration was reduced by 70%. This means that for small diameters, the concentration of ions in the pore is the dominating factor.

3.4.4 Improved model of ionic conductance

Finally, by inserting the analytical expression of $\Phi^i(d^*)$ and $\Gamma^i(d^*)$ into Eq. 3.24, we obtained:

$$\begin{aligned}
\sigma_{pore}(d^*) = \quad & \sigma_{bulk} \frac{1}{2} \sum \Phi^i(d^*) \Gamma^i(d^*) \\
= \quad & \sigma_{bulk} \left(\frac{1}{2} \sum_i exp\left(\frac{-4\varphi^i}{\pi d^{*2}} \right) \frac{d^*}{\delta^i + \epsilon^i d^*} \right).
\end{aligned} \tag{3.32}$$

Pore ionic conductivity $\sigma_{pore}(d^*)$ can be now inserted in the improved model of conductance of Eq. 3.15, leading to a model that now takes into account the effects of the spatial confinement of ion species at the nanoscale. The complete expression of the model is:

$$G_0 = \sigma_{bulk}\left(\frac{1}{2}\sum_i exp\left(\frac{-4\varphi^i}{\pi d^{*2}}\right)\frac{d^*}{\delta^i + \epsilon^i d^*}\right)\left(\frac{4h^* + \pi d^*}{\pi d^*}\right). \tag{3.33}$$

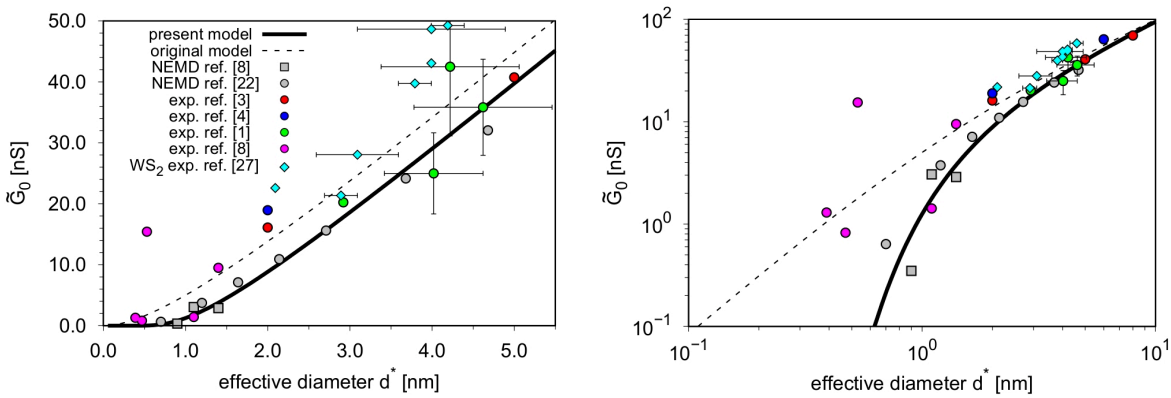

Figure 3.20: (a) Conductance $\tilde{G}_0$ (in nS) scaled to 1 M KCl at RT as a function of effective diameter d^* (in nm), extracted from experimental data (red, blue, green, and magenta filled circles) and from non-equilibrium MD simulations (gray filled circles and squares). Black dashed lines represent the original continuum model of conductance from Eq. 3.8. Black thick lines represent data obtained with the model of conductance developed in the present work and given in Eq. 3.33. (b) Same graph as panel (a) with the log-log scale.

3.4.5 Comparison with experimental ionic conductance data

To conclude, Eq. 3.33 is compared to conductance values obtained from $I-V$ curves extracted from NEMD simulations, that were presented in section 3.2.2, and to experimental data from sub 5-nm MoS_2 nanoporous membranes extracted from the literature. For all the different G_0 data reported in the literature, different experimental conditions were used leading to different values of ionic conductivity σ_{bulk} of KCl solutions depending on the temperature and the concentration of the electrolyte. In order to rationalize the data and as already done for Si pores [43], we decided to compute scaled conductance:

$$\tilde{G}_0 = \left(\frac{G_0}{\sigma_{bulk}}\right)_{given} \times {\sigma_{bulk}}^{1MKCl@RT}, \tag{3.34}$$

where G_0 and σ_{bulk} were directly extracted from the literature and ${\sigma_{bulk}}^{1M\ KCl@RT}$ is the value of 11.18 S m^{-1} measured experimentally recently [59]. First, as shown in Fig. 3.20, the difference between the pore and bulk conductivities has a significant effect on the value of the predicted conductance for pore with diameters lower than 2.0 nm. For such diameters, the original model (Eq. 3.8) overestimates conductance by a factor of 2. This overestimation becomes a factor 5 for the diameter around 1.0 nm. In addition, the improved model (Eq. 3.33) developed here using EMD simulations is in very good agreement with conductance computed from $I-V$ curves extracted

from NEMD simulations. Compared to the linear empirical model proposed previously in [60], the conductance for the SL-MoS_2 nanoporous membrane becomes negligible (10^{-1} nS) for diameters below 0.6 nm. Moreover, from experimental conductance data for SL-MoS_2 nanopores with diameters around 2.0 nm [40, 165], according to the present model (Eq. 3.33), the effective diameter of the pore would be closer to 3.0 nm than to 2.0 nm, since geometrical parameters of the nanoporous membranes can be also estimated from conductance values, by performing an appropriate fitting from a valid model to the conductance obtained.

Finally, experimental data [23] for diameters larger than 2.0 nm are very close to the model of Eq. 3.33 within the error bar, when available. We also added into the conductance graphs presented in Fig. 3.20 conductance values extracted from measurements of WS_2 nanopores [32]. As shown in Fig. 3.20, for nanopores of diameters between 2.0 and 5.0 nm, conductance values are similar within the error bars. Therefore, the present model may be used also for other TMDC such as WS_2. Finally, for few-Angstrom size defect pores (diameters lower than the limit of 0.6nm), according to our model, conductance values are often overestimated [61].

In a recent work [60], we showed using NEMD simulations in the presence of an applied voltage that defect pores characterized by effective diameter $d^* < 0.6$ nm do not conduct ions. In fact, they are characterized by negligible conductance below 20 pS. For those particularly tiny pores, more experimental measurements are needed to test the validity of the model since the passage of an ion across the membrane is a rare event. However, for pores with diameters around 1.0 nm, our model is in good agreement with experiments. In summary, we developed a model of ionic conductance for sub 5-nm SL-MoS_2 nanoporous membranes using MD simulations. Our model, which takes into account the concentration and the mobility of ions in the nanopores, shows that the behavior of KCl electrolyte deviates by 50% from bulk properties for diameters below 2.0 nm. Moreover, our model is in very good agreement with simulation and experimental data of conductances in MoS_2 nanoporous membranes. We showed that this model is essential for understanding the behavior of 2D nanopores in this range of diameters to design and fabricate sensors for DNA or protein sequencing applications, or for filtration applications.

Chapter 4

Translocation of biological peptides through MoS_2 nanopores

In the previous chapter, we discussed open pore characterization and performances of MoS_2 nanopores where conductance G_0 of different pores was studied. In the present chapter, we discuss the translocation of amino acids and peptides through MoS_2 nanoporous membranes, namely lysine residues and a model protein with poly-lysine tags. More precisely, we investigated the relationship between translocation events and ionic conductance signal drops in order to study the feasibility of using MoS_2 nanopore devices for protein sequencing applications.

4.1 MoS_2 nanopores for protein sequencing: A general context

Over the past decade, nanopores have become a very popular method to study analytes at the single-molecule level via translocation technology. Furthermore, proteins are increasingly becoming a prime target of investigation [50]. In general, translocation is detected as drops ΔG in the conductance signal, which yield information about the structure and the chemical properties of translocated biomolecules. For example, S. Shekar et al. [30], experimentally demonstrated that using a custom complementary metal-oxide-semiconductor (CMOS) nanopore amplifier, sub-microsecond temporal resolution of ssDNA translocation through a-Si nanopores can be achieved. Atomically thin 2D materials such as TMDC [23, 32] are ideal candidates for SSN, as they exhibit larger ionic conductance compared to thicker membranes such as silicon-based membranes [43]. Among all TMDC that have been explored theoretically and experimentally, MoS_2 layers are showing great potential thanks to the fact MoS_2 monolayer films and nanostructured materials can be fabricated using cost-effective and reliable methods [33–35, 122].

MoS_2 nanopores have been studied experimentally as SSN for DNA sequencing [23, 40, 151, 166] and for detection of DNA labeled with proteins [167, 168]. To the best of our knowledge there is to-date no experimental evidence of the translocation of single proteins through MoS_2 or any other TMDC yet. In contrast to DNA strands which are highly negatively charged biomolecules, i.e. the total charge being proportional to the number of bases, proteins can be globally neutral, independently of the number of residues, sequence or size. Therefore, driving such a biomolecule into SSN and detecting ionic conductance drops related to its amino acid sequence requires different strategies than using only an electric field as driving force. Indeed, a compromise must be made between facilitating the threading of the protein through the pore and the translocation speed, which should allow the detection of discernible conductance drops associated with its

specific sequence. In this way, SSNs with a very high translocation speed of proteins through the pore may limit their usability as sequencing devices. The threading of the biomolecule through SSN and the translocation speed can be controlled by adjusting different parameters in experiments, such as solvent properties [169, 170] (ionic species, concentration, temperature, viscosity, etc.) or material size and shape [36]. More drastically, the physical technique used to drive the biomolecule through the pore can also be modified (see Refs. [48] and [49]).

An alternative method to translocate proteins, is the use of tags made of positively or negatively charged amino acids such as lysine residues to functionalize the N- or C- terminal part of proteins. The test of this alternative method is the purpose of the present work [62]. In biochemistry, polyionic tags such as small lysine peptides are used as enhancers of protein solubility in recombinant protein production. Because of their small size and their repetitive amino acid content, they do not necessarily have an ordered three-dimensional (3D) conformation. As a result, they can exert their solubility-enhancing effect without interfering with the structure of the protein of interest or compromising its activity [171].

In the present work, we performed NEMD simulations to explore the feasibility of using poly-lysine tags to thread and fully translocate peptides through MoS_2 nanopores. First the threading and translocation of individual lysine residues were studied as a proof-of-principle of the proposed technique. The relationship between the passage of lysine residues through the pore and the detected ionic conductance is established. Second, different types of membranes were tested by changing the diameter of the nanopore from 2.0 to 1.5 nm, as well as the thickness of the membranes, from SL- to 2L-MoS_2. The best performing membrane was extracted from these initial simulations. Finally, tags made of poly-lysine residues (from 1 to 5 amino acid length) were attached to Met-Enkephalin protein and translocated through SL-MoS_2. Finally, ionic conductance and translocation sequence of events were analyzed and discussed. The summary of MD simulations performed on the translocation of the biological peptides through the MoS_2 nanoporous membranes is indicated in Table 2.6.

4.2 Analysis tools

MD trajectories were analyzed using the following tools:

4.2.1 Normal and radial distance of the peptide

We computed the normal distance to the membrane $z(t)$ and radial distance to the nanopore center $\rho(t)$ of the center of mass (COM) of each peptide as a function of the simulation time:

$$x_{com}(t) = \frac{\sum_{i=1}^{N} m_i x_i(t)}{M_{peptide}},\ y_{com}(t) = \frac{\sum_{i=1}^{N} m_i y_i(t)}{M_{peptide}},\ z_{com}(t) = \frac{\sum_{i=1}^{N} m_i z_i(t)}{M_{peptide}}, \tag{4.1}$$

$$\rho_{com}(t) = \sqrt{(x_{com}(t))^2 + (y_{com}(t))^2}\,, z(t) = z_{com}(t), \tag{4.2}$$

where $x_{com}(t)$, $y_{com}(t)$ and $z_{com}(t)$ are the coordinates of the COM of the peptide, N is the number of atoms, m_i is the mass of the atom i and $M_{peptide}$ is the total mass of the peptide.

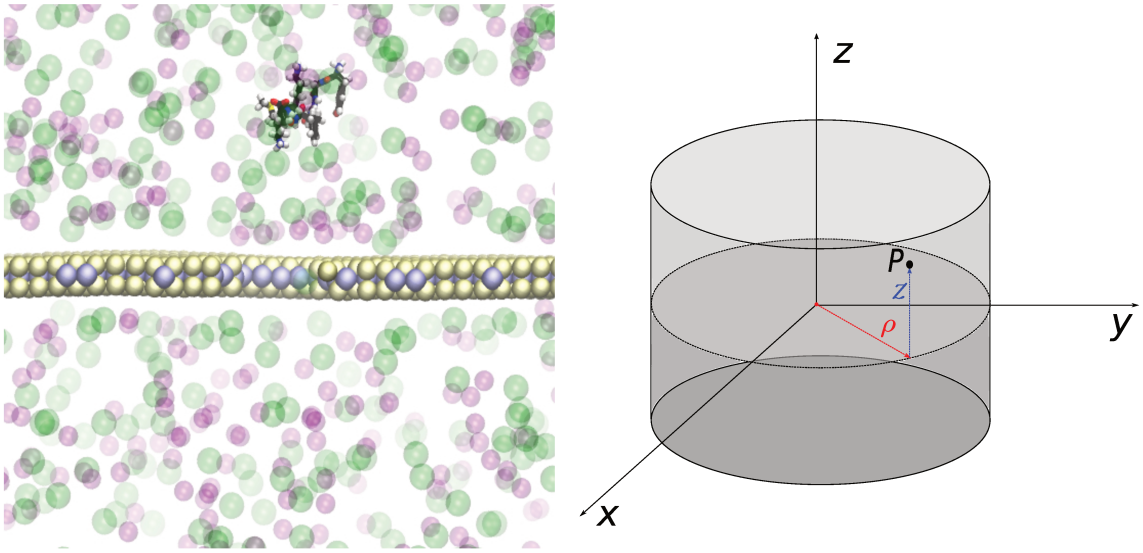

Figure 4.1: Representation of a single lysine residue (K) in the proximity of the nanopore. Mo and S atoms are colored as blue and yellow respectively. K^+ and Cl^- ions are represented as magenta and green spheres. C, H, N, O and S atoms are represented by black, white, blue, red and yellow, respectively.

4.2.2 Ionic conductance through MoS_2 nanopores

Ionic conductance $G(t)$ was computed from MD trajectories as the ratio between the total net ionic current $I(t)$ and the applied voltage V:

$$G(t) = \frac{1}{V}\left(\frac{1}{\Delta t L_z}\sum_{i=1}^{N} q_i[z_i(t+\Delta t) - z_i(t)]\right), \tag{4.3}$$

where V is the applied voltage, Δt is the time between MD frames chosen for the calculations (Δt = 100 ps or 1 ns depending on the runs), L_z is the dimension of the simulation box in the z-direction, which is the direction of the applied electric field, N is the total number of ions, q_i is the charge of the ion i and $z_i(t)$ is the z-coordinate of the ion i at time t.

4.2.3 Number of atoms of the peptide inside the pore

Translocation events observed during NEMD simulations are characterized by computing the number of atoms of each amino acid which are inside the pore as a function of time, $N_a(t)$. Two conditions are necessary to consider that an atom is in the pore: first, the radial distance ρ_i of an atom i from the center of the pore must be lower than the actual radius r and, second, the absolute value of the normal distance $|z_i|$ of an atom i to the center of the pore must be lower than half the effective thickness $h_{eff}/2$, which is taken in this case as the geometrical thickness of the MoS_2 membrane (i.e. 3.1 Å) plus two times the vdW radius of S atoms (i.e. 1.8 Å).

4.2.4 Root Mean-Square Deviation (RMSD) and Root Mean-Square Fluctuations (RMSF) of MoS_2 nanoporous membrane

We computed the RMSD of the atoms belonging to the membrane as a function of time during MD simulations:

$$RMSD(t) = \sqrt{\frac{1}{N_{atom}} \sum_{i=1}^{N_{atom}} |r_i(t) - r_i(t_0)|^2}, \tag{4.4}$$

where N_{atom} is the number of atoms of the nanoporous membrane, $r_i(t)$ the position of the atom i at the time t and $r_i(t_0)$ its position at the time $t = 0$. RMSF of the membrane atoms as a function of the average radial distance to the center of mass of the pore was computed as well using the following equation:

$$RMSF_i = \sqrt{\frac{1}{T} \sum_{t=1}^{T} |r_i(t) - \langle r_i \rangle|^2}, \tag{4.5}$$

where T is the total simulation time, $r_i(t)$ the position of the atom i at the time t and $\langle r_i \rangle$ is its average coordinate over the simulation time.

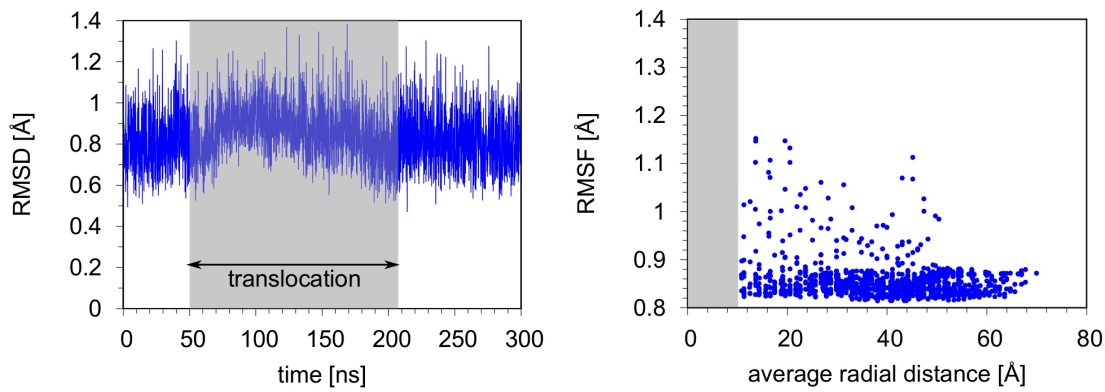

(a) (b)

Figure 4.2: (a) Root Mean-Square Deviation given in Å as a function of time. The gray rectangle represent the translocation event observed during MD. (b) Root Mean-Square Fluctuations given in Å for atoms of the nanoporous membrane as a function of average radial distance. The gray rectangle represents the radius of the pore. The data is extracted from MD run 2 of the translocation of YGGFM-3K peptide through SL-MoS_2 nanopore of $d = 2.0$ nm (see Table 2.6).

Since we used a flexible membrane in this work, we quantified the impact of this flexibility onto the dynamics of peptide translocation by the RMSD and RMSF. As shown in Fig. 4.2 (a), the fluctuations of the membrane atoms increase when the peptide is translocating through the pore. Furthermore, according to Fig. 4.2 (b) there is a difference of flexibility in the membrane between atoms at the perimeter of the pore and the others, even though the fluctuations are relatively small (~0.5 Å). It means that the fluctuations of the membrane atoms are dependent on their radial position relative to the center of mass of the pore. These two observations show that the dynamics of the nanoporous membrane plays a role in the diffusion of the biomolecule on the surface and in the threading of the biomolecule through the pore.

4.3 Translocation of lysine residues through MoS_2 nanopores

As a preliminary step to the study of poly-lysine tagged proteins, we studied the translocation of single lysine amino acid and lysine dipeptide through SL-MoS_2 nanopores of diameter $d = 2.0$ nm. Lysine residues are positively charged and interact with the external electric field. The electric field was chosen to correspond to a transmembrane applied voltage $V = 1.0$ V in all NEMD simulations presented below and indicated in Table 2.6. This value is relatively close to applied voltages used in experiments [172] (a few hundreds of mV). Lysine peptides were capped at each N- and C-terminal part using acetyl and N-methyl groups, respectively. In this work, peptides are initially positioned in bulk solvent, 20 Å above the membrane in order to simulate the complete translocation process, from diffusion in bulk solvent above the membrane to diffusion in bulk solvent below the membrane after threading and translocating through the pore. To the best of our knowledge, simulations of the full translocation process of peptides through MoS_2 nanopores has never been done. Several MD runs using different initial conditions were performed for each system, as indicated in Table 2.6 in the Computational Methods Chapter.

4.3.1 Translocation of a single lysine amino acid through SL-MoS_2 nanopores

As shown in Fig. 4.3, the translocation process is comprised of 3 distinct parts: first, the peptide diffuses in bulk solvent above the membrane but the interaction of the positively charged peptide with the electric field displaces the peptide towards the membrane in a few nanoseconds. Then, the peptide is adsorbed on the MoS_2 surface, diffusing on the top of the membrane. After around 5 nanoseconds, the peptide threads into the pore and the translocation through the nanopore occurs. At the end of the MD run (100 ns), the peptide diffuses at the bottom surface of the membrane and never detached from the membrane to go back to bulk solvent below the membrane, as expected originally. Longer runs are probably needed to observe the final part of the full translocation process.

In more details, the translocation takes place at $t = 6.25$ ns and its duration is $\tau_{trans.} = 0.4$ ns. Moreover, the peptide translocates near to the edge of the pore rather than at its center, as shown in Fig. 4.3 (c). The side-chain of the lysine residue translocates first in the pore, followed by its backbone. As shown in Fig. 4.3 (e), the long side-chain of lysine amino acid is aligned parallel to the electric field inside the pore. During the translocation process, we observe a maximum drop of conductance ΔG around 3 nS relative to the open pore conductance [Fig. 4.3 (b)]. The drop of conductance is maximum when the number of atoms N_a inside the pore is the largest, as indicated in Fig. 4.3 (d). The maximum drop of conductance due to the translocation of the amino acid is observed using a time resolution $\Delta t = 100$ ps for the calculation of the ionic current (Eq. 4.3). For a time resolution Δt of 1 ns, we do not observe a drop of conductance since the translocation time $\tau_{trans.}$ is faster than 1 ns. Fluctuations of conductance during translocation events are large. Thus, maximum conductance drops when the peptide is fully translocated are almost indiscernible compared to the fluctuations that precede the amino acid full translocation [Fig. 4.4 (b)]. Consequently, the average drop of conductance observed during the translocation of a single lysine residue is around 0.7 nS. The average drop $\overline{\Delta G}$ is computed as the difference between the average conductance when the peptide is outside the pore $\overline{G}_{out}$ (from $0 \leq t \leq 6.25$ ns and $6.65 \leq t \leq 100$ ns) and the average conductance when the peptide is in, i.e. $\overline{G}_{in}$ (from $6.25 \leq t \leq 6.65$ ns).

Using different initial conditions, we performed a second MD run of 100 ns of the translocation of a single lysine amino acid through MoS_2 nanopores (Fig. 4.4). Results are very similar to those

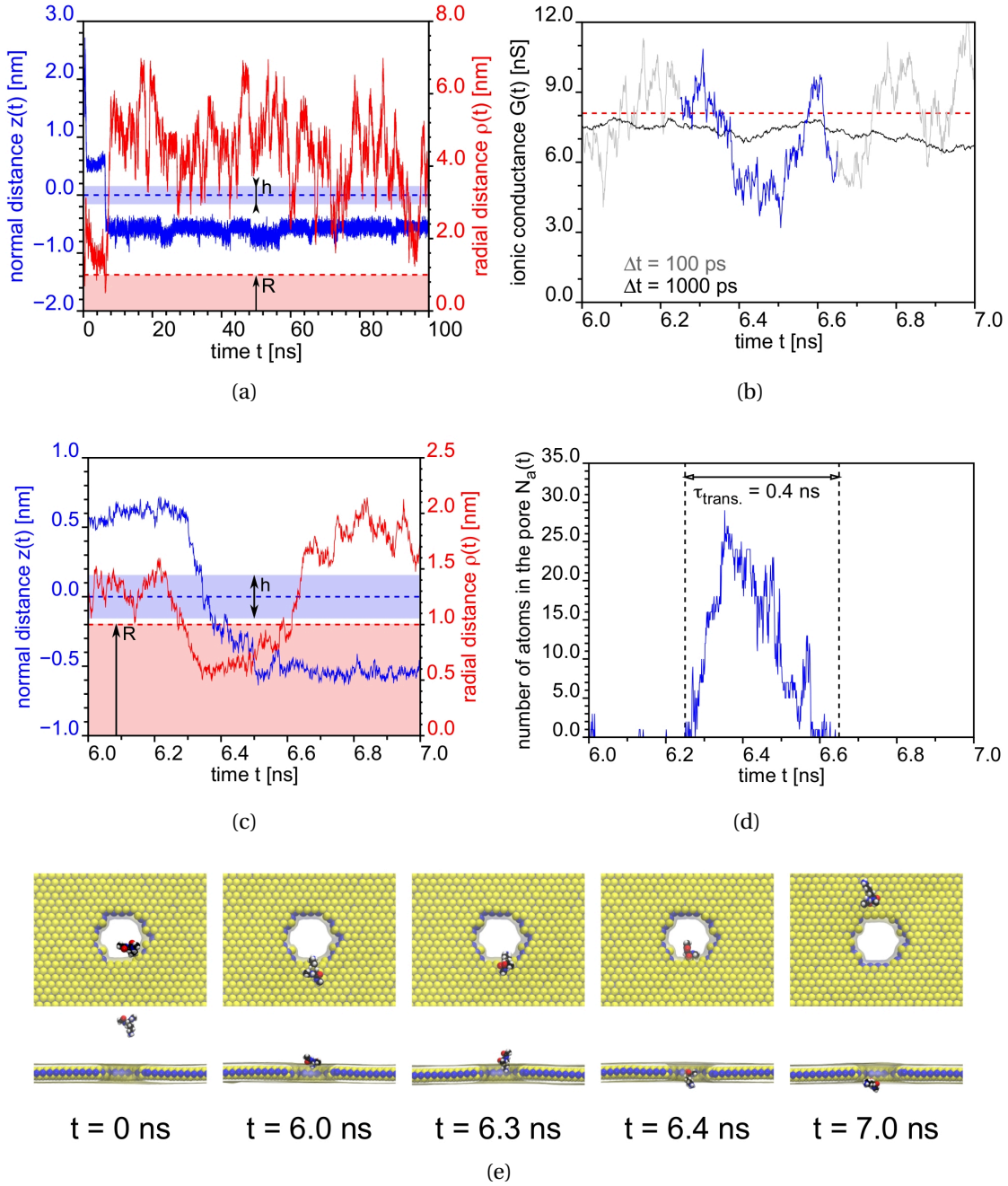

Figure 4.3: Translocation of single lysine amino acid through SL-MoS_2 extracted from MD run 1 (see Table 2.6 from Computational Methods Chapter). (a) and (c) Normal z and radial ρ distances of the center of mass of single lysine amino acid as a function of simulation time t. Dashed blue line represents the z-position of the middle of the membrane in the simulation box. Dotted red line represents the border of the pore. (b) Ionic conductance G as a function of simulation time t computed using $\Delta t = 100$ ps (gray line) and $\Delta t = 1$ ns (black line). The blue line represents the signal when the peptide is inside the pore. The red dashed line represents the open pore conductance. (d) Number of atoms inside the pore N_a as a function of simulation time t. (e) Snapshots extracted from the MD trajectory. Sphere representation is used here and the color code is the following: Mo (dark blue), S (yellow), C (black), O (red), N (blue) and H (white).

found in MD run 1. In this second MD run, we observed a translocation of the lysine residue at $t = 65$ ns. The translocation time is the same as for MD run 1 ($\tau_{trans.} = 0.4$ ns) and the same

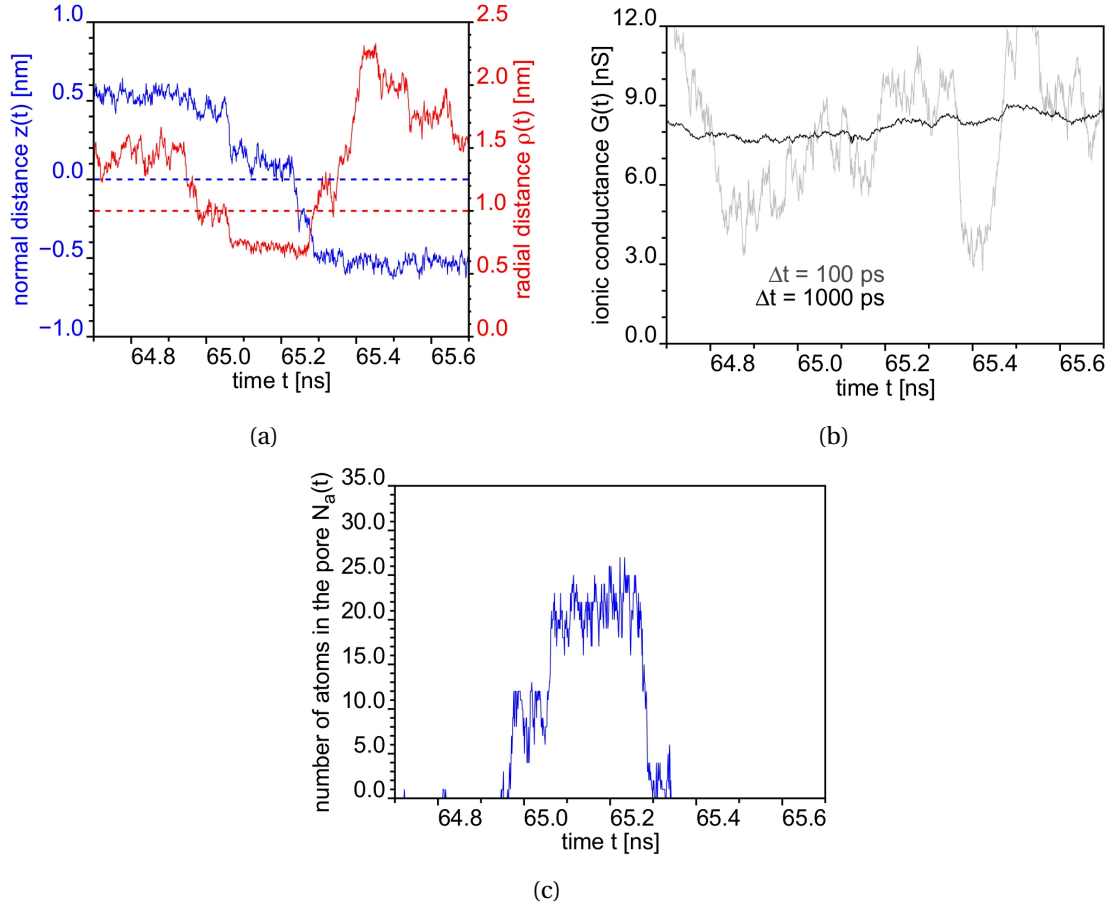

Figure 4.4: Translocation of single lysine amino acid through SL-MoS_2 extracted from MD run 2 (see Table 2.6 from Computational Methods Chapter). (a) Normal z and radial ρ distances of the center of mass of single lysine amino acid as a function of simulation time t. (b) Ionic conductance G as a function of simulation time t computed using $\Delta t = 100$ ps (gray line) and $\Delta t = 1$ ns (black line). (c) Number of atoms inside the pore N_a as a function of simulation time t.

translocation process is observed, i.e. the lysine residue translocates near the edge of the pore and the amino acid side-chain is the first part of the residue to thread into the pore due to its positive charge. Finally, the maximum conductance drop detected during the passage of the residue through the pore is around 3 nS and the average conductance drop is around 0.9 nS, fluctuations of G being as large as the ones observed in MD run 1.

4.3.2 Translocation of a lysine dipeptide through SL-MoS_2 nanopores

We performed 3 independent MD runs to study the translocation of a lysine dipeptide through SL-MoS_2 nanopores (Table 2.6). Fig. 4.5 shows data extracted from MD run 2 of the dipeptide translocation simulation. After around 15 ns of diffusion of the peptide in bulk solvent, the peptide is adsorbed on the MoS_2 top surface of the membrane and finally threads into the pore and translocates at $t = 34.1$ ns of the MD trajectory, as shown in Figs. 4.5 (a) and (c). As already observed for the single lysine amino acid, the translocation of the lysine dipeptide takes place at the edge of the pore [Fig. 4.5 (e)].

The translocation, which is characterized by a two-step process as indicated in Fig. 4.5 (c),

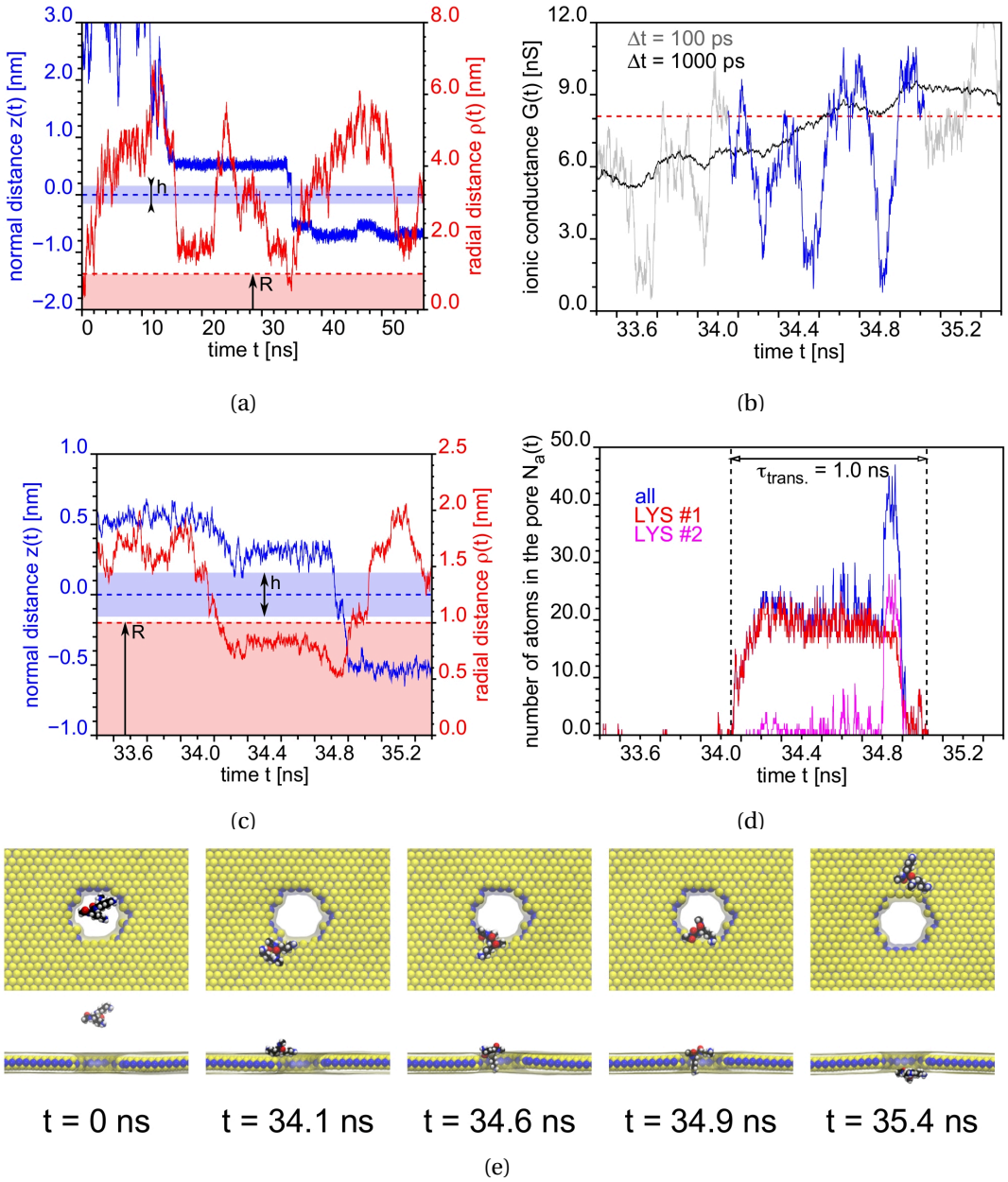

Figure 4.5: Translocation of a lysine dipeptide through SL-MoS_2 extracted from MD run 2 of the lysine dipeptide (see Table 2.6 from Computational Methods Chapter). (a) and (c) Normal z and radial ρ distances of the center of mass of lysine dipeptide as a function of simulation time t. (b) Ionic conductance G as a function of simulation time t. (d) Number of atoms inside the pore N_a as a function of simulation time t. (e) Snapshots extracted from MD trajectory. The color code is the same as in Fig. 4.3.

occurs as follows: first one lysine amino acid enters the pore at $t = 34.6$ ns, the side chain pointing in the direction of the electric field and staying there for around 0.7 ns and second. The next lysine amino acid threads into the nanopore and the whole peptide leaves the channel as one entity after $\tau_{trans.} = 1.0$ ns of translocation duration. During this two-step sequence of events, three maximum drops of conductance are observed of about 6 nS [Fig. 4.5 (b)]. The largest drop is detected when the second lysine threads into the pore, as shown in Fig. 4.5 (d).

At $t = 34.9$ ns [Fig. 4.5 (e)], the volume occupied by the two lysine residues inside the pore is

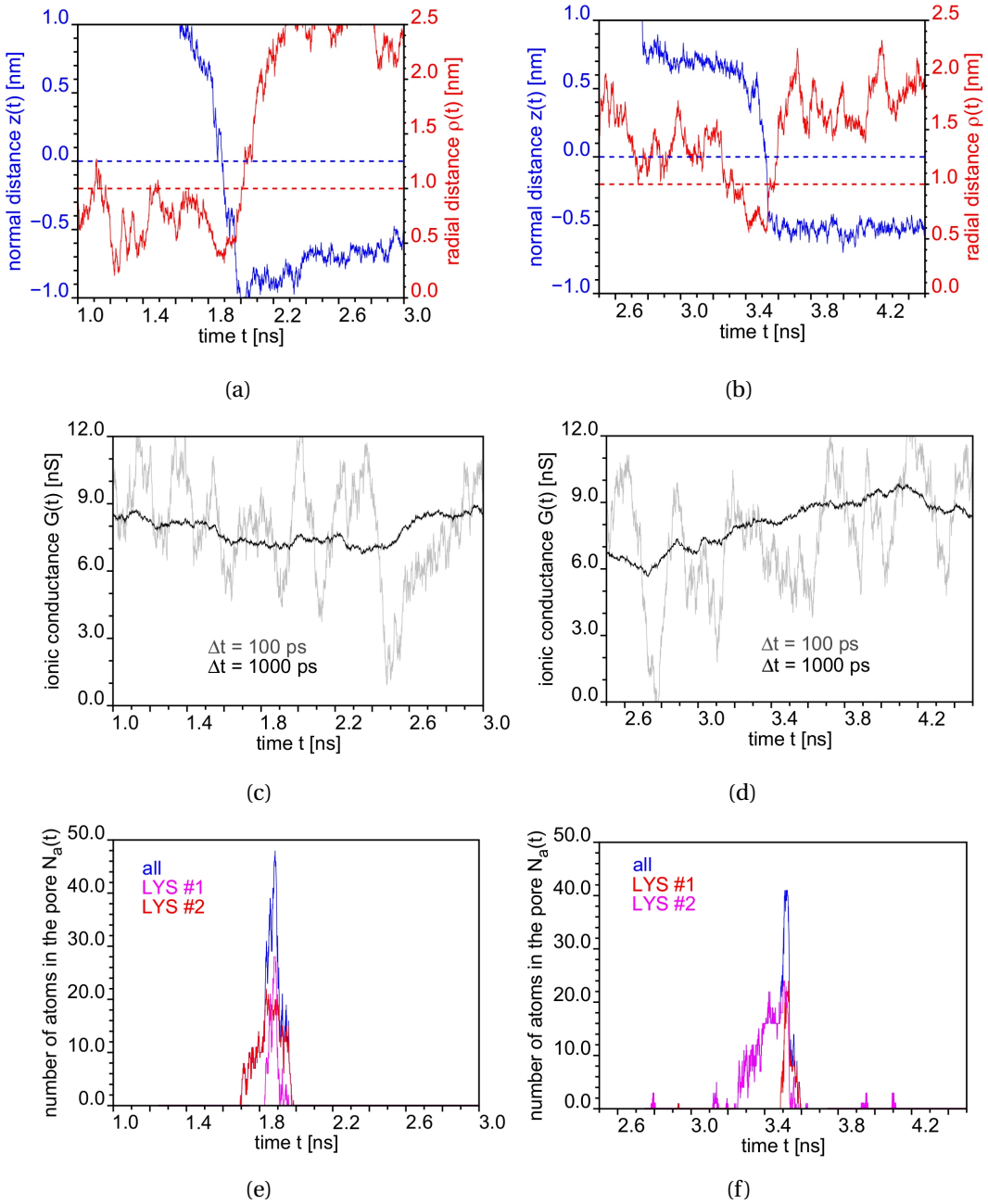

Figure 4.6: Translocation of a lysine dipeptide through SL-MoS_2 extracted from MD run 1 of a lysine dipeptide (left panels (a), (c) and (e)) and MD run 3 (right panels, (b), (d) and (f)). Normal z and radial ρ distances of the center of mass of lysine dipeptide, ionic conductance G and number of atoms inside the pore N_a as a function of simulation time t.

the largest ($N_a(t) > 40$), which increases the ionic current blockade. $G(t)$ signal computed using a $\Delta t = 1$ ns contains no information about translocation events, as it was the case for single lysine amino acid translocations since the translocation time $\tau_{trans.} \approx 1.0$ ns. The average conductance drop is around 0.7 nS, which is similar to the average drop detected for a single lysine amino acid. Although the translocation time is more than twice larger for the dipeptide than for the single lysine amino acid, fluctuations recorded in the conductance signal are still very large, making the drops almost indiscernible. Therefore, reducing the translocation speed in order to get discernible conductance drops out of the fluctuations of the signal is essential for the design of a sequencer. The fact that a two-step process, i.e. one residue translocating at a time, is observed for a lysine

dipeptide is an important preliminary result. In MD run 1 of the lysine dipeptide (Fig. 4.6), the translocation occurs faster than the one observed in MD run 2. The translocation time $\tau_{trans.}$ is around 0.4 ns in MD run 1, as observed in MD runs of single lysine peptides. According to the number of atoms inside the pore as a function of time $N_a(t)$, the N-terminal is translocating first in the pore followed by the C-terminal. The fact that the translocation process of the dipeptide is extremely fast in this particular MD run involves even larger fluctuations of the conductance signal $G(t)$ computed using a Δt = 100 ps and no discernible drops were observed. The same conclusions were drawn from MD run 3 of the lysine dipeptide [Fig. 4.6 (d)], the translocation being faster than MD run 2 of the lysine dipeptide (Fig. 4.5). However, as observed in MD run 2 (Fig. 4.5), the two-step process translocation, i.e. one lysine at a time, was observed in the 3 MD runs with different initial conditions. From these preliminary results extracted from NEMD simulations, we observed that lysine residues thread into the hole of the nanoporous membrane from the side-chains and translocate very fast through MoS_2 nanopores. In addition, a step-wise process exists during the translocation of the lysine dipeptide. From that, no discernible conductance drops can be associated to the step-wise process of translocation since the translocation speed is extremely fast involving large fluctuations of the conductance signals. As we previously showed, the geometry of the nanoporous membranes plays an important role on the performance of nanopore based sensors. A possibility to improve the nanopore sensor response is to adjust the geometry of the membrane in order to slow down the translocation process, where the peptide stays for several nanoseconds into the pore.

4.4 Slowing down the translocation of peptides through MoS_2 nanopores

Slowdown of the translocation of biological peptides through MoS_2 nanopores has been studied by modifying the geometry of the membrane system:

(i) reducing its diameter: from 2.0 to 1.5 nm,
(ii) increasing its thickness: from SL-MoS_2 to 2L-MoS_2.

4.4.1 Reducing the diameter of the nanopore

First, the diameter of the nanopore was reduced from 2.0 to 1.5 nm. This strategy leads to an open pore conductance reduction from 8.1 to 4.3 nS [60]. During MD run 2 with this new geometry presented in Fig. 4.7, two attempts of translocation for the dipeptide were observed, the first one occurring around t = 0.8 ns for which the two lysine residues tried to go through the pore as one but were rejected due to steric effects. The second attempt occurs at t = 2.6 ns and was successful. During this second attempt, the translocation follows a two-step process as observed for the membrane with a 2.0 nm diameter (Fig. 4.5). The N-terminal lysine side-chain enters the pore, pointing out in the direction of the electric field and at around t = 2 ns, the C-terminal lysine is threaded into the pore and the full translocation occurs. In opposition to the translocation of lysine dipeptide through SL-MoS_2 pore of diameter 2.0 nm, the translocation occurs closer to the center of the pore [Fig. 4.7 (a)]. The translocation time $\tau_{trans.}$ is around 2.8 ns, which is 3 times longer than the one detected for the 2.0 nm pore. In fact, since the translocation time is longer, the conductance signal $G(t)$ recorded every Δt = 1 ns is better suited to analyze conductance drops. Indeed, one discernible drop of around 2.5-3.0 nS is detected during the translocation process and lasts until the full passage of the peptide is completed. The corresponding average drop is around

1.4 nS, which is two times larger than the one detected for the 2.0 nm pore. The conductance signal in this case allows to detect the passage of the dipeptide but not the passage of the two residues separately.

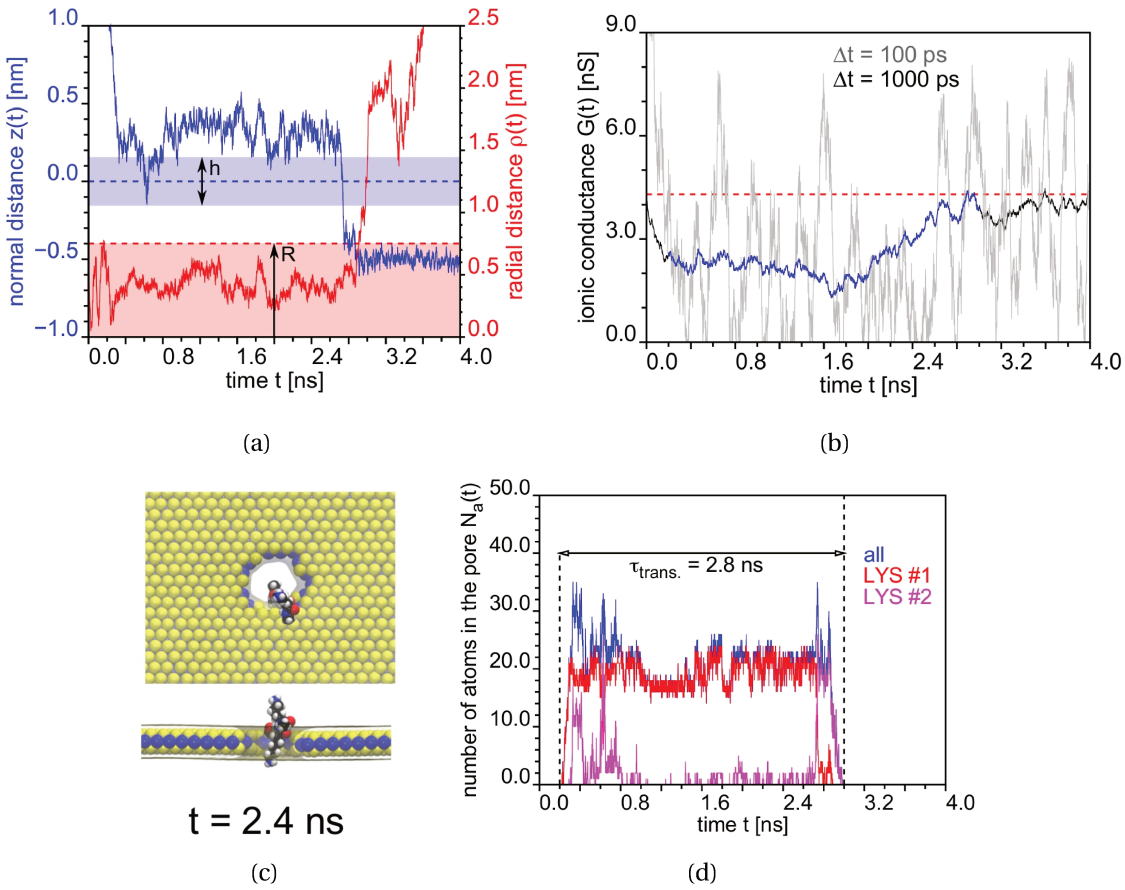

Figure 4.7: Translocation of a lysine dipeptide through SL-MoS_2 nanopore with d = 1.5 nm for MD run 2. (a) Normal z and radial ρ distances of the center of mass of lysine dipeptide as a function of simulation time t. (b) Ionic conductance G as a function of simulation time t. (c) Snapshots extracted from MD trajectory. The color code is the same as in Fig. 4.3. (d) Number of atoms inside the pore N_a as a function of simulation time t.

4.4.2 Increasing the thickness of the membrane

Second, the thickness of the membrane was slightly increased from 0.31 to 0.94 nm (from SL- to 2L-MoS_2) keeping a nanopore diameter of 2.0 nm. The open pore conductance only drops from 8.1 to 6.0 nS [compared to 4.3 nS for the reduction of the pore diameter of SL-MoS_2 (see Table 3.2)]. The expected maximum conductance drop is then larger by increasing the thickness than reducing the diameter. Therefore, a larger SNR is expected for the corresponding SSN device, leading to a good compromise sensor resolution. As shown in Fig. 4.8, the translocation of lysine dipeptide through 2L-MoS_2 occurs at $t = 50$ ns.

As already observed for SL-MoS_2 nanoporous membranes, the translocation process can be described in two steps, the N-terminal lysine threading first into the pore followed by the C-terminal lysine 15 ns later. In total, the translocation time is around 18 ns, which is 18 times larger than for SL-MoS_2. The initial goal, which was to increase the translocation time (i.e. reduce

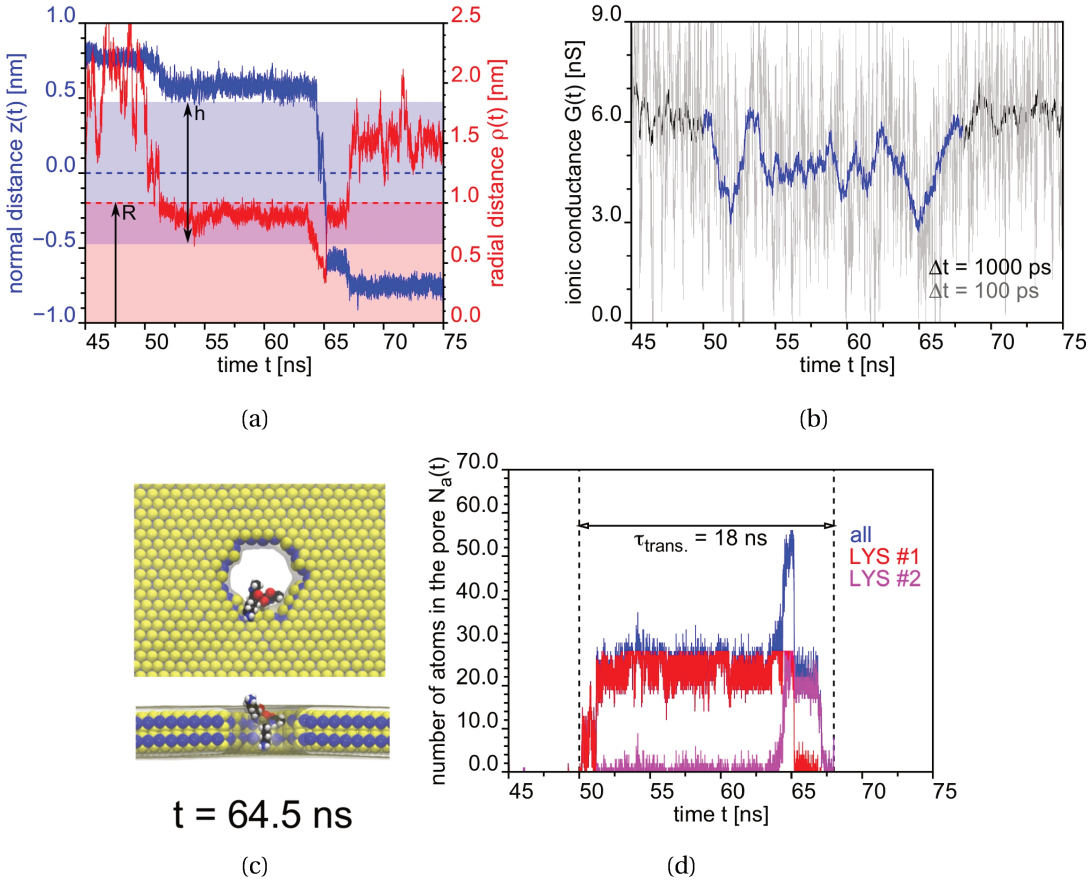

Figure 4.8: Translocation of a lysine dipeptide through 2L-MoS_2 nanopore with d = 2.0 nm for MD run 2. (a) Normal z and radial ρ distances of the center of mass of lysine dipeptide as a function of simulation time t. (b) Ionic conductance G as a function of simulation time t. (c) Snapshots extracted from MD trajectory corresponding to MD run 2. The color code is the same as in Fig. 4.3. (d) Number of atoms inside the pore N_a as a function of simulation time t.

the translocation speed) of the peptide in the pore, is thus achieved. Furthermore, the conductance signal recorded every $\Delta t = 1$ ns shows two distinct and discernible drops: the first one of around 3.0 nS, when the N-terminal lysine enters the pore at $t = 50$ ns and a second drop of the same magnitude, when the C-terminal lysine threads into the pore at $t = 65$ ns. The corresponding average drop is around 1.4 nS, the same as the one for the smaller diameter pore but this time, two traces of the signal are detected clearly as shown in Fig. 4.8 (b). This result is a major breakthrough for the design of protein sequencing devices.

For several years, experimentalists have been trying to reduce the thickness of the membranes, particularly using 2D materials in order to get a larger conductance signal (i.e. larger SNR) and a better spatial resolution. In the present work, we show that increasing slightly the thickness by considering bilayer 2D materials might lead to drops of conductance in relation with the number of residue translocating through the pore. The cost of increasing the signal resolution in the time domain by increasing the thickness is that the spatial resolution is reduced. In this example, the thickness of 2L-MoS_2 is around 1.0 nm. For comparison, the length of a lysine side-chain is around 0.6 nm and the distance between side-chains in two consecutive amino acids (C^{α}-C^{α} distance) is around 0.4 nm. These dimensions are very close to the thickness of the membrane. Considering 3L- or 4L-MoS_2 membranes increase the thickness of the membrane to 1.5 and 2.0 nm, respectively as observed in Chapter 3 (see page 47). This consequently decreases the spatial resolution of the

nanopore. Therefore, the ability of the nanopore sensor to detect details about the sequence of the amino acid of the peptide would be lower for those systems. Therefore, we did not test them here.

To conclude, the combination of the proper diameter of the pore according to the size of the molecule and the proper thickness according to the sensitivity of the sensor to be designed in terms of time and spatial resolution is the key to improve the efficiency of the sequencing sensors to detect single residues of proteins in the near future.

4.5 Translocation of Met-Enkephalin through MoS_2 nanopores

Met-Enkephalin is a five residue peptide of sequence TYR-GLY-GLY-PHE-MET (YGGFM). This biomolecule, which is one of the smallest neurotransmitter peptides has been extensively used as a reference model peptide in all-atom MD simulations [173]. This peptide is made of 5 neutral amino acids and, in order to study its threading and translocation through MoS_2 nanoporous membranes, it needs to be artificially charged. Therefore, we decided to attach poly-lysine tags of different lengths to Met-Enkephalin, from 1 lysine residue (1K) to 5 lysine residues (5K). For each of the 5 synthetic peptides created here, we performed several MD runs, as indicated in Table 2.6 to capture threading and translocation events and to establish the relationship between those events and the signal of the sensor, i.e. drops of ionic conductance ΔG. The electric field was chosen to correspond to a transmembrane applied voltage $V = 1.0$ V in all NEMD simulations presented below, as done for translocation of lysine residues above.

Fig. 4.9 shows the results of the translocation of YGGFM-3K peptide through SL-MoS_2 nanoporous membrane extracted from MD run 2 of duration $T = 300$ ns. After 50 ns of diffusion of the peptide in bulk solvent and on the MoS_2 top surface, the peptide threads into the pore. As shown in Fig. 4.9 (a), the translocation takes place between $t = 50.0$ and $t = 208.0$ ns and is characterized by a step-wise process. According to the normal distance $z(t)$ as a function of time, 5 or 6 steps can be distinguished [Fig. 4.9 (a)]. By looking at the number of atoms $N_a(t)$ of each amino acid that are inside the pore as a function of simulation time, the following sequence of translocation events is suggested. The C-terminal part of the peptide, corresponding to the poly-lysine tag (residues #6, #7 and #8), is entering the pore at $t = 51.2$ ns. LYS #8 translocates first, followed by LYS #7 and LYS #6, as shown in Fig. 4.9 (b). Then, at $t = 91.5$ ns, MET and PHE residues enter the pore and stay inside the channel for a long period, over 100 ns. Moreover, LYS #6 and #7 were detected to be in the pore but they were specifically at the bottom surface at the same time as MET and PHE were in [see snapshots 4, 5 and 6 extracted from MD trajectory in Fig. 4.9 (c)]. Translocation of MET residue occurs at $t = 176.8$ ns and takes place at the center of the pore when LYS #7 is completely outside the pore. Finally, at $t = 200.1$ ns, the two GLY residues translocate extremely fast and drag the N-terminal residue. TYR and the whole peptide leave the pore at $t = 208.0$ ns. Then, the peptide starts to diffuse at the bottom surface up to $t = 300$ ns, at the end of the MD trajectory.

In addition, as observed for individual lysine residues, the translocation was located at the edge of the pore and not at the center of the pore [Fig. 4.9 (a) and (c)]. Indeed, the peptide crawls from the top surface to the edge of the pore and crawls back to the bottom surface after passing through the hole, as clearly shown in step 4 at $t = 176.8$ ns in Fig. 4.9 (c). The total translocation time is estimated to be $\tau_{trans.} = 158$ ns.

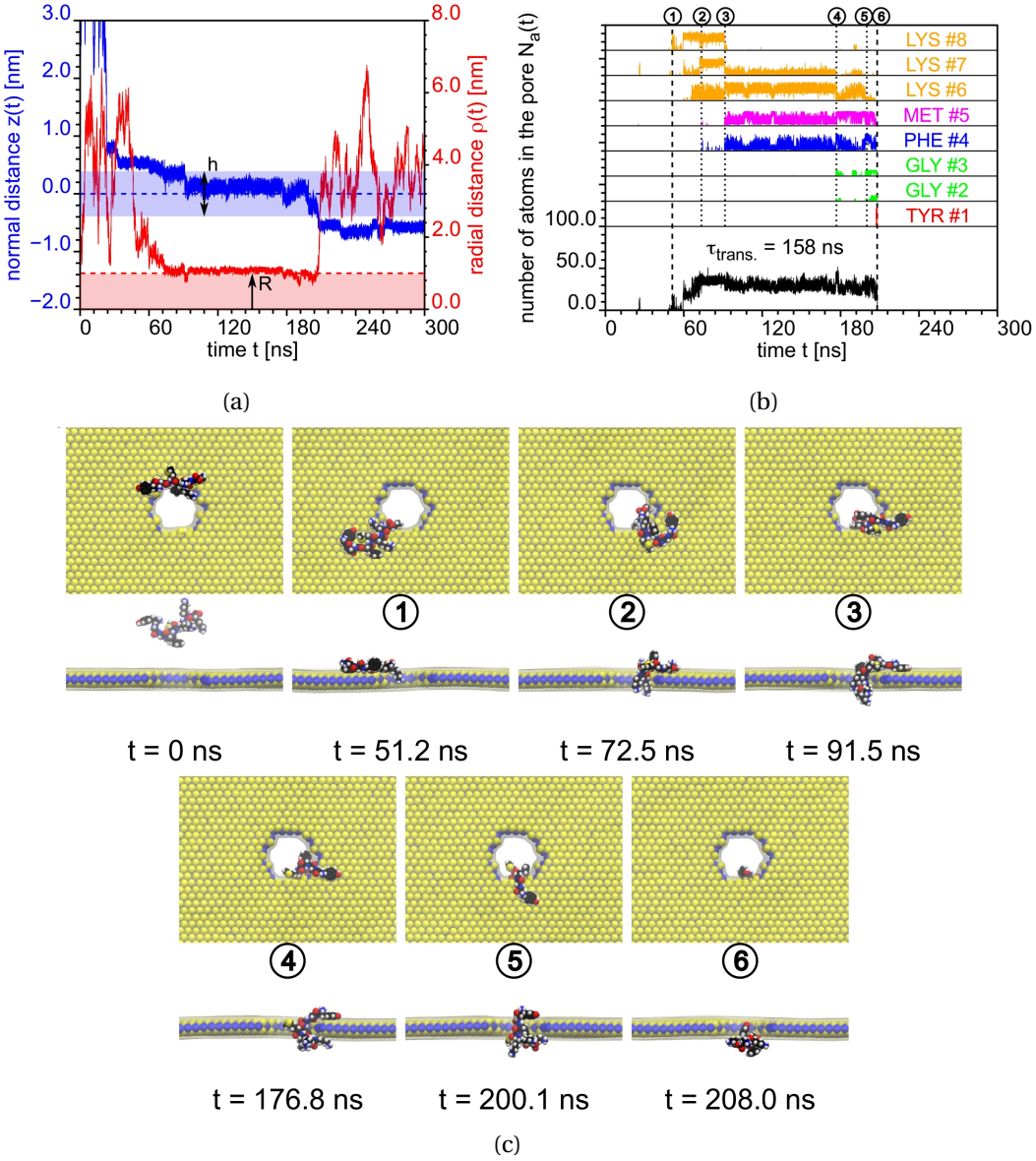

Figure 4.9: Translocation of Met-Enkephalin with poly-lysine tag (YGGFM-3K) through SL-MoS_2 extracted from MD run 2 (see Table 2.6). (a) Normal z and radial ρ distances of the center of mass of the peptide as a function of simulation time t. (b) Number of atoms N_a inside the pore as a function of simulation time t. (c) Snapshots extracted from MD trajectory. The color code is the same as in Fig. 4.3.

During the translocation of YGGFM-3K peptide, we recorded the ionic conductance $G(t)$ ($\Delta t = 1$ ns), as shown in Fig. 4.10 (a). First, we computed the average conductance observed during the 158 ns of translocation time, corresponding to $\overline{G}_{in}$. When the peptide is inside the pore, the average conductance is around 5.8 nS while the open pore conductance when the peptide is outside the pore $\overline{G}_{out}$ is around 7.5 nS. The corresponding average drop $\overline{\Delta G}$ is 1.7 nS, which represents around 23% of the open pore signal. Furthermore, for each of the sequence of events observed during the MD run, we computed the average ionic conductance between events, as shown in Figs. 4.10 (b) and (c). For the sequence of events 1-2-3, we observed the smallest conductance when the three lysine residues are simultaneously inside the pore [Fig. 4.10 (b)]. It leads to a drop of around 1.9 nS compared to the open pore conductance, $\overline{G}_{out}$.

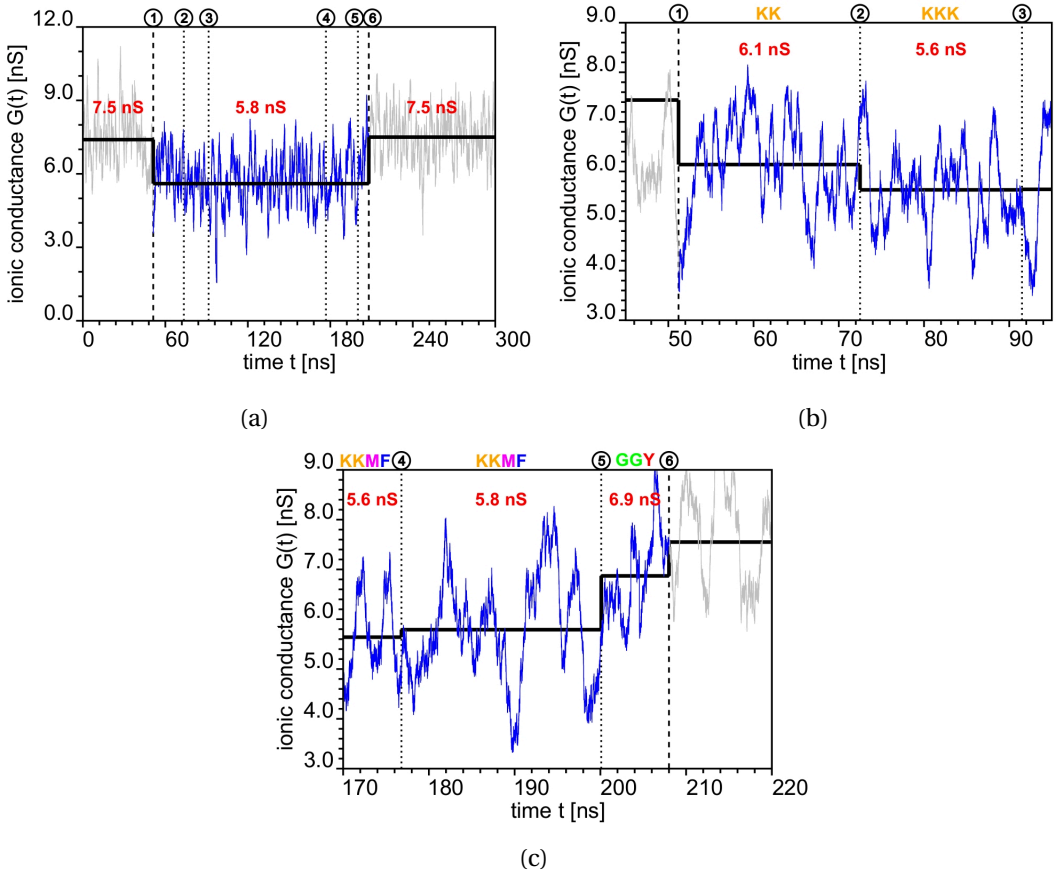

Figure 4.10: Ionic conductance G as a function of simulation time t recorded during the translocation of YGGFM-3K peptide through SL-MoS_2 (MD run 2, see Fig. 4.9). The conductance is computed using $\Delta t = 1$ ns (Eq. 4.3). Black lines represent the average conductance $\overline{G}$ computed before, during and after translocation. (a) Average conductances $\overline{G}$ from 0 to 300 ns. (b) Average conductances $\overline{G}$ computed from 45 to 95 ns (zoom into sequence of events 1-2-3). (c) Average conductances $\overline{G}$ from 170 to 220 ns (zoom into sequence of events 4-5-6).

The same drop is detected when PHE and MET residues joined two of the three lysine between events number 3 and 4. In addition, average drops $\overline{\Delta G}$ are more or less pronounced depending on the number and the type of residues that translocate through the pore. For instance, the same drop is detected when 3 or 4 residues are inside the pore, i.e. KKK or KKMF sequence ($\overline{G} = 5.6$ nS). For events 5 → 6, which corresponds to the passage of the N-terminal part of the peptide (GGY sequence), a smaller drop is detected compared to event 4 (passage of the KFM sequence). This behavior could be explained by steric effects since GLY residues are comprised of the smallest side-chain (H atom), whereas LYS, PHE and MET are characterized by long side-chains.

Finally, the detection of a single amino acid during the translocation of YGGFM-3K peptide through MoS_2 nanopores based on conductance signal is not clearly achieved in the present simulations although, detection of LYS residues at the C-terminal part of the peptide and the detection of TYR and GLY residues at the N-terminal part are observed. Similar results were observed in the work of Chen et al. for highly charged cationic and anionic peptides [48], with conductance drops between 1.0 and 3.0 nS for identical motifs made from 2 to 4 residues translocating at the same time.

For the other peptides tested in the present work (Table 2.6), similar results have been extracted

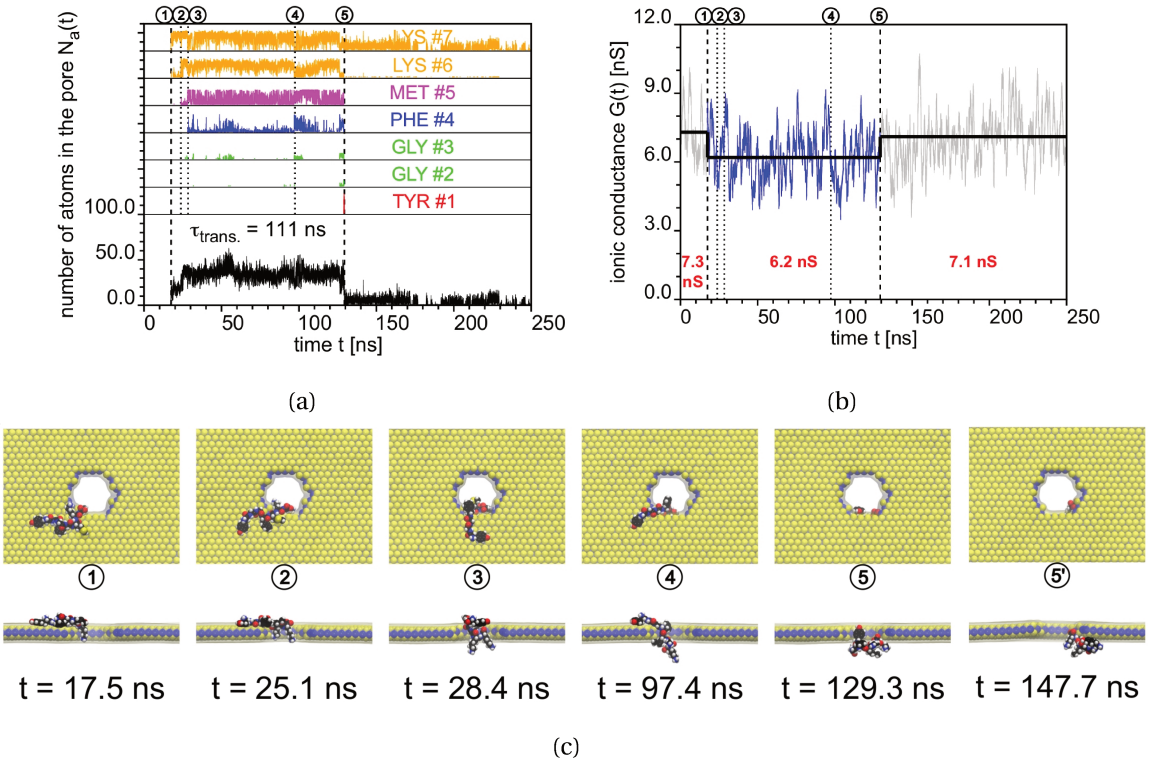

Figure 4.11: Translocation of Met-Enkephalin with poly-lysine tag YGGFM-2K (MD run 2). (a) Number of atoms N_a inside the pore as a function of simulation time t, and (b) ionic conductance G as a function of simulation time t. (c) Snapshots extracted from MD trajectories at different times. Sphere representation is used here and the color code is the following: Mo (dark blue), S (yellow), C (black), O (red), N (blue) and H (white).

from NEMD simulations (Figs. 4.11, 4.12, 4.13 and 4.14). First of all, translocation events are observed for peptides: YGGFM-2K, YGGFM-4K and YGGFM-5K. No translocation occurs for peptides YGGFM and YGGFM-1K for the duration of the present MD simulations. Translocation times of 111, 15, 16 and 71 ns have been recorded for YGGFM-2K (Fig. 4.11), YGGFM-4K MD run 1 (Fig. 4.12) and 2 (Fig. 4.13) and YGGFM-5K (Fig. 4.14), respectively. The fact that the translocation time is remarkably smaller for the peptide with a 4K tag is not really explained here, as the statistics to extrapolate trends about translocation time $\tau_{trans.}$ as a function of the tag length is not sufficient.

For YGGFM-2K peptide, after the complete passage of the biomolecule through the nanopore evidenced by the translocation of the tyrosine amino acid at t = 129.3 ns [Fig. 4.11 (c)], the C-terminal lysine came back to the pore interacting with sulfur atoms at the mouth of the pore. As shown in Fig. 4.11 (a), it stays in there up to the end of the MD trajectory [see also state 5' in Fig. 4.11 (c)]. It has no substantial impact on the average conductance calculations since only the side-chain of the lysine residue and particularly the $-NH_3^+$ termination interacts with the pore.

For each of the MD trajectories where a translocation occurs, a similar sequence of events was observed: first the passage of the poly-lysine tag located at the C-terminal part of the peptide through MoS_2 nanopore is detected, followed by the passage of PHE and MET residues. These two specific residues, which are the amino acids with the largest volume among the Met-Enkephalin sequence remain inside the pore for several tens of nanoseconds, blocking the most the passage of the ions through the hole and involving a discernible average drop of conductance. Finally, the

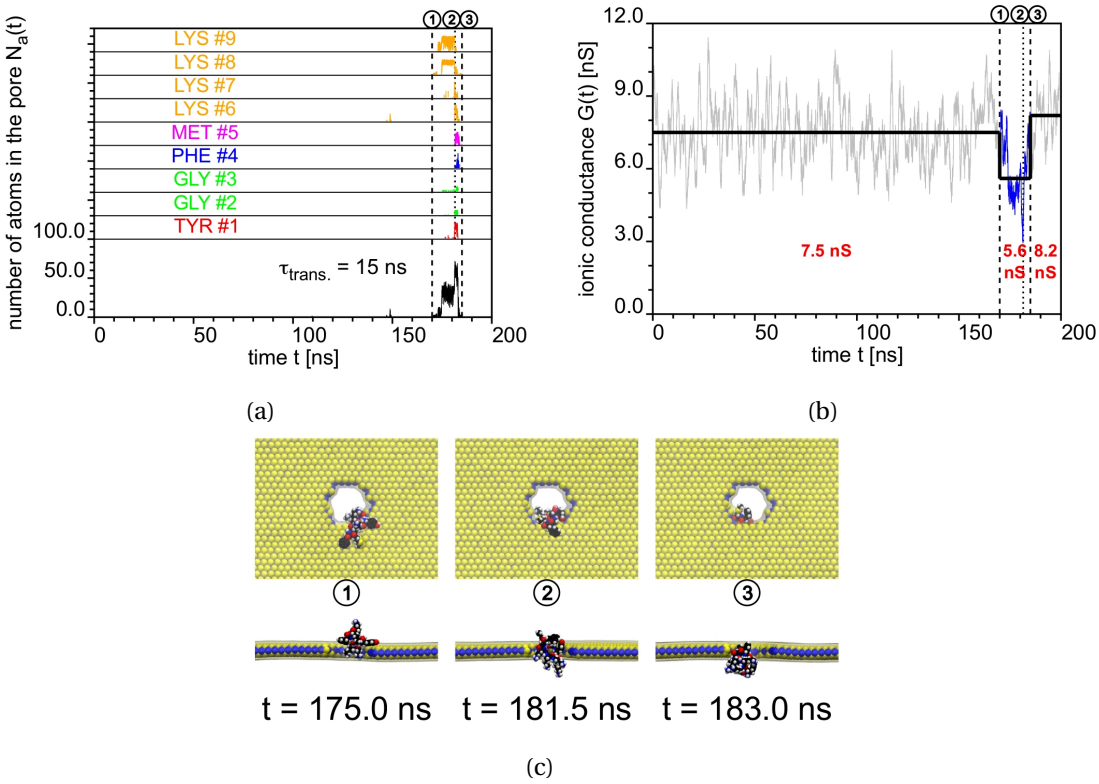

Figure 4.12: Translocation of Met-Enkephalin with poly-lysine tag YGGFM-4K (MD run 1). (a) Number of atoms N_a inside the pore as a function of simulation time t, and (b) ionic conductance G as a function of simulation time t. (c) Snapshots extracted from MD trajectories at different times. The color code is the same as in Fig. 4.11.

passage of the N-terminal sequence (GGY residues) is observed, the Tyrosine translocating extremely fast (less than a couple of nanoseconds) in each of the MD simulations performed here. The maximum average conductance drops between specific events and the open pore conductance observed during translocation are 1.1, 2.6, 1.7 and 1.4 nS for YGGFM-2K [Fig. 4.11 (b)], YGGFM-4K run 1 [Fig. 4.12 (b)] and run 2 [Fig. 4.13 (b)] and YGGFM-5K [Fig. 4.14 (b)], respectively. Note that the largest drops characterizing the full translocation of the peptide are detected for the peptide with 4K tag, the one that translocates the fastest. It comes from the fact that this specific peptide does not translocate as a thread peptide inside the pore but as a globular molecule [Fig. 4.12 (c)]. Therefore, the center of the pore is completely blocked during the translocation of the biomolecule and the conductance drop is maximum.

In summary, we investigated the translocation of biological peptides through MoS_2 nanoporous membranes using MD simulations, We showed that single lysine amino acid and lysine dipeptide, which are positively charged peptides, translocate easily through single-layer membranes with pore diameter of 2.0 nm. The translocation time is approximately several hundreds of picoseconds, which is extremely fast and cannot be detected experimentally with existing techniques, where the maximum resolution is 10 MHz bandwidth [30]. In the corresponding ionic conductance signal, the observed drops are not discernible due to the fast fluctuations in the conductance signal, which are as large as such drops due to the low residence time of peptides in the pore. To get discernible conductance drops associated with the passage of single amino acid through MoS_2 nanopores, increasing the thickness of the membranes is the best option at the cost of reducing the SNR (open pore conductance is reduced by a factor of ~ 1.3) and spatial resolution

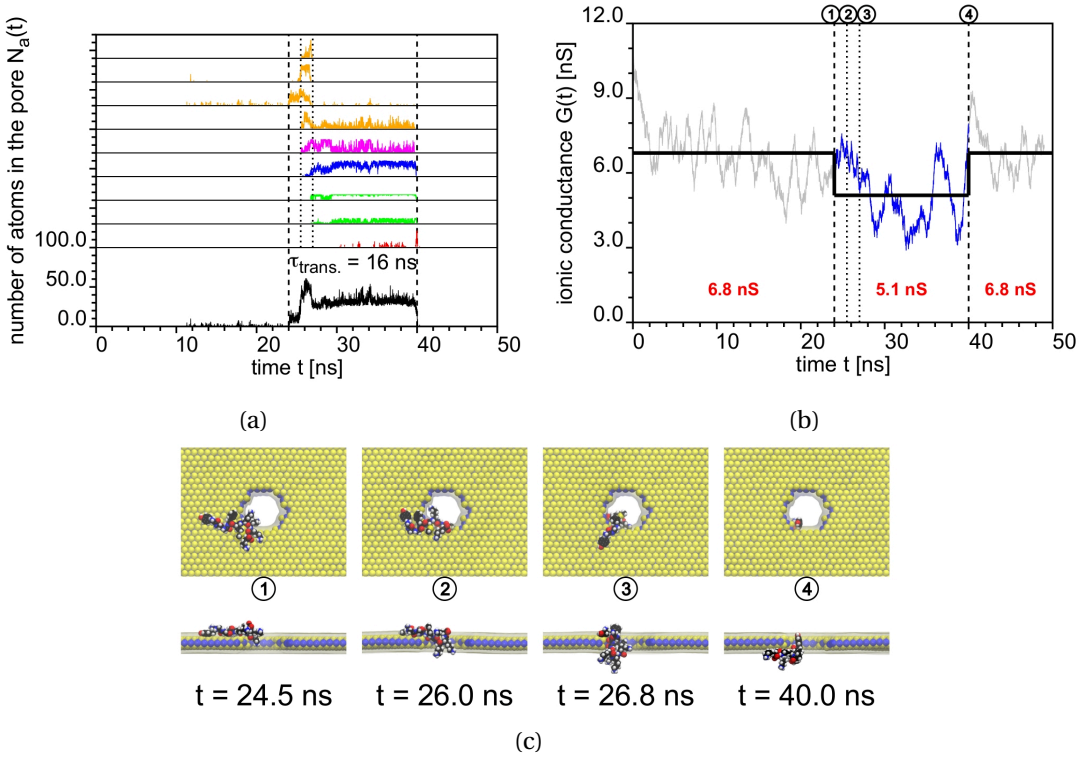

Figure 4.13: Translocation of Met-Enkephalin with poly-lysine tag YGGFM-4K (MD run 2). (a) Number of atoms N_a inside the pore as a function of simulation time t, and (b) ionic conductance G as a function of simulation time t. (c) Snapshots extracted from MD trajectories at different times. The color code is the same as in Fig. 4.11.

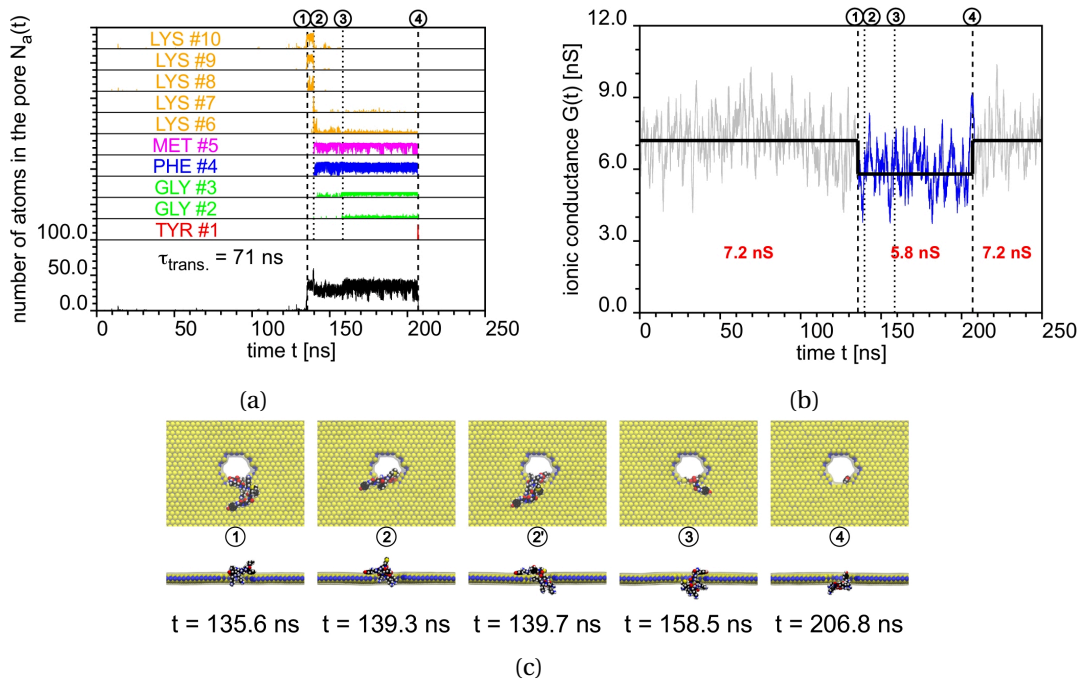

Figure 4.14: Translocation of Met-Enkephalin with poly-lysine tag YGGFM-5K (MD run 1). (a) Number of atoms N_a inside the pore as a function of simulation time t, and (b) ionic conductance G as a function of simulation time t. (c) Snapshots extracted from MD trajectories at different times. The color code is the same as in Fig. 4.11.

of the sensor (by a factor of ~ 3). For lysine dipeptides, we demonstrated that the translocation through 2L-MoS_2 leads to two conductance drops within the translocation event ~ 3 nS, directly related to the step-wise passage of the individual lysine residue. This specific result could be tested experimentally. Finally, we studied the threading and translocation of Met-Enkephalin protein with poly-lysine tags through MoS_2 nanopores. Adding poly-lysine tags increases the global charge of the peptide and facilitates the threading of the protein through the nanopore due to interactions between the charged biomolecule and the electric field. We showed also that poly-lysine tags translocate first through the pore, followed by specific motifs of the protein in a step-wise manner. However, from the conductance signal, single amino acids are not distinguishable. The use of 2L-MoS_2 with such small pores as membrane for sequencing device or the addition of negatively charged residues at the N-terminal part of the protein to counterbalance the positively charged C-terminal part are different options that will be tested in the near future.

Chapter 5

MD simulations of MoS_2 defect pores using Reax Force Field

In the rich family of 2D layered nanomaterials, TMDC have sparked great interest due to their unique properties and potential applications in electronic devices, optoelectronics, sensing, energy storage and catalysis [174]. In regards to the performances and sensitivity of SSN based sensors, many challenges exist in experimental and theoretical studies, such as limitations in the spatial and temporal resolutions, translocation speed and biomolecule adsorption on the nanoporous membrane surface [175]. Pore functionalization is a useful strategy to improve the sensitivity and diversity of nanopore-based detection [175]. In practical, functionalization involves depositing or covalently binding active material in the pore and membrane surface, which changes their physical and chemical properties. For ionic conductivity, functionalization of nanoporous membrane can substantially alter transport properties of the pore [120].

For example, functionalization of graphene has been widely studied over the past few years and several methods have been tested for controlled and selective functionalization of graphene edges [120]. In reactive plasma etching, graphene substrate reacts and forms a compound with atoms in the plasma, where the chemical reactivity of graphene edges result from its carbon atoms at the edge with unsaturated bonds [178]. Also preferential binding of peptides to graphene edges has been observed experimentally and from MD simulations, allowing the creation of non-covalent functionalized graphene, which can be used as an interesting hybrid material [179]. Common form of functionalized graphene observed experimentally is graphene oxide (GO) membranes [158], which are 2D networks consisting of oxidized zones made of polar oxygen functional groups and graphitic zones with great potential for nanofiltration applications [180]. Moreover, although controlled pore functionalization has been difficult to achieve, several computational studies have been reported on graphene pore functionalization and its effect on pore properties. For example, Cohen-Tanugi and Grossman [176] found using MD simulations, that applying hydrostatic pressure on hydrogenated (hydrophobic hydrogen groups) and hydroxylated (hydrophilic hydroxyl groups) single-layer graphene can effectively separate salt from water and could be used as a desalination membrane. Also, bioinspired graphene nanopores have been previously studied using MD simulations to mimic biological sodium (NavAb) and potassium (KcsA) channels [154, 155]. Another interesting form of functionalized graphene are crown ether structures [177, 181], which are a family of electrically neutral cyclic ethylene oxide molecules that exhibit marked selective affinity for metal cations. Crown ethers are a result of removing an entire carbon hexagon followed by replacing the remaining edge carbons with oxygen atoms. Such a pore is expected to exhibit significant binding preference for aqueous K^+ ions [177]. Crown

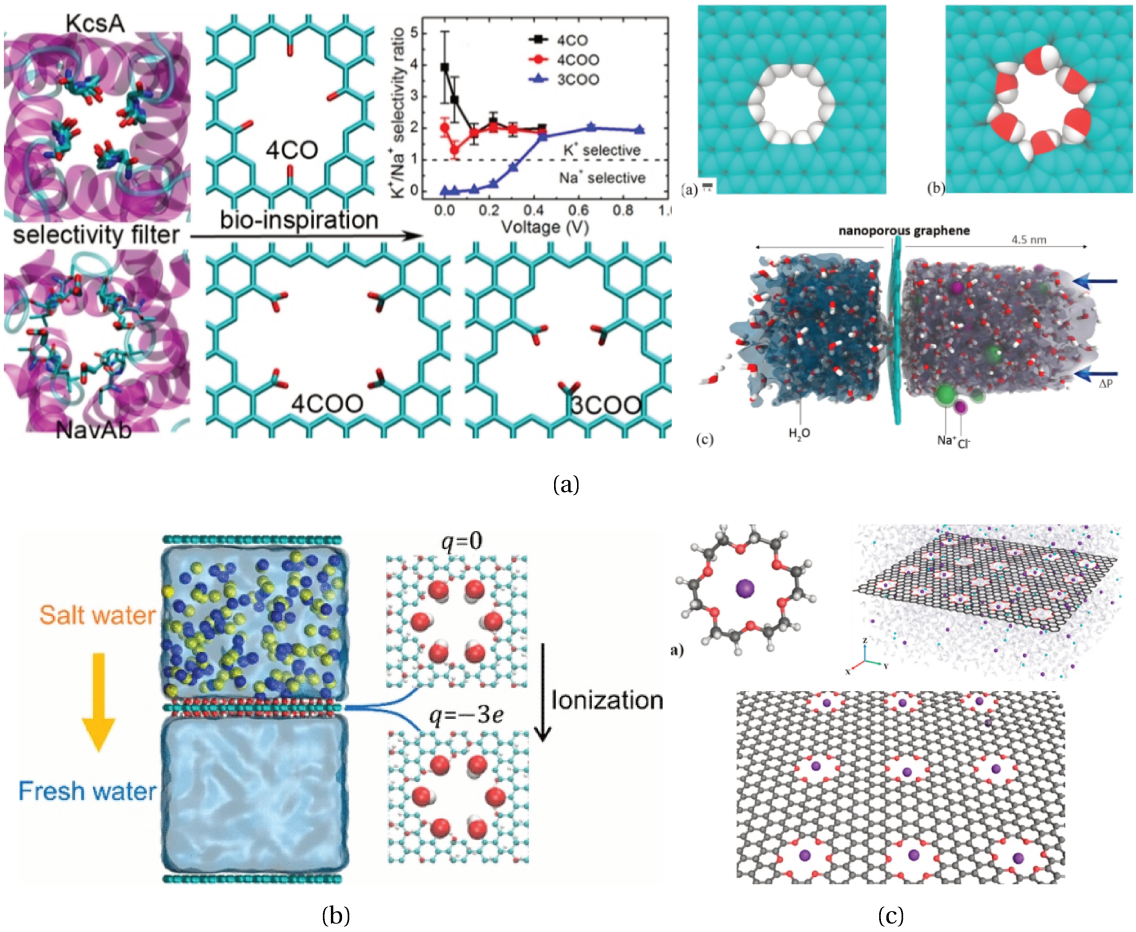

Figure 5.1: Functionalized forms of graphene. (a) Left panel: biological sodium (NavAb) and potassium (KcsA) channels and graphene nanopores functionalized by negatively charged carboxylate groups to mimic the selectivity of Na^+ and K^+ ions. Image extracted from Ref. [155]. Right panel: hydrogenated and hydroxylated graphene pores for water/salt separation in desalination systems via hydrostatic pressure. Image extracted from Ref. [176]. (b) Molecular system used for studying desalination by GO membranes. The GO membrane has a single nanopore at its center and the six atoms at the perimeter of the pore are functionalized using carboxyl groups. Image extracted from Ref. [158]. (c) A stand-alone 18-crown-6 ether with an embedded potassium ion and the simulated system: Graphene membrane with an embedded array of 20 18-crown-6 ethers, in an aqueous ionic bath. Crown ether structures are used for ion trapping, as shown in the final state obtained from MD simulations. Image extracted from Ref. [177].

ether-electrolyte interactions have been reported to allow nanopore detection of individual DNA abasic sites in single molecule, which has been shown to slow down the DNA motion during electrophoretic translocation and allowing more easily recordable levels [181].

Likewise nanopores made of graphene, MoS_2 nanopores selective functionalization is still a matter of study. In fact, to the best of our knowledge, most of the works based on MoS_2 nanopores are mainly focused on their pristine structures. As it has been discussed all along this work, 2D pores made from MoS_2 are among the best candidates for biomolecule translocation devices. Moreover, generating pores with nanometer size in a controllable manner is essential to achieve transmembrane devices with high efficiency. For example, S. Wang et al. [122] reported the use of the electron probe in an Aberration corrected Scanning Transmission Electron Microscopy (AC-STEM) for creating sub-nm pores (pore size down to 0.6 nm) in SL-MoS_2 membranes as well as

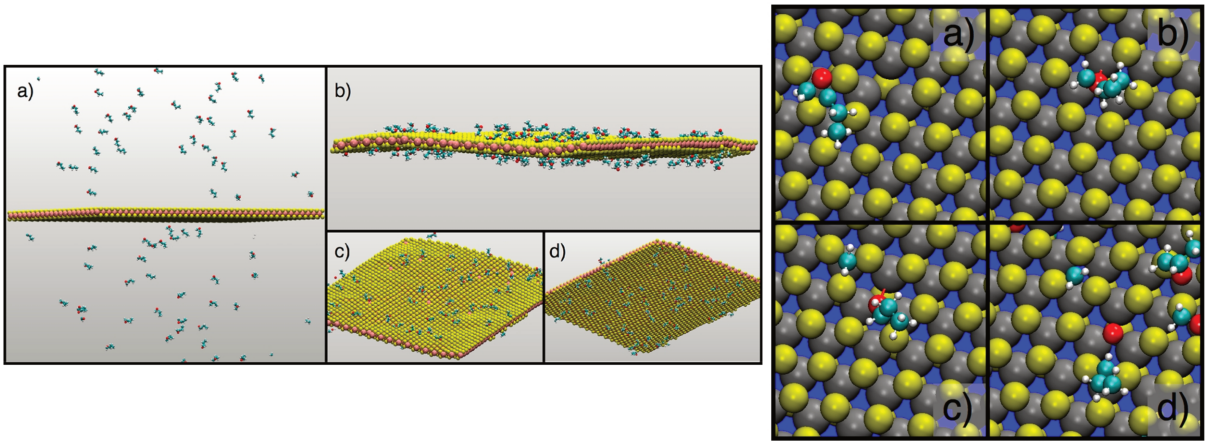

Figure 5.2: MoS_2 surface functionalization study performed using MD simualtions extracted from Yilmaz et al. [87]. The system comprised by a MoS_2 slab with S vacancies and 100 epoxybutane molecules (C_4H_8O). C_4H_8O molecules are randomly distributed in the simulation box and after 2.5 ns simulation time all of the epoxy molecules are bonded to the MoS_2 surface. Left panel shows the initial configuration, the cross sectional and perspective views. Color code: C, cyan; S, yellow; Mo, pink; O, red. Right panel shows the epoxy dissociation, where some O atoms of the epoxy molecule bonds to Mo. Color code: C, cyan; S, yellow; Mo, silver; O, red.

multiple sub-nm pores set out into a patterned array with separation distances less than 5 nm. In fact, atomic vacancies in the material correspond to atomic-scale pores, and the creation of atomic-level defects will precisely allow the fabrication of controlled ultra-small sized pores [59, 87, 123]. Furthermore, MoS_2 surface functionalization can be achieved via S vacancy sites [87, 182, 183], as reported by Nguyen et al. [182], who explored the functionalization of MoS_2 flakes with organic thiols, and its effects on the electronic structure of MoS_2. The possibility to selectively functionalize MoS_2 membranes via surface defects, and more specifically via pore edges, still involve significant challenges and will open the door to create more complex and effective transmembrane devices. As in biological channels, functional groups play a major role in selectivity and permeability. Very recently, Yilmaz et al. [87] parameterized interactions between MoS_2 and epoxybutane (C_4H_8O) using ReaxFF potential, for further surface functionalization studies. More specifically, they showed that epoxy molecules dissociate at S vacancy sites, in which exposed Mo atoms had catalytic activity. This has caught our attention since according to experimental evidence and hypotheses, the addition of functional groups in the mouth of the nanopore affects the transport properties through it. In our application, the functionalization is an interesting possible way to modify/control/improve translocation of charged biomolecules.

Generating pores with sub-nm size in a controllable manner, such as the creation of single-atom vacancies in SL-MoS_2, is essential for achieving membrane separation devices with high efficiency [184]. For example, ionic transport through MoS_2 membranes with sub-nm pores was studied by Thiruraman et al. [59] (Fig. 5.3), where single-atom vacancies are generated in SL-MoS_2 using ion irradiation. However, ionic transport through atomic scale pores is still at the state of the art, and a better understanding of their transport properties is still a matter of research. One way to gain further insight into the ionic transport through MoS_2 defect pores from a computational point of view, is to perform MD simulations in order to elucidate the ionic transport through such tiny systems. In addition, according to experimental protocols of sample preparation for DNA translocation and ionic conductance measurements in SSN devices [59, 130], a process known as pore wetting is used. Pore wetting consists on immersing the device on a mixture of ethanol (C_2H_5OH) and deionized water at 1:1 (vol/vol) ratio [59, 130], in order to help in the

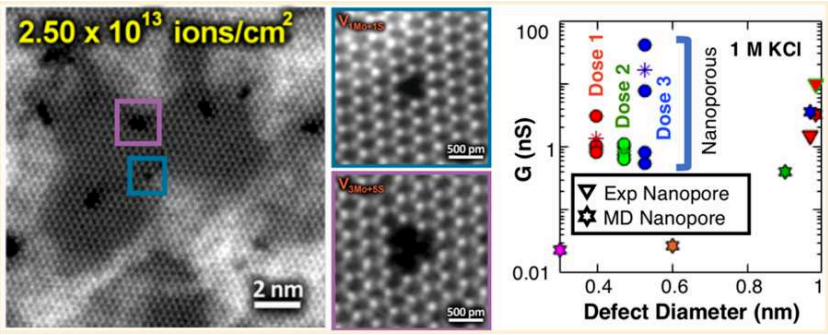

Figure 5.3: Sub-nm pores created from atomic-defect in SL-MoS_2 [59]. Ionic conductance characteristic for different pore sizes published by our collaborators from the experimental group of Pr. Marija Drndić at University of Pennsylvania (PA, USA).

formation of ionic channels by decreasing hydrophobic interactions between membrane and water from the electrolyte. Nevertheless, improper pore wetting could affect conductance measurements, which are extracted from $I-V$ dependence [130]. Based on this, we address the following question: how does ethanol affect the structure of sub-nm defect pores that are used in conductance experiments? To gain information at the atomic level about the effect of ethanol in the pore structure, we performed MD simulations of MoS_2 sub-nm pores systems created from atomic-defects in presence of ethanol molecules using ReaxFF potential in order to model chemical reactions that might happen.

The main motivations of the work presented in this chapter are the following: first, to characterize the dynamics of sub-nm defect pores made of SL-MoS_2 membranes, simulated using ReaxFF potential for further transport properties studies. Second, to evaluate the possibility of pore functionalization with ethanol using ReaxFF potential. Finally, to compute $I-V$ characteristics of sub-nm defect pore membranes in order to investigate their ionic conductance performance. Particularly, reactive potentials such as ReaxFF could provide useful insights into interfaces interactions. Thus, MD simulations were performed for the following systems:

1. Sub-nm MoS_2 membranes with defect pores in vacuum.
2. Sub-nm MoS_2 membranes with defect pores in presence of ethanol molecules.
3. Sub-nm MoS_2 membranes with defect pores in presence of 10 mM KCl.

To characterize the dynamics of defect pores, we performed equilibration MD simulations in vacuum in the NPT ensemble during 2 ps (time step = 0.25 fs) at $T = 300$ K and $P = 1$ bar. Sub-nm defect pores were created by removing 1 Mo + 5 S, 2 Mo + 7 S and 4 Mo + 14 S atoms as observed from experimental TEM images (see Fig. 5.4). Systems were labeled according to the nature of the defect and the removed atoms. The characterization of MD run was performed by computing, first RMSD and RMSF of membrane atoms in order to study structural fluctuations and dynamics of defect pores. Then, probability distributions of Mo and S atoms in the normal distance to the membrane was computed for membranes containing defect pores and compared with the pristine membrane (without the presence of pore). Then, connectivity of the atoms was also studied by computing their interatomic distances for porous membranes and compared with the pristine one. In addition, the surface area of defect pores was computed to quantify the changes in pore shape. Particularly from surface area calculations, we were able to estimate effective diameters of the pores. Lastly, the charges of the Mo and S atoms are shown as a function of the atomic index.

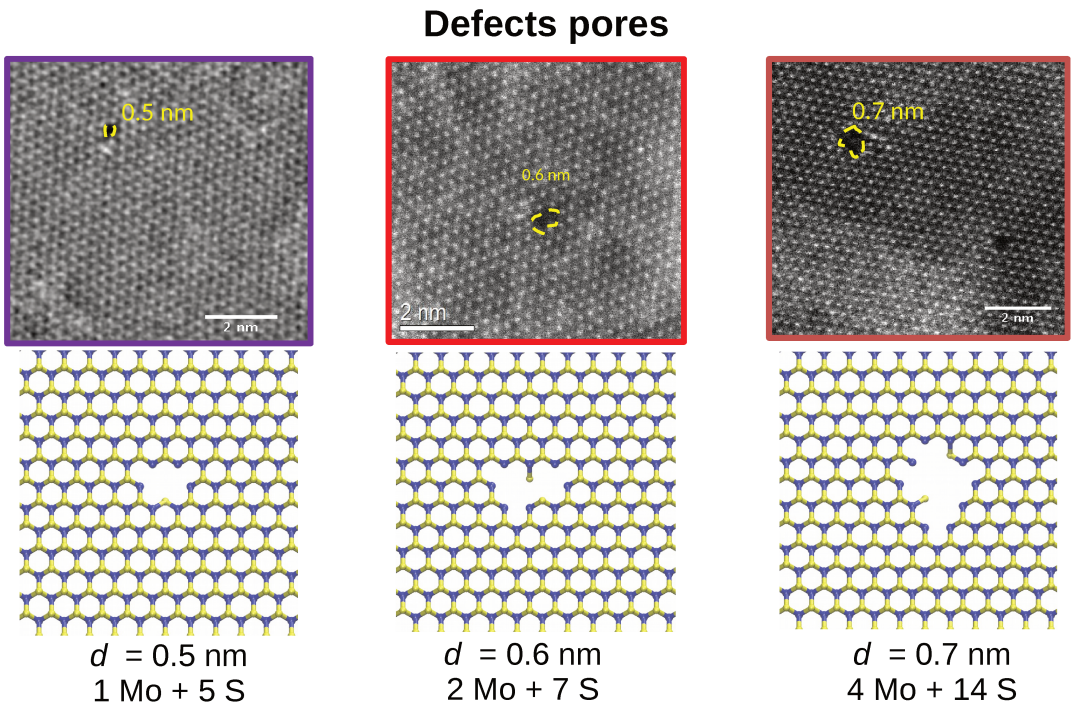

Figure 5.4: SL-MoS_2 sub-nm pore structures generated from atomic defects, where number and nature of removed atoms are indicated. TEM images correspond to the experimental samples fabricated by our collaborators at University of Pennsylvania (Prof. Drndić's group).

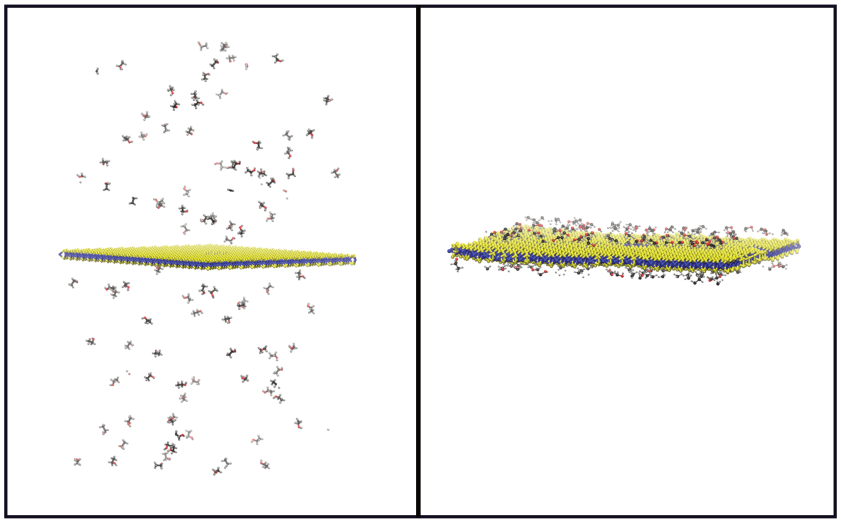

Figure 5.5: Left panel: initial configuration of the system where MoS_2 membrane with a 4 Mo + 14 S defect and 100 ethanol molecules (C_2H_6O) are randomly placed in the simulation box. Right panel: configuration of the system after 100 ps equilibration simulation, where ethanol molecules moved towards the MoS_2 membrane and were adsorbed on the surface.

Then, we performed MD simulations of MoS_2 defect pores in presence of 100 ethanol molecules placed randomly in the simulation box [Fig. 5.5 (left panel)]. Equilibration of the different systems was performed during 100 ps at $T = 300$ K and $P = 1$ bar. Then, production runs were carried out in the NVT ensemble at $T = 300$ K during 10 ns.

In order to compute the $I - V$ curves and the ionic conductance of the systems, we performed NEMD simulations of MoS_2 sub-nm pores using ReaxFF potential and LJ plus Coulomb potentials

for KCl electrolyte. The reason why we used such an hybrid potential is because ReaxFF has not been parameterized for solvent molecules. It is important to remark that simulations of systems that incorporate the use of ReaxFF and LJ plus Coulomb interactions are at the state of the art from a computational point of view, since combining ReaxFF with other potentials using hybrid pair-wise interactions is uncommon.

5.1 Characterization of the dynamics and structural properties of MoS_2 defect pores in vacuum

Sub-nm MoS_2 defect pores simulated using ReaxFF potential are presented in Fig. 5.6. Snapshots of the corresponding atomic structures at simulation times $t = 0$ and $t = 2$ ps indicate that pore shapes changed along MD simulations. It is also interesting to note that changes and reorganization in pore structure result from S atoms migration to Mo atomic plane (S atoms that migrated to the Mo atomic plane during MD simulations are represented highlighted in red circles at $t = 2$ ps). Furthermore, it is possible to observe the formation of new Mo-S and S-S bonds in the specific case of the 2 Mo + 7 S defect pore at the end of the simulation.

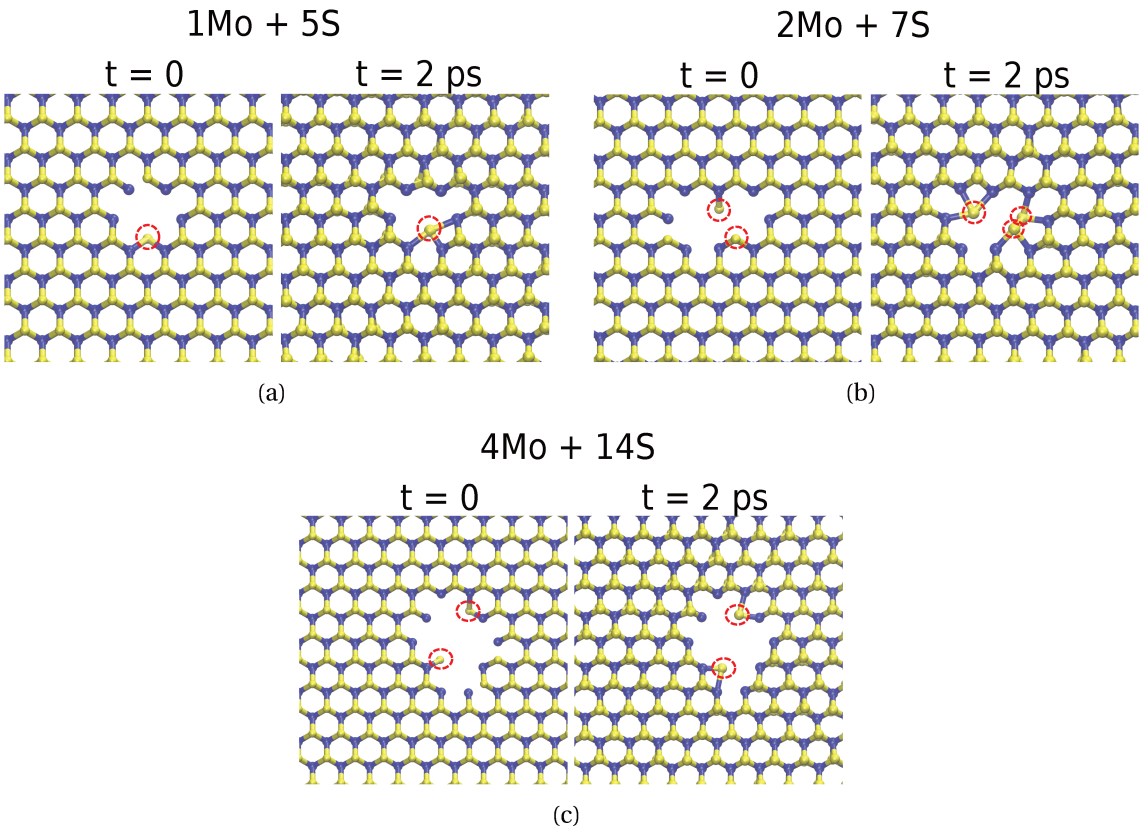

Figure 5.6: Atomic structure of SL-MoS_2 defect pores simulated in the present work. Pores (a) 1 Mo + 5 S, (b) 2 Mo + 7 S, and (c) 4 Mo + 14 S, are shown in their initial and final structure (at $t = 0$ and $t = 2$ ps, respectively). Atomic reorganization in the pore was observed along the simulation. S atoms enclosed in red circles migrate from their initial position to the Mo atomic plane by the end of the simulation at $t = 2$ ps. CPK and dynamic bonds (with cut-off = 2.9 Å) representation in *VMD* were used.

5.1.1 Structural fluctuations of MoS_2 membranes with defect pores

RMSD and RMSF of atoms belonging to SL-MoS_2 membranes were computed from Eqs. 4.4 and 4.5 presented in Chapter 2. RMSD and RMSF of atomic positions in the membrane allow us to quantify changes of the structure along the equilibration simulation, via the structural fluctuations. Fig. 5.7 (a) corresponds to RMSD of 1 Mo + 5 S defect pore, where an increase of the RMSD of ~ 0.85 Å was observed before the first 100 fs of simulation. This increase also corresponds to the period of time of the simulation where the relaxation of the system starts to occur. Then, fluctuations of RMSD values decrease in time as they start to reach a constant value after 800 fs simulation.

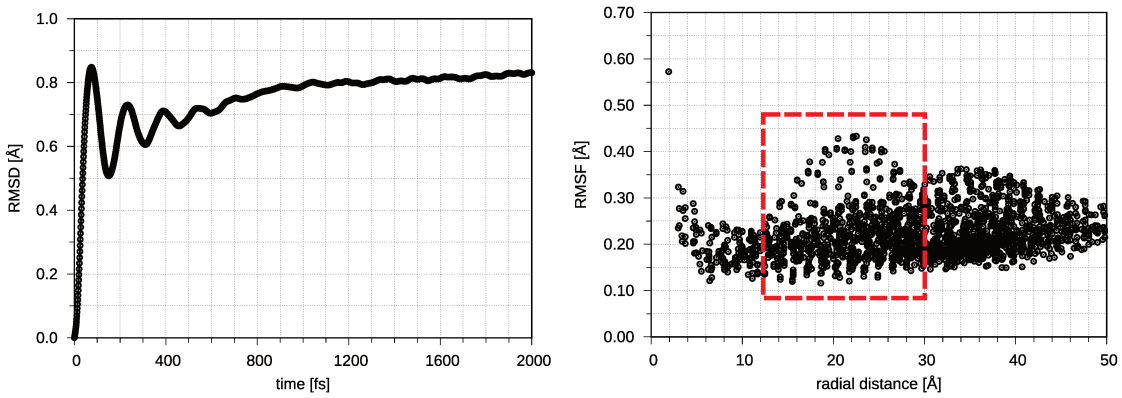

(a) (b)

Figure 5.7: (a) RMSD as a function of time, and (b) RMSF as a function of average radial distance for atoms of SL-MoS_2 membrane. The data is shown for defect pore 1 Mo + 5 S.

RMSF calculations as a function of the radial distance respect to the center of mass of the pore corresponding to the same membrane are shown in Fig. 5.7 (b). This figure evidences a higher flexibility for the atoms at the pore region respect to those far from the pore adjacency. This indicates that fluctuations during the simulation related to the average position of the atoms of the membrane, are dependent on their radial position relative to the center of mass of the pore. Although fluctuations tend to decrease with the atoms average radial distance, a difference in the membrane flexibility between 10 and 30 Å was observed (region highlighted in Fig. 5.7 (b)). Such fluctuations are related to the wavy structure of the membrane in the z-direction normal to the membrane surface (data not shown). The same trends are observed from RMSD and RMSF calculations of the membranes with defect pores 2 Mo + 7 S [Fig. 5.8 (a)] and 4 Mo + 14 S [Fig. 5.8 (b)]. An increase of ~8% was observed for RMSF of atoms at the pore perimeter when the defect pores are created by removing more atoms [Fig. 5.8 (a) and Fig. 5.8 (b)], leading to larger defect pores.

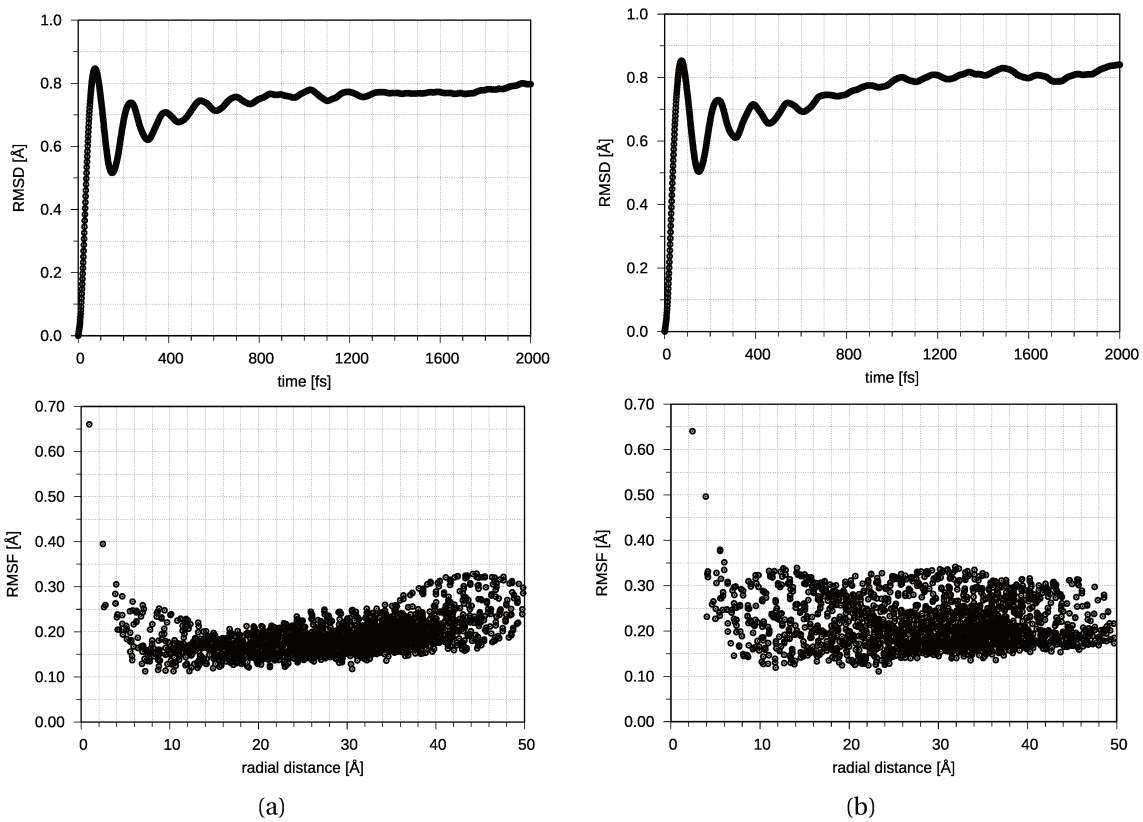

Figure 5.8: RMSD as a function of time, and RMSF as a function of average radial distance for atoms of SL-MoS_2 membranes. Panel (a) corresponds to the pore 2 Mo + 7 S, and panel (b) corresponds to the pore 4 Mo + 14 S.

5.1.2 Structural modifications of MoS_2 membranes with defect pores

Structural modifications of MoS_2 membranes with defect pores were characterized from probability distributions of Mo and S atoms in the normal direction of the membrane, as shown in Fig. 5.9. The advantage of this technique is to quantify the changes on the pore structure due to atomic reorganization, as observed in Fig. 5.6, where some S dangling atoms migrate to Mo atomic plane. The probability distributions corresponding to Mo and S atoms show three well-defined peaks that are related to the Mo atomic plane and the two S planes on both sides of the membrane.

According to the probability distribution of S atoms in the pore defect membranes, the values are different from zero in the region corresponding to the Mo atomic plane as highlighted in Fig. 5.9. It confirms the presence of S atoms in the Mo plane. This behavior was observed in defect pores 1 Mo + 5 S [Fig. 5.9 (a)] and 4 Mo + 14 S [Fig. 5.9 (c)], where S atoms left their atomic plane to the Mo one. In the case of the defect pore 2 Mo + 7 S [Fig. 5.9 (b)], the reorganization of the pore structure occurs due to the migration of three S dangling atoms. These results were compared with the corresponding calculations of MoS_2 pristine membrane, where Mo and S atoms probability distributions evidence atomic Mo and S planes.

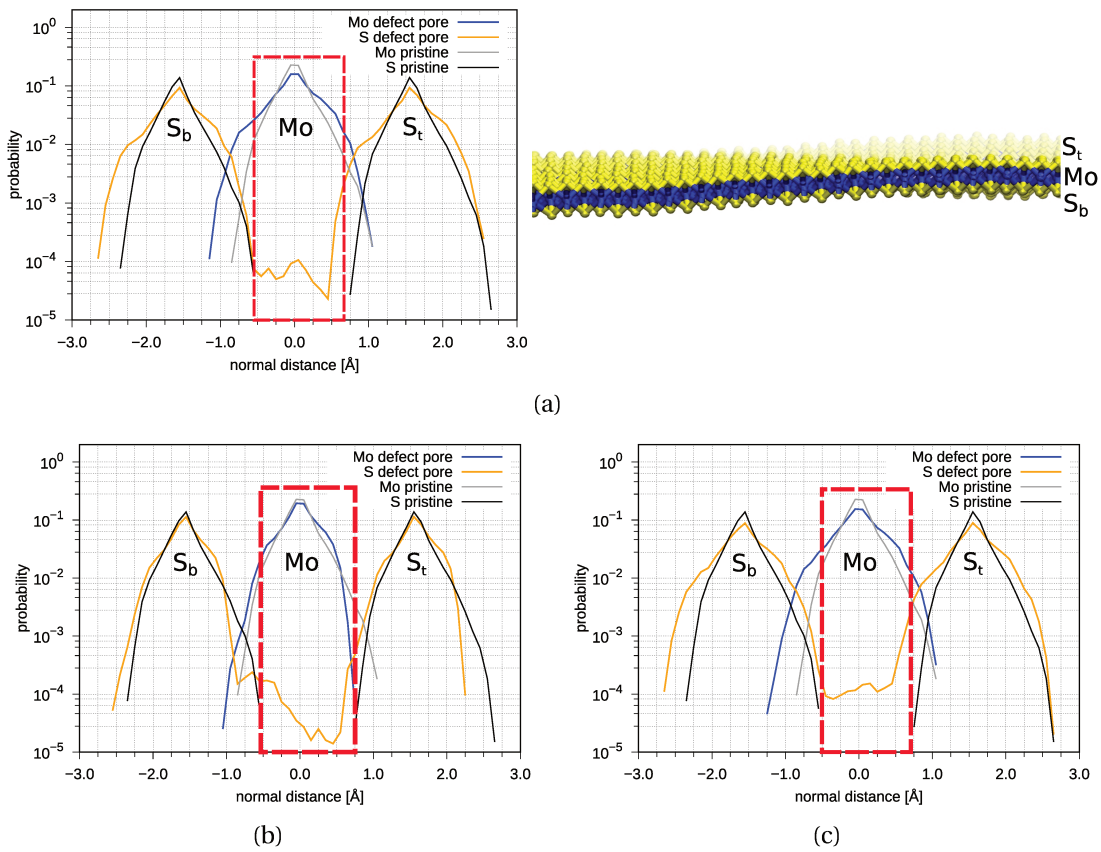

Figure 5.9: Probability distribution of Mo and S atoms in the normal direction of the membrane, for SL-MoS_2 defect pores presented in Fig. 5.6. Panel (a) corresponds to the pore 1 Mo + 5 S and also shows the atomic structure of this defect membrane, where S and Mo atomic planes are indicated. Panel (b) corresponds to the pore 2 Mo + 7 S, and panel (c) corresponds to the pore 4 Mo + 14 S. Blue line corresponds to Mo atoms and yellow line to S atoms from the membranes with defect pores. Gray and black line correspond to pristine Mo and S atoms, respectively. Labels S_b and S_t refer to bottom and top S atomic planes, respectively.

5.1.3 Impact of defect pores onto the connectivity of Mo and S atoms

To study the impact of defect pores onto Mo and S atom connectivity in SL-MoS_2 membranes, we calculated the probability distribution of interatomic distances, as shown in Fig. 5.10 for the defect pore 1 Mo + 5 S. Fig. 5.10 (a) shows distance distribution between Mo atoms of the membrane, where three well defined peaks correspond to the first, second and third Mo-Mo neighbors at ~3.2, ~5.5 and ~6.4 Å, respectively.

The results were also compared with a pristine membrane. We observed that peaks obtained from defect pore systems in Figs. 5.10 (a) slightly broaden in respect to the pristine membrane. Furthermore, a probability of finding Mo atoms between 4.5 and 5.6 Å distance is different from zero in the defect pore membrane, whereas is zero for the pristine one. The distance distributions between Mo-S and S-S atoms pairs were computed as well. Atomic reorganization in the pore region affects these interatomic distances and the atom connectivity, as evidenced in Figs. 5.10 (b) and (c). The presence of 1 Mo + 5 S defect pore in the membrane induces atomic fluctuations and alter the structure in such region, leading to the formation of a new Mo-S bond from one S atom that migrated to the Mo atomic plane.

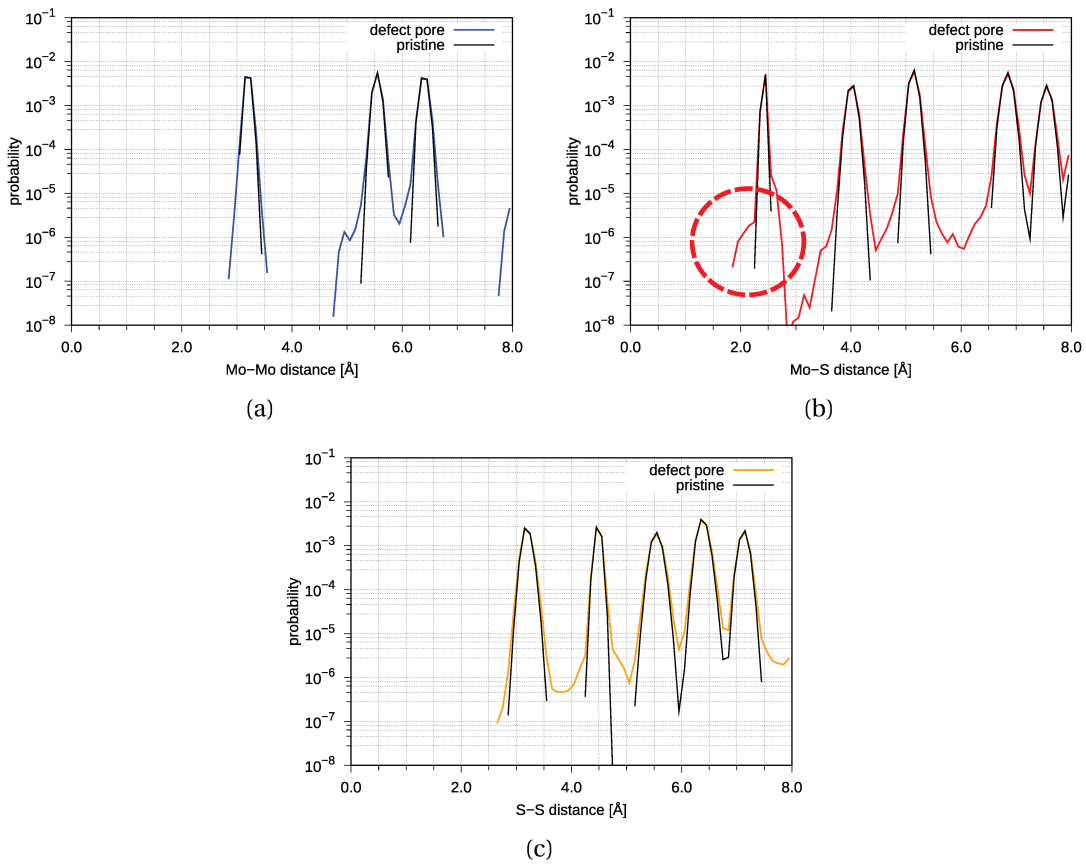

Figure 5.10: Probability distributions of (a) Mo-Mo, (b) Mo-S and (c) S-S atoms for the SL-MoS_2 defect pore 1 Mo + 5 S. Blue line corresponds to the Mo-Mo distance, red line to the Mo-S distance and yellow line to the S-S distance. Gray lines correspond to pristine membrane. Shorter Mo-S distance comes from the square formation as observed in Fig. 5.6 (a).

Figs. 5.10 (a) and (b) show a similar analysis for the 2 Mo + 7 S and 4 Mo + 14 S pores. According to the structures observed in Fig. 5.6, the pore 2 Mo + 7 S [Fig. 5.6 (b)] presents an important atomic reorganization, which is confirmed by the computed distance distributions. Here, the appearance of new peaks in the atom distance distributions is attributed to the fact that the membrane is more flexible in the pore region, thus atom connectivity tends to change along the MD simulation. For example, according to Mo-S and S-S distance distributions, we observed the formation of new Mo-S bonds from one S atom that migrated to Mo atomic plane (peak at 3.2 Å), and the formation of a S-S bond (peak at 2.0 Å). Although the largest defect pore (4 Mo + 14 S) does not present significant atomic reorganization and is the most stable pore structure, new Mo-S bonds are formed at shorter distances (< 2.0 Å). To conclude, changes in the hexagonal lattice are observed in the defect regions due to the S atoms migration and atomic reorganization, which are evidenced with the creation of squares and pentagons in the pore structure [Fig. 5.6].

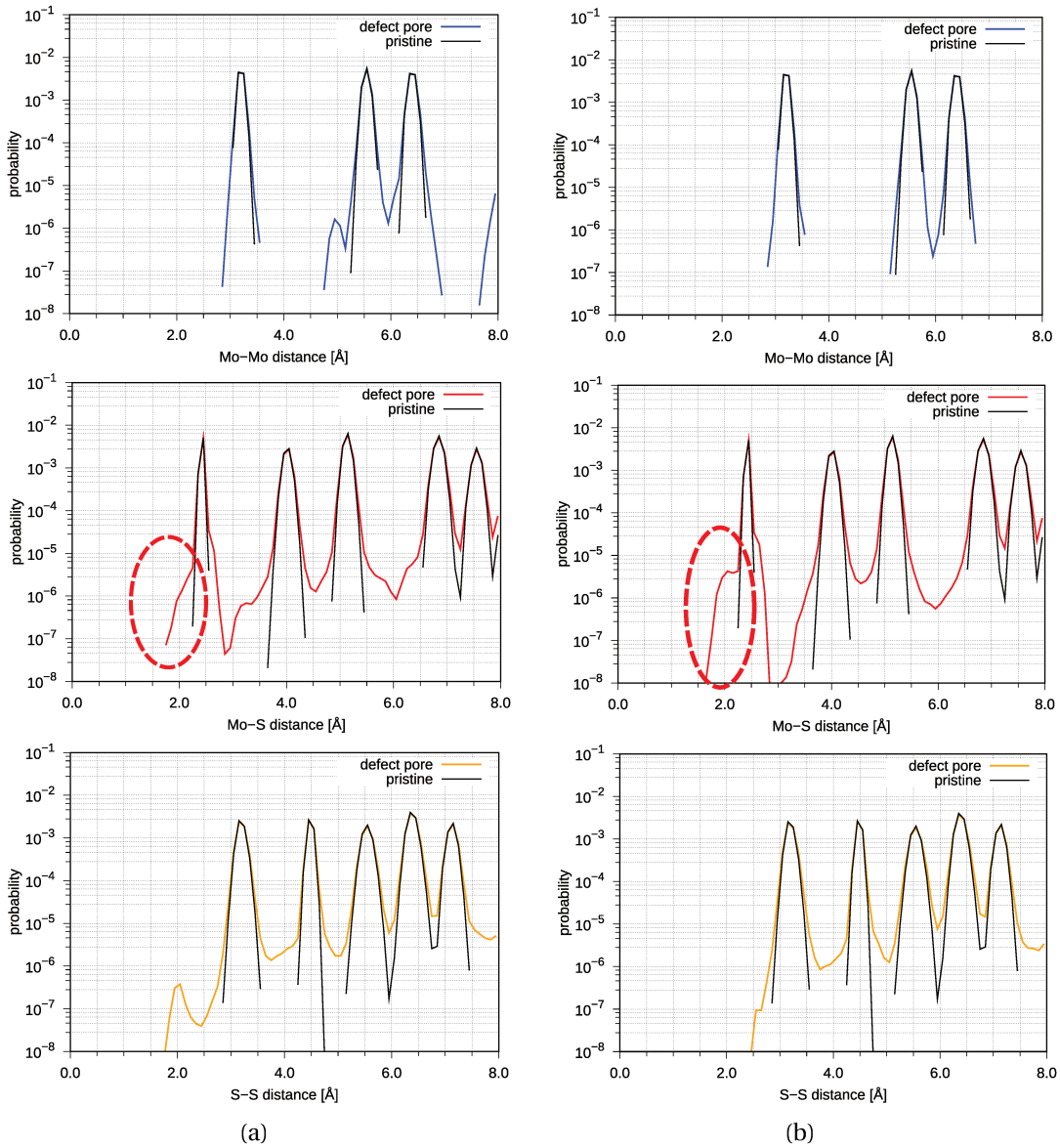

Figure 5.10: Probability distributions of interatomic distances for SL-MoS_2 defect pores (a) 2 Mo + 7 S, and (b) 4 Mo + 14 S. Blue line corresponds to Mo-Mo distance, red line to Mo-S distance and yellow line to S-S distance. Gray lines correspond to pristine membrane.

5.1.4 Surface area and estimation of sub-nm MoS_2 defect pores diameters

One difficult task for sub-nm MoS_2 defect pores structural characterization is to estimate the pore size, due to the fact that the pore shape is not trivial (see Fig. 5.6). One way to do this is by estimating the surface area of the pore, using the area formula of a polygon when the coordinates of its vertices are known. Such polygon is defined by the contour of the defect pore, where the vertices correspond to the (x, y)-in plane atomic positions of the pore atoms. Fig. 5.11 (a) shows the pore contour of the 1 Mo + 5 S pore, which is used for computing its surface area. The method for determining the area of the polygon consists in first, numbering the vertices in order, going either clockwise or counter-clockwise, starting at any vertex. The area is given by the formula:

$$S = \left| \frac{(x_1 y_2 - y_1 x_2) + (x_2 y_3 - y_2 x_3) ... + (x_n y_1 - y_n x_1)}{2} \right|, \tag{5.1}$$

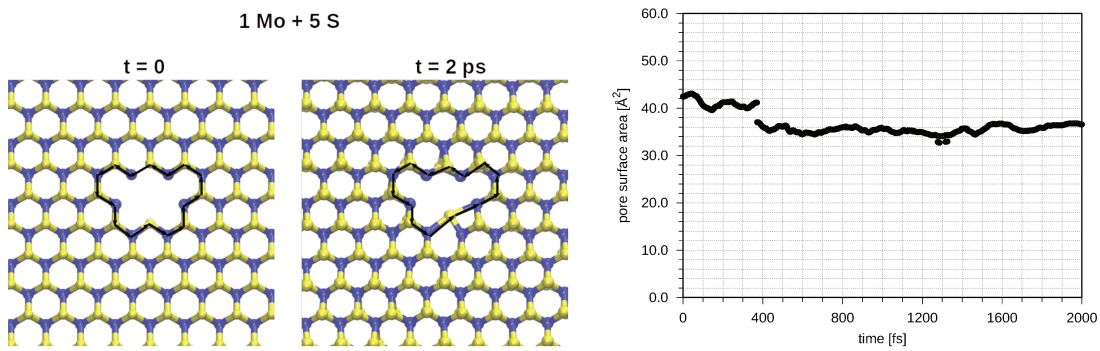

(c) (d)

Figure 5.11: (a) 1 Mo + 5 S MoS_2 defect pore and the representation of its contour (black lines), for its initial and final structure (t = 0 and t = 2 ps). (b) Surface area of the defect pore as a function of time.

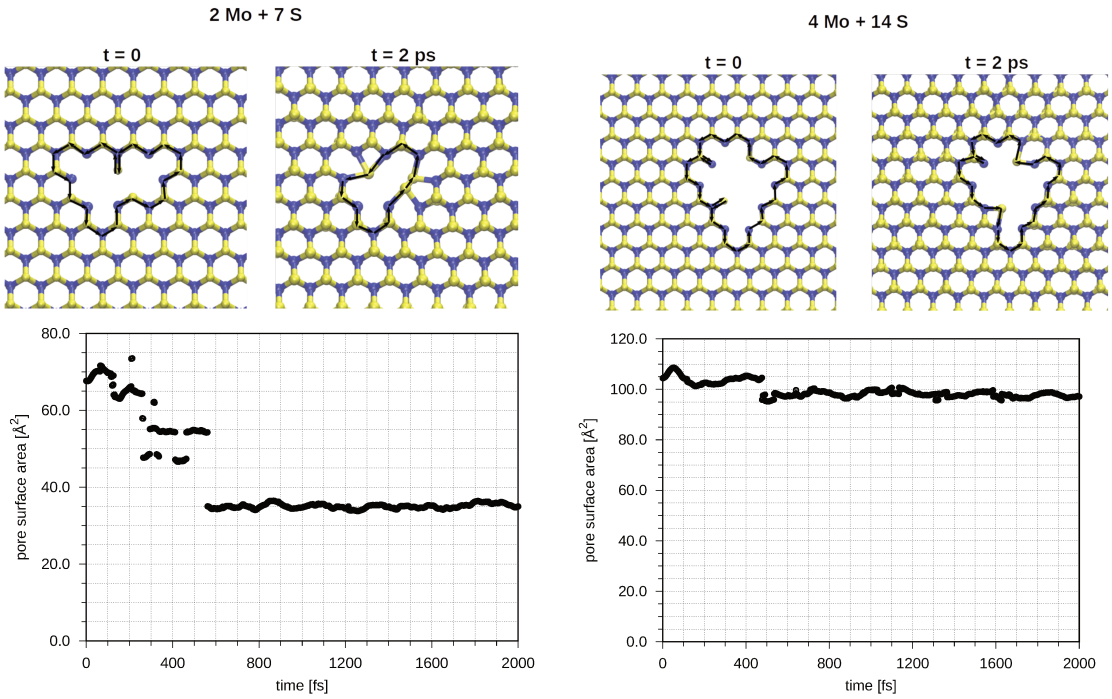

(a) (b)

Figure 5.12: Representation of the contour (black lines) in the initial and final structure (t = 0 and t = 2 ps), and surface area as a function of simulation time for SL-MoS_2 defect pores corresponding to (a) 2 Mo + 7 S, and (b) 4 Mo + 14 S.

where x_1 is the x coordinate of vertex 1 and y_n is the y coordinate of the nth vertex. Fig. 5.11 (b) shows the surface area of the pore 1 Mo + 5 S computed as a function of simulation time. Although the structure remains stable during MD simulation, a decrease of the surface area of ~ 12% is observed after t = 400 fs, the average value being ~ 36.060 Å^2. Figs. 5.12 (a) and (b) show the surface area calculated for defect pores 2 Mo + 7 S and 4 Mo + 14 S respectively. Large fluctuations before t = 600 fs simulations are observed for 2 Mo + 7 S pore, due to changes in its structure and atomic reorganization. After 600 fs, the pore structure remains stable, thus the surface area reaches an average value of ~ 35.059 Å^2. On the contrary, the largest defect pore presents less structural fluctuations along the simulation, where a decrease of ~ 6% of the pore surface area was observed after t = 500 fs simulation, and an average value of ~ 97.980 Å^2 was extracted.

Once surface areas S of defect pores were computed, we estimated the pore size by determining the diameter of the circumscribed circle, d_{MD}, inside each the corresponding polygons. Hence, the circle diameter is given by:

$$d_{MD} = \sqrt{\frac{4S}{\pi}}. \tag{5.2}$$

It is noteworthy to mention that experimentally, the pore size is estimated from TEM images, by measuring the surface area using *ImageJ* software [59]. In our work, values of the estimated diameters obtained for sub-nm MoS_2 defect pores from MD simulations and the corresponding experimental reference samples are indicated in Tab. 5.1. An increase of ~ 26%, ~ 10% and ~ 37% was observed for 1 Mo + 5 S, 2 Mo + 7 S and 4 Mo + 14 S pores, respectively in respect to experimental values. These differences are related to structural changes of the pore due to the dynamics of the systems.

defect nature	S [nm^2]	d_{MD} [nm]	d_{exp} [nm]
1 Mo + 5 S	0.36	0.68	0.50
2 Mo + 7 S	0.35	0.67	0.60
4 Mo + 14 S	0.98	1.12	0.70

Table 5.1: Pore surface area S, pore diameter determined from MD simulations d_{MD}, and pore diameter determined from experimental samples d_{exp}, for sub-nm SL-MoS_2 defect pores simulated using ReaxFF potential.

5.1.5 Atomic charges in MoS_2 defect pores

An important step in SL-MoS_2 defect pores characterization is also the examination of atomic Mo and S charges. Charge equilibration is an important feature of ReaxFF potential and partial charges of each atom change as it responds to changes of its chemical environment. Additionally, atomic partial charges are relevant properties from a chemical point of view, for further design and functionalization of MoS_2 porous membranes.

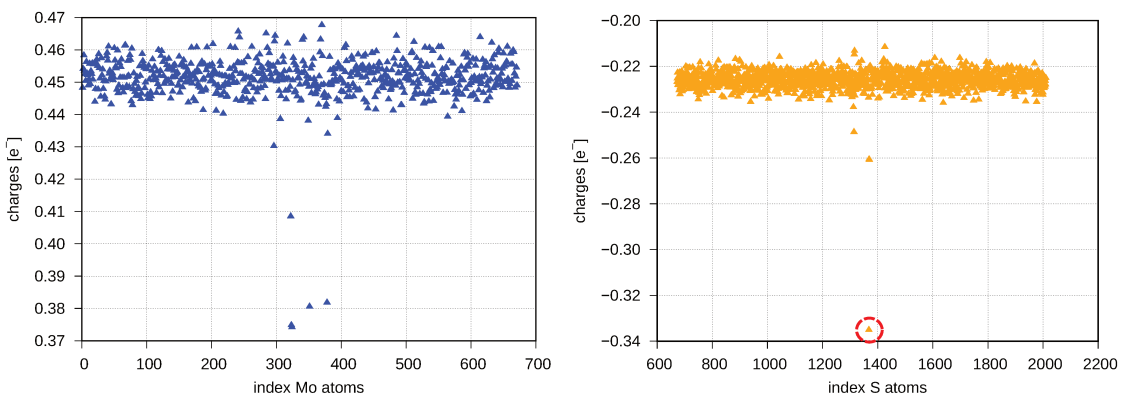

(a) (b)

Figure 5.13: (a) Mo charges as a function of the atom index. (b) S charges as a function of the atom index, for the the defect pore 1 Mo + 5 S. Data highlighted in red circle correspond to the partial charge of S atoms that migrated to the Mo atomic plane.

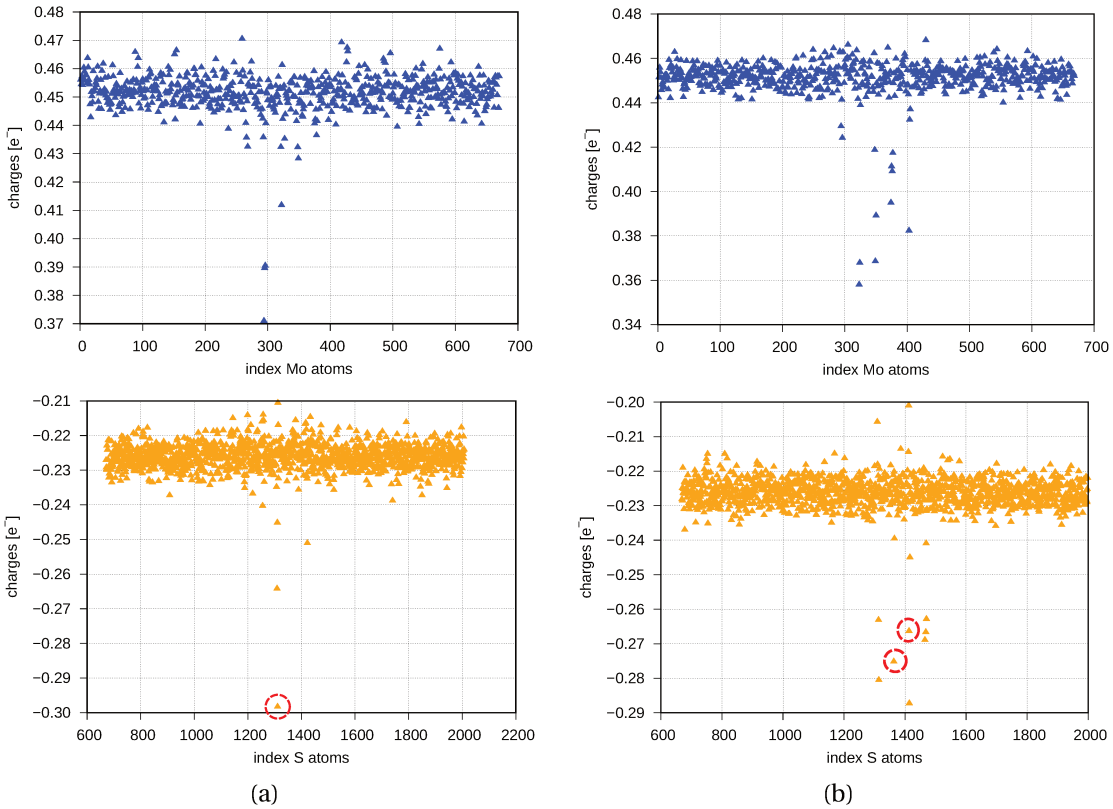

Figure 5.14: Mo and S charges as a function of the atom index. Panel (a) corresponds to the pore 2 Mo + 7 S, and panel (b) corresponds to the pore 4 Mo + 14 S. Data highlighted in red circle correspond to the partial charge of S atoms that migrated to the Mo atomic plane.

Atomic partial charges of Mo and S atoms from 1 Mo + 5 S porous membrane (Figs. 5.13 (a) and (b)) indicate that for atoms located in the pore and its vicinity (with unbalanced bonds), charges are smaller than in bulk MoS_2. Partial charges of the rest of Mo atoms in the membrane fluctuate between 0.44 and 0.47 e^-, and between -0.24 and -0.21 e^- for S atoms. For all defect pores simulated here, Mo atoms charge in the defect region (0.37 e^-) presented a change of ~ 24% respect to atoms far from the pore. S atoms on the contrary, presented a maximum change of ~ 34% (~ −0.34 e^- for 1 Mo + 5 S defect pore) to ~ 25% (~ −0.30 e^- for both defect pores 2 Mo + 7 S and 4 Mo + 14 S). Fig. 5.13 (b) shows for example, the partial charge corresponding to the S atom [enclosed in the red circle of Fig. 5.6 (a)] that migrated to the Mo atomic plane in the pore structure. The same behavior was observed for defect pores 2 Mo + 7 S and 4 Mo + 14 S, as indicated in Figs. 5.14 (a) and (b).

5.2 MoS_2 defect pores interacting with ethanol molecules: towards pore functionalization

In order to explore the feasibility of MoS_2 pores functionalization, we performed MD simulations of sub-nm defect pores in presence of ethanol molecules with ReaxFF potential. Atomic structure of the system after 100 ps equilibration is shown in Fig. 5.15 for 4 Mo + 14 S defect plus ethanol molecules.

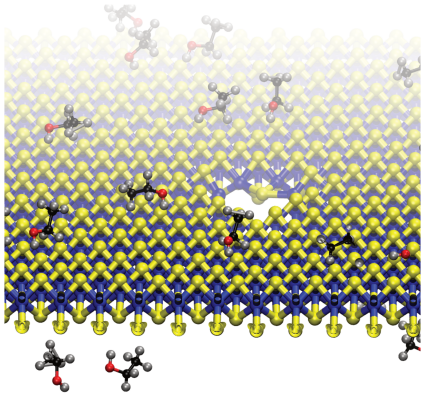

Figure 5.15: Atomic structure of 4 Mo + 14 S pore defect plus ethanol molecules, after 100 ps equilibration. Atoms colored in black, red and silver represent carbon, oxygen and hydrogen from ethanol.

Fig. 5.16 shows defect pores and ethanol molecules from snapshots extracted from MD run, at $t = 10$ ns. The corresponding atomic structures qualitatively show that overall ethanol molecules do not react with Mo and S atoms from defect pore membranes during production runs of 10 ns [Figs. 5.16]. However, qualitative observations from the atomic structure of 4 Mo + 14 S defect pore plus ethanol show that one ethanol molecule near the defect region, might dissociate into CH_3, CH_2 and OH. Also, we observed the possible formation of a S-OH bond resulting from the dissociated ethanol molecule that approached to the pore. We note that, although Yilmaz et al. [87] already observed epoxy dissociation at 700 K, dissociation of ethanol observed at room temperature as in the present work is not really expected. In fact, the reason of such dissociation is not yet clear since we should not observe ethanol dissociation at room temperature. It is an artifact that needs to be clarified before performing extensive MD simulations and the corresponding analyses of this system. In addition, we do not observe reaction between ethanol and pore defects, since defect regions are not filled with ethanol molecules.

Finally, more simulations with new initial conditions, larger number of ethanol molecules, higher temperature, different nature of defects, etc, are necessary to confront the results presented in this section and to study chemical reactions between organic molecules such as ethanol and MoS_2 membranes. We point out also that the improvement of the results presented here constitute a step forward to MoS_2 porous membranes functionalization from a computational point of view, and their design for biosensor and molecular selectivity applications.

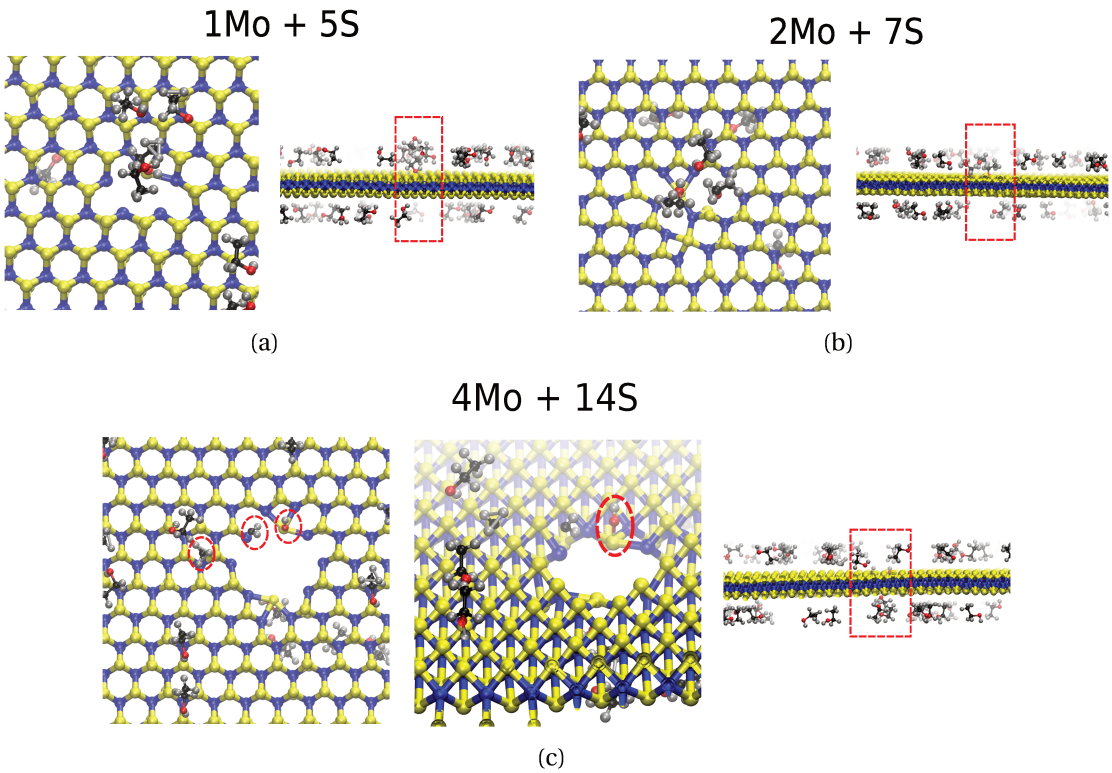

Figure 5.16: SL-MoS_2 defect pores and ethanol simulated using ReaxFF potential from all-atom MD simulations. The different defect pores and ethanol are presented in (a) 1 Mo + 5 S, (b) 2 Mo + 7 S, and (c) 4 Mo + 14 S. Highlighted regions indicates where defect pores are and show ethanol molecules close to the pore.

5.3 Estimation of ionic conductance performance of MoS_2 defect pore membrane

The increasing ability to fabricate MoS_2 pores made of atomic defects has opened new possibilities of corroborating ionic conductance performances and molecular transport properties at the sub-nm scale. Recently, experimental works on ionic conductance measurements in sub-nm single pores and porous membranes with defects distributions have been reported [59, 165] (see Fig. 5.3).

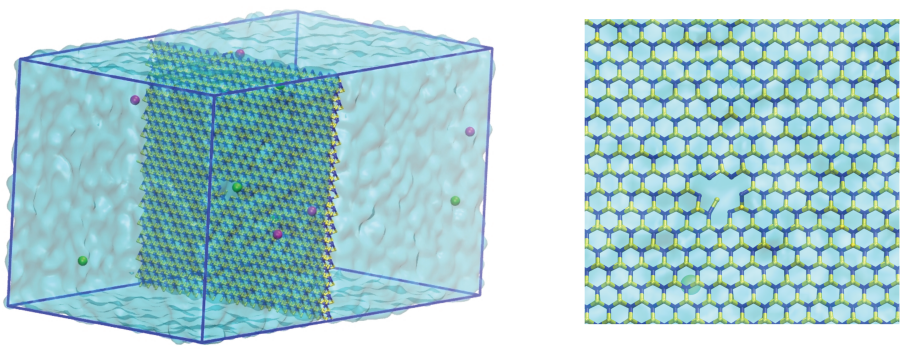

Figure 5.17: Simulation box of $L_x \times L_y \times L_z = 7.5 \times 7.5 \times 15.0$ nm^3 containing SL-MoS_2 sub-nm defect pore 1 Mo + 5 S and a 1 M KCl electrolyte. The system was simulated using a combination of ReaxFF potential for the porous membrane and LJ plus Coulomb potentials for the KCl electrolyte.

Moreover, the creation of nanoporous membranes containing large distribution of angstrom-size pores is now possible using aberration-corrected scanning transmission electron microscopy (AC-STEM) technique, as shown in Thiruraman's experimental work [59].

We discussed in Chapter 2 (page 47) ionic the transport of a KCl electrolyte through MoS_2 circular nanopores with diameters between 1 and 5 nm and presented their corresponding conductance performances. In the present chapter, we estimated ionic conductance performance of a MoS_2 defect pore membrane (1 Mo + 5 S defect). NEMD simulations were performed using voltages $V = 0$, 1.0, 2.0, 3.0 and 4.0 mV in NVT ensemble during 10 ns. Ionic current through the defect pore was computed from Eq. 3.2. Values of ionic current were then determined from simple moving average of $I(t)$ signals during each 10 ns MD run (see Fig.5.18).

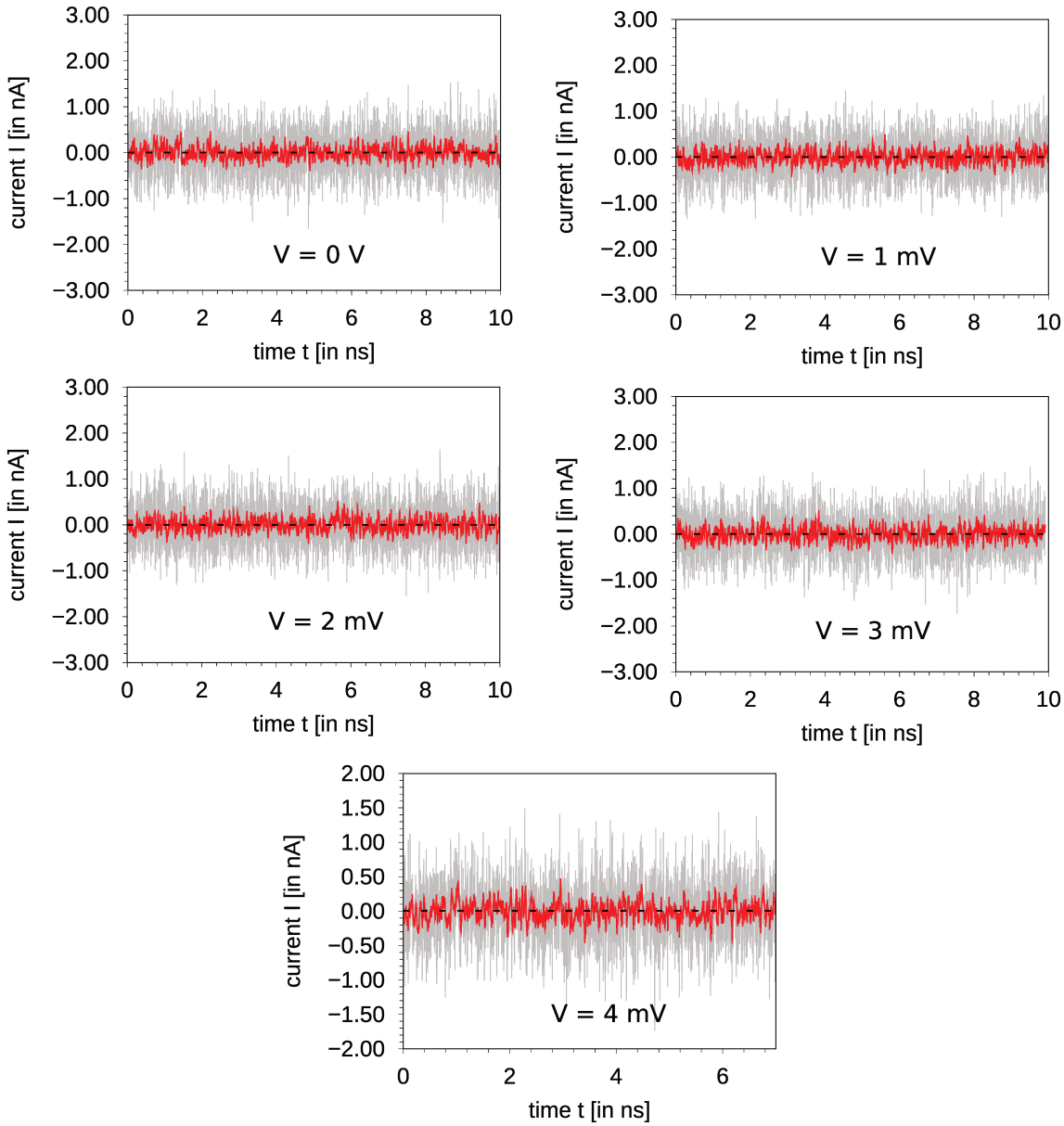

Figure 5.18: Variations of the ionic current as a function of the simulation time $I(t)$ depicted by the gray line, with the respective SMA represented by the red line, for the 1 Mo + 5 S pore defect in SL-MoS_2, where $d_{MD} = 6.776$ Å, for voltages from $V = 0$ to 4.0 mV.

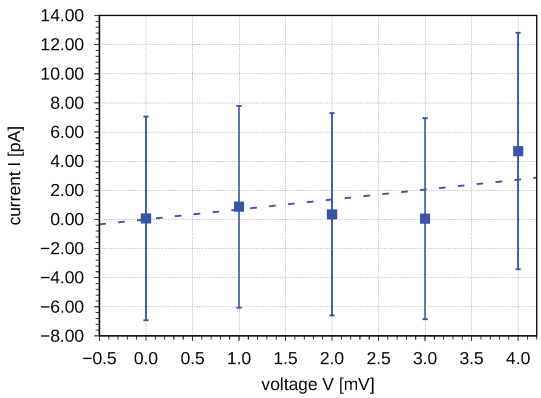

Figure 5.19: Current-voltage $I-V$ characteristic for the 1 Mo + 5 S pore defect in SL-MoS_2 with d_{MD} = 0.68 nm, from 0 to 4.0 mV. Error bars are computed from the $I(t)$ fluctuations standard error (Eq. 3.3).

The $I-V$ characteristic plot for 1 Mo + 5 S defect pore is shown in Fig. 5.19. The value of the ionic conductance G_0 obtained from the linear fitting to Eq. 3.4 is G_0 = 0.68 nS. Although we reported previously that G_0 obtained for a critical diameter of d = 1.0 nm is around 0.7 nS [59, 60], the later defect pore of size d_{MD} = 0.68 nm slightly still conducts ions.

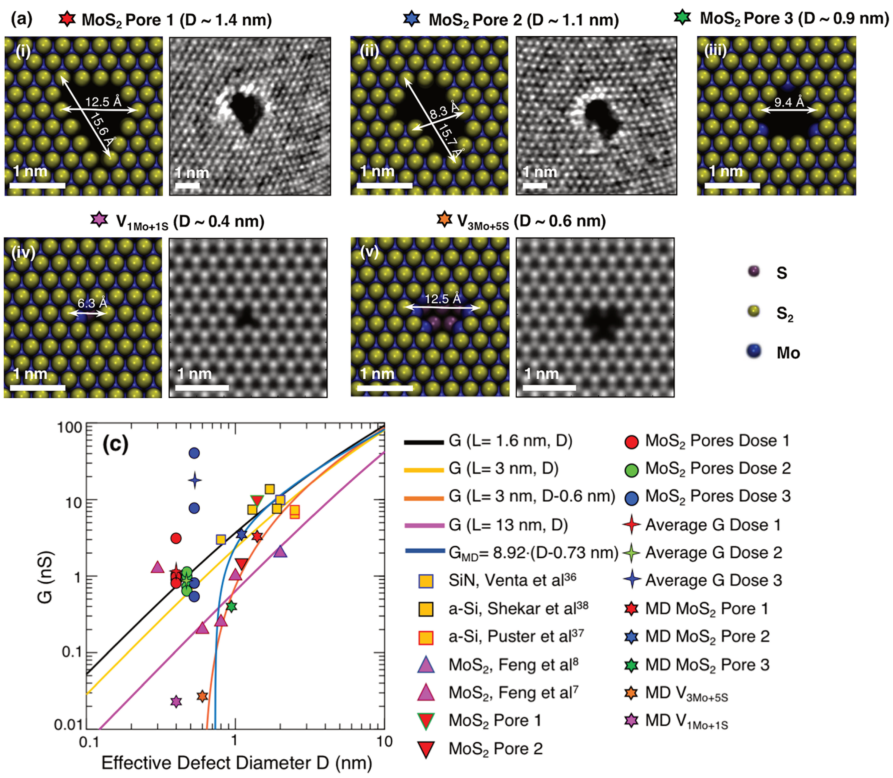

Figure 5.20: AC-STEM images of individual MoS_2 pores: (i) pore 1 and (ii) pore 2 with effective diameters of ~1.4 and 1.1 nm, respectively. Corresponding all-atom structures used in NEMD simulations are presented aside. Mo, S_2, and S atoms are shown in blue, yellow, and purple spheres, respectively. Simulations for vacancy-defects caused by removing (iv) 1 Mo + 1 S atoms (V_{1Mo+1S}), and (v) 3 Mo + 5 S atoms (V_{3Mo+5S}). Ionic conductance G as a function of pore diameter obtained experimentally for MoS_2 nanoporous membranes and from reported works on SiN, a-Si and MoS_2 nanopores. Black, yellow, orange and pink lines represent the continuum model from Eq. 3.8. Blue line represents the linear model from Eq. 3.10 obtained from MD simulations results. Figure extracted from Ref. [59].

Open pore conductance of SL-MoS_2 defect pore membrane was compared with experimental data from Ref. [59], shown in Fig. 5.20. According to Thiruramn et al. Ref. [59], conductance obtained for single pore devices with diameter $d \approx 0.3$ to 2.0 nm (MoS_2 Pore 1 and MoS_2 Pore 2) was $G_0 \approx 0.1$ to 10 nS. For porous membranes devices with average diameter $d \approx 0.5$ nm (MoS_2 Pores Dose 1, MoS_2 Pores Dose 2 and MoS_2 Pores Dose 3), conductance value was $G_0 \approx 1$ to 100 nS. Conductance of defect 1 Mo + 5 S was compared as well with MD simulations data from Ref. [59] (Fig. 5.20), where pores were simulated using SW potential. In Thiruraman's et al. work [59], pores made of defects V_{1Mo+1S} ($d \approx 0.4$ nm) and V_{3Mo+5S} (≈ 0.6 nm) exhibited negligible conductance $G_0 \approx 0.02 - 0.03$ nS, confirming the fact that pores made of defects smaller than ~ 0.6 nm do not conduct ions as shown experimentally. An interesting remark is that, although experiments show that pores made of defects smaller than ~ 0.6 nm present negligible conductance, nanoporous devices comprised of several defects (with pore density $\sim 1 - 4$ pore/nm^3), display an enhancement of conductance, which could be related to variations in atomic structure when they are introduced in the salt solutions [59]. To confirm this, we could perform analysis of structural properties of defect pores in presence of solvent. Also, this can be explored from a computational point of view by performing MD simulations of these systems to subsequently guide experiments.

In summary, we performed MD simulations of vacuum sub-nm MoS_2 pores modeled using ReaxFF potential, showing that defect pores present high structural stability during equilibration simulations at room temperature. Structural characterization of defect pores showed that atomic reorganization occurs during MD simulations, leading to changes in the pores shape. Pore surface area and pore size were also estimated from MD simulations for further analysis, such as the relationship between pore size and pore conductance performance. Sub-nm MoS_2 pores were simulated also in presence of ethanol molecules in order to study the reactivity of vacancy sites from defect pores and ethanol. Qualitatively we observed that no reactions occurred between ethanol and MoS_2 defects. Furthermore, although we observed the dissociation of one ethanol molecule located near 4 Mo + 14 S defect region, this is not an expected behavior at room temperature. The origin of this results must be identified. For this reason, more simulations with new initial conditions are needed to improve the quality of the current results. Last but not least, NEMD simulations were carried out to study the effect of ReaxFF potential onto the ionic conductance of MoS_2 defect porous membranes. We observed that for a defect pore of ~ 0.68 nm, the conduction of ions is still possible. However, more simulations with different salt concentrations and higher voltages are needed to obtain a full picture of defect pores conductance performances. In general, MD simulations of MoS_2 nanoporous membranes functionalization and closer to experimental conditions could provide a better insight into the creation of new hybrid materials, for the design of more efficient devices.

Chapter 6

General conclusions

In the present thesis, we performed all-atom MD simulations to investigate the feasibility of using ultra-thin MoS_2 nanoporous membranes for protein sequencing from the measurement of ionic current variations due to its translocation through such a pore. As discussed in Chapter 3, in order to investigate ionic transport properties of MoS_2 nanopores, we characterized the ionic conductance of a 1 M KCl electrolyte through different nanopores (open pore systems) without the presence of any biomolecule from NEMD simulations.

We studied open pore systems made of nanopores with diameters ranging from 1.0 to 5.0 nm and membrane thicknesses from single to five-layers. The study was carried out by investigating at the atomic level the interactions between MoS_2 nanopores and the KCl electrolyte. Interfacial interactions of water with MoS_2 membrane surface evidenced its hydrophobic behavior, as revealed by the water structure modification from the bulk. The water distribution of the MoS_2 surface allowed us to extract effective geometrical parameters of the membrane, i.e. effective membrane thickness h^* and effective pore diameter d^*. As an example, we found that in SL-MoS_2, h^* is ~ 3 times larger than the thickness value h (calculated from the atomic structure). On the contrary, for a 2.0 nm diameter pore, effective diameter d^* is $\sim 18\%$ smaller than the diameter value d (calculated from the atomic structure). This could be attributed to the presence of Mo hydrophilic atoms that decrease the hydrophobic influence of the membrane in the pore radial direction. Membrane effective parameters were used to estimate the ionic conductance as a function of nanopore dimensions. Moreover, the analysis at the atomic scale of the radial ionic concentration inside SL-MoS_2 nanopores provided information about its impact on conductance drops measured during experiments. More precisely, blockage ionic conductance is ~ 0 when a biomolecule that translocates into the nanopore displaces the ions near the the pore edges. This analysis is useful to determine the most efficient pore size to sequence a molecule according to its size.

The study of the open pore systems was followed by computing the ionic conductance of MoS_2 nanopores from $I-V$ characteristics, by monitoring the time-dependent ionic current in the nanopore for each applied voltage (between 0 and 3.0 V). The ultra-thin and symmetric nature of MoS_2 nanoporous membranes showed linear $I-V$ dependence for low voltages regime (between 0 and 1.0 V). Thus, $I-V$ curves allowed us to extract open pore conductance G_0 for MoS_2 nanopores with different diameters and thicknesses. By comparing ionic conductance values between the different nanopores, we observed that it decreases as the pore diameter decreases, where $d = 1.0$ nm is a critical diameter for MoS_2 nanoporous membranes. Here, G_0 value for $d = 1.5$ nm is ~ 6 times larger than G_0 for $d = 1.0$ nm. Multi-layer MoS_2 nanopores conductance performances

were characterized as well for a constant pore diameter (d = 2.0 nm). By comparing G_0 values between SL-MoS_2 and 2L-MoS_2, we observed a decrease of ~ 35% by increasing the thickness by a factor of 3. However, no significant difference was observed by increasing the membrane thickness from 2L- to 3L- (a decrease of ~ 13%). This implies that 3L-MoS_2 could be reasonable option for SSN sequencing devices since manipulating thicker objects at the nanoscale might be easier. Regarding the thickest nanoporous membrane, a decrease of ~ 50% was observed when thickness increases by a factor of 9. Multi-layer configurations may be an interesting alternative depending on the biomolecule size, due to the well established translocation signal and geometry of the nanopore.

We validated our results of ionic conductance through MoS_2 nanopores by comparing these values with the classical macroscopic model of conductance of nanopores used in experiments. The comparison between conductance values obtained from MD data and the classical model showed that G_0 values are overestimated by the classical model. Thus, we proposed a linear model of conductance that would better fit MD data, from which we determined that no current can be detected below a critical diameter ~ 0.7 nm. The results were in agreement with recent experimental data reported [59]. Additionally, we explored in more detail ionic transport properties of MoS_2 nanopores based on previous theoretical works, in which the source of the failure of the classical model is explained in terms of its dependency on bulk ionic conductivity σ_{bulk}. In the present thesis, we discussed the ionic conductivity and pore diameter dependency, showing that conductance model validity was restored for SL-MoS_2 sub-5 nm pores if $\sigma_{pore}(d^*)$ is used instead of σ_{bulk}. From equilibrium MD simulations, we developed a modified model of ionic conductance by considering that conductivity can be expressed as in terms of the product of concentration and electrical mobility of ionic species of the electrolyte. We showed that the behavior of the KCl electrolyte deviates by 50% from bulk properties for diameters below 2.0 nm. This is attributed to the fact that at the nanoscale, ions are confined in spaces whose dimensions are of similar sizes to that of the ionic radii. Thus, ionic concentrations, mobilities and hydration are different from their bulk counterpart.

To gain further insight into the origin of the deviations of ionic conductivity $\sigma_{pore}(d^*)$ at the nanoscale, we expressed the problem in terms of concentration and mobility partition coefficients. On one hand, concentration partition coefficient is related to the difference between the free-energy associated to an ion specie in the pore and in bulk electrolyte, being dependent on the pore size as well. On the other hand, we developed and empirical expression for the mobility partition coefficient where we observed that ions mobilities decrease by 70% through a pore of 1.0 nm diameter. We expressed the classic model of conductance in terms of $\sigma_{pore}(d^*)$ and obtained an improved model of ionic conductance for SL-MoS_2 sub-5 nm pores. By comparing the improved model of conductance with G_0 values extracted from the literature, we observed that our model is in very good agreement with simulations and experimental data. Furthermore, it can be used with nanopores made of other TMDC materials, such as WS_2. We showed that the model in terms of $\sigma_{pore}(d^*)$ can be used to interpret experimental data and is essential to understand the transport properties of pores of sub-5 nm diameter. Understanding of such transport properties is necessary for the design of SSN devices for DNA and protein sequencing via translocation technology using transverse applied voltage.

Once we characterized ionic conductance of open pore systems, we investigated biomolecule translocation system (nanopore + biomolecule). In Chapter 4, we proposed an alternative method to translocate proteins by using tags made of positively or negatively charges amino acids such as

lysine residues covalently bonded to the N- or C- terminal part of proteins. We started the study by first characterizing the impact of membrane flexibility onto the dynamics of peptide translocation. RMSD and RMSF results showed that fluctuations of the membrane atoms are dependent on their radial position relative to the center of mass of the pore and they increase when the peptide is translocating through the pore. We could verify at the atomic level that the dynamics of the nanoporous membrane plays a role in the diffusion of the biomolecule on the membrane surface and in its translocation process.

The next step was the investigation of the translocation of peptides made of lysine residues through SL-MoS_2 nanopores from non-equilibrium MD simulations. We performed MD simulations of the full translocation process of lysine residues through SL-MoS_2 nanopores of diameter d = 2.0 nm, which constituted a critical step before the study of poly-lysine tagged proteins. To study the translocation of a single amino acid through SL-MoS_2 nanopores, we performed 2 MD runs with different initial conditions. We observed that in both MD runs the threading process was comprised of 3 parts: first, the peptide diffused in bulk solvent above the membrane. Second, adsorption on the MoS_2 surface occurred due to the interaction of the positively charged amino acid with the electric field. Third, the peptide threaded into the pore (near the edge) leading to translocation through the nanopore. We observed also that the side-chain of the lysine residue was aligned parallel to electric field direction and translocated first in the pore, followed by its backbone. In both MD runs translocation of lysine residue lasted $\tau_{trans.}$ = 0.4 ns and the conductance fluctuations during and at the end of translocation process were almost indiscernible, being the average conductance detected in both cases $\overline{\Delta G} \sim 0.7$ nS (MD run 1) and $\overline{\Delta G} \sim 0.9$ nS (MD run 2). Translocation of lysine dipeptide through SL-Mo_2 nanopores was studied by performing 3 MD runs with different initial conditions. In all three 3 MD runs, we observed that a threading process similar to that of single lysine residue occurred for lysine dipeptide. We observed also that dipeptide translocation occurred in a two-step process: one lysine residue entered the pore with the side chain pointing in the direction of the electric field, and the next lysine residue entered into the nanopore and the whole peptide left the pore after translocation. In MD run 2 translocation occurred during $\tau_{trans.}$ = 1.0 ns and an average conductance drop of $\overline{\Delta G} \sim 0.7$ nS was detected. However, MD run 1 and 3 showed that the translocation time was extremely fast (translocation time decreased to $\tau_{trans.}$ = 0.4 ns) and no discernible drops associated to the process were detected due to the large fluctuations on the conductance signals.

As we previously discussed, ionic conductance performance of nanoporous membranes does depend on the geometry and size of the pore. Thus, a possibility to improve the resolution of ionic conductance drops associated to translocating biomolecule is by changing the nanopore size and geometry in order to slow down the translocation process and to increase the residence time of the peptide inside the pore. To achieve this goal, we modified the geometry of the membrane system: first, reducing its diameter from 2.0 to 1.5 nm, and second by increasing its thickness from single to bilayer MoS_2. We studied dipeptide translocation through 1.5 nm SL-MoS_2 nanopores. In this new geometry, we observed a two-step process translocation similar to that observed for the nanopore with d = 2.0 nm diameter. The N-terminal entered the pore aligned in the direction of the electric field, and the C-terminal threaded into the pore, leading to a full translocation. Contrary to the translocation of lysine dipeptide through SL-MoS_2 pore of d = 2.0 nm, translocation occurred closer to the center of the pore during $\tau_{trans.}$ = 2.8 ns, being 3 times larger than the one detected for 2.0 nm pore. The corresponding drop average $\overline{\Delta G} \sim 1.4$ nS was two times larger than the one detected by the 2.0 nm pore. We note that conductance signal with this pore geometry does not

allowed to detect the passage of two residues separately. Dipeptide translocation through a bilayer-MoS_2 nanopores was explored as well. We observed again that translocation occurred in a two-step process (N-terminal lysine entered into the pore and it was followed by the C-terminal), and this time we were able to detect two traces of the signal associated the passage to each lysine residue. Translocation time in this case was $\tau_{trans.}$ = 18 ns (18 times larger than for SL-MoS_2), which means that we were able to reduce the translocation speed with this pore geometry. As pointed out in Chapter 4, the cost of increasing the signal resolution in time domain by increasing the thickness of the nanopore is that the spatial resolution is reduced. Furthermore, this result represents a step forward for the design of protein sequencing devices. Here we showed that the key to improve the efficiency of the sequencing sensor for single residue detection in terms of time and spatial resolution, involves a proper combination between the diameter and thickness fo the nanopore according to the size of the biomolecule.

Last but not least, we examined the possibility of translocating proteins by attaching tags made of charged amino acids (lysine residues, for example) to functionalize N- or C- terminal of the protein. We tested this method with the five residue peptide Met-Enkephalin (YGGFM sequence) for the best performing membrane extracted from the previous simulations (SL-MoS_2 with d = 2.0 nm). We attached poly-lysine tags of different lengths to Met-Enkephalin, from 1 lysine residue (1K) to 5 lysine residues (5K) and we performed several MD runs for each of the synthetic peptides created here. Results extracted from the different MD runs for YGGFM-2K, YGGFM-3K, YGGFM-4K and YGGFM-5K peptides, showed that after peptide diffused in bulk solvent and on the MoS_2 top surface, it threaded into the pore by a step-wise process. The sequence that characterized the translocation events started with the threading of the C-terminal part of the peptide, which corresponds to the poly-lysine tags. Thereafter, M and F residues entered the pore and finally the two G residues translocated extremely fast dragging the N-terminal residue. Y residue and the whole peptide, left the pore and started to diffuse at the MoS_2 bottom surface. We detected drops of conductance associated to the translocation events. The detection of lysine residues at the C-terminal, Y and G residues at the N-terminal of the peptide were observed, although we did not detect single amino acid conductance signals. The maximum average conductance drops between specific events and the open pore conductance observed during translocation are 1.1 nS (YGGFM-2K for MD run 2), 1.7 nS (YGGFM-3K for MD run 2), 2.6 and 1.7 nS (YGGFM-4 K for MD run 1 and 2) and 1.4 nS (YGGFM-5K for MD run 1). The translocation time observed for the different peptides correspond to: YGGFM-2K ($\tau_{trans.}$ = 111 ns for MD run 2), YGGFM-3K ($\tau_{trans.}$ = 158 ns for MD run 2), YGGFM-4K ($\tau_{trans.}$ = 15 and 16 ns for MD run 1 and 2, respectively) and YGGFM-5K ($\tau_{trans.}$ = 71 ns for MD run 1).

From the presented results, we showed that the addition of poly-lysine tags increase the global charge of the peptide and facilitates the threading of the protein through the nanopore due to interactions between the charged biomolecule and the electric field. We showed also that poly-lysine tags translocate first through the nanopore, followed by the specific motifs of the protein in a step-wise manner. In this way, we determined that the chemical composition of a translocating biomolecule does affect the guidance process. Indeed, we confirmed that it is possible to detect the passage of a polypeptide and single residue amino acids using conductance signal.

Finally, the study of MoS_2 sub-nm defect pores discussed in Chapter 5, was performed by characterizing the dynamics and structural properties of pore defect membranes in vacuum simulated using reactive potential ReaxFF. We studied different defect pores labeled as the nature

of the removed atoms (1 Mo + 5 S, 2 Mo + 7 S and 4 Mo + 14 S). We observed from the corresponding atomic structures that sub-nm defect pores here simulated presented changes in pore shape, mainly attributed to atomic reorganization in the pore region. Structural fluctuations of membrane atoms corresponding to the system relaxation were quantified and we showed that such fluctuations depend on their radial position relative to the center of mass of the pore. Structural modifications of defect membranes confirmed also the presence of S atoms in Mo atomic plane due to their migration along the simulation. In addition, we observed changes in Mo and S atoms connectivity in the pore region, evidenced with changes in the hexagonal lattice in the pore mouth. We estimated the surface area and pore size of defect pores and compared these values to the corresponding experimental reference samples. An increase of $\sim 26, 10$ and 37% of the pore size extracted from MD data was observed due to the structural changes of the pore and the dynamics of the system. Furthermore, we examined atomic partial charges in MoS_2 defect pores. We observed that due to unbalanced bonds in the defect region, pore atoms presented smaller partial charge as a consequence of non-shared electrons.

We simulated MoS_2 membranes with defect pores in presence of ethanol molecules to explore the feasibility of MoS_2 pores functionalization. Qualitative observations of the atomic structures showed that in general, ethanol molecules did not interact with Mo and S atoms from defect pore membranes. However, we observed from atomic structure of defect 4 Mo + 14 S that one ethanol molecule unexpectedly dissociated near the pore region. However, this phenomenon is not expected in the current simulations conditions, since at room temperature the energy should not be sufficient to break ethanol bonds and could be produced by simulation artifacts. More simulations with different initial conditions, more ethanol molecules and deeper analysis about the impact of MoS_2 defects on ethanol, are needed in order to get a full understanding of chemical reactions between MoS_2 and organic molecules.

Lastly, we studied ionic conductance performance of 1 Mo + 5 S ($d = 0.68$ nm diameter) defect from NEMD simulations for voltages between $V = 0$ and 4.0 mV. Open pore conductance value obtained from $I - V$ characteristics showed that 1 Mo + 5 S defect pore slightly conduct ions ($G_0 \approx 0.68$ nS). Comparison with experimental data extracted from the literature indicates that 1 Mo + 5 S defect pore conducts within the range of single pore devices with diameter $d \approx 0.3$ to 2.0 nm ($G_0 \approx 0.1$ to 10 nS). However, MD data extracted from literature for defect pores simulated with Stillinger-Weber potential showed that pores of $d \approx 0.4$ and 0.6 nm exhibit negligible conductance ($G_0 \approx 0.02 - 0.03$ nS). This difference in conductance could be attributed to structural changes of the defect pore simulated using ReaxFF potential. We remark that more simulations with different initial conditions, different salt concentrations and higher voltages are needed for a full characterization and understanding of conductance performance of pores with sub-nm sizes.

To conclude, it is convenient to address some perspectives to continue this research work:

- First, a more general expression of the improved open pore conductance model could be obtained by investigating the dependency of the pore ionic conductivity σ_{pore} as a function of the membrane thickness h^*. The idea is to test the result with thicker 2D nanoporous membranes such as SiN_X, heterostructures made of graphene, hBN, glass nanopores and other TMDC materials. Moreover, ionic transport properties of MoS_2 could be also studied for different salt concentrations and different electrolytes such as NaCl, $MgCl_2$ or pure ionic liquids (ILs), which are used to slow down the fast permeation events through nanopores. Translocation speed could be slowed down with the use of other methods such as the use of viscosity gradients of the solvent, as shown experimentally in the literature. This technique,

could be combined with a proper pore geometry in order to optimize the conductance signal detection. Time series analysis techniques such as construction of effective free-energy landscape, permutation entropy or detrended fluctuations from time-series of biomolecule translocation through SSN could also be used to investigate hidden information in the signal fluctuations during translocation process. The idea is to decipher the fingerprints of the translocation of each residue in polypeptide translocation from conductance signals.

- It has been demonstrated in the literature that the presence of DNA basis can induce changes in the electronic structure of pore atoms, which is the base of transverse tunneling current in field-effect transistor detection devices. Thus, complementary signals obtained from spectral calculations such as electronic current, IR or Raman spectra via *ab initio* MD or density functional theory (DFT) can also be useful to study at the atomic level how do proteins and biomarkers interact with nanopores.

- A major challenge from a computational point of view, is the addition of chemical groups to functionalize the structure of TMDC materials. Nowadays, ReaxFF potential is a powerful tool that can be used to simulate chemical reactions, thus it opens the possibility to perform MD simulations closer to experimental conditions. Both ionic transport properties of sub-nm pores and translocation of biomolecules though nanopore are sensible to the chemical environment and new alternatives of nanopore sensing devices could be explored by taking advantage of 2D materials surface reactivity.

References

[1] Eric S. et al. Lander. Initial sequencing and analysis of the human genome. *Nature*, 409(6822):860–921, 2001.

[2] Bala Murali Venkatesan and Rashid Bashir. Nanopore sensors for nucleic acid analysis. *Nature Nanotechnology*, 6(10):615–624, 2011.

[3] F. Sanger, S. Nicklen, and A. R. Coulson. Dna sequencing with chain-terminating inhibitors. *Proceedings of the National Academy of Sciences of the United States of America*, 74(12):5463–5467, Dec 1977. 271968[pmid].

[4] Elaine Mardis. Next-generation dna sequencing methods. *Annual review of genomics and human genetics*, 9:387–402, 07 2008.

[5] Michael L. Metzker. Sequencing technologies – the next generation. *Nature Reviews Genetics*, 11(1):31–46, 2010.

[6] Stephanie Heerema and Cees Dekker. Graphene nanodevices for dna sequencing. *Nature Nanotechnology*, 11:127–136, 02 2016.

[7] Sam Behjati and Patrick S. Tarpey. What is next generation sequencing? *Archives of disease in childhood. Education and practice edition*, 98(6):236–238, Dec 2013. 23986538[pmid].

[8] Ayman Grada and Kate Weinbrecht. Next-generation sequencing: Methodology and application. *Journal of Investigative Dermatology*, 133(8):1 – 4, 2013.

[9] Alexander S. Mikheyev and Mandy M. Y. Tin. A first look at the oxford nanopore minion sequencer. *Molecular Ecology Resources*, 14(6):1097–1102, 2014.

[10] J. J. Kasianowicz, E. Brandin, D. Branton, and D. W. Deamer. Characterization of individual polynucleotide molecules using a membrane channel. *Proceedings of the National Academy of Sciences of the United States of America*, 93(24):13770–13773, Nov 1996. 8943010[pmid].

[11] Cees Dekker. Solid-state nanopores. *Nature nanotechnology*, 2:209–15, 04 2007.

[12] Emma Letizia Bonome, Fabio Cecconi, and Mauro Chinappi. Translocation intermediates of ubiquitin through an alpha-hemolysin nanopore: implications for detection of post-translational modifications. *Nanoscale*, 11:9920–9930, 2019.

[13] Jeff Nivala, Douglas B. Marks, and Mark Akeson. Unfoldase-mediated protein translocation through an a-hemolysin nanopore. *Nature Biotechnology*, 31:247 EP –, Feb 2013.

[14] Giovanni Di Muccio, Aldo Eugenio Rossini, Daniele Di Marino, Giuseppe Zollo, and Mauro Chinappi. Insights into protein sequencing with an a-hemolysin nanopore by atomistic simulations. *Scientific Reports*, 9(1):6440, 2019.

[15] Daniel Branton, David Deamer, Andre Marziali, Hagan Bayley, Steven Benner, Thomas Butler, Massimiliano Di Ventra, Slaven Garaj, Andrew Hibbs, Xiaohua Huang, Stevan Jovanovich, Predrag Krstic, Stuart Lindsay, X. Ling, C.H. Mastrangelo, Amit Meller, John Oliver, Yuriy Pershin, J Ramsey, and Jeffery Schloss. The potential and challenges of nanopore sequencing. *Nature biotechnology*, 26:1146–53, 11 2008.

[16] Adrian Balan, Bartholomeus Machielse, David Niedzwiecki, Jianxun Lin, Peijie Ong, Rebecca Engelke, Kenneth L. Shepard, and Marija Drndić. Improving signal-to-noise performance for DNA translocation in solid-state nanopores at MHz bandwidths. *Nano Letters*, 14(12):7215–7220, December 2014.

[17] Jiali Li, Derek Stein, Ciaran McMullan, Daniel Branton, M.J. Aziz, and J.A. Golovchenko. Ion-beam sculpting at nanometre length scales. *Nature*, 412:166–9, 08 2001.

[18] Bala Venkatesan. Solid-state nanopore sensors for nucleic acid analysis. *Nature nanotechnology*, 6:615–24, 09 2011.

[19] Yanxiao Feng, Yuechuan Zhang, Cuifeng Ying, Deqiang Wang, and Chunlei Du. Nanopore-based Fourth-generation DNA Sequencing Technology. *Genomics, Proteomics & Bioinformatics*, 13(1):4–16, February 2015.

[20] A. J. Storm, J. H. Chen, X. S. Ling, H. W. Zandbergen, and C. Dekker. Fabrication of solid-state nanopores with single-nanometre precision. *Nature Materials*, 2(8):537–540, August 2003.

[21] Jiali Li, Derek Stein, Ciaran McMullan, Daniel Branton, Michael J. Aziz, and Jene A. Golovchenko. Ion-beam sculpting at nanometre length scales. *Nature*, 412(6843):166–169, July 2001.

[22] Bala Murali Venkatesan, Amish B. Shah, Jian-Min Zuo, and Rashid Bashir. DNA Sensing Using Nanocrystalline Surface-Enhanced Al2o3 Nanopore Sensors. *Advanced Functional Materials*, 20(8):1266–1275, April 2010.

[23] Ke Liu, Jiandong Feng, Andras Kis, and Aleksandra Radenovic. Atomically thin molybdenum disulfide nanopores with high sensitivity for dna translocation. *ACS Nano*, 8(3):2504–2511, 2014. PMID: 24547924.

[24] Grégory Schneider, Stefan W Kowalczyk, Victor E Calado, Gregory Pandraud, Henny Zandbergen, Lieven M K Vandersypen, and Cees Dekker. Dna translocation through graphene nanopores. *Nano letters*, 10:3163–7, 08 2010.

[25] Christopher Merchant, Ken Healy, Meni Wanunu, Vishva Ray, Neil Peterman, John Bartel, Michael Fischbein, Kimberly Venta, Zhengtang Luo, a t charlie Johnson, and Marija Drndić. Dna translocation through graphene nanopores. *Nano letters*, 10:2915–21, 08 2010.

[26] S. Garaj, W. Hubbard, A. Reina, J. Kong, D. Branton, and J. A. Golovchenko. Graphene as a subnanometre trans-electrode membrane. *Nature*, 467(7312):190–193, September 2010.

[27] Kamal K. Saha, Marija Drndić, and Branislav K. Nikolić. DNA Base-Specific Modulation of Microampere Transverse Edge Currents through a Metallic Graphene Nanoribbon with a Nanopore. *Nano Letters*, 12(1):50–55, January 2012.

[28] Marija Drndić. Sequencing with graphene pores. *Nature Nanotechnology*, 9(10):743–743, October 2014.

[29] Owain Vaughan. Better than graphene? *Nature Nanotechnology*, pages EP –, Aug 2014.

[30] Siddharth Shekar, David J. Niedzwiecki, Chen-Chi Chien, Peijie Ong, Daniel A. Fleischer, Jianxun Lin, Jacob K. Rosenstein, Marija Drndić, and Kenneth L. Shepard. Measurement of dna translocation dynamics in a solid-state nanopore at 100 ns temporal resolution. *Nano Letters*, 16(7):4483–4489, 2016. PMID: 27332998.

[31] Song Liu, Bo Lu, Qing Zhao, Ji Li, Teng Gao, Yubin Chen, Yanfeng Zhang, Zhongfan Liu, Zhongchao Fan, Fuhua Yang, Liping You, and Dapeng Yu. Boron Nitride Nanopores: Highly Sensitive DNA Single-Molecule Detectors. *Advanced Materials*, 25(33):4549–4554, September 2013.

[32] Gopinath Danda, Paul Masih Das, Yung-Chien Chou, Jerome Mlack, William M. Parkin, Carl Naylor, Kazunori Fujisawa, Tianyi Zhang, Laura Beth Fulton, Mauricio Terrones, Alan T. Charlie Johnson, and Marija Drndić. Monolayer ws2 nanopores for dna translocation with light-adjustable sizes. *ACS Nano*, 11, 01 2017.

[33] Seon Joon Kim, Dae Woo Kim, Joonwon Lim, Soo-Yeon Cho, Sang Kim, and Hee-Tae Jung. Large-area buckled mos2 films on the graphene substrate. *ACS applied materials and interfaces*, 8, 05 2016.

[34] Taeyeong Yun, Jong-Seon Kim, Jongwon Shim, Dong Sung Choi, Kyung Eun Lee, SungHwan Koo, InHo Kim, Hong Ju Jung, Hae-Wook Yoo, Hee-Tae Jung, and Sang Kim. Ultrafast interfacial self-assembly of 2d transition metal dichalcogenides monolayer films and their vertical and in-plane heterostructures. *ACS Applied Materials and Interfaces*, 9, 12 2016.

[35] Taeyeong Yun, Hyeong Min Jin, Dong Ha Kim, Kyu Hyo Han, Geon Gug Yang, Gil Yong Lee, Gang San Lee, Jin Young Choi, Il Doo Kim, and Sang Kim. 2d nanopatterning: 2d metal chalcogenide nanopatterns by block copolymer lithography. *Advanced Functional Materials*, 28, 12 2018.

[36] Ke Liu, Martina Lihter, Aditya Sarathy, Sabina Caneva, Hu Qiu, Davide Deiana, Vasiliki Tileli, Duncan Alexander, Stephan Hofmann, Dumitru Dumcenco, Andras Kis, Jean-Pierre Leburton, and Aleksandra Radenovic. Geometrical effect in 2d nanopores. *Nano Letters*, 17, 06 2017.

[37] Lorenz Steinbock and Aleksandra Radenovic. The emergence of nanopores in next-generation sequencing. *Nanotechnology*, 26:074003, 02 2015.

[38] Ruitao Lv, Joshua A. Robinson, Raymond E. Schaak, Du Sun, Yifan Sun, Thomas E. Mallouk, and Mauricio Terrones. Transition metal dichalcogenides and beyond: Synthesis, properties, and applications of single- and few-layer nanosheets. *Accounts of Chemical Research*, 48(1):56–64, 2015. PMID: 25490673.

[39] B. Radisavljevic, A. Radenovic, J. Brivio, V. Giacometti, and A. Kis. Single-layer mos2 transistors. *Nature Nanotechnology*, 6(3):147–150, 2011.

[40] Jiandong Feng, Ke Liu, Roman Bulushev, Sergey Khlybov, Dumitru Dumcenco, Andras Kis, and Aleksandra Radenovic. Identification of single nucleotides in mos2 nanopores. *Nature Nanotechnology*, 10, 05 2015.

[41] Angel Diaz Carral, Chandra Shekar Sarap, Ke Liu, Aleksandra Radenovic, and Maria Fyta. 2d MoS2 nanopores: ionic current blockade height for clustering DNA events. *2D Materials*, 6(4):045011, jul 2019.

[42] Maria Fyta, Simone Melchionna, and Sauro Succi. Translocation of biomolecules through solid-state nanopores: Theory meets experiments. *J. Polym. Sci. B Polym. Phys.*, 49(14):985–1011, July 2011.

[43] Julio A Rodriguez-Manzo, Matthew Puster, Adrien Nicolaï, Vincent Meunier, and Marija Drndić. Dna translocation in nm-thick silicon nanopores. *ACS nano*, 9, 06 2015.

[44] Niraj Modi, Mathias Winterhalter, and Ulrich Kleinekathöfer. Computational modeling of ion transport through nanopores. *Nanoscale*, 4(20):6166–6180, September 2012.

[45] Aleksei Aksimentiev, Robert K. Brunner, Eduardo Cruz-Chú, Jeffrey Comer, and Klaus Schulten. Modeling Transport Through Synthetic Nanopores. *IEEE Nanotechnol Mag*, 3(1):20–28, March 2009.

[46] Amir Barati Farimani, Kyoungmin Min, and Narayana R. Aluru. DNA Base Detection Using a Single-Layer MoS2. *ACS Nano*, 8(8):7914–7922, August 2014.

[47] Chaitanya Sathe, Xueqing Zou, Jean-Pierre Leburton, and Klaus Schulten. Computational Investigation of DNA Detection Using Graphene Nanopores. *ACS Nano*, 5(11):8842–8851, November 2011.

[48] Huang Chen, Libo Li, Tao Zhang, Zhiwei Qiao, Jinhui Tang, and Jian Zhou. Protein translocation through a mos2 nanopore:a molecular dynamics study. *The Journal of Physical Chemistry C*, 122(4):2070–2080, 2018.

[49] Binquan Luan and Ruhong Zhou. Single-file protein translocations through graphene–mos2 heterostructure nanopores. *The Journal of Physical Chemistry Letters*, 9(12):3409–3415, 2018.

[50] Calin Plesa, Stefan W. Kowalczyk, Ruben Zinsmeester, Alexander Y. Grosberg, Yitzhak Rabin, and Cees Dekker. Fast translocation of proteins through solid state nanopores. *Nano Letters*, 13(2):658–663, 2013. PMID: 23343345.

[51] Joseph Larkin, Robert Y. Henley, Murugappan Muthukumar, Jacob K. Rosenstein, and Meni Wanunu. High-bandwidth protein analysis using solid-state nanopores. *Biophysical Journal*, 106(3):696 – 704, 2014.

[52] David J. Niedzwiecki, Christopher J. Lanci, Gabriel Shemer, Phillip S. Cheng, Jeffery G. Saven, and Marija Drndić. Observing changes in the structure and oligomerization state of a helical protein dimer using solid-state nanopores. *ACS Nano*, 9(9):8907–8915, 2015. PMID: 26262433.

[53] Eamonn Kennedy, Zhuxin Dong, Clare Tennant, and Gregory Timp. Reading the primary structure of a protein with 0.07 nm3 resolution using a subnanometre-diameter pore. *Nature Nanotechnology*, 11:968 EP –, Jul 2016. Article.

[54] Amir Barati Farimani, Mohammad Heiranian, and Narayana R. Aluru. Identification of amino acids with sensitive nanoporous mos2: towards machine learning-based prediction. *npj 2D Materials and Applications*, 2(1):14, 2018.

[55] Dae-Sik Lee, Seokhan Park, Yong Duk Han, Jae Eun Lee, Hu Young Jeong, Hyun C. Yoon, Moon Yeon Jung, Sang Ouk Kim, and Sung-Yool Choi. Selective protein transport through ultra-thin suspended reduced graphene oxide nanopores. *Nanoscale*, 9:13457–13464, 2017.

[56] D. Frenkel. Simulations: The dark side. *The European Physical Journal Plus*, 128(1):10, January 2013.

[57] Michael P. Allen. *Introduction to molecular dynamics simulation.* 2004.

[58] Saman Alavi. Statistical Mechanics: Theory and Molecular Simulation. By Mark E. Tuckerman. *Angewandte Chemie International Edition*, 50(51):12138–12139, 2011.

[59] Jothi Priyanka Thiruraman, Kazunori Fujisawa, Gopinath Danda, Paul Masih Das, Tianyi Zhang, Adam Bolotsky, Nestor Perea-Lopez, Adrien Nicolaï, Patrick Senet, Mauricio Terrones, and Marija Drndić. Angstrom-Size Defect Creation and Ionic Transport through Pores in Single-Layer MoS2. *Nano Letters*, 18(3):1651–1659, 2018.

[60] Maria Daniela Barrios Perez, Patrick Senet, Vincent Meunier, and Adrien Nicolaï. Computational Investigation of the Ionic Conductance through Molybdenum Disulfide (MoS2) Nanopores. *WSEAS Transactions On Circuits And Systems*, 16, 2017.

[61] Maria Daniela Barrios Perez, Adrien Nicolaï, Patrice Delarue, Vincent Meunier, Marija Drndić, and Patrick Senet. Improved model of ionic transport in 2-D MoS2 membranes with sub-5 nm pores. *Applied Physics Letters*, 114(2):023107, 2019.

[62] Adrien Nicolaï, Maria Daniela Barrios Perez, Patrice Delarue, Vincent Meunier, Marija Drndić, and Patrick Senet. Molecular Dynamics Investigation of Polylysine Peptide Translocation through MoS2 Nanopores. *The Journal of Physical Chemistry B*, 123(10):2342–2353, March 2019.

[63] William Humphrey, Andrew Dalke, and Klaus Schulten. VMD: Visual molecular dynamics. *Journal of Molecular Graphics*, 14(1):33–38, February 1996.

[64] Andrew Jewett and Shea Lab. *Moltemplate Manual.* August 2015.

[65] H.J.C. Berendsen, D. van der Spoel, and R. van Drunen. GROMACS: A message-passing parallel molecular dynamics implementation. *Computer Physics Communication*, 91:43–56, December 1994.

[66] David A. Pearlman, David A. Case, James W. Cadwell, Wilson S. Ross, Thomas E. Cheatham III, Steve DeBolt, David Ferguson, George Seibel, and Peter Kollman. AMBER,a package of computer programs for applying molecular mechanics, normal mode analysis, molecular dynamics and free energy calculations to simulate the structural and energetic properties of molecules. *Computer Physics Communications*, 91:1–41, October 1994.

[67] William L. Jorgensen, Jayaraman Chandrasekhar, Jeffry D. Madura, Roger W. Impey, and Michael L. Klein. Comparison of simple potential functions for simulating liquid water. *The Journal of Chemical Physics*, 79(2):926–935, July 1983.

[68] In Suk Joung and Thomas E. Cheatham. Determination of Alkali and Halide Monovalent Ion Parameters for Use in Explicitly Solvated Biomolecular Simulations. *J. Phys. Chem. B*, 112(30):9020–9041, July 2008.

[69] Daan Frenkel and Berend Smit. *Understanding Molecular Simulation: from Algorithms to Applications*. Academic Press, San Diego, CA, 2002.

[70] Luca Monticelli and Emppu Salonen. *Biomolecular Simulations: Methods and Protocols*, volume 924. 2013.

[71] Adam Hospital, Josep Ramon Goñi, Modesto Orozco, and Josep L Gelpí. Molecular dynamics simulations: advances and applications. *Advances and applications in bioinformatics and chemistry : AABC*, 8:37–47, November 2015.

[72] Michael P. Howard, Joshua A. Anderson, Arash Nikoubashman, Sharon C. Glotzer, and Athanassios Z. Panagiotopoulos. Efficient neighbor list calculation for molecular simulation of colloidal systems using graphics processing units. *Computer Physics Communications*, 203:45 – 52, 2016.

[73] Ariel A. Chialvo and Pablo G. Debenedetti. On the use of the verlet neighbor list in molecular dynamics. *Computer Physics Communications*, 60(2):215 – 224, 1990.

[74] W. C. Swope, H. C. Andersen, P. H. Berens, and K. R. Wilson. A computer simulation method for the calculation of equilibrium constants for the formation of physical clusters of molecules: Application to small water clusters. *\jcp*, 76:637–649, January 1982.

[75] Dimitrios Vlachakis, Elena Bencurova, Nikitas Papangelopoulos, and Sophia Kossida. Chapter seven - current state-of-the-art molecular dynamics methods and applications. volume 94 of *Advances in Protein Chemistry and Structural Biology*, pages 269 – 313. Academic Press, 2014.

[76] Shuichi Nose. A unified formulation of the constant temperature molecular dynamics methods. *The Journal of Chemical Physics*, 81(1):511–519, 1984.

[77] Hans C. Andersen. Molecular dynamics simulations at constant pressure and/or temperature. *The Journal of Chemical Physics*, 72(4):2384–2393, 1980.

[78] William G. Hoover. Canonical dynamics: Equilibrium phase-space distributions. *Phys. Rev. A*, 31(3):1695–1697, March 1985.

[79] N. Wakabayashi, H. G. Smith, and R. M. Nicklow. Lattice dynamics of hexagonal mos_2 studied by neutron scattering. *Phys. Rev. B*, 12:659–663, Jul 1975.

[80] Frank H. Stillinger and Thomas A. Weber. Computer simulation of local order in condensed phases of silicon. *Phys. Rev. B*, 31:5262–5271, Apr 1985.

[81] Jin Wu Jiang, Harold S. Park, and Timon Rabczuk. Molecular dynamics simulations of single-layer molybdenum disulphide (mos2): Stillinger-weber parametrization, mechanical properties, and thermal conductivity. *Journal of Applied Physics*, 114(6), 8 2013.

[82] J. Tersoff. New empirical model for the structural properties of silicon. *Phys. Rev. Lett.*, 56:632–635, Feb 1986.

[83] Donald W Brenner, Olga A Shenderova, Judith A Harrison, Steven J Stuart, Boris Ni, and Susan B Sinnott. A second-generation reactive empirical bond order (REBO) potential energy expression for hydrocarbons. *Journal of Physics: Condensed Matter*, 14(4):783–802, jan 2002.

[84] Jin-Wu Jiang. Parametrization of Stillinger–Weber potential based on valence force field model: application to single-layer MoS 2 and black phosphorus. *Nanotechnology*, 26(31):315706, 2015.

[85] Thomas P Senftle, Sungwook Hong, Md Mahbubul Islam, Sudhir B Kylasa, Yuanxia Zheng, Yun Kyung Shin, Chad Junkermeier, Roman Engel-Herbert, Michael J Janik, Hasan Metin Aktulga, Toon Verstraelen, Ananth Grama, and Adri CT van Duin. The reaxff reactive force-field : development, applications and future directions. *NPJ COMPUTATIONAL MATERIALS*, 2:14, 2016.

[86] Alireza Ostadhossein, Ali Rahnamoun, Yuanxi Wang, Peng Zhao, Sulin Zhang, Vincent H. Crespi, and Adri C. T. van Duin. Reaxff reactive force-field study of molybdenum disulfide (mos2). *The Journal of Physical Chemistry Letters*, 8(3):631–640, 2017. PMID: 28103669.

[87] Dundar E. Yilmaz, Roghayyeh Lotfi, Chowdhury Ashraf, Sungwook Hong, and Adri C. T. van Duin. Defect design of two-dimensional mos2 structures by using a graphene layer and potato stamp concept. *The Journal of Physical Chemistry C*, 122(22):11911–11917, 2018.

[88] van Duin Adri. *ReaxFF User Manual.* California Institute of Technology Pasadena, CA 91125 USA, 2002.

[89] H. Yukawa and M. Morinaga. The nature of the chemical bond in hydrogen storage compounds. volume 29 of *Advances in Quantum Chemistry*, pages 83 – 108. Academic Press, 1998.

[90] Adri C. T. van Duin, Siddharth Dasgupta, Francois Lorant, and William A. Goddard. *The Journal of Physical Chemistry A*, 105(41):9396–9409, 2001.

[91] Kimberly Chenoweth, Adri C. T. van Duin, and William A. Goddard. Reaxff reactive force field for molecular dynamics simulations of hydrocarbon oxidation. *The Journal of Physical Chemistry A*, 112(5):1040–1053, 2008. PMID: 18197648.

[92] Chowdhury Ashraf and Adri C.T. van Duin. Extension of the reaxff combustion force field toward syngas combustion and initial oxidation kinetics. *The Journal of Physical Chemistry A*, 121(5):1051–1068, 2017. PMID: 28072539.

[93] Jonathan E. Mueller, Adri C. T. van Duin, and William A. Goddard. Development and validation of reaxff reactive force field for hydrocarbon chemistry catalyzed by nickel. *The Journal of Physical Chemistry C*, 114(11):4939–4949, 2010.

[94] Kuan Lu, Chun-Fang Huo, Wen-Ping Guo, Xing-Wu Liu, Yuwei Zhou, Qing Peng, Yong Yang, Yong-Wang Li, and Xiao-Dong Wen. Development of a reactive force field for the fe–c interaction to investigate the carburization of iron. *Phys. Chem. Chem. Phys.*, 20:775–783, 2018.

[95] Anthony K. Rappe and William A. Goddard. Charge equilibration for molecular dynamics simulations. *The Journal of Physical Chemistry*, 95(8):3358–3363, 1991.

[96] H. M. Aktulga, J. C. Fogarty, S. A. Pandit, and A. Y. Grama. Parallel reactive molecular dynamics: Numerical methods and algorithmic techniques. *Parallel Comput.*, 38(4-5):245–259, April 2012.

[97] Lemont B. Kier. *Journal of Medicinal Chemistry*, 40(18):2969–2969, 1997.

[98] Junmei Wang, Romain M. Wolf, James W. Caldwell, Peter A. Kollman, and David A. Case. Development and testing of a general amber force field. *Journal of Computational Chemistry*, 25(9):1157–1174.

[99] Wendy D. Cornell, Piotr Cieplak, Christopher I. Bayly, Ian R. Gould, Kenneth M. Merz, David M. Ferguson, David C. Spellmeyer, Thomas Fox, James W. Caldwell, and Peter A. Kollman. A second generation force field for the simulation of proteins, nucleic acids, and organic molecules. *Journal of the American Chemical Society*, 117(19):5179–5197, 1995.

[100] Kresten Lindorff-Larsen, Stefano Piana, Kim Palmo, Paul Maragakis, John Klepeis, Ron O Dror, and David E Shaw. Improved side-chain torsion potentials for the amber ff99sb protein force field. *Proteins*, 78:1950–8, 03 2010.

[101] Pekka Mark and Lennart Nilsson. Structure and dynamics of the tip3p, spc, and spc/e water models at 298 k. *The Journal of Physical Chemistry A*, 105(43):9954–9960, 2001.

[102] Saeed Izadi, Ramu Anandakrishnan, and Alexey V. Onufriev. Building water models: A different approach. *The Journal of Physical Chemistry Letters*, 5(21):3863–3871, 2014. PMID: 25400877.

[103] Jean-Paul Ryckaert, Giovanni Ciccotti, and Herman J.C Berendsen. Numerical integration of the cartesian equations of motion of a system with constraints: molecular dynamics of n-alkanes. *Journal of Computational Physics*, 23(3):327 – 341, 1977.

[104] Hans C Andersen. Rattle: A "velocity" version of the shake algorithm for molecular dynamics calculations. *Journal of Computational Physics*, 52(1):24 – 34, 1983.

[105] Ron Elber, A Peter Ruymgaart, and Berk Hess. Shake parallelization. *The European physical journal. Special topics*, 200:211–223, 11 2011.

[106] Daniel J. Price and Charles L. Brooks. A modified tip3p water potential for simulation with ewald summation. *The Journal of Chemical Physics*, 121(20):10096–10103, 2004.

[107] William McDoniel, Markus Höhnerbach, Rodrigo Canales, Ahmed Ismail, and Paolo Bientinesi. Lammps' pppm long-range solver for the second generation xeon phi. pages 61–78, 02 2017.

[108] Rolf E. Isele-Holder, Wayne Mitchell, and Ahmed E. Ismail. Development and application of a particle-particle particle-mesh ewald method for dispersion interactions. *The Journal of Chemical Physics*, 137(17):174107, 2012.

[109] Tao Liang, Simon R. Phillpot, and Susan B. Sinnott. Parametrization of a reactive many-body potential for Mo-S systems. *Phys. Rev. B*, 79(24):245110, June 2009.

[110] Martin Fodslette Møller. A scaled conjugate gradient algorithm for fast supervised learning. *Neural Networks*, 6(4):525 – 533, 1993.

[111] M. J. D. Powell. Restart procedures for the conjugate gradient method. *Mathematical Programming*, 12(1):241–254, Dec 1977.

[112] Michael Zwolak, Johan Lagerqvist, and Massimiliano Di Ventra. Quantized ionic conductance in nanopores. *Phys. Rev. Lett.*, 103:128102, Sep 2009.

[113] Stefan W Kowalczyk, Alexander Y Grosberg, Yitzhak Rabin, and Cees Dekker. Modeling the conductance and DNA blockade of solid-state nanopores. *Nanotechnology*, 22(31):315101, jul 2011.

[114] Myungeun Suk and N R Aluru. Ion transport in sub-5-nm graphene nanopores. *The Journal of chemical physics*, 140:084707, 02 2014.

[115] Sean C. O'Hern, Doojoon Jang, Suman Bose, Juan-Carlos Idrobo, Yi Song, Tahar Laoui, Jing Kong, and Rohit Karnik. Nanofiltration across defect-sealed nanoporous monolayer graphene. *Nano Letters*, 15(5):3254–3260, 2015. PMID: 25915708.

[116] Sean C. O'Hern, Michael S. H. Boutilier, Juan-Carlos Idrobo, Yi Song, Jing Kong, Tahar Laoui, Muataz Atieh, and Rohit Karnik. Selective ionic transport through tunable subnanometer pores in single-layer graphene membranes. *Nano Letters*, 14(3):1234–1241, 2014. PMID: 24490698.

[117] Sean C. O'Hern, Cameron A. Stewart, Michael S. H. Boutilier, Juan-Carlos Idrobo, Sreekar Bhaviripudi, Sarit K. Das, Jing Kong, Tahar Laoui, Muataz Atieh, and Rohit Karnik. Selective molecular transport through intrinsic defects in a single layer of cvd graphene. *ACS Nano*, 6(11):10130–10138, 2012. PMID: 23030691.

[118] Subin Sahu and Michael Zwolak. Ionic selectivity and filtration from fragmented dehydration in multilayer graphene nanopores. *Nanoscale*, 9, 04 2017.

[119] Subin Sahu, Massimiliano Di Ventra, and Michael Zwolak. Dehydration as a universal mechanism for ion selectivity in graphene and other atomically thin pores. *Nano Letters*, 17, 05 2016.

[120] Subin Sahu and Michael Zwolak. Colloquium : Ionic phenomena in nanoscale pores through 2d materials. *Reviews of Modern Physics*, 91, 06 2019.

[121] Myungeun Suk and N R. Aluru. Water transport through ultrathin graphene. *Journal of Physical Chemistry Letters - J PHYS CHEM LETT*, 1:1590–1594, 05 2010.

[122] Shanshan Wang, Huashan Li, Hidetaka Sawada, Christopher S. Allen, Angus I. Kirkland, Jeffrey C. Grossman, and Jamie H. Warner. Atomic structure and formation mechanism of sub-nanometer pores in 2d monolayer mos2. *Nanoscale*, 9:6417–6426, 2017.

[123] Jothi Priyanka Thiruraman, Paul Masih Das, and Marija Drndić. Irradiation of transition metal dichalcogenides using a focused ion beam: Controlled single-atom defect creation. *Advanced Functional Materials*, 0(0):1904668.

[124] Manuel Uhlig, Daniel Martin-Jimenez, and Ricardo Garcia. Atomic-scale mapping of hydrophobic layers on graphene and few-layer mos2 and wse2 in water. *Nature Communications*, 10, 12 2019.

[125] Vishnu Sresht, Ananth Govind Rajan, Emilie Bordes, Michael S. Strano, Agílio A.H. Pádua, and Daniel Blankschtein. Quantitative modeling of mos2 solvent interfaces: Predicting contact angles and exfoliation performance using molecular dynamics. *The Journal of Physical Chemistry C*, 121(16):9022–9031, 2017.

[126] Anand P. S. Gaur, Satyaprakash Sahoo, Majid Ahmadi, Saroj P. Dash, Maxime J.-F. Guinel, and Ram S. Katiyar. Surface energy engineering for tunable wettability through controlled synthesis of mos2. *Nano Letters*, 14(8):4314–4321, 2014. PMID: 25073904.

[127] Philippe K. Chow, Eklavya Singh, Bartolomeu Cruz Viana, Jian Gao, Jian Luo, Jing Li, Zhong Lin, Ana L. Elías, Yunfeng Shi, Zuankai Wang, Mauricio Terrones, and Nikhil Koratkar. Wetting of mono and few-layered ws2 and mos2 films supported on si/sio2 substrates. *ACS Nano*, 9(3):3023–3031, 2015. PMID: 25752871.

[128] M. Salmeron, G.A. Somorjai, A. Wold, R. Chianelli, and K.S. Liang. The adsorption and binding of thiophene, butene and h2s on the basal plane of mos2 single crystals. *Chemical Physics Letters*, 90(2):105 – 107, 1982.

[129] Allison Squires, Tal Gilboa, C. Torfstein, Nitinun Varongchayakul, and Amit Meller. *Single-Molecule Characterization of DNA–Protein Interactions Using Nanopore Biosensors*, volume 582. 11 2016.

[130] Michael Graf, Martina Lihter, Mukeshchand Thakur, Vasileia Georgiou, Juraj Topolancik, B. Ilic, Ke Liu, Jiandong Feng, Yann Astier, and Aleksandra Radenovic. Fabrication and practical applications of molybdenum disulfide nanopores. *Nature Protocols*, 14:1–39, 03 2019.

[131] Diane Lipscombe and Cecilia P. Toro. Chapter 13 - biophysics of voltage-gated ion channels. In John H. Byrne, Ruth Heidelberger, and M. Neal Waxham, editors, *From Molecules to Networks (Third Edition)*, pages 377 – 407. Academic Press, Boston, third edition edition, 2014.

[132] J I Schroeder. K+ transport properties of k+ channels in the plasma membrane of vicia faba guard cells. *The Journal of General Physiology*, 92(5):667–683, 1988.

[133] Eleonora Gianti and Vincenzo Carnevale. Chapter two - computational approaches to studying voltage-gated ion channel modulation by general anesthetics. In Roderic G. Eckenhoff and Ivan J. Dmochowski, editors, *Chemical and Biochemical Approaches for the Study of Anesthetic Function, Part A*, volume 602 of *Methods in Enzymology*, pages 25 – 59. Academic Press, 2018.

[134] Chang Wei and Allen J. Bard. Current rectification at quartz nanopipet electrodes. *Analytical Chemistry - ANAL CHEM*, 69, 11 1997.

[135] Xiao long Deng, Tomohide Takami, Jong Wan Son, Eun Ji Kang, Tomoji Kawai, and Bae Park. Effect of concentration gradient on ionic current rectification in polyethyleneimine modified glass nano-pipettes. *Scientific reports*, 4:4005, 02 2014.

[136] Eduardo R Cruz Chu, Aleksei Aksimentiev, and Klaus Schulten. Ionic current rectification through silica nanopores. *The journal of physical chemistry. C, Nanomaterials and interfaces*, 113:1850, 02 2009.

[137] Liuxuan Cao, Wei Guo, Yugang Wang, and Lei Jiang. Concentration-gradient-dependent ion current rectification in charged conical nanopores. *Langmuir : the ACS journal of surfaces and colloids*, 28:2194–9, 12 2011.

[138] Mubarak Ali, Basit Yameen, Javier Cervera, Patricio Ramirez, Reinhard Neumann, Wolfgang J. Ensinger, Wolfgang Knoll, and Omar Azzaroni. Layer-by-layer assembly of polyelectrolytes into ionic current rectifying solid-state nanopores: insights from theory and experiment. *Journal of the American Chemical Society*, 132 24:8338–48, 2010.

[139] Rohit Karnik, Chuanhua Duan, Kenneth Castelino, Hirofumi Daiguji, and Arun Majumdar. Rectification of ionic current in a nanofluidic diode. *Nano letters*, 7:547–51, 04 2007.

[140] Li-Hsien Yeh, Mingkan Zhang, Shizhi Qian, Jyh-Ping Hsu, and Shiojenn Tseng. Ion concentration polarization in polyelectrolyte-modified nanopores. *The Journal of Physical Chemistry C*, 116:8672–8677, 04 2012.

[141] Erik Yusko, Ran An, and Michael Mayer. Electroosmotic flow can generate ion current rectification in nano- and micropores. *ACS nano*, 4:477–87, 12 2009.

[142] Sandip Ghosal, John D Sherwood, and Hsueh-Chia Chang. Solid-state nanopore hydrodynamics and transport. *Biomicrofluidics*, 13, 01 2019.

[143] Kunwar Pal Singh and Manoj Kumar. Effect of nanochannel diameter and debye length on ion current rectification in a fluidic bipolar diode. *The Journal of Physical Chemistry C*, 115(46):22917–22924, 2011.

[144] Ryan C. Rollings, Aaron T. Kuan, and Jene A. Golovchenko. Ion selectivity of graphene nanopores. *Nature Communications*, 7:11408, 04 2016.

[145] Huacheng Zhang, Xu Hou, Lu Zeng, Fu Yang, Lin Li, Dadong Yan, Ye Tian, and Lei Jiang. Bioinspired artificial single ion pump. *Journal of the American Chemical Society*, 135, 06 2013.

[146] Z. Siwy, I. D. Kosinska, A. Fulinski, and C. R. Martin. Asymmetric diffusion through synthetic nanopores. *Phys. Rev. Lett.*, 94:048102, Feb 2005.

[147] Bertil Hille. *Ion Channels of Excitable Membranes*, volume 18. 01 2001.

[148] Olaf Andersen. Ion movement through gramicidin a channels. studies on the diffusion-controlled association step. *Biophysical journal*, 41:147–65, 02 1983.

[149] P Läuger. Diffusion-limited ion flow through pores. *Biochimica et Biophysica Acta (BBA) - Biomembranes*, 455(2):493 – 509, 1976.

[150] Takashi Sumikama. Origin of the shape of current-voltage curve through nanopores: A molecular dynamics study. *Scientific reports*, 6:25750, 05 2016.

[151] Jiwook Shim, Shouvik Banerjee, Hu Qiu, Kirby K. H. Smithe, David Estrada, Julian Bello, Eric Pop, Klaus Schulten, and Rashid Bashir. Detection of methylation on dsdna using nanopores in a mos2 membrane. *Nanoscale*, 9:14836–14845, 2017.

[152] Fangqiang Zhu, Emad Tajkhorshid, and Klaus Schulten. Theory and simulation of water permeation in aquaporin-1. *Biophysical Journal*, 86(1):50 – 57, 2004.

[153] Bert L. de Groot, D. Peter Tieleman, Peter Pohl, and Helmut Grubmüller. Water permeation through gramicidin a: Desformylation and the double helix: A molecular dynamics study. *Biophysical Journal*, 82(6):2934 – 2942, 2002.

[154] Kyaw Sint, Boyang Wang, and Petr Král. Selective ion passage through functionalized graphene nanopores. *Journal of the American Chemical Society*, 130(49):16448–16449, 2008. PMID: 19554715.

[155] Zhongjin He, Jian Zhou, Xiaohua Lu, and Ben Corry. Bioinspired graphene nanopores with voltage-tunable ion selectivity for na+ and k+. *ACS Nano*, 7(11):10148–10157, 2013. PMID: 24151957.

[156] Mohammad Heiranian, Amir Barati Farimani, and Narayana R. Aluru. Water desalination with a single-layer mos2 nanopore. *Nature Communications*, 6, 10 2015.

[157] Mengmeng Deng, Kijeong Kwac, Meng Li, Yousung Jung, and Hyung Gyu Park. Stability, molecular sieving, and ion diffusion selectivity of a lamellar membrane from two-dimensional molybdenum disulfide. *Nano Letters*, 17(4):2342–2348, 2017. PMID: 28296407.

[158] Chao Fang, Zhou Yu, and Rui Qiao. Impact of surface ionization on water transport and salt leakage through graphene oxide membranes. *The Journal of Physical Chemistry C*, 121(24):13412–13420, 2017.

[159] Victor Levadny, Vicente M Aguilella, and Marina Belaya. Access resistance of a single conducting membrane channel. *Biochimica et Biophysica Acta (BBA) - Biomembranes*, 1368(2):338 – 342, 1998.

[160] J E Hall. Access resistance of a small circular pore. *The Journal of General Physiology*, 66(4):531–532, 1975.

[161] Bertil Hille. Ionic channels in nerve membranes. *Progress in Biophysics and Molecular Biology*, 21:1 – 32, 1970.

[162] Bertil Hille. Pharmacological modifications of the sodium channels of frog nerve. *The Journal of general physiology*, 51:199–219, 03 1968.

[163] Michael Zwolak, James Wilson, and Massimiliano Di Ventra. Dehydration and ionic conductance quantization in nanopores. *Journal of physics. Condensed matter : an Institute of Physics journal*, 22:454126, 11 2010.

[164] Charles Kittel. *Introduction to Solid State Physics*. John Wiley & Sons, Inc., New York, 8th edition, 2004.

[165] Jiandong Feng, Ke Liu, Michael Graf, Dumitru Dumcenco, Andras Kis, Massimiliano Di Ventra, and Aleksandra Radenovic. Observation of ionic coulomb blockade in nanopores. *Nature materials*, 15, 03 2016.

[166] Michael Graf, Ke Liu, Aditya Sarathy, Jean-Pierre Leburton, and Aleksandra Radenovic. Transverse detection of dna in a mos 2 nanopore. *Biophysical Journal*, 114:180a, 02 2018.

[167] Hu Qiu, Aditya Sarathy, Klaus Schulten, and Jean-Pierre Leburton. Detection and mapping of dna methylation with 2d material nanopores. *npj 2D Materials and Applications*, 1:3, 04 2017.

[168] Aditya Sarathy, Nagendra B. Athreya, Lav R. Varshney, and Jean-Pierre Leburton. Classification of epigenetic biomarkers with atomically thin nanopores. *The Journal of Physical Chemistry Letters*, 9:5718–5725, 09 2018.

[169] Daniel Fologea, James Uplinger, Brian Thomas, David S. McNabb, and Jiali Li. Slowing dna translocation in a solid-state nanopore. *Nano Letters*, 5(9):1734–1737, 2005. PMID: 16159215.

[170] Stefan W. Kowalczyk, David B. Wells, Aleksei Aksimentiev, and Cees Dekker. Slowing down dna translocation through a nanopore in lithium chloride. *Nano Letters*, 12(2):1038–1044, 2012. PMID: 22229707.

[171] Vasiliki Paraskevopoulou and Franco Falcone. Polyionic tags as enhancers of protein solubility in recombinant protein expression. *Microorganisms*, 6, 05 2018.

[172] Lingzhi Wu, Hang Liu, Wenyuan Zhao, Lei Wang, Chuanrong Hou, Quanjun Liu, and Zuhong Lu. Electrically facilitated translocation of protein through solid nanopore. *Nanoscale research letters*, 9:140, 03 2014.

[173] Francois Sicard and Patrick Senet. Reconstructing the free-energy landscape of met-enkephalin using dihedral principal component analysis and well-tempered metadynamics. *The Journal of chemical physics*, 138:235101, 06 2013.

[174] Xin Chen, Nina Berner, Claudia Backes, Georg Duesberg, and Aidan R McDonald. Functionalization of two-dimensional mos2 : On the reaction between mos2 and organic thiols. *Angewandte Chemie (International ed. in English)*, 55, 04 2016.

[175] Qi Chen and Zewen Liu. Fabrication and applications of solid-state nanopores. *Sensors*, 19:1886, 04 2019.

[176] David Cohen-Tanugi and Jeffrey C. Grossman. Water desalination across nanoporous graphene. *Nano Letters*, 12(7):3602–3608, 2012. PMID: 22668008.

[177] Alex Smolyanitsky, Eugene Paulechka, and Kenneth Kroenlein. Aqueous ion trapping and transport in graphene-embedded 18-crown-6 ether pores. *ACS Nano*, 12(7):6677–6684, 2018. PMID: 29940107.

[178] Amedeo Bellunato, Hadi Arjmandi-Tash, Y. Cesa, and Grégory Schneider. Chemistry at the edge of graphene. *Chemphyschem : a European journal of chemical physics and physical chemistry*, 17, 12 2015.

[179] Sang N. Kim, Zhifeng Kuang, Joseph M. Slocik, Sharon E. Jones, Yue Cui, Barry L. Farmer, Michael C. McAlpine, and Rajesh R. Naik. Preferential binding of peptides to graphene edges and planes. *Journal of the American Chemical Society*, 133(37):14480–14483, 2011. PMID: 21861527.

[180] Khalid Hussain Thebo, Xitang Qian, Qing ling Zhang, Long Chen, Hui-Ming Cheng, and Wencai Ren. Highly stable graphene-oxide-based membranes with superior permeability. In *Nature Communications*, 2018.

[181] Na An, Aaron Fleming, Henry White, and Cynthia Burrows. Crown ether-electrolyte interactions permit nanopore detection of individual dna abasic sites in single molecules. *Proceedings of the National Academy of Sciences of the United States of America*, 109:11504–9, 06 2012.

[182] Emily Nguyen, Benjamin Carey, Jian Ou, Joel van Embden, Enrico Della Gaspera, Adam Chrimes, Michelle Spencer, Serge Zhuiykov, Kourosh Kalantar-zadeh, and Torben Daeneke. Electronic tuning of 2d mos2 through surface functionalization. *Advanced materials (Deerfield Beach, Fla.)*, 27, 09 2015.

[183] Anastasios Stergiou and Nikos Tagmatarchis. Molecular functionalization of 2d mos2 nanosheets. *Chemistry - A European Journal*, 24, 10 2018.

[184] Kedi Yin, Shengxi Huang, Xiaofei Chen, Xinwei Wang, Jing Kong, Yan Chen, and Jianming Xue. Generating sub-nanometer pores in single-layer mos2 by heavy-ion bombardment for gas separation: A theoretical perspective. *ACS Applied Materials & Interfaces*, 10(34):28909–28917, 2018. PMID: 30062872.

Appendices

Appendix A

Computational investigation of the ionic conductance through molybdenum disulfide (MoS_2) nanopores

Computational investigation of the ionic conductance through molybdenum disulfide (MoS_2) nanopores

María Daniela BARRIOS PEREZ[1], Patrick SENET[1,†], Vincent MEUNIER[2], Adrien NICOLAÏ[1,‡]
[1]Laboratoire Interdisciplinaire Carnot de Bourgogne UMR 6303 CNRS-Université de Bourgogne Franche-Comté, 9 Avenue Alain Savary, BP 47870, F-21078 Dijon Cedex, FRANCE.
[2]Department of Physics, Applied Physics, and Astronomy, Rensselaer Polytechnic Institute, 110 8th street, Troy, NY 12180, USA.
Corresponding authors: †psenet@u-bourgogne.fr, ‡adrien.nicolai@u-bourgogne.fr

Abstract: Solid-state nanopores have emerged as versatile devices for probing single molecules. Because the channel conductance of the ionic flow through nanopores scales inversely with the membrane thickness, few-atoms thick materials are ideal candidates with an expected high signal-to-noise ratio. On one hand, graphene nanopores have been extensively studied because they exhibit the highest signal. However, they also exhibit high noise. On the other hand, transition metal dichalcogenides such as molybdenum disulfide (MoS_2) are potentially advantageous due to their rich optoelectronic and mechanical properties. In this paper, we investigate the dynamics of KCl ions through MoS_2 nanopores using non-equilibrium molecular dynamics (MD) simulations. MoS_2 nanopores with different diameters, from 1.0 to 3.0 nm and nanoporous membranes with different thicknesses, from single-layer to trilayers MoS_2 are studied. The structural properties of ions and water inside MoS_2 nanopores are discussed and the performance of MoS_2 nanopores to conduct ions at low voltages is quantified by computing I-V curves in order to extract open pore conductance and by comparing MD data to analytical models. This comparison reveals that ionic conductance and *effective* geometrical parameters for MoS_2 nanoporous membranes extracted from models are overestimated. We provide open pore benchmark signals for further translocation simulations/experiments using MoS_2 nanopores.

Key–Words: nanopores, MoS_2, MD simulations, open pore conductance, bulk conductivity, effective diameter, effective thickness

1 Introduction

Solid-state nanopores (SSN), which are typically synthesized using stimuli-responsive materials as the body component, arise as sensor for the detection of single molecules [1]. One of the highest-profile applications of SSN is DNA sequencing, as they hold the potential to do that faster and cheaper than current industrial standards [2]. SSN sequencing is based on experimental measurement of the variations in ionic current as the molecules translocate through nanometer-sized channels when an external voltage is applied across the membrane. As charged molecules in ionic solution pass through nanopores, they displace ions from the pore volume. Therefore, ultrafast monitoring of ion flow [3] during the passage of a particle through SSN yields information about the particle structure and chemical properties. Precisely, SSN detect the presence of individual molecules via a change in ionic conductance ΔG. ΔG represents a drop in ionic conductance, such as $\Delta G = G_0 - G_m$, where G_0 is the open pore conductance and G_m is the conductance when the nanopore is obstructed by a translocating molecule, also called translocation conductance. Therefore, increasing ΔG and decreasing the signal noise yield a higher signal-to-noise ratio (SNR). Thus, assuming constant noise, increasing ΔG improves the performance of nanopore devices. Hence, the magnitude and statistical properties of ΔG provide good metrics for the nanopore sensing capability [4].

For instance, if the molecule translocating through a SSN is characterized by the same size as the pore dimension, for instance a double strand DNA molecule translocating in a SSN of diameter $D \sim 2.2$ nm, the theoretical conductance drop is equal to the open pore conductance, $\Delta G = G_0$. In order to fabricate DNA sequencing devices with a high-resolution recognition and detection of DNA bases, the diameter of the nanopore must be of the same order of magnitude as that of the molecule to be detected. SSN are characterized by two parameters: the diameter of the pore D and the thickness of the membrane h. These two parameters can be easily characterized in all-atom simulations compared to

experiments where they are usually estimated and named *effective* parameters. Since the diameter of the pore is chosen according to the size of the molecule that is probed, the thickness h is the controllable parameter. Therefore, nanopores drilled in solid-state thin films improve significantly the signal for molecule detection because the conductance of the ionic flow through SSN scales inversely with the nanoporous membrane thickness [5]. It follows that both the magnitudes of the open pore current G_0 and of the blockade current G_m increase with the decreasing thickness of the film.

Based on the above discussion, ultra-thin membranes are thus ideal candidates for single-molecule sequencing with a high SNR. Over the past decade, stable nanomaterials have enabled the investigation of advanced thin-film nanopores, in which single-residue discrimination should be possible and has already been done using biological nanopores [8]. For example, graphene nanopores have emerged as ideal candidates due to the fact they exhibit the highest signal (one-atom thick layer). In particular, experiments on DNA translocation through single-layer graphene nanopores have been successfully performed in 2010 by three independent groups [9–11]. However, the high noise that characterizes graphene nanopores experimentally have made them poor devices [12], leading to a SNR around 3.5. Furthermore, efforts to fabricate nanoporous membranes including thinning silicon nitride (SiN_x) films can be an alternative path but drilling a nanometer-sized pore with reactive-ion etching [6, 7] or using an electron beam [4] is very sensitive to the mechanical strength of such thin-films. For instance, in a previous work on amorphous silicon (a-Si) membranes, we showed that the thickness limit lies at about 1.0 nm [4]. In parallel to experiments, molecular dynamics (MD) simulations were also performed to study the performances of solid-state nanopores for DNA translocation through ionic current measurements [13]. In particular, graphene nanopores have been extensively studied [14–16].

New two-dimensional (2-D) materials in which nanopores can be drilled experimentally with a high reproducibility are therefore needed. Transition-metal dichalcogenides (TMD) are a class of 2-D materials in the form of MeX_2 (Me = transition metal such as Mo, W, Ti, Nb, etc. and X = S, Se, or Te), which are potentially advantageous for SSN applications due to their rich optoelectronic and mechanical properties [17]. Structurally, one layer of Me atoms is sandwiched between two layers of X atoms and TMD bulk crystals are formed of monolayers bound to each other by van der Waals (vdW) attraction (Figure 1a). In addition, encouraging experimental results on MoS_2 nanopores published in 2014 indicate improved signal-to-noise ratio (SNR $>$ 10) [18], ease of DNA translocation, and no special surface treatment requirement. However, the diameters of the nanopores studied in this early work were too large for DNA sequencing (from 5 to 20 nm). Since then, only one computational study has been carried out on DNA base detection using a single-layer MoS_2 [19].

In the present paper, we focus on the open pore conductance of a 1M KCl ionic solution through MoS_2 nanoporous membranes using classical MD simulations. SSN with diameters ranging from 1.0 to 3.0 nm are studied here. The characteristics of SSN with a diameter $D = 2.0$ nm made of single-layer (SL), bilayers (BL) and trilayers (TL) MoS_2 are also presented (Figure 1). Current-voltage characteristics (I-V curves), water distribution around MoS_2 nanoporous membranes and concentration of ions inside SSN are discussed. Finally, the data extracted from MD simulations are compared to a theoretical model commonly used to characterize ionic conductance and *effective* parameters of SSN in experiments [5, 6], with a combination of access resistance and pore resistance:

$$\frac{1}{G} = R = R_{access} + R_{pore} = \frac{1}{D\sigma} + \frac{4h}{\pi\sigma D^2} \quad (1)$$

where D is the pore diameter, σ is the ionic bulk conductivity, and h is the thickness of the membrane. The aim of this work is to provide a benchmark of expected open pore conductances G_0 and to estimate ideal conductance drops ΔG of MoS_2 nanopores for further simulations/experiments. A comparison of MoS_2 with graphene nanopores is also discussed.

2 Materials and Methods

2.1 System Setup

Initially, MoS_2 layers were constructed using 2-D unit cell lattice vectors $\vec{a} = (3.13, 0, 0)$ and $\vec{b} = (0, 5.42, 0)$. Each rectangular unit cell for MoS_2 has 6 atoms, 2 Mo and 4 S atoms. The Mo-S bond length was taken as $d_{Mo-S} = 2.38$ Å and the S-S distance was taken as $d_{S-S} = 3.11$ Å. The unit cell was replicated in both x and y direction in order to generate layers of dimension 10 $\times$ 10 nm^2. For multiple-layers MoS_2 membranes, as shown in Figure 1a, the interlayer spacing was taken as $d_{is} = 3.15$ Å. MoS_2 pores were constructed by removing atoms whose coordinates satisfy $x^2 + y^2 < R^2$, where $D = 2R$ is the diameter of the

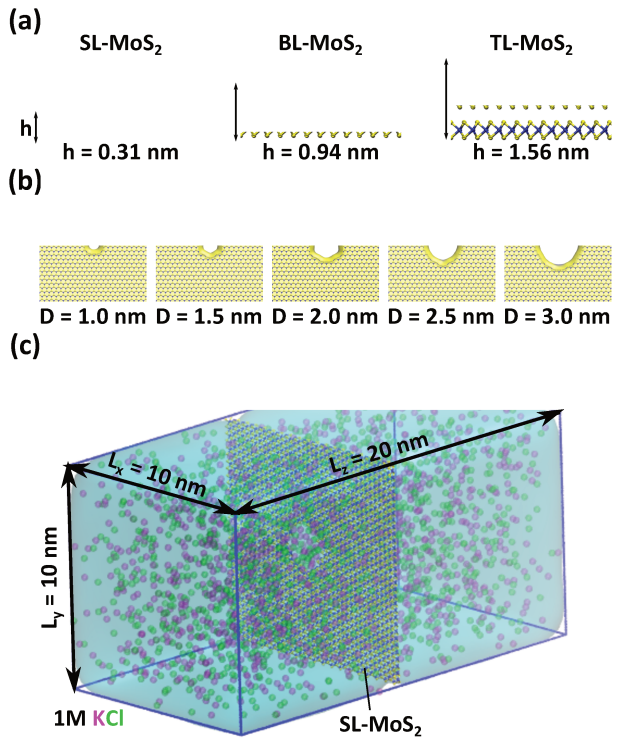

Figure 1: (a) All-atom structures of the MoS_2 membranes studied in the present work. MoS_2 membranes are shown in ball and stick representations with Mo atoms colored in blue and S atoms in yellow. Single-layer (SL), bilayers (BL) and trilayers (TL) MoS_2 are shown with their respective thicknesses. (b) All-atom structures of the MoS_2 nanopores studied in the present work. The color code is the same as in panel a. (c) Snapshot of MD simulation of ion transport through a SL-MoS_2 nanopore. Nanopore diameter is $D = 2.0$ nm. Water molecules are represented by a blue surface. K^+ and Cl^- ions are represented by magenta and green spheres, respectively.

pore and considering the center of the pore at the origin of the box. The pore diameters that we considered in this work are 1.0, 1.5, 2.0, 2.5 and 3.0 nm, as shown in Figure 1(b). A Stillinger-Weber (SW) potential was used during MD simulations to characterize Mo-S interactions [20].

A MoS_2 nanoporous membrane is located at the center of the simulation box of dimension $L_x \times L_y \times L_z = 10 \times 10 \times 20$ nm^3, filled with water molecules and 1M KCl. It represents more than 62,000 water molecules and more than 2,400 ions. The non-bonded interactions between MoS_2 nanopore, water and ions were described using a Lennard-Jones (LJ) plus Coulomb potential. The water model used in the present work is the TIP3P model [21]. LJ parameters for K^+ and Cl^- ions were taken from reference [22], where specific parameters were developed for the water model employed. LJ parameters for Mo and S atoms were taken from reference [23], as already used in other works [24]. Lorentz-Berthelot mixing rules were applied to compute cross-interactions between the different species.

For graphene nanopores, the same procedure was followed using the same dimension for the nanoporous membranes. 2-D unit cell lattice vectors are $\vec{a} = (2.46, 0, 0)$ and $\vec{b} = (0, 4.26, 0)$. Each rectangular unit cell for graphene has 4 C atoms. The C-C bond length was taken as $d_{C-C} = 2.46$ Å. C-C interactions during MD simulations were described using a Tersoff potential [25]. Water model and LJ parameters for ions are the same as for MoS_2. Finally, LJ parameters for C atoms were taken from reference [26].

2.2 Non-equilibrium MD simulations

Non-equilibrium MD simulations (NEMD) were performed using the LAMMPS software package [27] employing periodic boundary conditions in all directions. An external applied electric field was used to investigate ionic currents and conductance through MoS_2 and graphene nanopores. Before running the MD part, an equilibration of the system in the NPT ensemble ($T = 300$ K and $P = 1$ bar) without any electric field was performed during 100 ps to relax the simulation box and the solvent at the target temperature and pressure. Relaxation was followed by MD runs of 10 ns carried out in the NVT ensemble using the velocity-Verlet algorithm [28] with a time step of 1 fs. A Nosé-Hoover thermostat [29, 30] was used to maintain the temperature at 300 K with a time constant of 0.1 ps. Particle-particle particle-mesh method [31] was used to describe long range electrostatic interactions. A cutoff of 1.0 nm was applied to LJ and Coulomb potential for non-bonded interactions. A SHAKE algorithm [32] was used to constrain the bond lengths and angle of TIP3P water molecules. Finally, simulations were carried out by applying a uniform electric field, directed normal to the nanoporous membrane (z-direction), to all atomic partial charges in the system. The corresponding applied potential is $V = EL_z$, where L_z is the length of the simulation box in the z-direction. For each system presented in Table 1, simulations with $V = 0$, 0.25, 0.5, 0.75, 1.0, 1.5, 2.0, 2.5 and 3.0 V were performed.

2.3 Data Analysis

Ionic current

In order to compute the current-voltage ($I - V$) characteristics of MoS_2 nanopores, we computed the

total net ionic current $I(t)$ as

$$I(t) = \frac{1}{\Delta t L_z} \sum_{i=1}^{N} q_i [z_i(t + \Delta t) - z_i(t)] \quad (2)$$

where Δt is the time between MD frames chosen to be 10 ps here), L_z is the dimension of the simulation box in the z-direction, which is the direction of the applied electric field, N is the total number of ions, q_i is the charge of the ion i and $z_i(t)$ is the z-coordinate of the ion i at time t. Ionic currents reported later are computed as the simple moving average of the 10 ns MD runs. The standard error of the ionic current was computed using $\sigma/\sqrt{N_f}$, where N_f is the number of frames used for calculating the average current and σ is the standard deviation. Error bars are of the order of magnitude of 0.2 nS for MoS_2 nanopores of diameter $D = 2.0$ nm with an applied voltage $V = 1.0$ V. Therefore, they are not represented in $I - V$ curves shown in Figure 2.

Normal and in-plane radial distributions of water

In order to estimate the *effective* thickness and diameter of the different nanoporous membranes made of MoS_2 layers, we computed the radial distribution of water molecules inside the pore (ρ direction) as well as the distribution of water molecules in the direction normal to the membrane (z direction here). First, the normal distribution was computed by counting the number of water molecules in boxes of dimension $L_x \times L_y \times \Delta z$, with Δz =1 Å. Starting from the membrane, the box was displaced by 0.1 Å in the normal direction up to reaching the top of the simulations box. Second, the in-plane radial distribution of water was computed over concentric cylinders with the pore axis. Each ring is characterized with a height corresponding to the z-position of the center of the nanopore ± 1 Å (total height of 2 Å) and with a 1 Å width from the inner to the outer boundaries. Starting from the center of the pore, the inner boundary of each cylinder was displaced by 0.25 Å in the radial direction, up to reaching the nanopore edge. The radial and normal distributions reported below were averaged over the 10 ns MD runs with voltages $0 < V \leq 1.0$ V, for a total duration of 40 ns (4 runs).

Radial ionic concentration

In order to investigate the ion distribution inside the nanopores and particularly near the nanopore edges, we computed the ion concentration (number of ions/nm^3) as a function of the radial distance ρ from the center of the pore ($\rho = 0$) from MD trajectories. For that purpose, we averaged the ion concentration over concentric cylinders with the pore axis. Each ring has a height corresponding to the *effective* height of the nanopore h_{eff} and a width of 1 Å from the inner to the outer boundaries. Starting from the center of the pore, the inner boundary of each cylinder was displaced by 0.25 Å in the radial direction, up to reaching the nanopore edge. The radial ionic concentrations reported below are average values over positively and negatively charged ions, for the 10 ns MD runs with voltages $0 < V \leq 1.0$ V, for a total duration of 40 ns (4 runs).

3 Results and Discussion

3.1 Current-Voltage characteristics

$I - V$ curves for each system were computed as explained in section 2 and are presented in Figure 2. First, $I - V$ curves were only computed from simulation with positive voltages since nanoporous membranes made of graphene and MoS_2 are symmetric and extremely thin along the normal direction of the membrane (z-direction). Therefore, no ionic rectification is observed [33]. However, negative voltages were tested for one system (SL-MoS_2 with $D = 2.0$ nm) and the absence of rectification was confirmed (data not shown).

From simulations with $V = 0$ to 3.0 V, two types of regime were detected: a linear regime from 0 to 1.0 V, corresponding to an ohmic behavior of the nanopore, and a sublinear regime from 1.0 to 3.0 V (inset Figure 2a). Several interpretations of the physical meaning of this sublinear behavior of $I - V$ curves at high voltages are still being debated in the literature. In particular, permeation of ions through small confined spaces such as ionic channels has been considered diffusion-limited. Recently, in contrast with the permeation theory, factors such as ion hydration and their configurational restraint due to the coordination with water molecules while crossing the channel, can induce a free-energy barrier that leads to a saturation of the current I at high voltages [34]. In the present work, we only focus on the linear part of the $I - V$ curves since experimentally, the applied voltages are usually of magnitude of several hundreds of mV at maximum. The values of open pore conductance were extracted from the linear response regime, as the slope of the $I - V$ characteristics.

By comparing graphene and MoS_2 nanopores of diameter $D = 2.0$ nm, we observed that the slope of the $I - V$ curves are relatively close, leading to open

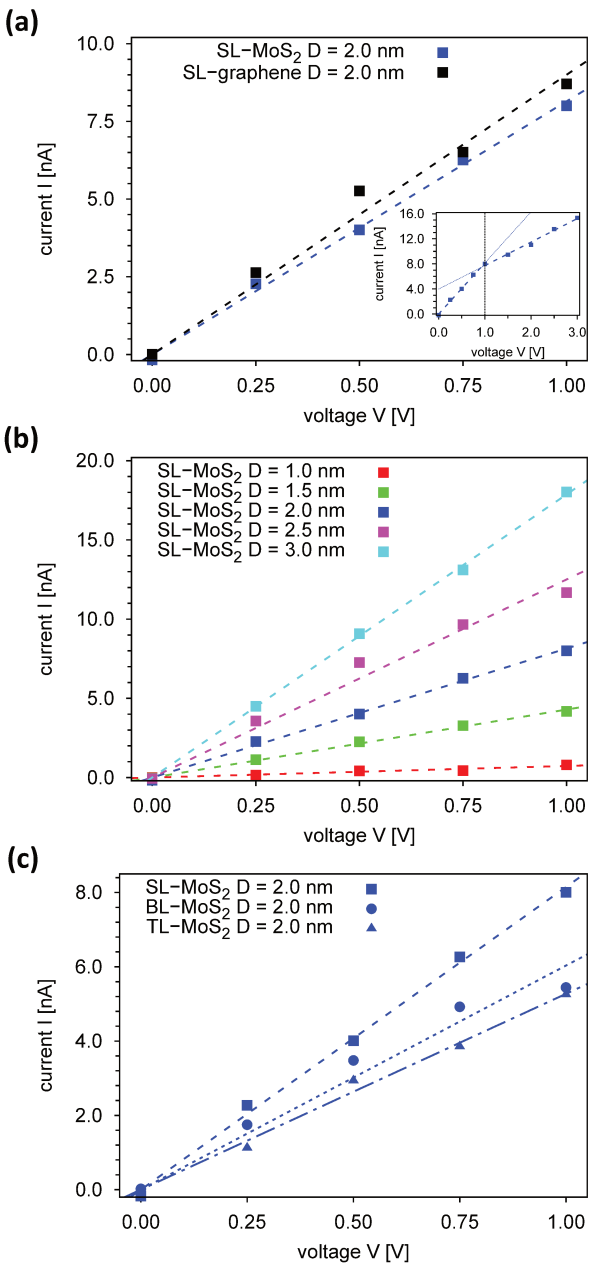

Figure 2: Current-voltage $I-V$ characteristics of nanopores studied in the present work. Data from 0 to 1.0 V are shown except inset of panel a. (a) $I-V$ curves for single-layer graphene (black) and MoS_2 (blue) nanopores of diameter $D = 2.0$ nm. The inset in panel a represents the $I-V$ curve for MoS_2 up to 3.0 V. (b) $I-V$ curves for single-layer MoS_2 nanopores of diameter $D = 1.0$ (red), 1.5 (green), 2.0 (blue), 2.5 (magenta) and 3.0 nm (cyan). (c) $I-V$ curves for single-layer (blue squares), bilayers (blue circles) and trilayers (blue triangles) MoS_2 nanopores of diameter $D = 2.0$ nm. Dashed lines represent the linear behavior fitted onto the MD data. Open pore conductances G_0 were obtained as the slope of the linear fits.

pore conductances G_0 of 9.0 and 8.1 nS, respectively. Despite the fact that MoS_2 has a thickness larger than graphene, it can still be considered as an ultra-thin membrane. In addition, MD simulations show that a diameter $D = 1.0$ nm is a critical diameter for MoS_2 nanopores since G_0 is around 0.7 nS, whereas $G_0 = 4.3$ nS for $D = 1.5$ nm (Table 1). Finally, we compared open pore conductances G_0 of SL, BL and TL-MoS_2. As shown in panel c of Figure 2, there is a difference of 2.1 nS between SL and BL-MoS_2, which represents a variation of $\sim 30\%$ by increasing the thickness by a factor 3. However, there is no significant difference between BL and TL-MoS_2 (0.8 nS). It means that TL-MoS_2 could be a efficient alternative to BL-MoS_2 in terms of open pore conductances G_0 and fabrication process since at the nanoscale, manipulating thicker objects is easier. Furthermore, it has been shown for graphene that the noise reduces with layer thickness [12].

3.2 Interfacial interactions of water with MoS_2 nanoporous membranes and *effective* geometrical parameters

Experimentally, in lieu of using techniques to measure the geometrical parameters of the nanoporous membranes (diameter D and thickness h) that might deteriorate the sample, the measured G_0 is used to extract the *effective* pore diameter D_{eff} and membrane thickness h_{eff} using a cylindrical model for nanopore conductance [4, 5]. Using MD simulations, *effective* parameters can also be extracted and in particular by characterizing the interfacial interactions between the solvent and the nanoporous membrane. In fact, the interactions at the interface between a SSN and the ionic solution made of water molecules and K^+ and Cl^- ions are strongly influenced by the nature of the 2-D materials and can be fully described at the atomic level using all-atom MD simulations.

The interactions between water molecules and the nanoporous membrane in the normal direction of the membrane (z-direction, Figure 1) bring

SSN	h	h_{eff}	D	D_{eff}	G_0
			1.0	-	0.7
			1.5	1.20	4.3
SL-MoS_2	0.31	0.96	2.0	1.64	8.1
			2.5	2.14	12.5
			3.0	2.72	17.9
BL-MoS_2	0.94	1.44	2.0	1.64	6.0
TL-MoS_2	1.56	2.16	2.0	1.64	5.3
graphene	-	0.74	2.0	1.72	9.0

Table 1: Solid-state nanopores studied in the present work using NEMD simulations. Diameters D and D_{eff} as well as thicknesses h and h_{eff} are given in nm. Conductances G_0 are given in nS.

information into the modification of the bulk water properties due to the presence of the membrane. As explained in section 2, we computed the probability distribution $P(z)$ to find a water molecule at a certain normal distance z from the membrane. Figure 3a shows the results extracted from simulations for a graphene and a MoS_2 nanopore of diameter $D = 2.0$ nm. From this distribution, we extracted the *effective* thickness of the nanoporous membrane, which represents the minimum thickness from which the water structure is significantly modified. Our definition is the following: starting from the surface of the membrane, $P(z) \sim 0$, the first value of z giving the bulk value of P is considered as $h_{eff}/2$ (Figure 3a). According to our simulations, the *effective* thickness is found to be ~0.74 nm for graphene and 0.96 nm for MoS_2 (Table 1). We performed the same analysis for bilayers and trilayers MoS_2 and the *effective* thicknesses are 1.44 and 2.16 nm, respectively (Table 1). It corresponds to a factor of ~3 between h and h_{eff} for SL-MoS_2 whereas it is associated with a factor ~ 1.5 for BL and TL-MoS_2. In contrast, the diameter D has no influence on the structural properties of water in the normal direction of the membrane (data not shown) since the surface of the pore ($S = \pi R^2 < 10$ nm^2) represents a small fraction of the total surface of the nanoporous membrane ($L_x \times L_y = 100$ nm^2).

We performed the same type of analysis in order to extract the *effective* diameter of a SSN from the water in-plane radial distribution inside the pore. Figure 3b shows the results extracted from MD simulations for a graphene and a MoS_2 nanopore of diameter $D = 2.0$ nm. Our definition of the *effective* diameter is the following: starting from the center of the pore which corresponds to the value $C(\rho)_0$, the last value of ρ for which the radial distribution completely decreases approaching the edges is considered as $R_{eff} = D_{eff}/2$ (Figure 3b). It leads to *effective* diameters D_{eff} values of 1.72 and 1.64 nm for graphene and MoS_2, respectively. Despite this difference of 0.8 Å for the *effective* diameter between graphene and MoS_2, the profiles of water concentration are similar in shape with a maximum at 0.80 and 0.75 nm, respectively (Figure 3). The maximum is located at a larger ρ for graphene due to the significant hydrophobicity of the carbon material. Moreover, the concentration of water at the mouth of the graphene nanopore is larger than the one at the mouth of the MoS_2 nanopore ($D = 2.0$ nm). These two properties can be explained by a steric effect due to the fact that Mo atoms are characterized by a larger vdW diameter than C atoms. LJ parameters σ of Mo and C atoms are 3.4 and 4.2Å, respectively. It

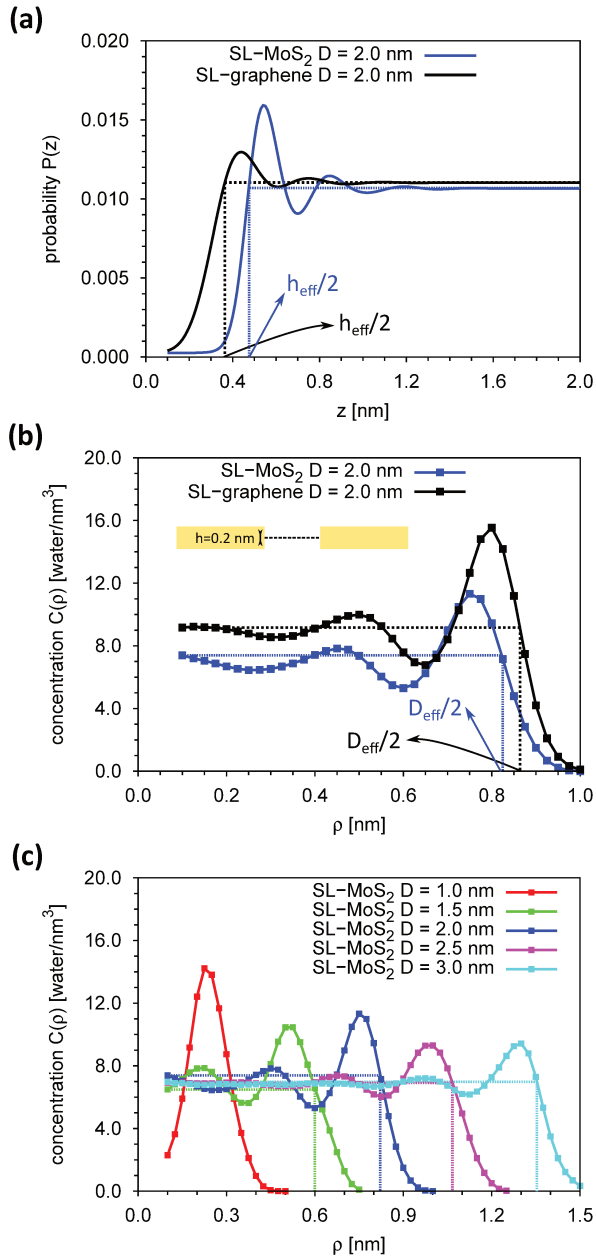

Figure 3: (a) Probability distribution functions $P(z)$ of water molecules in the normal direction (z-direction) of the nanoporous membrane. Graphene is shown in black and SL-MoS_2 in blue for a diameter $D = 2.0$ nm.(b) In-plane radial distribution $C(\rho)$ of water molecules inside the nanopore. Graphene is shown in black and SL-MoS_2 in blue for a diameter $D = 2.0$ nm. The inset in panel b corresponds to a schematic representation of the in-plane calculation. (c) In-plane radial distribution $C(\rho)$ of water molecules inside single-layer MoS_2 nanopores of diameters $D = 1.0$ (red), 1.5 (green), 2.0 (blue), 2.5 (magenta) and 3.0 nm (cyan). Dashed lines represent the value of the *effective* thicknesses (panel a) and diameters (panels b and c) extracted from the distributions.

corresponds exactly to the difference of *effective* diameters between the two nanopores.

For SSN made of a SL-MoS_2 and of different

diameters D as shown in Figure 3c, the shape of the concentration profiles is identical. The property which is modified by the increase or decrease of the diameter D of the nanopore is the length of the plateau $C(\rho)$, leading to larger *effective* diameters D_{eff} for larger diameters D (Table 1). For SL-MoS_2, the ratio D_{eff}/D is found to be around 0.8 from MD simulations. For SSN of diameters $D = 2.0$ nm and of different thicknesses h, *effective* diameters extracted from the water in-plane radial distribution are the same as for SL-MoS_2 (data not shown).

3.3 Concentration of ions in MoS_2 nanopores

Using the *effective* thickness h_{eff} of graphene and MoS_2 membranes, we computed the radial ionic concentration in cylindrical pores (Figure 4), as explained in section 2. The advantage of this analysis is to quantify the effect of the dangling atoms on the edges of the pore onto the concentration of ions in MoS_2 nanopores. As shown in Figure 4b, the radial concentration of ions inside a MoS_2 nanopore of diameter $D = 2.0$ nm is characterized by a plateau starting at $\rho = 0$ up to ρ_{max}, followed by a linear decrease from ρ_{max} to R_{eff}, the *effective* radius of the nanopore (see section 3.2). The same behavior is observed for graphene with the same diameter, except that first, the length of the plateau (ρ_{max}) is larger than the one observed for MoS_2. Second, the concentration at the center of the pore is larger for MoS_2 than for graphene since the volume of the cylindrical pore is larger ($V_{cyl} = 3.0$ and 2.3 nm^3, respectively). Third, the decrease of the concentration is faster for MoS_2 nanopores. It comes from the fact that Mo atoms are characterized by larger vdW diameters than C atoms, which involves a larger repulsion.

The same behavior is also observed in MoS_2 nanopores of different diameters D, as shown in Figure 4d. In fact, the length of the plateau is larger as the diameter increases. In addition, the concentration of ions at the center of the pore decreases with the diameter from 1.5 nm to 3 nm. For larger diameters, KCl ions tend to occupy the entire space of the pore whereas for smaller diameter they are confined at the center of the pore due to the repulsion forces involved by the edges of the pore. Finally, as already stated previously, the behavior of MoS_2 nanopores with a diameter $D = 1.0$ nm is completely different. In this case, the concentration of ions is so low that it can be considered as a null concentration. For MoS_2 nanopores made of multiple layers, the ionic concentration profiles are similar to those of the single layer. The concentration at the

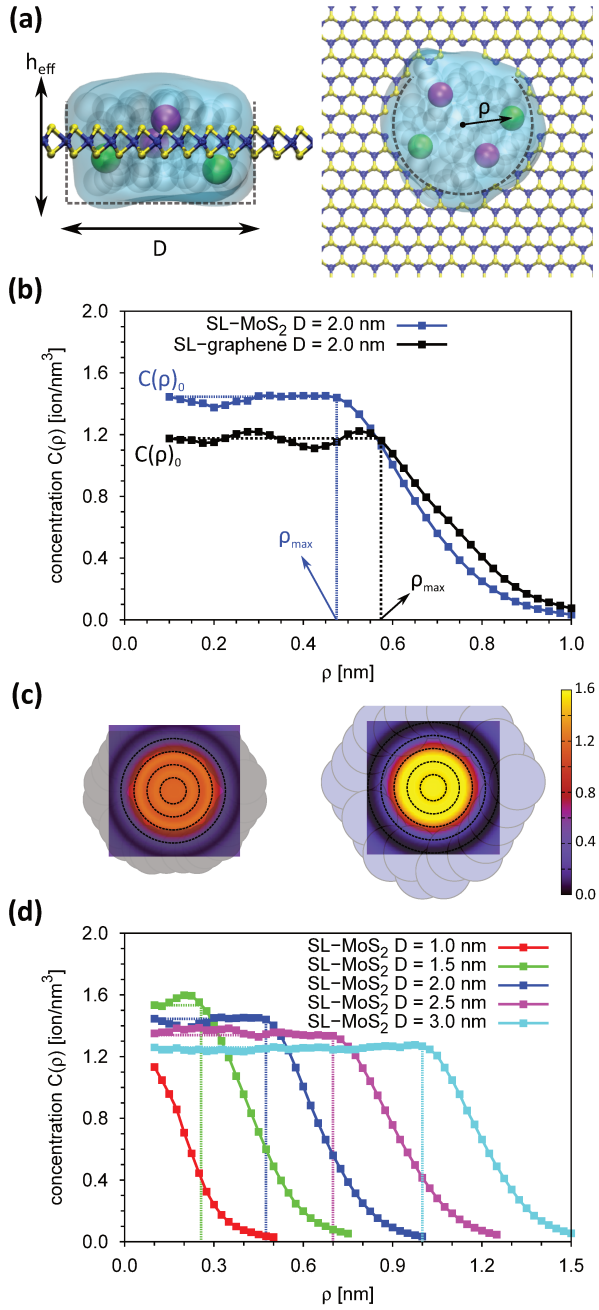

Figure 4: (a) Snapshot of MD simulations representing water molecules and KCl ions inside a SL-MoS_2 nanopore of diameter $D = 2.0$ nm. Water molecules are represented with blue transparent spheres and a blue surface. K^+ and Cl^- ions are represented by magenta and green spheres, respectively. (b) Radial concentration of KCl ions inside a graphene (black) and a SL-MoS_2 (blue) nanopore of diameter $D = 2.0$ nm. (c) Color map of ionic concentration (colorbox in ion/nm^3) in a graphene (left panel) and MoS_2 nanopore of diameter $D = 2.0$ nm. Transparent black and blue circles represent spheres centered on the C and Mo atoms with a radius equal to the parameters σ_C and σ_{Mo} atoms of the LJ potential, respectively. (d) Radial concentration of KCl ions inside a SL-MoS_2 (blue) nanopore of diameters $D = 1.0$ (red), 1.5 (green), 2.0 (blue), 2.5 (magenta) and 3.0 nm (cyan). Dashed lines indicate the length of the plateau ρ_{max}.

center of the pore is larger than in single-layer nanopores ($C(\rho)_0 \sim 2.0$ ions/nm^3) due to the fact that the *effective* volume of the cylinders is larger.

The main question that arises here is: what is the impact of such ionic concentration profiles on conductance drop measurements during an experiment? The answer to this question is not simple and we will provide a number of hypotheses. Consider a SL-MoS_2 nanopore of diameter $D = 3.0$ nm. From the concentration profile shown in Figure 4d, we estimate the length of the plateau $C(\rho)_0$ to be around 2.0 nm. This means that if a molecule such as a rigid double-strand B-DNA molecule ($D_{DNA} = 2.0$ nm) translocates into the nanopore, the ionic concentration between the molecule and the edges of the pore would be $\sim$0. Therefore, the conductance drop ΔG would be similar to G_0, the open pore conductance. Compared to graphene for which the plateau is larger, the conductance drop ΔG would be smaller than G_0 despite the fact that the same object is translocated in a pore of the same diameter.

3.4 Comparison of MD data for MoS_2 nanopores with analytical model of conductance

The values of the open pore conductance G_0 obtained for MoS_2 nanopores from NEMD simulations have been compared to the analytical model of conductance (Eq. 1) by inserting the bulk conductivity σ of 1M KCl. The bulk conductivity was computed by performing NEMD simulations of the ionic solution without nanopore in a simulation box of the same size as that used for the MD simulations including the nanopore. The value extracted from MD is $\sigma = 12.8$ S m^{-1} which is relatively close to values reported in the literature, *i.e.* $\sigma \sim$10-12 S m^{-1} [4]. The fit of the MD data was performed in two steps: first, we fitted the MD data of SL-MoS_2 for different diameters D using different definitions for the thickness h as shown in Figure 5a. Second, we fitted the MD data of MoS_2 nanopores of diameter $D = 2.0$ nm for different thicknesses h using different definitions for the diameter D as shown in Figure 5b.

As shown in Figure 5 using the actual geometrical parameters h and D from the atomic structure, values of open pore conductance G_0 are largely overestimated by the model. Moreover, using the *effective* geometrical parameters h_{eff} and D_{eff} estimated from the water distributions (see section 3.2), open pore conductances G_0 are also overestimated by the model. Particularly using the *effective* thickness $h_{eff} = 0.96$ nm. Therefore, we decided to extract the values of h and D by fitting the model defined in Eq. 1 using h as a free parameter from $G_0 = f(D)$ (panel a of Figure 5) and using D as a free parameter from $G_0 = f(h)$ (panel b of Figure 5). Doing this, we got $h_{fit} = 3.1$ nm and $D_{fit} = 0.98$ nm, respectively. The value of h_{fit} is 10 times larger than the actual thickness of SL-MoS_2, *i.e.* $h = 0.31$ nm, whereas the value of D_{fit} is 2 times smaller than the actual diameter, *i.e.* $D = 2.0$ nm. It means that there is a discrepancy between bulk conductivity σ and the pore conductivity for diameters comprised ranging from 1.5 to 3.0 nm.

As suggested by Suk and Aluru in their paper about sub-5 nm graphene nanopores [35], the bulk conductivity σ should be replaced in the model defined in Eq. 1 for diameters $D \sim 2.0$ nm by an

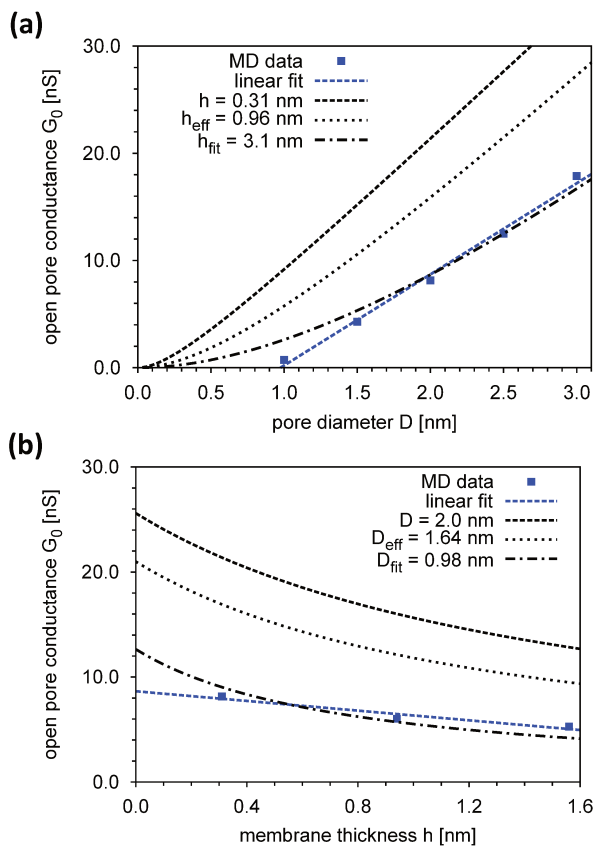

Figure 5: (a) Open pore conductances G_0 as a function of the pore diameter D for SL-MoS_2 nanopores. (b) Open pore conductances G_0 as a function of the membrane thickness h for MoS_2 nanopores of diameter $D = 2.0$ nm. MD data are represented by blue squares. Black lines represent the results of the fit obtained using the analytical model defined in Eq. 1 using: the actual geometrical parameters (dashed line), the *effective* geometrical parameters (dotted line), the fitted geometrical parameters (dash-dotted line). Blue dashed lines represent a linear fitting of the MD data.

ionic conductivity which depends on the diameter of the pore $\sigma(D)$. In fact, it also depends on the thickness h for multiple layers SSN and on the interactions between the ionic solution and the 2-D materials. In the present work, the goal was not to give the exact analytical expression of $\sigma(D, h, ...)$ but to provide a benchmark of G_0 values for further experiments. As shown in Figure 5, a linear model of conductance could also be used to represent the MD data, *i.e.* $G_0(D) = \alpha D + \beta$ (panel a) and $G_0(h) = \gamma h + \delta$ (panel b). It actually provides a better fit than the model defined in Eq. 1. The values of the linear fit are: α = 8.5 nS m^{-1}, β = -8.3 nS, γ = -2.3 nS m^{-1} and δ = 8.6 nS. Finally, from MD simulations data shown in Figure 5a, *i.e.* $G_0 = f(D)$, the value of the critical diameter for MoS_2 nanopores observed earlier in the paper (Figure 3c) can be extracted from $G_0(D_{min}) = 0$, leading to $D_{min} = -\beta/\alpha$ = 0.98 nm.

4 Conclusion

We have studied the ionic conductance through MoS_2 nanopores of different diameters (D = 1.0, 1.5, 2.0, 2.5 and 3.0 nm) and different thicknesses (single, bi- and trilayers). Using MD simulations, we extracted values of open pore conductance G_0 that can be related directly to conductance drops ΔG measured in single molecule detection experiments. If the size of the molecule to be translocated through the nanopore is similar to the diameter of the pore, we find that $\Delta G \sim G_0$. Therefore, there is a strong interest to provide benchmarks of conductance signals using MD simulations. Here, we provide linear conductance models to estimate $G_0 = f(D)$ and $G_0 = f(h)$ and we show that there exists a critical diameter D_{min} = 1.0 nm for SL-MoS_2 nanopores. In addition, these models extracted from the present MD simulations allow us to estimate the geometrical parameters of MoS_2 nanopores from conductance measurements. The estimation of the pore diameter and thickness of the nanoporous membranes from conductance measurements is commonly used in experiments with the analytical model presented in Eq. 1. This approach can lead to large error bars according to the present computational study.

Acknowledgements: The calculations were performed using HPC resources from DSI-CCuB (Université de Bourgogne). This work was supported by a grant from the Air Force Office of Scientific Research (AFOSR), as part of a joint program with the Directorate for Engineering of the National Science Foundation (NSF), Emerging Frontiers and Multidisciplinary Office grant No. FA9550-17-1-0047. The authors also thank the Conseil Régional de Bourgogne for the funding (grant PARI Nano2bio).

References:

[1] C. Dekker, Solid-state nanopores, *Nat. Nanotechnol.* 2, 2007, pp. 209–215.

[2] H. Arjmandi-Tash, L. Belyaeva and G. Schneider, Single molecule detection with graphene and other two-dimensional materials: nanopores and beyond, *Chem. Soc. Rev.* 45, 2016, pp. 476–493.

[3] J. K. Rosenstein, M. Wanunu, C. A. Merchant, M. Drndić, K. L. Shepard, Integrated nanopore sensing platform with sub-microsecond temporal resolution, *Nat. Methods* 9, 2012, pp. 487–492.

[4] J. Rodríguez-Manzo, M. Puster, A. Nicolaï, V. Meunier, M. Drndić, DNA translocation in nanometer thick silicon nanopores, *ACS. Nano* 9, 2015, pp. 6555–6564.

[5] S. W. Kowalczyk, A. Y. Grosberg, Y. Rabin and C. Dekker. Modeling the conductance and DNA blockade of solid-state nanopores, *Nanotechnology* 22, 2011, pp. 315101.

[6] M. Wanunu, T. Dadosh, V. Ray, J. Jin, L. McReynolds, M. Drndić, Rapid electronic detection of probe-specific microRNAs using thin nanopore sensors, *Nat. Nanotechnol.*, 5, 2010, pp. 807–814.

[7] K. Venta, G. Shemer, M. Puster, J. A. Rodríguez-Manzo, A. Balan, J. K. Rosenstein, K. Shepard, M. Drndić, Differentiation of short, single-stranded DNA homopolymers in solid-state nanopores, *ACS Nano*, 7, 2013, pp. 4629–4636.

[8] E. A. Manrao, I. M. Derrington, A. H. Laszlo, K. W. Langford, M. K. Hopper, N. Gillgren, M. Pavlenok, M. Niederweis, J. H. Gundlach, Reading DNA at single-nucleotide resolution with a mutant MspA nanopore and phi29 DNA polymerase, *Nat. Biotechnol.* 30, 2012, pp. 349-353.

[9] C. A. Merchant, K. Healy, M. Wanunu, R. Vishva, N. Peterman, J. Bartel, M. D. Fischbein, K. Venta, Z. Luo, A. T. C. Johnson, M. Drndić, DNA translocation through graphene nanopores, *Nano Lett.* 10, 2010, pp. 2915–2921.

[10] G. F. Schneider, S. W. Kowalczyk, V. E. Calado, G. Pandraud, H. W. Zandbergen, L. M. K. Vandersypen, C. Dekker, DNA translocation through graphene nanopores, *Nano Lett.* 10, 2010, pp. 3163-3167.

[11] S. Garaj, W. Hubbard, A. Reina, J. Kong, D. Branton, J. A. Golovchenko, Graphene as a sub-nanometer trans-electrode membrane, *Nature* 467, 2010, pp. 190–193.

[12] S. J. Heerema, G. F. Schneider, M. Rozemuller, L. Vicarelli, H. W. Zandbergen, C. Dekker, 1/f noise in graphene nanopores, *Nanotechnology* 26, 2015, pp. 074001.

[13] A. Aksimentiev, Deciphering ionic current signatures of DNA transport through a nanopore, *Nanoscale* 2, 2010, pp. 468–483.

[14] C. Sathe, X. Zou, J.-P. Leburton, K. Schulten, Computational investigation of DNA detection using graphene nanopores, *ACS Nano* 5, 2011, pp. 8842–8851.

[15] D. B. Wells, M. Belkin, J. Comer, A. Aksimentiev, Assessing graphene nanopores for sequencing DNA, *Nano Lett.* 12, 2012, pp. 4117–4123.

[16] W. Lv, S. Liu, X. Li, R. Wu, Spatial blockage of ionic current for electrophoretic translocation of DNA through a graphene nanopore, *Electrophoresis* 35, 2014, pp. 1144–1151.

[17] R. Lv, J. A. Robinson, R. E. Schaak, D. Sun, Y. Sun, T. E. Mallouk, M. Terrones, Transition Metal Dichalcogenides and Beyond: Synthesis, Properties, and Applications of Single- and Few-Layer Nanosheets, *Acc. Chem. Res.* 48, 2015, pp. 56–64.

[18] K. Liu, J. Feng, A. Kis, A. Radenovic, Atomically thin molybdenum disulfide nanopores with high sensitivity for DNA translocation, *ACS Nano* 8, 2014, pp. 2504–2511.

[19] A. B. Farimani, K. Min, N. R. Aluru, DNA base detection using a single-layer MoS_2, *ACS Nano* 8, 2014, pp. 7914-7922.

[20] J. W. Jiang, Parametrization of Stillinger-Weber potential based on valence force field model: application to single-layer MoS_2 and black phosphorus, *Nanotechnology* 26, 2015, pp. 315706.

[21] W. L. Jorgensen, J. Chandrasekhar, J. Madura, R. W. Impey, M. L. Klein, Comparison of simple potential functions for simulating liquid water, *J. Chem. Phys.* 79, 1983, pp. 926–935.

[22] I. S. Joung, T. E. Cheatham, Determination of alkali and halide monovalent ion parameters for use in explicitly solvated biomolecular simulations, *J. Phys. Chem. B* 112, 2008, pp. 9020–9041.

[23] T. Liang, S. R. Phillpot, S. B. Sinnott, Parametrization of a reactive many-body potential for Mo-S systems, *Phys. Rev. B* 79, 2009, pp. 245110.

[24] M. Heiranian, A. B. Farimani, N. R. Aluru, Water desalination with a single-layer MoS_2 nanopore, *Nat. Commun.* 6:8616, 2015.

[25] J. Tersoff, New empirical approach for the structure and energy of covalent systems, *Phys. Rev. B* 37, 1988, pp. 6991–7000.

[26] R. Saito, R. Matsuo, T. Kimura, G. Dresselhaus, M. S. Dresselhaus, Anomalous potential barrier of double-wall carbon nanotube, *Chem. Phys. Lett.* 348, 2001, pp. 187–193.

[27] S. Plimpton, Fast parallel algorithms for short-range molecular dynamics, *J. Comp. Phys.* 117, 1995, pp. 1–19.

[28] W. C. Swope, H. C. Andersen, P. H. Berens, K. R. Wilson, A computer simulation method for the calculation of equilibrium constants for the formation of physical clusters of molecules: Application to small water clusters, *J. Chem. Phys.* 76, 1982, pp. 637–649.

[29] S. Nosé, A unified formulation of the constant temperature molecular-dynamics methods, *J. Chem. Phys.* 81, 1984, pp. 511–519.

[30] W. G. Hoover, Canonical dynamics: Equilibrium phase-space distributions, *Phys. Rev. A* 31, 1985, pp. 1695-1697.

[31] R. W. Hockney, J. W. Eastwood, *Computer Simulation Using Particles*, Adam–Hilger, New York 1989.

[32] J.-P. Ryckaert, G. Ciccotti, H. J. C. Berendsen, Numerical integration of the cartesian equations of motion of a system with constraints: molecular dynamics of n-alkanes, *J. Comp. Phys.* 23, 1977, pp. 327-341.

[33] E. R. Cruz-Chu, A. Aksimentiev, K. Schulten, Ionic current rectification through silica nanopores, *J. Phys. Chem. C* 113, 2009, pp. 1850-1862.

[34] T. Sumikama, Origin of the shape of current-voltage curve through nanopores: a molecular dynamics study, *Sci. Rep.* 6, 2016, pp.25750.

[35] M. E. Suk, N. R. Aluru, Ion transport in sub-5-nm graphene nanopores, *J. Chem. Phys.* 140, 2014, pp. 084707.

Appendix B

Improved model of ionic transport in 2-D MoS_2 membranes with sub-5 nm pores

Applied Physics Letters ARTICLE scitation.org/journal/apl

Improved model of ionic transport in 2-D MoS_2 membranes with sub-5 nm pores

Cite as: Appl. Phys. Lett. **114**, 023107 (2019); doi: 10.1063/1.5061825
Submitted: 24 September 2018 · Accepted: 16 December 2018 · Published Online: 16 January 2019

María Daniela Barrios Pérez,[1] Adrien Nicolaï,[1] Patrice Delarue,[1] Vincent Meunier,[2] Marija Drndić,[3] and Patrick Senet[1,a)]

AFFILIATIONS

[1] Laboratoire Interdisciplinaire Carnot de Bourgogne, UMR 6303 CNRS-University Bourgogne Franche-Comté, 9 Av. A. Savary, BP 47 870, F-21078 Dijon Cedex, France
[2] Department of Physics, Applied Physics, and Astronomy, Rensselaer Polytechnic Institute, 110 8th Street, Troy, New York 12180, USA
[3] Department of Physics and Astronomy, University of Pennsylvania, Philadelphia, Pennsylvania 19104, USA

[a)] **Electronic mail:** psenet@u-bourgogne.fr

ABSTRACT

Solid-state nanopores made of two-dimensional materials such as molybdenum disulfide are of great interest thanks in part to promising applications such as ion filtration and biomolecule translocation. Controlled fabrication and tunability of nanoporous membranes require a better understanding of their ionic conductivity capabilities at the nanoscale. Here, we developed a model of ionic conductivity for a KCl electrolyte through sub 5-nm single-layer MoS_2 nanopores using equilibrium all-atom molecular dynamics simulations. We investigate the dynamics of K^+ and Cl^- ions inside the pores in terms of concentration and mobility. We report that, for pore dimensions below 2.0 nm, which are of particular interest for biomolecule translocation applications, the behaviors of the concentration and mobility of ions strongly deviate from bulk properties. Specifically, we show that the free-energy difference for insertion of an ion within the pore is proportional to the inverse surface area of the pore and that the inverse mobility scales linearly as the inverse diameter. Finally, we provide an improved analytical model taking into account the deviation of ion dynamics from bulk properties, suitable for direct comparison with experiments.

Solid-state nanopores (SSNs) made of two-dimensional (2D) materials such as MoS_2 have emerged as versatile sensors for ion and biomolecule manipulation.[1–10] One of the most promising applications of SSN is the sequencing of biological molecules.[11] SSN sequencing experiments are based on the measurement of ionic current variations when a biomolecule immersed in an ionic solution is driven through the nanoporous membrane by applying a transverse electric field. During the process of translocation, the molecule occupies the pore volume, blocking the passage of ions. Consequently, an ultrafast monitoring of ionic flow during the passage of the biomolecule yields information about its structure and chemical properties, as experimentally demonstrated with sub-microsecond temporal resolution.[12,13] However, understanding atomic and sub-nanometer sized pores in bare and functionalized 2-D membranes used for molecular and ionic selectivity are still a matter of study,[14–19] since the fundamental principles behind electrical transport of ionic solution through those pores have not been explored in detail yet. Only two experimental studies of ionic conductance through MoS_2 nanoporous membranes with diameters lower than 2.0 nm have been reported.[3,8]

The analytical model used to predict the conductance G_0 of nanoporous MoS_2 membranes from the knowledge of their dimensions is a continuum model, which results from a combination of three resistors in series: one pore resistance R_{pore} modeled as a cylindrical resistor and two access resistances constituted by the mouth of the pore at each side of the membrane[20]

$$G_0 = \sigma_{bulk}\left(\frac{4h^* + \pi d^*}{\pi d^{*2}}\right)^{-1}, \tag{1}$$

where d^* and h^* represent the effective pore diameter and membrane thickness, respectively. Effective pore diameter d^* and membrane thickness h^* correspond to the effective dimensions of the ionic conducting cylindrical channel of the nanoporous membrane experienced by solvent molecules and are

extracted from the probability distributions of solvent molecules inside the pore. In Eq. (1), the only term related to the ionic properties is the bulk conductivity of the electrolyte, σ_{bulk}. In physical chemistry, the conductivity exhibited by an ionic solution is expressed as the product of the concentration c^i of the ionic species, their charge $q^i = ez^i$, and their electrical mobility μ^i

$$\sigma_{bulk} = e \sum_i |z^i|\, c^i_{bulk}\, \mu^i_{bulk}, \tag{2}$$

where e is the elementary (positive) charge, z is the charge number, and the index i represents the ionic species. For a neutral KCl ionic solution, Eq. (2) becomes $\sigma_{bulk} = 2ec_{bulk}\langle\mu_{bulk}\rangle$, where c_{bulk} is the concentration of K^+ or Cl^- ions and $\langle\mu_{bulk}\rangle = (\mu^{K^+}_{bulk} + \mu^{Cl^-}_{bulk})/2$. At the nanoscale, ions are confined in space whose dimensions are of similar sizes to that of the ionic radii. It follows that their concentration, mobilities, and hydration are different than their bulk counterparts, as already shown for graphene nanopores.[21] Consequently, the conductivity of the electrolyte in nanopores is expected to deviate from its bulk value and the conductance of open nanopores predicted by Eq. (1) is likely to be inaccurate for the smallest pores. We found previously that open pore conductance G_0 predicted from Eq. (1) using σ_{bulk} and the values obtained from experimental I-V curves[8] and molecular dynamics (MD) simulations[22] were overestimated for single-layer (SL) MoS_2 nanopores with diameters ranging from 1 to 3 nm. We showed that MD values of G_0 for this system were better represented by a simple linear interpolation model $G_0(d^*) = \alpha d^* + \beta$ where α and β are fitted parameters. In this simple linear relation, no current can be detected below a critical diameter $d^*_{min} = -\beta/\alpha \sim 0.7$ nm.[22] Recent experimental measurements of ionic transport through sub-nanometer sized pores made of atomic vacancies fabricated in SL-MoS_2 show indeed that pores with diameters <0.6 nm display negligible conductance.[8]

Failure of Eq. (1) to reproduce experimental and MD data demands to reexamine the modeling of G_0 at the atomic scale. Here, thanks to all-atom MD simulations for SL-MoS_2 membranes with diameters ranging from 1 to 5 nm [Fig. 1(a)], we derive an analytical model of the electrolyte conductivity at room temperature in SL-MoS_2 nanopores as a function of the pore diameter, and we named $\sigma_{pore}(d^*)$. As shown in Fig. 1(b), the ion conductivity inside the pore deviates significantly from the bulk electrolyte conductivity for the range of diameters studied here, which corresponds to those used for biomolecule sensing. Replacing the bulk electrolyte conductivity σ_{bulk} in Eq. (1) by $\sigma_{pore}(d^*)$ restores the validity of the continuum model, provided that the diameter dependence of the electrolyte conductivity is taken into account. The corrected continuum model derived here is given by Eq. (7) which can be used by experimentalists to extract the effective diameter of the SL-MoS_2 nanoporous membranes. We will now describe how the improved analytical model was derived from all-atom MD data at 300 K.

For each pore diameter, we performed a 10 ns all-atom MD simulation of the SL-MoS_2 membrane with a 1 M KCl electrolyte as detailed in the supplementary material. We computed the ionic conductivity of each pore presented in Fig. 1(a), i.e., σ_{pore}, using Eq. (2). Ionic concentrations in nanopores were defined as

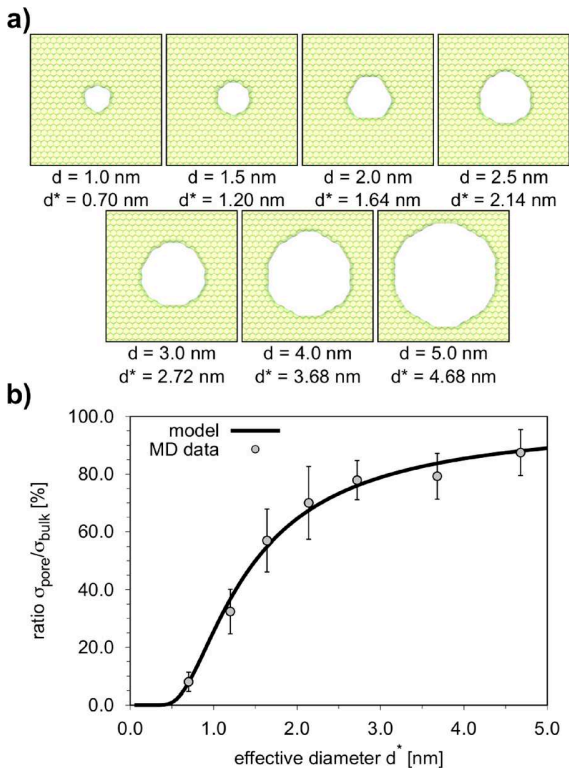

FIG. 1. (a) Atomic structures of single-layer MoS_2 nanopores studied in the present work. The color code is the following: Mo atoms in green and S atoms in yellow. Diameters d and effective diameters d^* are given in nm. (b) Ratio between KCl bulk and pore conductivity as a function of effective diameters d^* extracted from equilibrium MD simulations. The solid black line represents the ratio of σ_{pore} over σ_{bulk} (in %) as a function of d^* (in nm), obtained from Eq. (3).

the average number of ions inside each pore computed from the 10 ns MD run divided by the pore volume represented by a cylinder with effective diameter d^* and thickness h^*. Pore effective diameters (see Table SI) and thickness (0.96 nm for SL-MoS_2) were defined from the water density profiles at the interface with the membrane (see Fig. S1). The bulk 1M KCl, i.e., σ_{bulk}, was computed from Eq. (2) for a 10 ns all-atom MD simulation of the bulk electrolyte without the MoS_2 membrane.[22] Ion mobilities were computed from the MD trajectories by applying the Einstein equation with the ion diffusion coefficients calculated from the mean-square displacements of K^+ and Cl^- inside the pores. More details about this procedure can be found in the supplementary material. The exact same procedure was applied to extract the bulk ion mobilities from the MD run of the bulk electrolyte. All the values and their error bars extracted from MD runs are given in Table SI. Figure 1(b) presents the ratio between bulk and pore conductivities extracted from MD simulations for each pore diameter (gray filled circles). For diameters around 2 nm, the ion pore conductivity is about half the bulk value, which means that Eq. (1) overestimates the membrane conductance by a factor of 2. For diameters approaching 1 nm, the pore conductivity is only a third of the bulk value. To gain

further insight into the origin of the deviations of the conductivity at the nanoscale, we reformulate the problem in terms of partition coefficients $\Phi^i \equiv c^i_{pore}/c_{bulk}$ (concentration) and $\Gamma^i \equiv \mu^i_{pore}/\langle\mu_{bulk}\rangle$ (mobility). From Eq. (2), we have

$$\frac{\sigma_{pore}}{\sigma_{bulk}} = \frac{1}{2}\sum_i \frac{c^i_{pore}\,\mu^i_{pore}}{c_{bulk}\langle\mu_{bulk}\rangle} = \frac{1}{2}\sum_i \Phi^i\Gamma^i. \tag{3}$$

Similar to σ_{pore}, the partition coefficients are diameter-dependent. The coefficient Φ^i can be written as $\Phi^i = P^i_{pore}/P^i_{bulk}$ with P^i_{pore} and P^i_{bulk} the probabilities to find an ion of species i in the pore and in an equivalent volume in the bulk electrolyte, respectively. Therefore, Φ^i is related to the difference between the free-energy of an ion of species i in the pore and in the bulk electrolyte, named ΔG^i, by the Boltzmann law: $\Phi^i = P^i_{pore}/P^i_{bulk} = \exp(-\Delta G^i/RT)$, where R is the perfect gas constant and T the temperature. The free-energy difference is expected to be positive due to the loss of entropy and to the dehydration phenomenon[21,23,24] in the nanopore, both causes being dependent on the pore size. From the ion concentrations computed from MD data, we found that ΔG^i is well represented by the following relation [see Fig. 2(a)] for the range of diameters studied (1 nm $\leq d^* \leq$ 3 nm):

$$\Delta G^i = \varphi^i\left(\frac{RT}{A^*}\right), \tag{4}$$

where $A^* = \frac{\pi d^{*2}}{4}$ is the nanopore effective area and ϕ_i is a positive fitted parameter. The variation of the free-energy difference ΔG^i as a function of $1/d^{*2}$ observed in MD data is significantly different from the one found in graphene nanopores[21] where ΔG^i was fitted by the $1/d^*$ law. Finally, as shown in Fig. 2(b) for $\Phi^i = \exp(-4\varphi^i/\pi d^{*2})$, there is no large difference observed between K^+ and Cl^- species. The values obtained from least-squares fitting are $\varphi^{K^+} = 0.832\,\mathrm{nm}^2$ and $\varphi^{Cl^-} = 0.793\,\mathrm{nm}^2$.

Next, we study the mobility partition coefficient Γ^i inside MoS_2 nanopores. By plotting the inverse mobility as a function of the inverse effective diameter [Fig. 3(a)], we find that $(1/\mu^i_{pore} - 1/\mu^i_{bulk})$ scales as $1/d^*$. A similar behavior for mobilities was observed in graphene nanopores.[21] This result leads to an expression of pore mobility μ^i_{pore} for each ionic species i

$$\mu^i_{pore} = \left(\frac{\gamma^i}{d^*} + \frac{1}{\mu^i_{bulk}}\right)^{-1}, \tag{5}$$

where γ^i are fitted parameters: $\gamma^{K+} = 4.27 \times 10^{-3}\,\mathrm{V\,s\,m^{-1}}$ and $\gamma^{Cl^-} = 4.61 \times 10^{-3}\,\mathrm{V\,s\,m^{-1}}$.

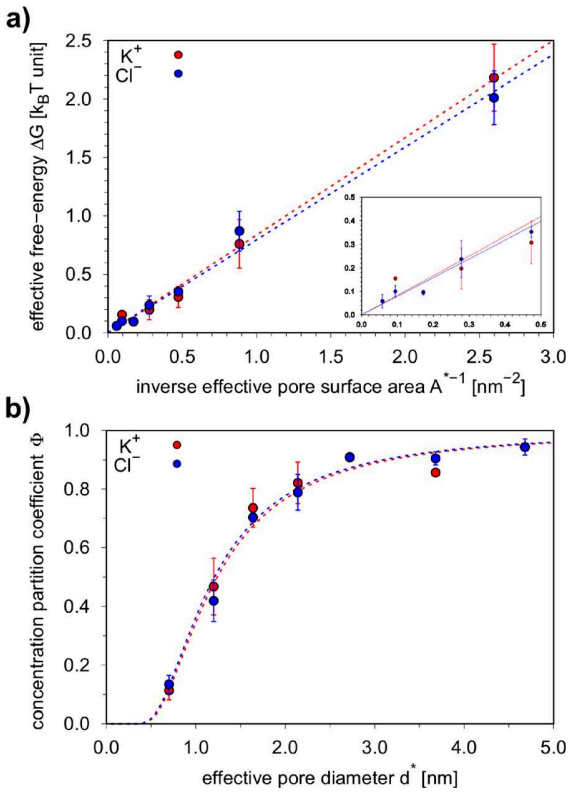

FIG. 2. (a) Effective free-energy ΔG as a function of the inverse of the effective pore surface area $A*^{-1}$. Dashed lines represent a linear fitting of the MD data (filled circles). (b) Concentration partition coefficient as a function of effective diameter d^*. Dashed lines represent the model given by $\Phi^i = \exp(-4\varphi^i/\pi d^{*2})$.

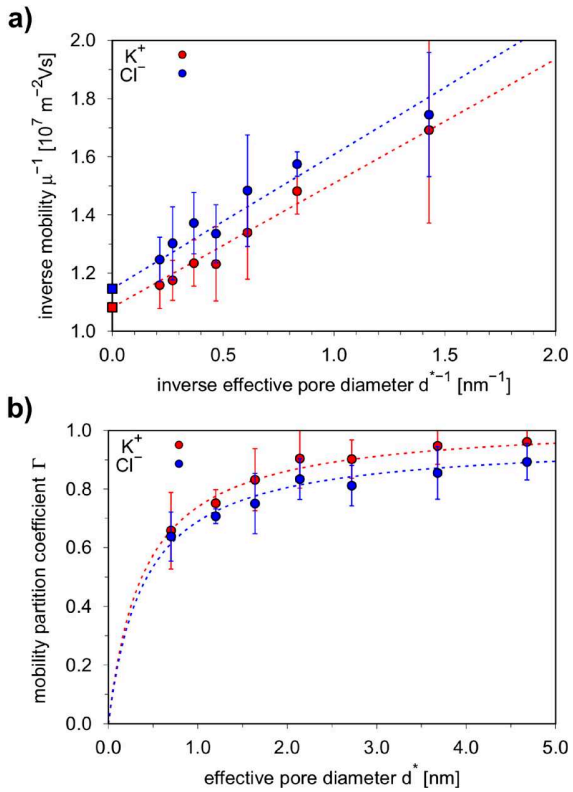

FIG. 3. (a) Inverse mobility μ^{-1} as a function of inverse effective diameter d^{*-1}. Dashed lines represent a linear fitting of the data (filled circles). (b) Mobility partition coefficient as a function of effective diameter d^*. Dashed lines represent the model given by Eq. (6).

It is worth noting that there is a significant difference between K^+ and Cl^- mobilities, K^+ having a larger diffusion coefficient D than Cl^-, as it can be explained from Stoke's law. Indeed, from Stoke's law, $D(K^+)/D(Cl^-) = R(Cl^-)/R(K^+) \approx 1.1$, where $R(K^+)$ and $R(Cl^-)$ are the ionic radii.[25] Using Eq. (5), we can write an analytical expression for Γ and plot its evolution as a function of effective diameter d^* [Fig. 3(b)]

$$\Gamma^i = \frac{\mu^i_{pore}}{\langle \mu_{bulk} \rangle} = \frac{d^* \mu^i_{bulk}}{\langle \mu_{bulk} \rangle (\gamma^i \mu^i_{bulk} + d^*)} = \frac{d^*}{\delta^i + \epsilon^i d^*}, \tag{6}$$

where $\delta^i = \gamma^i \langle \mu_{bulk} \rangle$ and $\epsilon^i = \langle \mu_{bulk} \rangle / \mu^i_{bulk}$, the corresponding values being $\delta^{K^+} = 0.38$ nm and $\delta^{Cl^-} = 0.41$ nm, $\epsilon^{K^+} = 1.03$ and $\epsilon^{Cl^-} = 0.97$. As shown in Fig. 3(b), when the pore diameter is around 1.0 nm, mobility is reduced from the bulk value by about 40%. For the same diameter, the concentration was reduced by 70%. This means that for small diameters, the concentration of ions in the pore is the dominating factor. Finally, the analytical model for σ_{pore} developed in the present work is inserted in the continuum model of conductance [Eq. (1)] leading to the final model described by Eq. (7), which is compared to conductance values obtained from I-V curves extracted from non-equilibrium MD simulations with an external voltage performed in a previous work and to experimental data for sub 5-nm MoS_2 nanoporous membranes (Fig. 4)

$$G_0 = \sigma_{bulk} \left(\frac{1}{2} \sum_i \exp\left(\frac{-4\varphi^i}{\pi d^{*2}} \right) \frac{d^*}{\delta^i + \epsilon^i d^*} \right) \left(\frac{4h^* + \pi d^*}{\pi d^{*2}} \right)^{-1}. \tag{7}$$

For all the different G_0 data reported in the literature, different experimental conditions were used leading to different values of ionic conductivity σ_{bulk} of KCl solutions depending on the temperature and the concentration of the electrolyte. In order to rationalize the data and as already done elsewhere for Si pores,[26] we decided to compute scaled conductance $\tilde{G}_0 = (G_0/\sigma_{bulk})_{given} \times \sigma^{1MKCl@RT}_{bulk}$, where G_0 and σ_{bulk} were directly extracted from the literature and $\sigma^{1MKCl@RT}_{bulk}$ is the value of 11.18 S m^{-1} measured experimentally recently.[8] First, as shown in Fig. 4, the difference between the pore and bulk conductivities has a significant effect on the value of the predicted conductance for pore with diameters lower than 2.0 nm. For such diameters, the original model [Eq. (1)] overestimates conductance by a factor of 2. This overestimation becomes a factor 5 for the diameter around 1.0 nm. In addition, Eq. (7) developed here using equilibrium MD simulations is in very good agreement with conductances computed from I-V curves extracted from non-equilibrium MD simulations using an external electric field. Compared to the linear empirical model proposed elsewhere,[22] the conductance for the SL-MoS_2 nanoporous membrane becomes negligible (10^{-1} nS) for diameters below 0.6 nm. Moreover, from experimental conductance data for SL-MoS_2 nanopores with diameters around 2.0 nm,[3,4] according to the present model [Eq. (7)], the effective diameter of the pore would be closer to 3.0 nm than to 2.0 nm. Finally, experimental data[1] for diameters larger than 2.0 nm are very close to the present model [Eq. (7)] within the error bar when available. We also added into the conductance graphs presented in Fig. 4 conductance values extracted from measurements of WS_2 nanopores.[27] As shown in Fig. 4, for

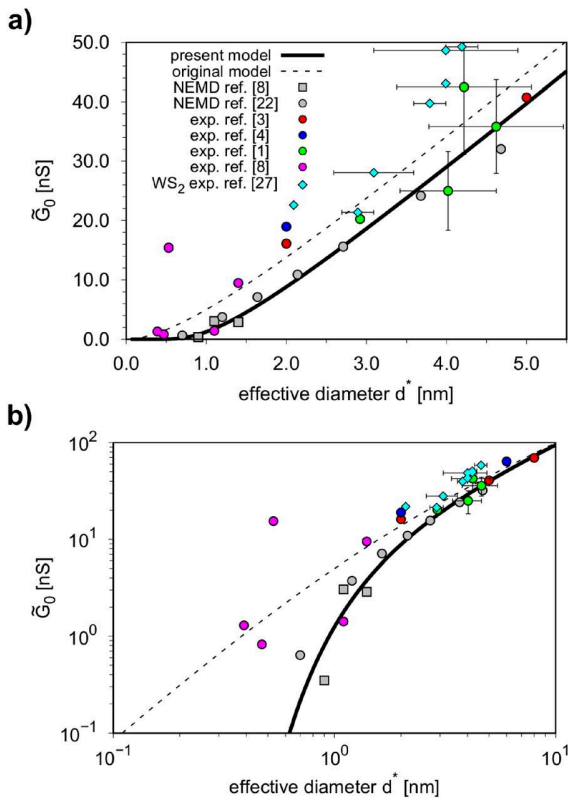

FIG. 4. (a) Conductance $\tilde{G}_0$ (in nS) scaled to 1 M KCl at RT as a function of effective diameter d^* (in nm), extracted from experimental data (red, blue, green, and magenta filled circles) and from non-equilibrium MD simulations (gray filled circles and squares). Black dashed lines represent the original continuum model of conductance from Eq. (1). Black thick lines represent data obtained with the model of conductance developed in the present work and given in Eq. (7). (b) Same graph as panel (a) with the log-log scale.

nanopores of diameters between 2 and 5 nm, conductance values are similar within the error bars. Therefore, the present model may be used also for other TMDs such as WS_2. Finally, for few-Angstrom size defect pores (diameters lower than the limit of 0.6 nm), according to our model, conductance values are often overestimated. In a recent work,[8] we showed using MD simulations in the presence of an applied voltage that defect pores characterized by effective diameter $d^* < 0.6$ nm do not conduct ions, characterized by negligible conductance below 20 pS. For those particularly tiny pores, more experimental measurements are needed to test the validity of the model since the passage of an ion across the membrane is a rare event. However, for pores with diameters around 1.0 nm, our model is in good agreement with experiments.

In summary, we developed a model of ionic conductance for sub 5-nm SL-MoS_2 nanoporous membranes using MD simulations. Our model, which takes into account the concentration and the mobility of ions in the nanopores, shows that the behavior of the KCl electrolyte deviates by 50% from bulk properties

for diameters below 2.0 nm. Moreover, our model is in very good agreement with simulation and experimental data of conductances in MoS_2 nanoporous membranes. This model is essential for understanding the behavior of 2-D nanopores in this range of diameters to design and fabricate sensors for DNA or protein sequencing applications.

See supplementary material for nanopore modeling and numerical calculations, the ion concentrations and mobilities (Table SI), radial distribution of water molecules (supplementary Fig. S1), number of ions in the nanopore (supplementary Fig. S2), ion mean square displacements (supplementary Fig. S3), ion residence time (supplementary Fig. S4), and trajectories of ions crossing the nanopore (supplementary Fig. S5).

The simulations were performed using HPC resources from DSI-CCuB (Université de Bourgogne). This work was supported by a grant from the Air Force Office of Scientific Research (AFOSR), as part of a joint program with the Directorate for Engineering of the National Science Foundation (NSF), Emerging Frontiers and Multidisciplinary Office Grant No. FA9550-17-1-0047, and the NSF Grant No. EFRI 2-DARE (EFRI-1542707). Part of the work was funded by the Conseil Régional de Bourgogne Franche-Comté (Grant Nos. PARI NANO2BIO and ANER NANOSEQ).

REFERENCES

[1]K. Liu, J. Feng, A. Kis, and A. Radenovic, "Atomically thin molybdenum disulfide nanopores with high sensitivity for DNA translocation," ACS Nano **8**, 2504–2511 (2014).
[2]J. Feng, K. Liu, R. D. Bulushev, S. Khlybov, D. Dumcenco, A. Kis, and A. Radenovic, "Identification of single nucleotides in MoS2 nanopores," Nat. Nanotechnol. **10**, 1070–1076 (2015).
[3]J. Feng, K. Liu, M. Graf, D. Dumcenco, A. Kis, M. Di Ventra, and A. Radenovic, "Observation of ionic Coulomb blockade in nanopores," Nat. Mater. **15**, 850–855 (2016).
[4]J. Feng, M. Graf, K. Liu, D. Ovchinnikov, D. Dumcenco, M. Heiranian, V. Nandigana, N. R. Aluru, A. Kis, and A. Radenovic, "Single-layer MoS2 nanopores as nanopower generators," Nature **536**, 197–200 (2016).
[5]J. Shim, S. Banerjee, H. Qiu, K. K. H. Smithe, D. Estrada, J. Bello, E. Pop, K. Schulten, and R. Bashir, "Detection of methylation on dsDNA using nanopores in MoS2 membrane," Nanoscale **9**, 14836–14845 (2017).
[6]B. Luan and R. Zhou, "Spontaneous transport of single-stranded DNA through graphene-MoS2 heterostructure nanopores," ACS Nano **12**, 3886–3891 (2018).
[7]M. Graf, K. Liu, A. Sarathy, J.-P. Leburton, and A. Radenovic, "Transverse detection of DNA in a MoS2 nanopore," Biophys. J. **114**, 180a (2018).
[8]J. P. Thiruraman, K. Fujisawa, G. Danda, P. M. Das, T. Zhang, A. Bolotsky, N. Perea-López, A. Nicolaï, P. Senet, M. Terrones, and M. Drndić, "Angstrom-size defect creation and ionic transport through pores in single-layer MoS2," Nano Lett. **18**, 1651–1659 (2018).
[9]M. H. Köhler, J. R. Bordin, and M. C. Barbosa, "2d nanoporous membrane for cation removal from water: Effects of ionic valence, membrane hydrophobicity, and pore size," J. Chem. Phys. **148**, 222804 (2018).
[10]H. Chen, L. Li, T. Zhang, Z. Qiao, J. Tang, and J. Zhou, "Protein translocation through a MoS2 nanopore: A molecular dynamics study," J. Phys. Chem. C **122**, 2070–2080 (2018).
[11]D. Branton, D. W. Deamer, A. Marziali, H. Bayley, S. A. Benner, T. Butler, M. Di Ventra, S. Garaj, A. Hibbs, X. Huang, S. B. Jovanovich, P. S. Krstic, S. Lindsay, X. S. Ling, C. H. Mastrangelo, A. Meller, J. S. Oliver, Y. V. Pershin, J. M. Ramsey, R. Riehn, G. V. Soni, V. Tabard-Cossa, M. Wanunu, M. Wiggin, and J. A. Schloss, "The potential and challenges of nanopore sequencing," Nat. Biotechnol. **26**, 1146–1153 (2008).
[12]J. K. Rosenstein, M. Wanunu, C. A. Merchant, M. Drndić, and K. L. Shepard, "Integrated nanopore sensing platform with sub-microsecond temporal resolution," Nat. Methods **9**, 487–492 (2012).
[13]S. Shekar, D. J. Niedzwiecki, C.-C. Chien, P. Ong, D. A. Fleischer, J. Lin, J. K. Rosenstein, M. Drndić, and K. L. Shepard, "Measurement of DNA translocation dynamics in a solid-state nanopore at 100 ns temporal resolution," Nano Lett. **16**, 4483–4489 (2016).
[14]K. Sint, B. Wang, and P. Král, "Selective ion passage through functionalized graphene nanopores," J. Am. Chem. Soc. **130**, 16448–16449 (2008).
[15]Z. He, J. Zhou, X. Lu, and B. Corry, "Bioinspired graphene nanopores with voltage-tunable ion selectivity for Na+ and K+," ACS Nano **7**, 10148–10157 (2013).
[16]M. Heiranian, A. B. Farimani, and N. R. Aluru, "Water desalination with a single-layer MoS2 nanopore," Nat. Commun. **6**, 8616 (2015).
[17]S. Sahu and M. Zwolak, "Ionic selectivity and filtration from fragmented dehydration in multilayer graphene nanopores," Nanoscale **9**, 11424–11428 (2017).
[18]M. Deng, K. Kwac, M. Li, Y. Jung, and H. G. Park, "Stability, molecular sieving, and ion diffusion selectivity of a lamellar membrane from two-dimensional molybdenum disulfide," Nano Lett. **17**, 2342–2348 (2017).
[19]C. Fang, Z. Yu, and R. Qiao, "Impact of surface ionization on water transport and salt leakage through graphene oxide membranes," J. Phys. Chem. C **121**, 13412–13420 (2017).
[20]J. E. Hall, "Access resistance of a small circular pore," J. Gen. Physiol. **66**, 531–532 (1975).
[21]M. E. Suk and N. R. Aluru, "Ion transport in sub-5-nm graphene nanopores," J. Chem. Phys. **140**, 084707 (2014).
[22]M. D. B. Pérez, P. Senet, V. Meunier, and A. Nicolaï, "Computational investigation of the ionic conductance through molybdenum disulfide (MoS2) nanopores," Wseas Trans. Circuits Syst. **16**, 35–44 (2017); available at https://www.semanticscholar.org/paper/Computational-investigation-of-the-ionic-through-(-P%C3%A9rez-Senet/2fadd88631a0de3597d64267f4fb8df7dacd692f.
[23]M. Zwolak, J. Wilson, and M. D. Ventra, "Dehydration and ionic conductance quantization in nanopores," J. Phys. Condens. Matter **22**, 454126 (2010).
[24]S. Sahu, M. Di Ventra, and M. Zwolak, "Dehydration as a universal mechanism for ion selectivity in graphene and other atomically thin pores," Nano Lett. **17**, 4719–4724 (2017).
[25]C. Kittel, *Introduction to Solid State Physics*, 8th ed. (Wiley, 2004).
[26]J. A. Rodríguez-Manzo, M. Puster, A. Nicolaï, V. Meunier, and M. Drndić, "DNA translocation in nanometer thick silicon nanopores," ACS Nano **9**, 6555–6564 (2015).
[27]G. Danda, P. M. Das, Y.-C. Chou, J. T. Mlack, W. M. Parkin, C. H. Naylor, K. Fujisawa, T. Zhang, L. B. Fulton, M. Terrones, A. T. Charlie Johnson, and M. Drndić, "Monolayer WS2 nanopores for DNA translocation with light-adjustable sizes," ACS Nano **11**, 1937–1945 (2017).

Appendix C

Molecular Dynamics Investigation of Polylysine Peptide Translocation through MoS_2 Nanopores

THE JOURNAL OF PHYSICAL CHEMISTRY B

Article

Cite This: J. Phys. Chem. B 2019, 123, 2342−2353

pubs.acs.org/JPCB

Molecular Dynamics Investigation of Polylysine Peptide Translocation through MoS_2 Nanopores

Published as part of The Journal of Physical Chemistry virtual special issue "Deciphering Molecular Complexity in Dynamics and Kinetics from the Single Molecule to the Single Cell Level".

Adrien Nicolaï,*,† Maria Daniela Barrios Pérez,† Patrice Delarue,† Vincent Meunier,‡ Marija Drndić,§ and Patrick Senet†

†Laboratoire Interdisciplinaire Carnot de Bourgogne, UMR 6303 CNRS-Univ. Bourgogne Franche-Comté, 9 Av. A. Savary, BP 47 870, F-21078 Dijon Cedex, France

‡Department of Physics, Applied Physics, and Astronomy, Rensselaer Polytechnic Institute, 110 Eighth Street, Troy, New York 12180, United States

§Department of Physics and Astronomy, University of Pennsylvania, Philadelphia, Pennsylvania 19104, United States

Supporting Information

ABSTRACT: Solid-state nanopores (SSN) made of two-dimensional materials such as molybdenum disulfide (MoS_2) have emerged as candidate devices for biomolecules sequencing. SSN sequencing is based on measuring the variations in ionic conductance as charged biomolecules translocate through nanometer-sized channels, in response to an external voltage applied across the membrane. Although several experiments on DNA translocation through SSNs have been performed in the past decade, translocation of proteins has been less studied, partly due to small protein size and detection limits. Moreover, the threading of proteins through nanopore channels is challenging, because proteins can exhibit neutral global charge and not be sensitive to the electric field. In this paper, we investigate the translocation of lysine residues and a model protein with polylysine tags through MoS_2 nanoporous membranes using molecular dynamics simulations. Adding lysine tags to biological peptides is the method proposed here to promote the entrance of proteins through SSN. Specifically, we study the relationship existing between the translocation events and the ionic conductance signal drops. We show that individual lysine residues translocate easily through MoS_2 nanopores, but the translocation speed is extremely fast, which leads to indiscernible ionic conductance drops. To reduce the translocation speed, we demonstrate that increasing the thickness of the membrane from single-layer to bilayer MoS_2 reveals a stepwise process of translocation with discernible conductance drops that could be measured experimentally. Finally, a study of the threading of proteins with polylysine tags through MoS_2 nanopores is presented. The addition of the positively charged tag to the neutral protein allows the threading and full translocation of the protein through the pore (at least two lysine residues are necessary in this case to observe translocation) and a similar sequence of translocation events is detected, independently of the tag length.

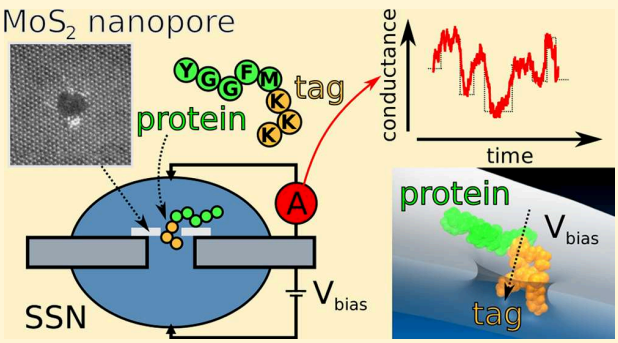

INTRODUCTION

Solid-state nanopore (SSN)-based sensor for the detection of biomolecules is an emerging experimental tool with promising applications in medical diagnostics.[1−4] In SSN experiments, biomolecules, which are suspended in an ionic solution, are driven by a transverse electric field through a nanopore within an ultrathin membrane, while the ionic conductance G is monitored to detect the translocation of molecules across the nanopore. Typically, translocation is detected as drops in conductance signal ΔG. The passage of the biomolecule yields information about its structure and chemical properties, as experimentally demonstrated with sub-microsecond temporal resolution.[5] Atomically thin two-dimensional (2D) materials such as transition-metal dichalcogenides[6,7] (TMDs) are ideal candidates for SSN, as they exhibit larger ionic conductance compared to thicker membranes such as silicon-based membranes.[8] Among all TMDs that have been explored theoretically and experimentally, molybdenum disulfide (MoS_2) layers are showing great potential thanks to the fact MoS_2 monolayer films and nanostructured materials can be

Received: October 31, 2018
Revised: February 15, 2019
Published: February 15, 2019

DOI: 10.1021/acs.jpcb.8b10634
J. Phys. Chem. B 2019, 123, 2342−2353

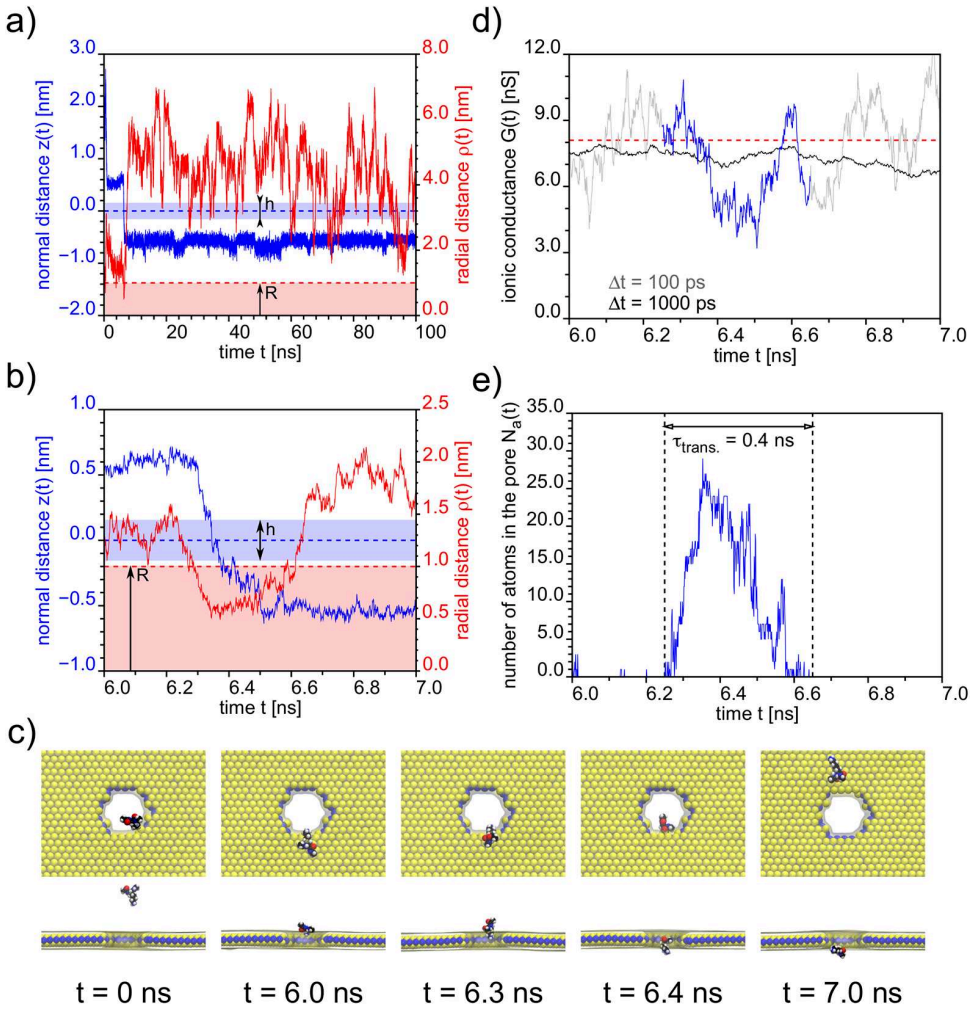

Figure 1. Translocation of single lysine amino acid through SL-MoS_2 extracted from MD run 1 (see Table 1). (a, b) Normal z and radial ρ distances of the center of mass of single lysine amino acid as a function of simulation time t. Dashed blue line represents the z-position of the membrane in the simulation box. Dotted red line represents the center of the pore. (c) Snapshots extracted from MD trajectory. Sphere representation is used here, and the color code is the following: Mo (dark blue), S (yellow), C (black), O (red), N (blue), and H (white). (d) Ionic conductance G as a function of simulation time t computed using Δt = 100 ps (gray line) and Δt = 1 ns (black line). The blue line represents the signal when the peptide is inside the pore. The red dashed line represents the open pore conductance. (e) Number of atoms inside the pore N_a as a function of simulation time t.

fabricated using cost-effective and reliable methods.[9−11] Moreover, pores smaller than 5 nm can be drilled experimentally with high reproducibility.[12,13] Finally, MoS_2 layers are also potentially advantageous for such applications due to their rich optoelectronic and mechanical properties.[14]

MoS_2 nanopores have been studied experimentally as SSN for DNA sequencing[6,15−17] and for detection of DNA labeled with proteins.[18,19] To the best of our knowledge there is to-date no experimental evidence of the translocation of single proteins through MoS_2 or any other TMDs yet. Only a few experimental studies about protein translocation through silicon-nitride nanoporous membranes have been reported.[20−22] In contrast to DNA strands, which are highly negatively charged biomolecules, that is, the total charge being proportional to the number of bases, proteins can be globally neutral, independently of its number of residues, sequence, or size. Therefore, driving such a biomolecule into SSN and detecting ionic conductance drops related to its amino acid sequence requires a different strategy than using an electric field as driving force. Indeed, a compromise must be made between facilitating the threading of the protein through the pore and the translocation speed, which should allow the detection of discernible conductance drops associated with its specific sequence. In this way, SSNs with a very high translocation speed of proteins through the pore may limit their usability as sequencing devices. The threading of the biomolecule through SSN and the translocation speed can be tuned by adjusting different parameters in experiments such as solvent properties[23,24] (ionic species, concentration, temperature, viscosity, etc.) or by tuning the material's size and shape.[25] More drastically, the physical technique used to drive the biomolecule through the pore can also be modified. Recently, a theoretical study has shown the feasibility of translocating uniformly (repetition of identical motifs) and highly charged (up to ±24e) proteins through single-layer MoS_2 (SL-MoS_2) nanoporous membranes in a bias electric field and in a water-flow, used to generate a hydrostatic pressure gradient.[26] The authors of the study showed that this

DOI: 10.1021/acs.jpcb.8b10634
J. Phys. Chem. B 2019, 123, 2342−2353

latter method offers an alternative possibility, other than transmembrane bias, to drive peptides through MoS_2 nanopores, even though the fragility of such ultrathin nanoporous membranes might be problematic.[27] Another theoretical work, based on nanoporous membranes made of graphene MoS_2/heterostructures, showed as proof-of-principle that mixing 2D materials with different van der Waals interactions and consequently different chemical potentials might be the solution to transport and translocate neutral or weakly charged biomolecules through SSNs.[28] In that work, the authors did not present ionic conductance signals recorded during the translocation of proteins and, therefore, no drops related to the passage of specific amino acids through the graphene/MoS_2 pores were shown. Finally, the use of tags made of positively or negatively charged amino acid such as lysine residues to functionalize the N- or C-terminal part of proteins to promote their entrance inside SSN might be an alternative approach to the two previous methods. The test of this alternative method is the purpose of the present work. In biochemistry, polyionic tags such as small lysine peptides are used as enhancers of protein solubility in recombinant protein production. Because of their small size and their repetitive amino acid content, they do not necessarily have an ordered three-dimensional (3D) conformation. As a result, they can exert their solubility-enhancing effect without interfering with the structure of the protein of interest or compromising its activity.[29]

In this work, we performed all-atom non-equilibrium molecular dynamics (NEMD) simulations to explore the feasibility of using polylysine tags to thread and fully translocate peptides through MoS_2 nanopores. First, the threading and translocation of individual lysine residues were studied as a proof-of-principle of the proposed technique. The relationship between the passage of lysine residues through the pore and the detected ionic conductance is established. Second, different types of membranes were tested by tuning the diameter of the nanopore from 1.5 to 2.0 nm and by tuning the thickness of the membranes, from single-layer to bilayer MoS_2. The best performing membrane was extracted from these initial simulations. Finally, tags made of polylysine residues, from 1 to 5 amino acid length, were attached to Met-Enkephalin protein and translocated through single-layer MoS_2. Finally, ionic conductance and translocation sequence of events were analyzed and discussed.

■ MATERIALS AND METHOD

NEMD Simulations. All-atom NEMD simulations using periodic boundary conditions (PBC) were performed using the LAMMPS (http://lammps.sandia.gov) software package.[30] Each simulation box of dimension 10 × 10 × 20 nm^3 is comprised of a MoS_2 nanoporous membrane, a biological peptide, and a 1 M KCL ionic solution, and it is globally neutral. Initially, MoS_2 single-layer (SL) is constructed using 2D unit cell lattice vectors $\vec{a}$ = (3.13, 0, 0) and $\vec{b}$ = (0, 5.42, 0). Each rectangular unit cell for MoS_2 has six atoms, two Mo and four S atoms. The Mo−S bond length was taken as d_{Mo-S} = 2.38 Å, and the S−S distance was taken as d_{S-S} = 3.11 Å. The unit cell was replicated in both x and y directions to generate layers of dimension 10 × 10 nm^2. For bilayer MoS_2 membranes, the interlayer spacing was taken as d_{is} = 3.15 Å. MoS_2 pores were constructed by removing atoms whose coordinates satisfy $x^2 + y^2 < R^2$, where $D = 2R$ is the diameter of the pore and considering the center of the pore at the origin of the box. The pore diameters considered in this work are D = 1.5 and 2.0 nm. In total, the simulation box is comprised of ∼200 000 atoms. For instance, the simulation box used for the translocation of an individual lysine residue (positively charged, +1e) through SL-MoS_2 nanopore of diameter D = 2.0 nm and presented in Figure 1 is comprised of 1115 Mo atoms, 2230 S atoms, 34 peptide atoms, 59 927 water molecules, 1177 K^+ ions, and 1178 Cl^- ions. In the present simulations, we do not consider the membrane to be rigid as was done in recent works about protein translocation through MoS_2 nanopores[26] and graphene/MoS_2 heterostructures.[28] As shown in Figure S1 of the Supporting Information, the fluctuations of the membrane atoms are dependent on their radial position relative to the center of mass of the pore, even though they are relatively small in terms of amplitude. In addition, according to root-mean-square deviation (RMSD), fluctuations of the membrane atoms increase when the peptide translocates through the pore. Therefore, the dynamics of the nanoporous membrane play a role in the diffusion of the biomolecule on the surface and in the threading of the biomolecule through the pore. Consequently, a Stillinger-Weber potential[31] is used to simulate the dynamics of Mo−S bonded interactions. The peptide is modeled using the Amber ff99SB-ILDN force-field.[32] The water model used in the present work is the TIP3P model.[33] Non-bonded interactions between MoS_2, peptide atoms, water, and ions are described using a Lennard-Jones (LJ) plus Coulomb potential. LJ parameters for K^+ and Cl^- ions were taken from ref 34, where specific parameters were developed for the water model employed. LJ parameters and bulk partial charges for Mo and S atoms were taken from refs 35 and 36, respectively, as already used in other works.[13,26,37−39] Initially, the biological peptide is placed above the MoS_2 nanoporous membrane at a vertical distance of 20 Å. By doing so, we avoid biased threading when the peptide is originally placed into the pore. Before running NEMD simulations, an equilibration of the system in the NPT ensemble (T = 300 K and P = 1 bar) without any electric field was performed during 100 ps to relax the system at the target temperature and pressure. Equilibration was followed by molecular dynamics (MD) production runs of different duration times (see Tables 1 and 2), which were performed in the NVT ensemble using the velocity-Verlet algorithm[40] with a time step of 1 fs. A Nosé−Hoover thermostat[41,42] was used to maintain the temperature at 300 K with a time constant of 0.1 ps. Particle−particle particle-mesh method[43] was used to describe long-range electrostatic interactions. A cutoff of 1.0 nm was applied to LJ and Coulomb potentials for nonbonded interactions. A SHAKE algorithm[44,45] was used to constrain the bond lengths and angle of TIP3P water

Table 1. Summary of MD Simulations Performed on Translocation of Single Lysine Amino Acid through MoS_2 Nanoporous Membranes with Diameter D and N_{layer} Layers of 2D Materials[a]

D [nm]	N_{layer}	peptide	run 1	run 2	run 3	total
2.0	1	K	100*	100*		200
2.0	1	KK	50*	57*	23*	130
1.5	1	KK	100	88*		188
2.0	2	KK	100	100*		200

[a]The total simulation time is 718 ns distributed across nine different runs with different initial conditions. (*) indicate trajectories for which a complete translocation event was observed.

DOI: 10.1021/acs.jpcb.8b10634
J. Phys. Chem. B 2019, 123, 2342−2353

Table 2. Summary of MD Simulations Performed on Translocation of Met-Enkephalin with Polylysine Tags through Single-Layer MoS_2 Nanoporous Membranes (D = 2.0 nm)[a]

peptide	run 1	run 2	total	τ_{trans}^{run1}	τ_{trans}^{run2}
YGGFM	100	100	200		
YGGFM-1K	100	150	250		
YGGFM-2K	200	250*	450		111
YGGFM-3K	100	300*	400		158
YGGFM-4K	200*	50*	250	15	16
YGGFM-5K	250*	150	400	71	

[a]The total simulation time is 1.95 μs distributed across 12 different runs with different sequences of peptides and initial conditions. (*) indicate trajectories for which a complete translocation event was observed.

molecules. Finally, simulations were performed by applying a uniform electric field, oriented normal to the nanoporous membrane (z-direction), to all atomic partial charges in the system. The corresponding applied voltage is $V = -EL_z$, where L_z is the length of the simulation box in the z-direction, with V = 1 V for all MD runs presented below. The value of 1 V, corresponding to an electric field of 5×10^{-3} V/nm, was used to accelerate MD simulations to observe translocation events. The order of magnitude of the potential used in the present work is similar to the ones used in previous works.[26,46]

Trajectory Analysis. *Ionic Conductance.* Ionic conductance $G(t)$ is computed from MD trajectories as the ratio between the total net ionic current $I(t)$ and the applied voltage V, with

$$G(t) = \frac{1}{V}\left(\frac{1}{\Delta t L_z}\sum_{i=1}^{N} q_i[z_i(t+\Delta t) - z_i(t)]\right) \quad (1)$$

where V is the applied voltage, Δt is the time between MD frames chosen for the calculations (Δt = 100 ps or 1 ns depending on the runs, see text), L_z is the dimension of the simulation box in the z-direction, which is the direction of the applied electric field, N is the total number of ions, q_i is the charge of the ion i, and $z_i(t)$ is the z-coordinate of the ion i at time t.

Number of Atoms Inside the Pore. Translocation events observed during NEMD simulations are characterized by computing the number of atoms of each amino acid that are inside the pore as a function of time, $N_a(t)$. Two conditions are necessary to consider that an atom is in the pore: first, the radial distance ρ_i of an atom i from the center of the pore must be lower than the radius R, and, second, the absolute value of the normal distance $|z_i|$ of an atom i to the center of the pore must be lower than half the effective thickness $h_{eff}/2$, which is taken as the geometrical thickness of the MoS_2 membrane (i.e., 3.1 Å) plus twice the van der Waals radius of sulfur atoms (i.e., 1.8 Å).

RESULTS AND DISCUSSION

Translocation of Lysine Residues through MoS_2 Nanopores. Before attaching polylysine tags onto proteins, we studied the translocation of single lysine amino acid and lysine dipeptide through SL-MoS_2 nanopores of diameter D = 2.0 nm. Lysine residues are positively charged and interact with the external electric field. The electric field was chosen to correspond to a transmembrane applied voltage V = 1 V in all NEMD simulations presented below, which is relatively close to applied voltages used in experiments[47] (a few hundreds of mV). Lysine peptides were capped at each N- and C-terminal part using acetyl and N-methyl groups, respectively. As explained in the Materials and Methods section, biological peptides are initially positioned in the bulk solvent, 20 Å above the membrane, to simulate the complete translocation process, from diffusion in bulk solvent above the membrane to diffusion in bulk solvent below the membrane after threading and translocating through the pore. To the best of our knowledge, simulations of the full translocation process of peptides through MoS_2 nanopores has never been done. Several MD runs using different initial conditions were performed for each system (see Table 1 for more details).

Translocation of Single Lysine Amino Acid through Single-Layer MoS_2 Nanopores. As shown in Figure 1, the translocation process is comprised of three distinct parts: first, the peptide diffuses in the bulk solvent, but the interaction of the positively charged peptide with the electric field makes it really fast (a few nanoseconds), and second, the peptide is adsorbed on the MoS_2 surface, diffusing on the top of the membrane. After ~5 ns, the peptide threads into the pore, and the translocation through the nanopore occurs. At the end of the MD run (100 ns), the peptide has diffused at the bottom surface of the membrane and never detached from the membrane to go back to the bulk solvent, as expected originally. Longer runs are probably needed to observe the final stage of the full translocation process. In more details, the translocation takes place at t = 6.25 ns and lasts for τ_{trans} = 0.4 ns. Moreover, the peptide translocates close to the edge of the pore rather than its center, as shown in Figure 1b. The side chain of the lysine residue translocates first in the pore, followed by its backbone. As shown in Figure 1c, the long side chain of lysine amino acid is aligned parallel to the electric field inside the pore. During the translocation process, we observe a maximum drop of conductance ΔG of ~3 nS relative to the open pore conductance (Figure 1d). The drop of conductance is maximum when the number of atoms N_a inside the pore is the largest (Figure 1e). The maximum drop of conductance related to the translocation is observed using Δt = 100 ps for the calculation of the ionic current. Using a Δt of 1 ns, we do not observe drops of conductance, indicating that the translocation time τ_{trans} is faster than 1 ns. Fluctuations of conductance during the translocation are large, making the instantaneous maximum conductance drops detected almost indiscernible compared to the fluctuations. Consequently, the average drop of conductance observed during the translocation of a single lysine residue is ~0.7 nS. The average drop $\Delta\overline{G}$ is computed as the difference between the average conductance when the peptide is outside the pore $\overline{G}_{out}$ (from $0 \le t \le 6.25$ ns and $6.65 \le t \le 100$ ns) and the average conductance when the peptide is in, that is, $\overline{G}_{in}$ (from $6.25 \le t \le 6.65$ ns).

Using different initial conditions, we performed a second MD run of 100 ns for the translocation of a single lysine amino acid through MoS_2 nanopores (see Figure S2). Results are very similar to MD run 1. In this second MD run, we observed a translocation of the lysine residue at t = 65 ns. The translocation time is the same as for MD run 1 (τ_{trans} = 0.4 ns), and the same translocation process is observed, that is, the lysine residue translocates close to the edge of the pore, and the side chain is the first part of the residue to thread into the pore due to its positively charged characteristics. Finally, the maximum conductance drop detected during the passage of

DOI: 10.1021/acs.jpcb.8b10634
J. Phys. Chem. B 2019, 123, 2342−2353

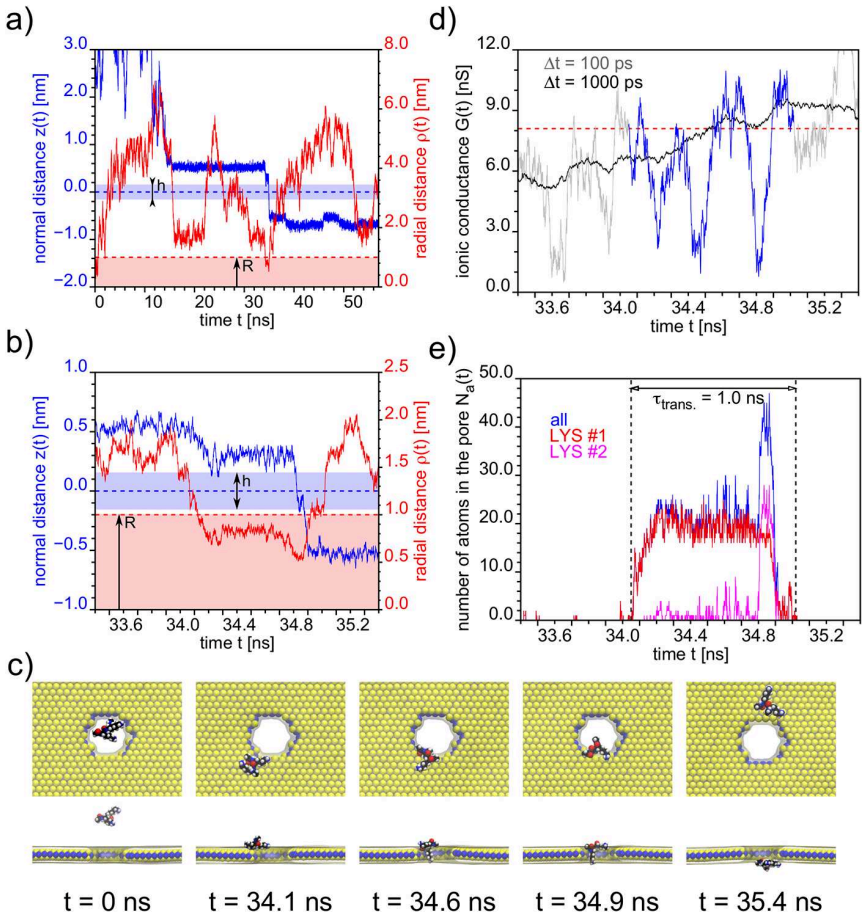

Figure 2. Translocation of a lysine dipeptide through SL-MoS_2 extracted from MD run 2 (see Table 1). (a, b) Normal z and radial ρ distances of the center of mass of lysine dipeptide as a function of simulation time t. (c) Snapshots extracted from MD trajectory. The color code is the same as in Figure 1. (d) Ionic conductance G as a function of simulation time t. (e) Number of atoms inside the pore N_a as a function of simulation time t.

the residue through the pore is ∼3 nS, and the average conductance drop is ∼0.9 nS, the fluctuations of G being as large as the ones observed in MD run 1.

Translocation of Lysine Dipeptide through Single-Layer MoS_2 Nanopores. We performed three independent MD runs to study the translocation of the lysine dipeptide through single-layer MoS_2 nanopores. Figure 2 shows data extracted from MD run 2. After ∼15 ns of diffusion of the peptide in bulk solvent, the peptide is adsorbed on the MoS_2 top surface of the membrane and finally threads into the pore and translocates at t = 34.1 ns of the MD trajectory (Figure 2a,b). As already observed for single lysine amino acid, the translocation of lysine dipeptide takes place at the edge of the pore (Figure 2c). Furthermore, the translocation process is characterized by a two-step process (Figure 2b): first one lysine amino acid enters the pore at t = 34.6 ns, the side chain pointing in the direction of the electric field, and stays there for ∼0.7 ns, and then the second lysine amino acid threads into the nanopore, and the whole peptide leaves the channel as one entity after τ_{trans} = 1.0 ns of translocation duration. During this two-step sequence of event, three maximum drops of conductance are observed and are ∼6 nS (Figure 2d). The largest drop is detected when the second lysine threads into the pore, as shown in Figure 2e. At t = 34.9 ns (Figure 2c), the volume occupied by the two lysine residues inside the pore is the largest (N_a = 40), which increases the ionic current blockade. $G(t)$ signal computed using a Δt = 1 ns contains no information about translocation events, as it was the case for single lysine amino acid translocation, because the translocation time $\tau_{trans} \approx$ 1.0 ns. The average conductance drop is ∼0.7 nS, which is similar to the average drop detected for a single lysine amino acid. Although the translocation time is more than twice larger for the dipeptide than for the single lysine amino acid, the fluctuations recorded in the conductance signal are still very large, making the drops almost indiscernible. Therefore, reducing the translocation speed to get discernible conductance drops out of the fluctuations of the signal is essential for the design of such a sequencing sensor. Nevertheless, the fact that a two-step process, that is, one residue translocating at a time, is observed for a lysine dipeptide is an important preliminary result. In MD run 1 (Figure S3), the translocation occurs faster than the one observed in MD run 2. The translocation time τ_{trans} is ∼0.4 ns, as observed for single lysine peptide. According to the number of atoms inside the pore as a function of time $N_a(t)$, the N-terminal lysine is translocating first in the pore followed by the C-terminal lysine after 0.1 ns of translocation. The fact that the translocation process is extremely fast in this particular MD run involves even larger fluctuations of the conductance signal $G(t)$ computed using a Δt = 100 ps, and no discernible drops are observed. The same conclusions are drawn from MD run 3, the translocation being faster than MD run 2 (Figure S3).

DOI: 10.1021/acs.jpcb.8b10634
J. Phys. Chem. B 2019, 123, 2342−2353

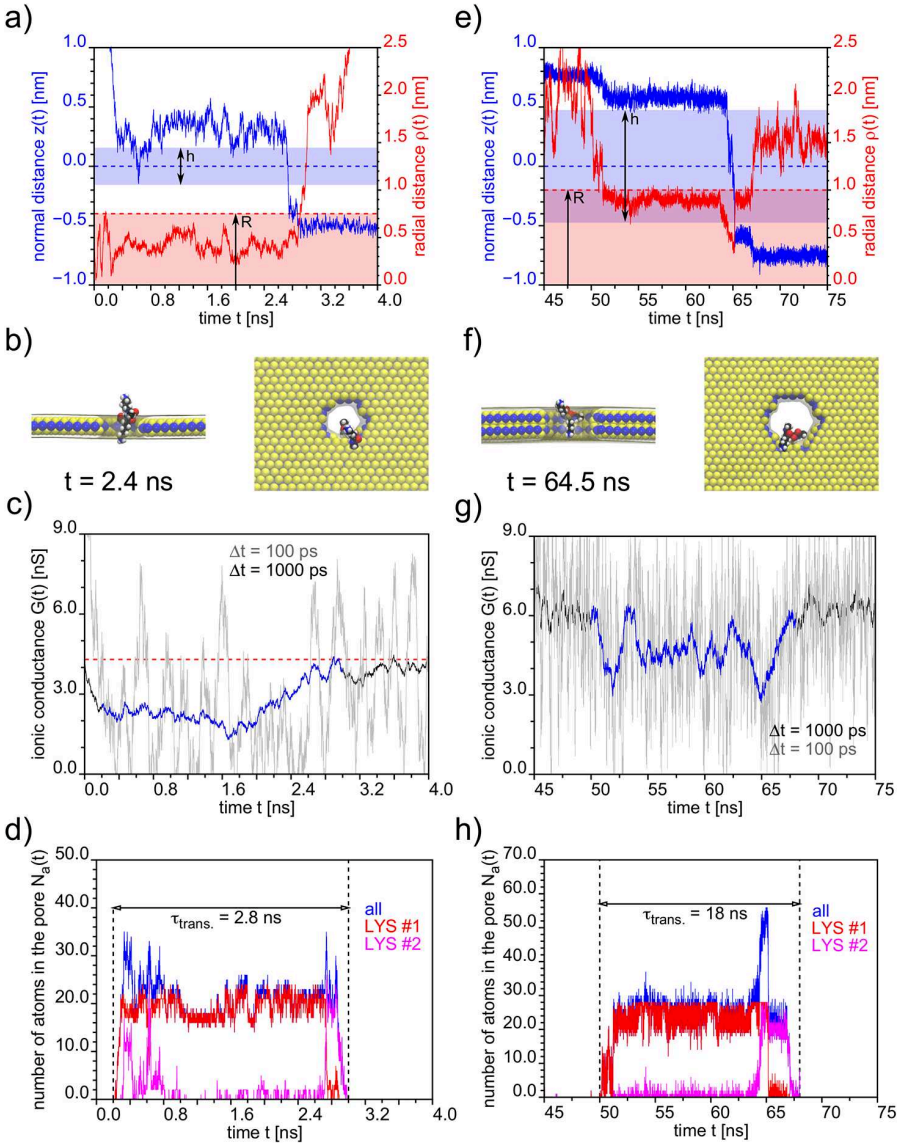

Figure 3. Translocation of a lysine dipeptide through MoS_2 nanoporous membranes with different diameters (D = 1.5 nm, MD run 2, left panels) and thickness (bilayer MoS_2, MD run 2, right panels, see Table 1). (a) Normal z and radial ρ distances of the center of mass of lysine dipeptide as a function of simulation time t for SL-MoS_2 nanopores with D = 1.5 nm. (b) Snapshots extracted from MD trajectory. The color code is the same as in Figure 1. (c) Ionic conductance G as a function of simulation time t. (e) Number of atoms inside the pore N_a as a function of simulation time t. Panels (e−h) are equivalent to panels (a−d) for the translocation of lysine dipeptide through bilayer MoS_2 (D = 2.0 nm), respectively.

However, as observed in MD run 2, the two-step process translocation, that is, one lysine at a time, is observed in the three MD runs with different initial conditions.

From these preliminary results extracted from NEMD simulations, we saw that lysine residues thread into the hole of the nanoporous membrane from the side chain and translocate very fast through MoS_2 nanopores. In addition, a stepwise process exists during the translocation of lysine dipeptide. From that, no discernible conductance drops can be associated with the stepwise process of translocation, since the translocation speed is extremely fast involving large fluctuations of the conductance signals. A possibility to improve the nanopore sensor response is to tune the membrane system to slow the translocation process, having the peptide staying for several nanoseconds into the pore. To do so, we modified the geometrical parameters of the MoS_2 nanoporous membrane one at a time, that is, by reducing the diameter from 2.0 to 1.5 nm and by increasing the thickness of the membrane considering a bilayer instead of a single-layer MoS_2.

Slowing the Translocation by Reducing Diameter of the Pore or Increasing Thickness of the Membrane. First, the diameter of the nanopore was reduced from 2.0 to 1.5 nm. This strategy leads to an open pore conductance reduction from 8.1 to 4.3 nS.[38] During MD run 2 presented in Figure 3a−d, two attempts of translocation for the dipeptide were observed, the first one occurring at $t \approx 0.8$ ns, for which the two lysine residues tried to go through the pore as one but were rejected due to steric effects. The second attempt occurs at t = 2.6 ns and was successful. During this second attempt, the translocation follows a two-step process as observed for the membrane with a 2.0 nm pore diameter (Figure 2). The N-terminal lysine side chain enters into the pore, pointing out in

DOI: 10.1021/acs.jpcb.8b10634
J. Phys. Chem. B 2019, 123, 2342−2353

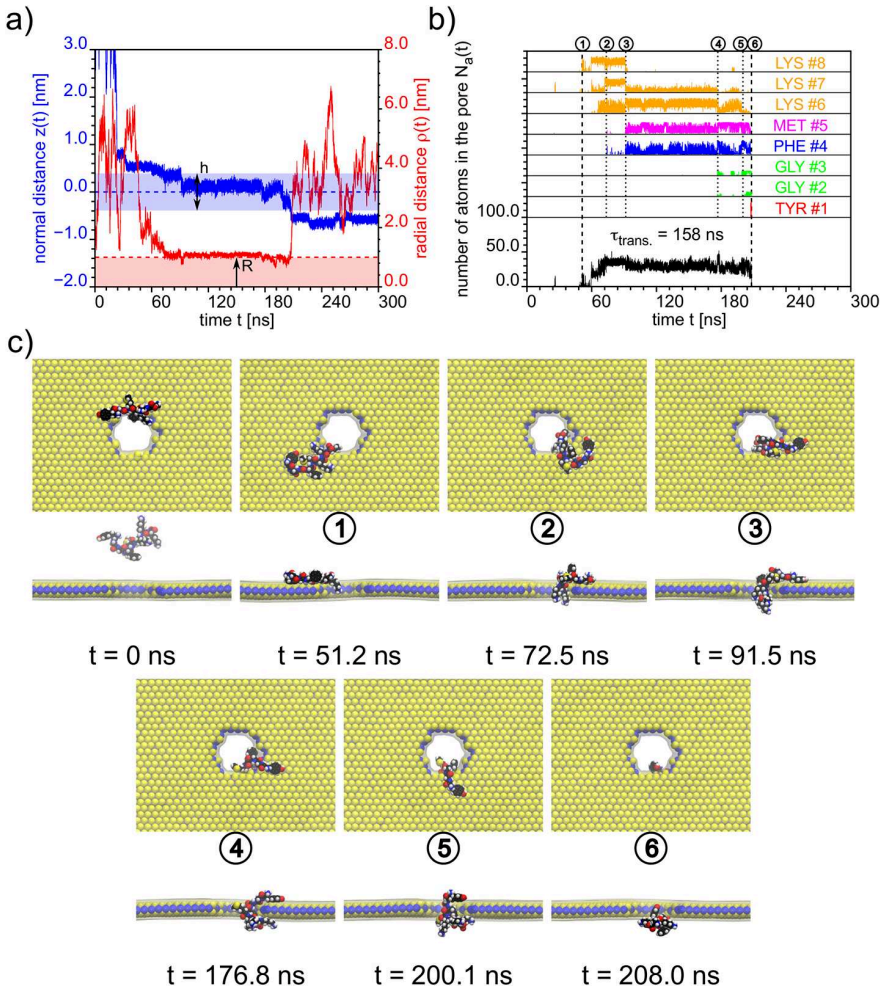

Figure 4. Translocation of Met-Enkephalin with polylysine tag (YGGFM-3K) through SL-MoS_2 extracted from MD run 2 (see Table 2). (a) Normal z and radial ρ distances of the center of mass of the peptide as a function of simulation time t. (b) Number of atoms N_a inside the pore as a function of simulation time t. (c) Snapshots extracted from MD trajectory. The color code is the same as in Figure 1.

the direction of the electric field, and at $t \approx 2$ ns the C-terminal lysine is threaded into the pore, and the full translocation occurs. In opposition to the translocation of lysine dipeptide through SL-MoS_2 pore of diameter 2.0 nm, the translocation takes place closer to the center of the pore (Figure 3a). The translocation time τ_{trans} is ~2.8 ns, which is 3 times longer than the one detected for the larger pore. In fact, the translocation time being longer, the conductance signal $G(t)$ recorded every Δt = 1 ns is better suited to analyze conductance drops. Indeed, one discernible drop of ~2.5−3.0 nS is detected during the translocation process and lasts until the full passage of the peptide is completed. The corresponding average drop is ~1.4 nS, which is twice larger than the one detected for the larger pore. The conductance signal in this case allows to detect the passage of the dipeptide but is not relevant to distinguish the two residues separately.

Second, the thickness of the membrane was increased from 0.31 to 0.94 nm (from single-layer to bilayer MoS_2). Compared to the decrease of the pore diameter, the open pore conductance only drops from 8.1 to 6.0 nS.[38] The expected maximum conductance drop is then larger by increasing the thickness than reducing the diameter. Therefore, a larger signal-to-noise ratio is expected for the corresponding SSN device, leading to a good compromise sensor resolution. As shown in Figure 3 e−h, the translocation of lysine dipeptide through bilayer MoS_2 occurs at t = 50 ns of MD simulation (see Movie S1). As already observed for single-layer MoS_2 nanoporous membranes, the translocation process can de described in two steps, the N-terminal lysine threading first into the pore followed by the C-terminal lysine 15 ns later. In total, the translocation time is ~18 ns, which is 18 times larger than for single-layer MoS_2. The initial goal, which was to increase the translocation time (i.e., reduce the translocation speed) of the peptide in the pore, is thus achieved. Furthermore, the conductance signal recorded every Δt = 1 ns shows two distinct and discernible drops: the first one of ~3.0 nS when the N-terminal lysine enters the pore at t = 50 ns and a second drop of the same magnitude when the C-terminal lysine threads into the pore at t = 65 ns. The corresponding average drop is ~1.4 nS, the same as the one for the smaller diameter pore, but this time, two traces of the signal are detected clearly (Figure 3g). This result is important for the design of protein sequencing devices. Indeed, for several years, experimentalists have been trying to reduce the thickness of the membranes, particularly using 2D materials to get a larger conductance signal (i.e., larger signal-to-noise

DOI: 10.1021/acs.jpcb.8b10634
J. Phys. Chem. B 2019, 123, 2342−2353

ratio) and a better spatial resolution. In the present work, we show that increasing slightly the thickness by considering bilayer 2D materials might lead to drops of conductance in relationship with the number of residue translocating through. The cost of increasing the signal resolution in the time domain by increasing the thickness is that the spatial resolution is reduced. In this example, the thickness of bilayer MoS_2 is ~1 nm. For comparison, the length of a lysine side chain is ~0.6 nm, and the distance between side chains in two consecutive amino acids ($C^{\alpha}-C^{\alpha}$ distance) is ~0.4 nm, dimensions that are very close to the thickness of the membrane. Considering three- or four-layer MoS_2 membranes increase the thickness of the membrane to 1.5 and 2.0 nm, respectively, which consequently decreases the spatial resolution of the nanopore. Therefore, the ability of the nanopore sensor to detect details about the sequence of the amino acids of the peptide would be lower for those systems and were not considered here. To conclude, the combination of the proper pore diameter according to the size of the molecule and the proper thickness according to the sensitivity of the sensor to be designed in terms of time and spatial resolution is the key to improve the efficiency of the sequencing sensors to detect single residues of proteins in the near future.

Translocation of Met-Enkephalin through MoS_2 Nanopores. Met-Enkephalin is a five-residue protein of sequence TYR-GLY-GLY-PHE-MET (YGGFM). This biomolecule, which is one of the smallest neurotransmitter peptides, has been extensively used as a reference model peptide in all-atom MD simulations.[48] This peptide is made of five neutral amino acids, and, to study its threading and translocation through MoS_2 nanoporous membranes, it needs to be artificially charged. The electric field was chosen to correspond to a transmembrane applied voltage $V = 1$ V in all NEMD simulations presented below, as done for translocation of lysine residues above. We attached polylysine tags of different lengths to Met-Enkephalin, from 1 lysine residue (1K) to 5 lysine residues (5K). For each of the five synthetic peptides created here, we performed several MD runs (see Table 2) to capture threading and translocation events and to establish the relationship between those events and the signal of the sensor, that is, drops of ionic conductance ΔG.

Figure 4 shows the results of the translocation of a YGGFM-3K peptide through SL-MoS_2 nanoporous membrane extracted from MD run 2 of duration $T = 300$ ns (see Movie S2). After 50 ns of diffusion of the peptide in bulk solvent and on the MoS_2 top surface, the peptide threads into the pore. As shown in Figure 4a, the translocation takes place between $t = 50.0$ and $t = 208.0$ ns and is characterized by a stepwise process. According to the normal distance $z(t)$ as a function of time, five or six steps can be distinguished (Figure 4a). By monitoring the number of atoms $N_a(t)$ of each amino acid that are inside the pore as a function of simulation time, the following sequence of translocation events is suggested. The C-terminal part of the peptide, corresponding to the polylysine tag (residues #6, #7, and #8), is entering the pore at $t = 51.2$ ns. LYS #8 translocates first, followed by LYS #7 and LYS #6 (Figure 4b,c). Then, at $t = 91.5$ ns, MET and PHE residues enter the pore and stay inside the channel for a long period, over 100 ns. Moreover, LYS #6 and #7 are detected to be in the pore, but they are specifically at the bottom surface at the same time as MET and PHE are in (see snapshots 4, 5, and 6 extracted from MD run in Figure 4b). Translocation of MET residue occurs at $t = 176.8$ ns and takes place at the center of the pore when LYS #7 is completely outside the pore. Finally, at $t = 200.1$ ns, the two GLY residues translocate extremely fast and drag the N-terminal residue; that is, TYR and the whole peptide leave the pore at $t = 208.0$ ns and start to diffuse at the bottom surface up to $t = 300$ ns, the end of the MD trajectory. In addition, as observed for individual lysine residues, the translocation takes place at the edge of the pore rather than at the center of the pore (Figure 4a,c). Indeed, the peptide crawls from the top surface to the edge of the pore and crawls back to the bottom surface after passing through the hole, as clearly shown in step 4 at $t = 176.8$ ns in Figure 4c. The total translocation time is estimated to be $\tau_{trans} = 158$ ns.

During the translocation of YGGFM-3K peptide, we recorded the ionic conductance $G(t)$ ($\Delta t = 1$ ns), as shown in Figure 5a. First, we computed the average conductance observed during the 158 ns of translocation time, correspond-

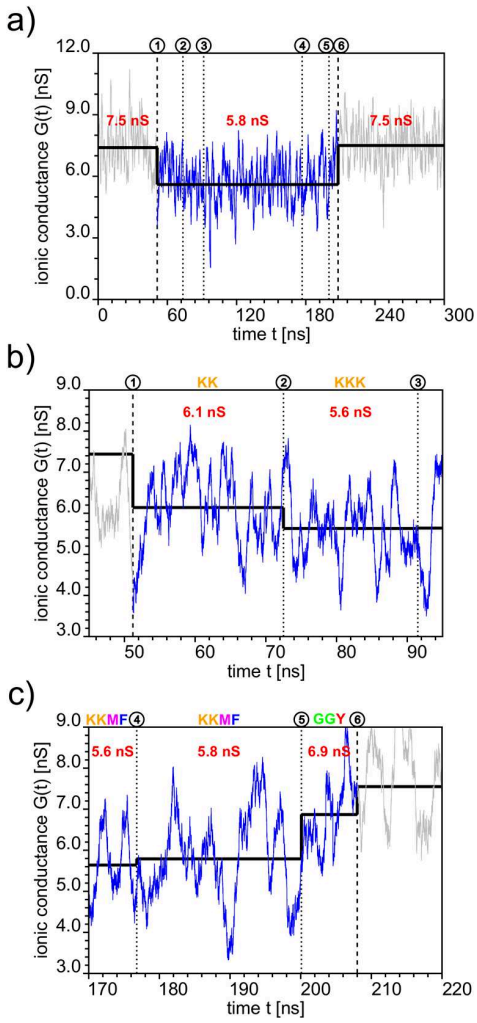

Figure 5. Ionic conductance G as a function of simulation time t recorded during the translocation of YGGFM-3K peptide through SL-MoS_2 (MD run 2, see Figure 4). The conductance is computed using $\Delta t = 1$ ns (eq 1). Black lines represent the average conductance $\overline{G}$ computed before, during, and after translocation. (a) Average conductances $\overline{G}$ from 0 to 300 ns. (b) Average conductances $\overline{G}$ computed from 45 to 95 ns (enlarged sequence of events 1−2−3). (c) Average conductances $\overline{G}$ from 170 to 220 ns (enlarged sequence of events 4−5−6).

DOI: 10.1021/acs.jpcb.8b10634
J. Phys. Chem. B 2019, 123, 2342−2353

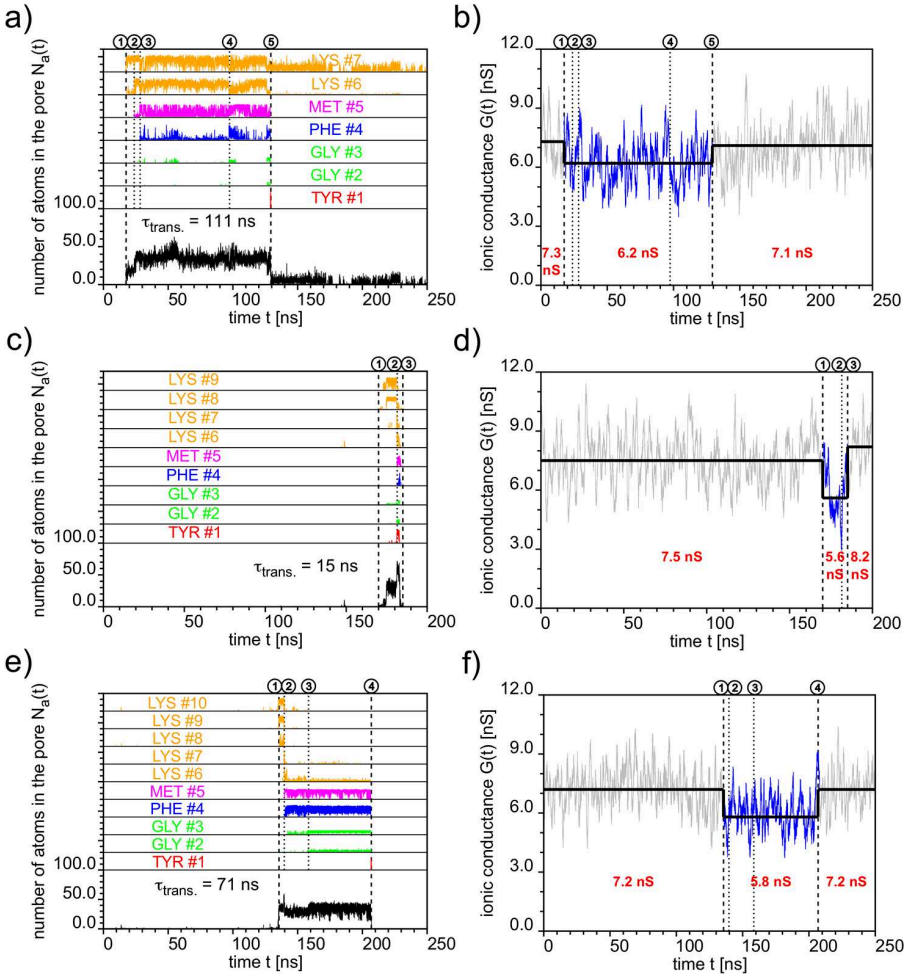

Figure 6. Translocation of Met-Enkephalin with polylysine tag YGGFM-2K (MD run 2, panels a and b), YGGFM-4K (MD run 1, panels c and d), and YGGFM-5K (MD run 1, panels e and f) through SL-MoS_2 (see Table 2). Panels (a, c, e) represent the number of atoms N_a inside the pore as a function of simulation time t, and panels (b, d, f) represent the ionic conductance G as a function of simulation time t.

ing to $\overline{G}_{in}$. When the peptide is inside the pore, the average conductance is ~5.8 nS, whereas the open pore conductance when the peptide is outside the pore $\overline{G}_{out}$ is ~7.5 nS. The corresponding average drop $\Delta\overline{G}$ is 1.7 nS, which represents ~23% of the open pore signal. Furthermore, for each of the sequence of events observed during the MD run, we computed the average ionic conductance between events, as shown in Figure 5b,c. For the sequence of events 1−2−3, we observed the smallest conductance when the three lysine residues are simultaneously inside the pore (Figure 5b), leading to a drop of ~1.9 nS compared to the open pore conductance, $\overline{G}_{out}$. The same drop is detected when PHE and MET residues joined two of the three lysine between events number 3 and 4. In addition, the average drops $\Delta\overline{G}$ are more or less pronounced depending on the number and the type of residues that translocate through the pore. For instance, the same drop is detected when 3 or 4 residues are inside the pore, that is, KKK or KKMF sequence ($\overline{G}$ = 5.6 nS). For event number 5 → 6, which corresponds to the passage of the N-terminal part of the peptide (GGY sequence), a smaller drop is detected compared to event 4 (passage of the KKMF sequence). This behavior could be explained by steric effects, since GLY residues are comprised of the smallest side chain (H atom), whereas LYS, PHE, and MET are characterized by long side chains. Finally, the detection of a single amino acid during the translocation of YGGFM-3K peptide through MoS_2 nanopores based on conductance signal is not clearly achieved in the present simulations, although detection of LYS residues at the C-terminal part of the peptide and the detection of TYR and GLY residues at the N-terminal part is observed. Similar results were observed in the work of Chen et al. for highly charged cationic and anionic peptides,[26] with conductance drops between 1.0 and 3.0 nS reported for identical motifs made from 2 to 4 residues translocating at the same time.

For the other peptides tested in the present work (Table 2), similar results were extracted from NEMD simulations (Figure 6 and Figure S4). First, translocation events are observed for peptides: YGGFM-2K, YGGFM-4K, and YGGFM-5K. No translocation occurs for peptides YGGFM and YGGFM-1K for the duration of the MD simulations presented in this work (see Table 2). Translocation times of 111, 15, 16, and 71 ns were recorded for YGGFM-2K (Figure 6a), YGGFM-4K run 1 (Figure 6c) and 2 (Figure S5), and YGGFM-5K (Figure 6e), respectively. The fact that the translocation time is remarkably smaller for peptides with a 4K tag is not explained here, as our statistics to extrapolate trends about translocation time τ_{trans} as

DOI: 10.1021/acs.jpcb.8b10634
J. Phys. Chem. B 2019, 123, 2342−2353

a function of the polylysine tag length are not sufficient. For the YGGFM-2K peptide, after the complete passage of the biomolecule through the nanopore evidenced by the translocation of the tyrosine amino acid at t = 129.3 ns (Figure S4a), the C-terminal lysine came back to the pore interacting with sulfur atoms at the mouth of the pore. As shown in Figure 6a, it stays in there up to the end of the MD trajectory (see also state 5′ in Figure S4a). It has no substantial impact on the average conductance calculations, since only the side chain of the lysine residue and particularly the $-NH_3^+$ termination interacts with the pore (see Figure S4a in Supporting Information).

For each of the MD trajectories where a translocation occurs, a similar sequence of events is observed: first the passage of the polylysine tag located at the C-terminal part of the peptide through MoS_2 nanopore is detected, followed by the passage of PHE and MET residues. These two specific residues, which are the amino acids with the largest volume among the Met-Enkephalin sequence, remain inside the pore for several tens of nanoseconds, blocking the most the passage of the ions through the hole and involving a discernible average drop of conductance. Finally, the passage of the N-terminal sequence (GGY residues) is observed, the tyrosine translocating extremely fast (less than a couple of nanoseconds) in each of the MD simulations performed here. The maximum average conductance drops between specific events and the open pore conductance observed during translocation are 1.1, 2.6, 1.7, and 1.4 nS for YGGFM-2K (Figure 6b), YGGFM-4K run 1 (Figure 6d) and run 2 (Figure S5), and YGGFM-5K (Figure 6f), respectively. Note that the largest drops characterizing the full translocation of the peptide are detected for the peptide with 4K tag, the one that translocates the fastest. It comes from the fact that this specific peptide does not translocate as a thread peptide inside the pore but as a globular molecule (Figure S4b). Therefore, the center of the pore is completely blocked during the translocation of the biomolecule, and the conductance drop is maximum.

CONCLUSION

In this work, we investigated the translocation of biological peptides through MoS_2 nanoporous membranes using MD simulations. We showed that single lysine amino acid and lysine dipeptide, which are positively charged peptides, translocate easily through single-layer membranes with pore diameter of 2.0 nm. The translocation time is approximately several hundreds of picoseconds, which is extremely fast and cannot be detected experimentally with existing techniques, the maximum resolution being 10 MHz bandwidth so far.[5] In the corresponding ionic conductance signal, drops are observed, but they are not discernible due to the fast fluctuations in the conductance signal as large as the drops because of the low residence time of peptides in the pore. To get discernible conductance drops associated with the passage of single amino acid through MoS_2 nanopores, increasing the thickness of the membranes is the best option at the cost of reducing the signal-to-noise ratio (open pore conductance is reduced by a factor of ∼1.3) and spatial resolution of the sensor (by a factor of ∼3). For lysine dipeptides, we demonstrated that the translocation through bilayer MoS_2 leads to two conductance drops within the translocation event ∼3 nS, directly related to the stepwise passage of individual lysine residue. This specific result could be tested experimentally. Finally, we studied the threading and translocation of Met-Enkephalin protein with polylysine tags through MoS_2 nanopores. Adding polylysine tags increases the global charge of the peptide and facilitates the threading of the protein through the nanopore due to interactions between the charged biomolecule and the electric field. We showed that polylysine tags translocate first through the pore, followed by specific motifs of the protein in a stepwise manner. However, from the conductance signal, single amino acids are not distinguishable. The use of bilayer MoS_2 with such small pores as membrane for sequencing device or the addition of negatively charged residues at the N-terminal part of the protein to counterbalance the positively charged C-terminal part are different options that will be tested in the near future.

ASSOCIATED CONTENT

Supporting Information

The Supporting Information is available free of charge on the ACS Publications website at DOI: 10.1021/acs.jpcb.8b10634.

Results from all MD runs performed that are not presented in the main text (PDF)

Movie S1: Translocation of KK peptide through bilayer MoS_2 nanopore. Movie S2: Translocation of YGGFM-KKK peptide through single-layer MoS_2 nanopore (MP4)

AUTHOR INFORMATION

Corresponding Author

*E-mail: adrien.nicolai@u-bourgogne.fr.

ORCID

Adrien Nicolaï: 0000-0001-7779-4652
Vincent Meunier: 0000-0002-7013-179X
Marija Drndić: 0000-0002-8104-2231
Patrick Senet: 0000-0002-2339-0019

Notes

The authors declare no competing financial interest.

ACKNOWLEDGMENTS

The simulations were performed using HPC resources from DSI-CCuB (Université de Bourgogne). The work was supported by a grant from the Air Force Office of Scientific Research, as part of a joint program with the Directorate for Engineering of the National Science Foundation (NSF), Emerging Frontiers and Multidisciplinary Office, Grant No. FA9550-17-1-0047 and by the NSF Grant No. EFRI 2-DARE (EFRI-1542707). The authors also thank the Conseil Régional de Bourgogne-Franche-Comté for the funding (Grant No. ANER NANOSEQ). A.N. thanks W. Parkin for providing a transmission electron microscopy image of MoS_2 pore.

REFERENCES

(1) Wang, L.; Boutilier, M. S. H.; Kidambi, P. R.; Jang, D.; Hadjiconstantinou, N. G.; Karnik, R. Fundamental transport mechanisms, fabrication and potential applications of nanoporous atomically thin membranes. *Nat. Nanotechnol.* **2017**, *12*, 509−522.

(2) Shi, W.; Friedman, A. K.; Baker, L. A. Nanopore Sensing. *Anal. Chem.* **2017**, *89*, 157−188.

(3) Robertson, J. W. F.; Reiner, J. E. The Utility of Nanopore Technology for Protein and Peptide Sensing. *Proteomics* **2018**, *18*, 1800026.

(4) Danda, G.; Drndić, M. Two-dimensional nanopores and nanoporous membranes for ion and molecule transport. *Curr. Opin. Biotechnol.* **2019**, *55*, 124−133.

DOI: 10.1021/acs.jpcb.8b10634
J. Phys. Chem. B 2019, 123, 2342−2353

(5) Shekar, S.; Niedzwiecki, D. J.; Chien, C.-C.; Ong, P.; Fleischer, D. A.; Lin, J.; Rosenstein, J. K.; Drndić, M.; Shepard, K. L. Measurement of DNA Translocation Dynamics in a Solid-State Nanopore at 100 ns Temporal Resolution. *Nano Lett.* **2016**, *16*, 4483−4489.
(6) Liu, K.; Feng, J.; Kis, A.; Radenovic, A. Atomically thin molybdenum disulfide nanopores with high sensitivity for DNA translocation. *ACS Nano* **2014**, *8*, 2504−2511.
(7) Danda, G.; Das, P. M.; Chou, Y.-C.; Mlack, J. T.; Parkin, W. M.; Naylor, C. H.; Fujisawa, K.; Zhang, T.; Fulton, L. B.; Terrones, M.; et al. Monolayer WS2 Nanopores for DNA Translocation with Light-Adjustable Sizes. *ACS Nano* **2017**, *11*, 1937−1945.
(8) Rodríguez-Manzo, J. A.; Puster, M.; Nicolaï, A.; Meunier, V.; Drndić, M. DNA Translocation in Nanometer Thick Silicon Nanopores. *ACS Nano* **2015**, *9*, 6555−6564.
(9) Kim, S. J.; Kim, D. W.; Lim, J.; Cho, S.-Y.; Kim, S. O.; Jung, H.-T. Large-Area Buckled MoS2 Films on the Graphene Substrate. *ACS Appl. Mater. Interfaces* **2016**, *8*, 13512−13519.
(10) Yun, T.; Kim, J.-S.; Shim, J.; Choi, D. S.; Lee, K. E.; Koo, S. H.; Kim, I.; Jung, H. J.; Yoo, H.-W.; Jung, H.-T.; et al. Ultrafast Interfacial Self-Assembly of 2D Transition Metal Dichalcogenides Monolayer Films and Their Vertical and In-Plane Heterostructures. *ACS Appl. Mater. Interfaces* **2017**, *9*, 1021−1028.
(11) Yun, T.; Jin, H. M.; Kim, D.-H.; Han, K. H.; Yang, G. G.; Lee, G. Y.; Lee, G. S.; Choi, J. Y.; Kim, I.-D.; Kim, S. O. 2D Nanopatterning: 2D Metal Chalcogenide Nanopatterns by Block Copolymer Lithography. *Adv. Funct. Mater.* **2018**, *28*, 1870354.
(12) Feng, J.; Liu, K.; Graf, M.; Lihter, M.; Bulushev, R. D.; Dumcenco, D.; Alexander, D. T. L.; Krasnozhon, D.; Vuletic, T.; Kis, A.; et al. Electrochemical Reaction in Single Layer MoS2: Nanopores Opened Atom by Atom. *Nano Lett.* **2015**, *15*, 3431−3438.
(13) Thiruraman, J. P.; Fujisawa, K.; Danda, G.; Das, P. M.; Zhang, T.; Bolotsky, A.; Perea-López, N.; Nicolaï, A.; Senet, P.; Terrones, M.; et al. Angstrom-Size Defect Creation and Ionic Transport through Pores in Single-Layer MoS2. *Nano Lett.* **2018**, *18*, 1651−1659.
(14) Lv, R.; Robinson, J. A.; Schaak, R. E.; Sun, D.; Sun, Y.; Mallouk, T. E.; Terrones, M. Transition Metal Dichalcogenides and Beyond: Synthesis, Properties, and Applications of Single- and Few-Layer Nanosheets. *Acc. Chem. Res.* **2015**, *48*, 56−64.
(15) Feng, J.; Liu, K.; Bulushev, R. D.; Khlybov, S.; Dumcenco, D.; Kis, A.; Radenovic, A. Identification of single nucleotides in MoS2 nanopores. *Nat. Nanotechnol.* **2015**, *10*, 1070−1076.
(16) Shim, J.; Banerjee, S.; Qiu, H.; Smithe, K. K. H.; Estrada, D.; Bello, J.; Pop, E.; Schulten, K.; Bashir, R. Detection of methylation on dsDNA using nanopores in a MoS2 membrane. *Nanoscale* **2017**, *9*, 14836−14845.
(17) Graf, M.; Liu, K.; Sarathy, A.; Leburton, J.-P.; Radenovic, A. Transverse Detection of DNA in a MoS2 Nanopore. *Biophys. J.* **2018**, *114*, 180a.
(18) Qiu, H.; Sarathy, A.; Schulten, K.; Leburton, J.-P. Detection and mapping of DNA methylation with 2D material nanopores. *NPJ. 2D Mater. Appl.* **2017**, *1*, 3.
(19) Sarathy, A.; Athreya, N. B.; Varshney, L. R.; Leburton, J.-P. Classification of Epigenetic Biomarkers with Atomically Thin Nanopores. *J. Phys. Chem. Lett.* **2018**, *9*, 5718−5725.
(20) Plesa, C.; Kowalczyk, S. W.; Zinsmeester, R.; Grosberg, A. Y.; Rabin, Y.; Dekker, C. Fast Translocation of Proteins through Solid State Nanopores. *Nano Lett.* **2013**, *13*, 658−663.
(21) Larkin, J.; Henley, R. Y.; Muthukumar, M.; Rosenstein, J. K.; Wanunu, M. High-bandwidth protein analysis using solid-state nanopores. *Biophys. J.* **2014**, *106*, 696−704.
(22) Niedzwiecki, D. J.; Lanci, C. J.; Shemer, G.; Cheng, P. S.; Saven, J. G.; Drndić, M. Observing Changes in the Structure and Oligomerization State of a Helical Protein Dimer Using Solid-State Nanopores. *ACS Nano* **2015**, *9*, 8907−8915.
(23) Fologea, D.; Uplinger, J.; Thomas, B.; McNabb, D. S.; Li, J. Slowing DNA Translocation in a Solid-State Nanopore. *Nano Lett.* **2005**, *5*, 1734−1737.
(24) Kowalczyk, S. W.; Wells, D. B.; Aksimentiev, A.; Dekker, C. Slowing down DNA Translocation through a Nanopore in Lithium Chloride. *Nano Lett.* **2012**, *12*, 1038−1044.
(25) Liu, K.; Lihter, M.; Sarathy, A.; Caneva, S.; Qiu, H.; Deiana, D.; Tileli, V.; Alexander, D. T. L.; Hofmann, S.; Dumcenco, D.; et al. Geometrical Effect in 2D Nanopores. *Nano Lett.* **2017**, *17*, 4223−4230.
(26) Chen, H.; Li, L.; Zhang, T.; Qiao, Z.; Tang, J.; Zhou, J. Protein Translocation through a MoS2 Nanopore:A Molecular Dynamics Study. *J. Phys. Chem. C* **2018**, *122*, 2070−2080.
(27) Lee, D.-S.; Park, S.; Han, Y. D.; Lee, J. E.; Jeong, H. Y.; Yoon, H. C.; Jung, M. Y.; Kim, S. O.; Choi, S.-Y. Selective protein transport through ultra-thin suspended reduced graphene oxide nanopores. *Nanoscale* **2017**, *9*, 13457−13464.
(28) Luan, B.; Zhou, R. Single-File Protein Translocations through Graphene-MoS2 Heterostructure Nanopores. *J. Phys. Chem. Lett.* **2018**, *9*, 3409−3415.
(29) Paraskevopoulou, V.; Falcone, F. H. Polyionic Tags as Enhancers of Protein Solubility in Recombinant Protein Expression. *Microorganisms* **2018**, *6*, 47.
(30) Plimpton, S. Fast Parallel Algorithms for Short-Range Molecular Dynamics. *J. Comput. Phys.* **1995**, *117*, 1−19.
(31) Jiang, J.-W. Parametrization of StillingerWeber potential based on valence force field model: application to single-layer MoS 2 and black phosphorus. *Nanotechnology* **2015**, *26*, 315706.
(32) Lindorff-Larsen, K.; Piana, S.; Palmo, K.; Maragakis, P.; Klepeis, J. L.; Dror, R. O.; Shaw, D. E. Improved side-chain torsion potentials for the Amber ff99SB protein force field. *Proteins: Struct., Funct., Genet.* **2010**, *78*, 1950−1958.
(33) Jorgensen, W. L.; Chandrasekhar, J.; Madura, J. D.; Impey, R. W.; Klein, M. L. Comparison of simple potential functions for simulating liquid water. *J. Chem. Phys.* **1983**, *79*, 926−935.
(34) Joung, I. S.; Cheatham, T. E. Determination of alkali and halide monovalent ion parameters for use in explicitly solvated biomolecular simulations. *J. Phys. Chem. B* **2008**, *112*, 9020−9041.
(35) Liang, T.; Phillpot, S. R.; Sinnott, S. B. Parametrization of a reactive many-body potential for Mo−S systems. *Phys. Rev. B: Condens. Matter Mater. Phys.* **2009**, *79*, 245110.
(36) Varshney, V.; Patnaik, S. S.; Muratore, C.; Roy, A. K.; Voevodin, A. A.; Farmer, B. L. MD simulations of molybdenum disulphide (MoS2): Force-field parameterization and thermal transport behavior. *Comput. Mater. Sci.* **2010**, *48*, 101−108.
(37) Heiranian, M.; Farimani, A. B.; Aluru, N. R. Water desalination with a single-layer MoS_2 nanopore. *Nat. Commun.* **2015**, *6*, 8616.
(38) Perez, M. D. B.; Senet, P.; Meunier, V.; Nicolaï, A. Computational Investigation of the Ionic Conductance through Molybdenum Disulfide (MoS2) Nanopores. *WSEAS Transactions On Circuits And Systems* **2017**, *16*, 35.
(39) Pérez, M. D. B.; Nicolaï, A.; Delarue, P.; Meunier, V.; Drndić, M.; Senet, P. Improved model of ionic transport in 2-D MoS2 membranes with sub-5nm pores. *Appl. Phys. Lett.* **2019**, *114*, 023107.
(40) Swope, W. C.; Andersen, H. C.; Berens, P. H.; Wilson, K. R. A computer simulation method for the calculation of equilibrium constants for the formation of physical clusters of molecules: Application to small water clusters. *J. Chem. Phys.* **1982**, *76*, 637−649.
(41) Nosé, S. A unified formulation of the constant temperature molecular dynamics methods. *J. Chem. Phys.* **1984**, *81*, 511−519.
(42) Hoover, W. G. Canonical dynamics: Equilibrium phase-space distributions. *Phys. Rev. A: At., Mol., Opt. Phys.* **1985**, *31*, 1695−1697.
(43) Isele-Holder, R. E.; Mitchell, W.; Ismail, A. E. Development and application of a particle-particle particle-mesh Ewald method for dispersion interactions. *J. Chem. Phys.* **2012**, *137*, 174107.
(44) Ryckaert, J.-P.; Ciccotti, G.; Berendsen, H. J. C. Numerical integration of the cartesian equations of motion of a system with constraints: molecular dynamics of n-alkanes. *J. Comput. Phys.* **1977**, *23*, 327−341.
(45) Andersen, H. C. Rattle: A velocity version of the shake algorithm for molecular dynamics calculations. *J. Comput. Phys.* **1983**, *52*, 24−34.

DOI: 10.1021/acs.jpcb.8b10634
J. Phys. Chem. B 2019, 123, 2342−2353

(46) Barati Farimani, A.; Heiranian, M.; Aluru, N. R. Identification of amino acids with sensitive nanoporous MoS 2: towards machine learning-based prediction. *NPJ. 2D Materials and Applications* **2018**, *2*, 14.
(47) Wu, L.; Liu, H.; Zhao, W.; Wang, L.; Hou, C.; Liu, Q.; Lu, Z. Electrically facilitated translocation of protein through solid nanopore. *Nanoscale Res. Lett.* **2014**, *9*, 140.
(48) Sicard, F.; Senet, P. Reconstructing the free-energy landscape of Met-enkephalin using dihedral principal component analysis and well-tempered metadynamics. *J. Chem. Phys.* **2013**, *138*, 235101.

DOI: 10.1021/acs.jpcb.8b10634
J. Phys. Chem. B 2019, 123, 2342−2353